Heteroepitaxy of Group-III-Nitrides for the Application in Laser Diodes

Tim Böttcher

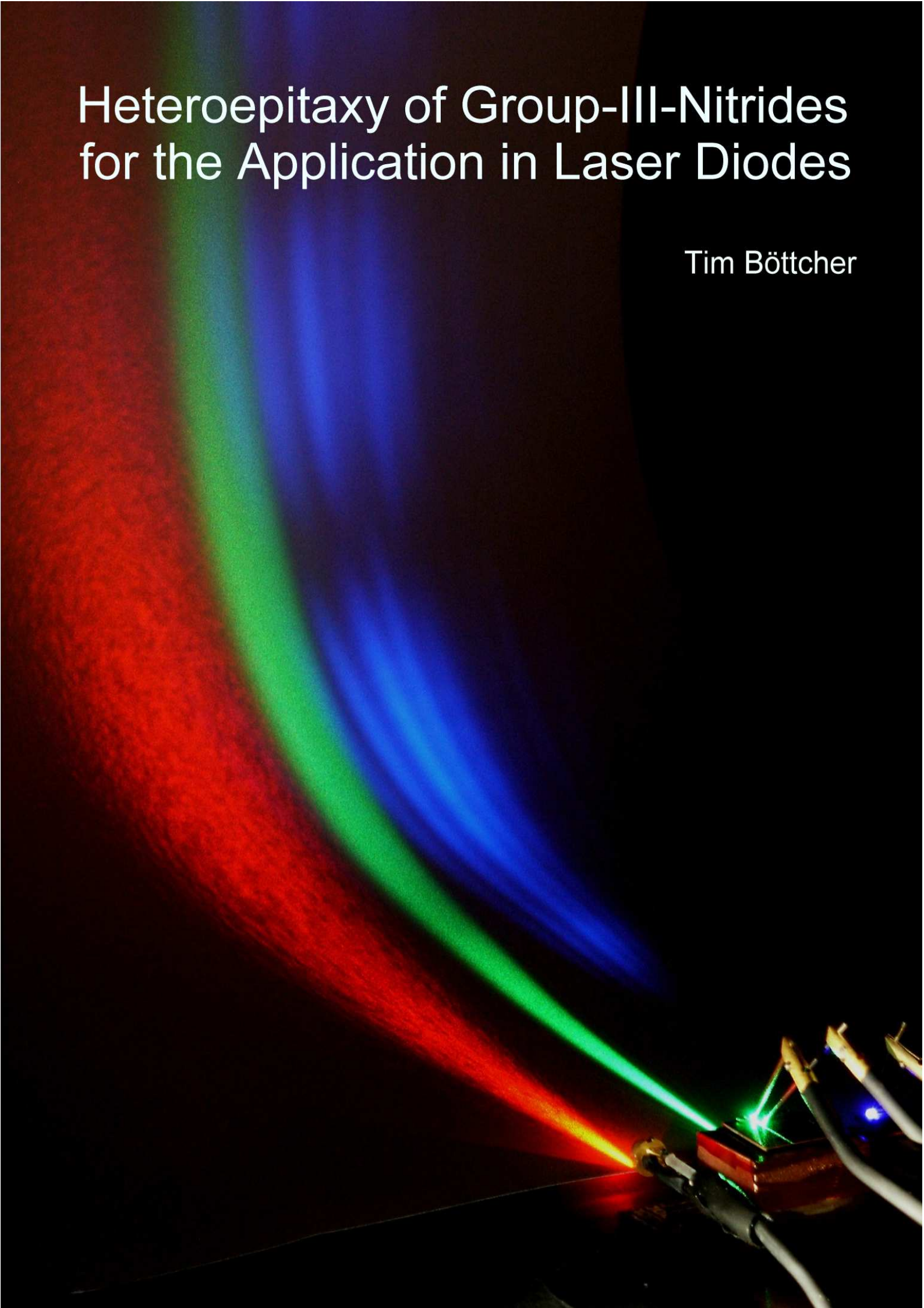

University of Bremen

Heteroepitaxy of Group-III Nitrides for the Application in Laser Diodes

Tim Böttcher

A dissertation submitted in partial satisfaction of the requirements for the degree of Doktor der Naturwissenschaften.

Committee :

Prof. Detlef Hommel
Prof. James S. Speck
Prof. Jens Falta
Prof. Bernd Meinerzhagen

February, 2002

" In physics, you don't have to go around making trouble for yourself – nature does it for you. "

Frank Wilczek
Longing for the Harmonies

Contents

Introduction

In spite of the rapid evolution of the group-III nitrides over the last years, this thesis is founded on one of the oldest compound semiconductor material systems. The first report is from 1907 and treats the binary compound AlN [1]. The basic compound GaN was synthesized as early as 1932 by Johnson *et al.* [2]. Furthermore, GaN was even one of the first materials grown by metalorganic vapor phase epitaxy (MOVPE). Manasevit himself has performed these growth experiments soon after he invented this growth technique in 1968 [3]. The fundamental data of GaN was known in the late 60s and beginning 70s, when the first publications on the band gap energy and the crystal structure appeared together with the first deposition on sapphire [4, 5].

When GaAs and all the other "classic" semiconductors started their victorious career to revolutionize the optoelectronic industry in the late 70s, GaN remained in the research laboratories. What happened ? Although it was possible to manufacture light emitting devices, using deep luminescent centers, conducting p-type GaN has never been obtained. It took until 1988, when Akasaki and Amano accidently discovered that the p-type dopant magnesium has to be activated [6]. They investigated the cathodoluminescence of Mg-doped GaN in a scanning electron microscope and observed the luminescence intensity to increase with the scanning time [7]. Later, this was explained by the passivation of the Mg acceptor by hydrogen, which are released due to the energy of the electron beam. Among other discoveries made during the same period, this was probably the breakthrough for the nitrides, since it was now possible to grow and fabricate pn-junctions. It took two more years until Nakamura developed an alternative activation technique, which was a simple annealing step in nitrogen to remove the hydrogen [8]. The following boom of the nitrides was enormous, since there was a huge market and no competitive products were available. The unchallenged leader during this period was Nakamura working at the company Nichia. He always stayed ahead of anybody else, such that during the first years people measured their device performance in "milli-Nichia". The first injection laser was presented in 1995 - it took only six years from the first p-type doping to the first laser diode [9]. Interestingly, the reason for Nakamura to start with the nitride business was the lack of competition from big companies in this field, and not the expectation of huge profit from these devices [10].

The group-III nitrides incorporate many new developments of modern semiconductor research. For example, no suitable substrate for homoepitaxy has been available so far, such that a large fraction of the research is involved with the heteroepitaxy on substrates having a huge lattice mismatch. This requires the growth on a buffer layer, similar to the growth of GaAs on silicon. Lateral overgrowth techniques have approached a new summit, as it is currently the only way to obtain almost dislocation-free material in

large quantities. Strain engineering became an important aspect of device development, since the lattice mismatch of all the alloys is significant and quarternaries are not yet fully developed. And the concepts of strained-layer superlattices and good knowledge of the band structure are essential to understand the operation of the devices. In spite of this, the growth of the nitrides sometimes gives the impression of modern alchemy, caused by the extreme sensitivity to the particular reactor geometry. It is almost impossible to transfer growth parameters directly from one MOVPE reactor to another, as minor modifications can have a huge impact on flow geometry or pre-reactions, making the comparison of results very hard. But there is also a positive aspect, since it gives more freedom to discuss the time-consuming but mostly publication-irrelevant work of growth optimization.

Course of the experimental work

The main goal of the Ph.D. thesis was to establish the MOVPE growth of group-III nitrides at the University of Bremen. But since the delivery of the reactor was scheduled for 1999, which was the second year of the research, the molecular beam epitaxy (MBE) of these materials was the main research activity during the first one and a half years. The main focus was the growth of quantum-well structures and the quasi-homoepitaxy on MOVPE templates. In September of 1999 the long-awaited MOVPE reactor was ready to start operation and the research changed from the "scientific" world of MBE to the "magic" world of MOVPE. At the institute, nobody had experience with that technique, such that the whole growth had to be started from scratch. Luckily, this time full of success and disappointments could be shared with Sven Einfeldt and later on with Stephan Figge, who were the other two members of the MOVPE triad. A major step forwards was the development of a reflectometry system for our reactor soon after. It provided much better insight into the growth process, in particular it allowed control of the high-temperature island coalescence process. In 2000, the basics were established and the research fields were splitted. I worked on $In_xGa_{1-x}N$-based quantum-well structures, on the doping of the active region in devices and investigated the high temperature island coalescence in more detail. $Al_xGa_{1-x}N$ was the field of Sven Einfeldt and Marc Dießelberg. Doping, specially p-type doping, was investigated by Stephan Figge. From time to time, the most recent results were collected and combined to grow injection laser structures. The design of these structures was commonly done in collaboration with Stephan Figge. Most of the device-relevant work was done during the last year, after a better understanding of the growth of quantum wells and the p-type doping. It was hampered by the device technology, which stayed underdeveloped until recently due to the lack of dry etching equipment. Therefore we founded a very fruitful collaboration with Christoph Zellweger from the University of Lausanne, Switzerland, for the processing of the laser structures. Recently, the institute has acquired a chemical assisted ion beam etching system, which will hopefully enable us to establish our own device processing.

Part of the work on transmission electron microscopy was done during a visit of the research group of Prof. Speck at the University of California at Santa Barbara in the second half of 2000. Furthermore, during this stay the model of high temperature

island coalescence was developed and the simulation of quantum well band structures was started.

Thesis synopsis

This thesis mainly covers the results obtained for the growth by MOVPE, and summarizes the relevant aspects of MBE-grown quantum-well structures. The appendices will provide additional details as a background to the presented work.

The first chapter will provide the most relevant background to understand the properties of quantum wells and nitride-based laser structures. This includes a review of material parameters available in literature as well as the description of some nitride-relevant aspects, like piezoelectricity and the layer sequence of a group-III nitride laser diode. Since the chapter can only provide a framework of available information, some recommended books and review articles are listed at the end. The second chapter describes the most important experimental methods used within this work. Particular emphasis is put onto the description of reflectometry and x-ray diffraction, since the aspects relevant for the nitrides are not well covered in literature. The growth by MOVPE is detailed in the third chapter, and starts with the thermodynamic description of the nitride synthesis. As the formation of the dislocation structure is closely connected to the nucleation layer overgrowth process at high temperature, the relevant growth parameters to control the high temperature island growth mode are discussed thereafter. The consequences of this overgrowth process for the threading dislocation density and the strain state of the layer are explained in the fourth chapter in the framework of quantitative models. These allow to determine the edge and screw type threading dislocation densities from x-ray diffraction and to understand the observed variation of the strain state with coalescence. The former model is based on previous work by Heidrun Heinke. The fifth chapter treats $In_xGa_{1-x}N/GaN$ multiple quantum wells, grown by MBE as well as MOVPE. Special interest was laid upon the experimentally observed rise in photoluminescence peak intensity with the Si-doping of the GaN barriers. Experimental results were compared to transition energies obtained from band structure calculations to understand this phenomenon. The appendices contain additional information about the reflectometer electronics, about the program used for the band structure calculations and about specific growth aspects of the Thomas Swan MOVPE reactor. Although a significant fraction of the last year was spent on the development of the laser diode, this will not be discussed within this thesis, as all the grown structures were collections of the most recent results at a time.

The development of nitride-based devices requires a very interdisciplinary orientation of the research work, which I enjoyed throughout my whole studies. Accordingly, all external data presented within this thesis will be explicitly mentioned.

Chapter 1

Basics

This chapter will sketch some of the basic knowledge to understand the design of laser diodes based on group-III nitrides. It does not claim to be a complete reference, since much more is involved to understand the operation of these devices. Most of this is published in books and review articles, which will be listed at the end of the chapter.

1.1 Some fundamentals

The group-III nitrides are commonly found to grow in the hexagonal crystal structure, as this is the thermodynamically more stable modification. It is possible to obtain films showing a cubic lattice, but this requires the epitaxy on suitable cubic substrates. Up to now, the material of the highest perfection material has been grown in the hexagonal phase, which will be discussed in the remainder of this section. The GaN (InN, AlN) unit cell is sketched in Fig. 1.1, where the two sublattices of Ga (In,Al) and nitrogen atoms are shown in different colors. The c-axis is aligned perpendicular to the plane of the hexagons. The hexagonal stacking sequence ..ABABAB.. is found for the stacking of GaN (InN,AlN) bilayers, since the two sublattices are shifted relative to each other by 5/8 of the c-axis lattice parameter. The bonding to the next neighbors is tetrahedral, such that each group-III atom is coordinated by four nitrogen atoms, and vice versa. The unit cell is described by the two lattice parameters c and a, and the dimensionless parameter u, which characterizes the bond aligned along the main axis. The latter is measured in units of the c-axis lattice parameter, and provides information about the distortion of the unit cell. For an ideal hexagonal lattice u amounts to 3/8. The lattice parameters and the elastic properties will be discussed in more depth in Section 1.5.

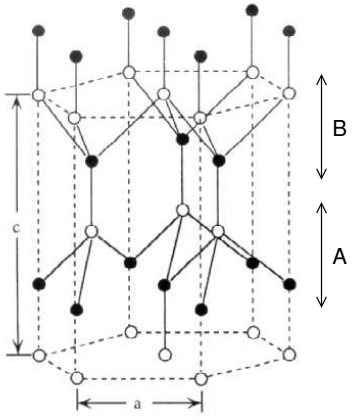

Figure 1.1: Unit cell of GaN [11].

The substructure of the unit cell creates an asymmetry of the unit cell along the c-axis, i.e. the directions of the bonds are different along [0001] and [000$\overline{1}$]. This asym-

metry is called *polarity* of the film, and is defined by the direction of the (group-III)-N bond aligned parallel to the *c*-axis with respect to the orientation of the surface normal of the layer. A film is called Ga- or [0001]-polar, if the nitrogen atoms are placed on top of the group-III atoms, and N- or [000$\bar{1}$]-polar for the group-III elements residing on top the nitrogen. This is illustrated in Fig. 1.2.

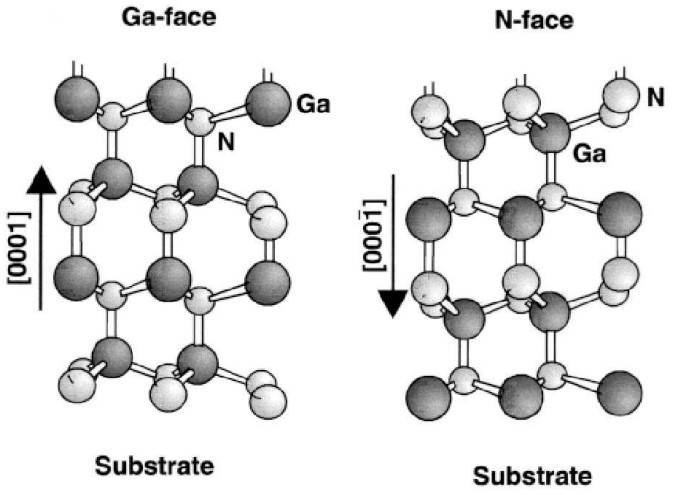

Figure 1.2: The two polarities of the group-III nitrides. The layer normal is pointing upwards [12].

The polarity of the film is important to know due to its implication for the surface properties and the piezoelectric field present in group-III nitrides (see Section 1.4). The bond arrangement on the surface is different for Ga- and N-polar material, which strongly influences the adatom mobilities on the surface and therefore determines the surface perfection. This has been widely investigated theoretically as well as experimentally for example by Neugebauer *et al.* and Feenstra *et al.* (i.e. [13, 14, 15] and references therein). In particular, this is relevant for the molecular beam epitaxy (MBE) of this material, since GaN grown by MBE onto sapphire is commonly N-polar, whereas Ga-polar material is obtained for the growth by metalorganic vapor phase epitaxy (MOVPE).

Another very interesting feature of the group-III nitrides is their exceptional hardness and chemical inertness even at high temperature combined with a good thermal conductivity [11]. This makes semiconductor devices based on this material system very stable, since high operation temperatures are possible without destroying the lattice. But it generates problems during for the processing of devices, as not suitable wet chemical etchant has been developed so far. The only possibility to pattern group-III nitrides with the required high perfection is to use dry etching techniques like reactive ion etching (RIE) or chemical assisted ion beam etching (CAIBE) [16]. For devices based on heteroepitaxial GaN on sapphire, another problem arises from the low thermal conductivity of the sapphire substrate. This blocks the dissipation of heat from the active region and the contacts, such that significant technological effort is necessary to achieve industry-relevant device lifetimes.

1.2 Ternary alloys

Ternary or quaternary alloys are inevitable for the production of heterostructures, as they allow the free design of the band structure. Depending on the composition of the alloys, the band structure parameter can be precisely adjusted according to the requirements of the particular structure. Up to now, only the ternaries $In_xGa_{1-x}N$ and $Al_xGa_{1-x}N$ found usage in devices besides GaN due to good understanding of the growth conditions. However, future devices might employ quaternary alloys. The section will concentrate on these two ternaries and will list the most important parameters for laser structures, namely band gap, band offset, lattice parameter and refractive index.

1.2.1 Band gap and lattice parameters

In order to achieve a high external quantum efficiency, optoelectronic devices require a direct band gap of the semiconductor they are based on. The group-III nitrides are such direct gap semiconductors with the emission in the short wavelength region of the visible spectrum. The only alternative material system is (Cd,Mg,Zn)(S,Se), which explains the enormous interest of the optoelectronic industry. The problem of the II-VI based devices is their relatively rapid degradation, arising from the low stability of the lattice. This allows the generation and glide of dislocations in operating devices, which destroys the active region and accordingly limits the lifetime.

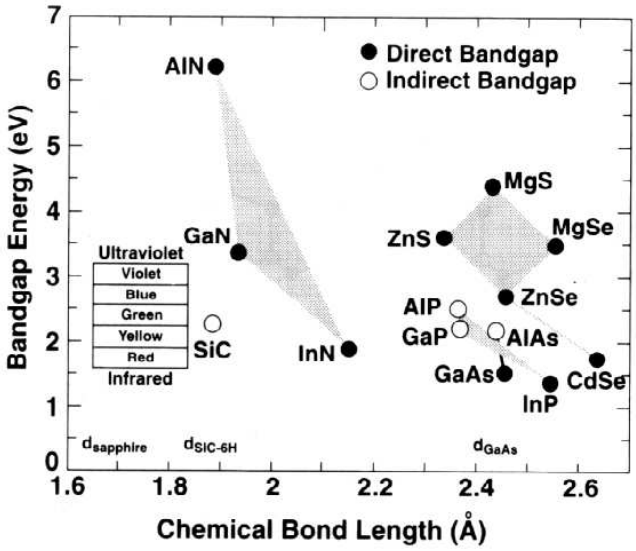

Figure 1.3: The band gap in dependence on the chemical bond length for the three most important material systems covering the visible spectral region [17].

The probably most often shown graph in the optoelectronic GaN community is the plot of the band gap energy versus the *a*-axis lattice parameter or the bond length as seen in Fig. 1.3. Shown are the three key systems for light emitters, the II-VI system (Cd,Mg,Zn)(S,Se), and the III-V systems (In,Al,Ga)(As,P) and (In,Al,Ga)N. Within the II-VI system it is theoretically possible to access the whole visible spectrum, depending on the cadmium content of the active region. The same applies to the group-III nitrides,

where the emitting wavelength is defined by the indium content of the commonly used ternary $In_xGa_{1-x}N$. The very successful (In,Al,Ga)(As,P) system is restricted to longer wavelength in the infrared-yellow range of the spectrum, but has been unsurpassed so far. The plot also illustrates the big advantage of the concurrent II-VI material system, which is the availability of the (almost) lattice-matched substrate GaAs. This allows to obtain structures with low dislocation densities, and it possible to prepare laser facets of high perfection by cleaving of the substrate. For the group-III nitrides, bulk GaN as a homoepitaxial substrate is not available yet, which imposes big difficulties in the fabrication of laser diodes.

The change of the band gap energy with composition of a ternary is most commonly described by the *bowing parameter*, which is the quadratic correction to the linear band gap variation described by Vegard´s law :

$$E_g = (1-x)\,E_g(\mathrm{GaN}) + x\,E_g(\mathrm{AlN/InN}) - b\,x(1-x) \tag{1.1}$$

The bowing of $Al_xGa_{1-x}N$ can be satisfactorily described with the bowing parameter. It is still under discussion for $In_xGa_{1-x}N$, such that Table 1.1 contains reported bowing parameters as well as other relations for the band gap variation of $In_xGa_{1-x}N$. In the listing, reports for strained structures grown by MOVPE on GaN as well as theoretical calculations were considered.

To describe the bowing of pseudomorphic $Al_xGa_{1-x}N$ grown on GaN, a bowing parameter of 0.62 as published in Ref. [21] is recommended. For $In_xGa_{1-x}N$ with molar indium fractions below 0.15 the linear relation given by McCluskey *et al.* has been proven to be very successful [26]. Since the alloys under investigation fall in this composition range, it will be used within this thesis.

1.2.2 Band offsets

To understand band structures, it is necessary to know the band offsets of the binary componds InN, AlN and GaN. The band alignment of the heterojunctions is found to be of Type-I, where the band gap of the semiconductor with the lower energy lies completely within the band gap of the other. Measurements of the valence band offset are difficult and often employ indirect methods like the characterization of electron core-level energy levels obtained from XPS. These results can additionally be superimposed by polarization or interface preparation effects, such that the experimental literature values available are subject to significant scatter. Theoretical calculations are not yet developed enough to make reliable predictions, so they scatter as well. Values for the junctions AlN-GaN, InN-GaN and InN-AlN are shown in Table 1.2. The table contains theoretical as well as experimental data points.

The average, relative band offsets obtained from these references are almost the same for all three interfaces, which is similar to other known semiconductor systems like InAs-GaAs [42]. It amounts to roughly 30% of the band gap difference, which will be assumed for all further calculations. This band alignment is visualized in Fig. 1.4.

$Al_xGa_{1-x}N$

Parameter	Value	Reference
Band gap GaN (300 K)	3.42 eV	[18]
Band gap AlN (300 K)	6.2 eV	[19]
Bowing parameter [eV]	0.53	[20]
	0.62	[21]
	0.0	[18]
	0.6	[22]
	0.25	[23]

$In_xGa_{1-x}N$

Parameter	Value	Reference
Band gap GaN (300 K)	3.42 eV	[18]
Band gap InN (300 K)	1.89 eV	[24]
Band gap $In_xGa_{1-x}N$ [eV]	3.42 - 3.8 x	[25]
	3.42 - 3.95 x	[26]
Bowing parameter [eV]	4.0 (for x≈0.1)	[27]
	2.65	[28]
	3.2	[23]

Table 1.1: Bowing of $Al_xGa_{1-x}N$ and $In_xGa_{1-x}N$ as published in literature.

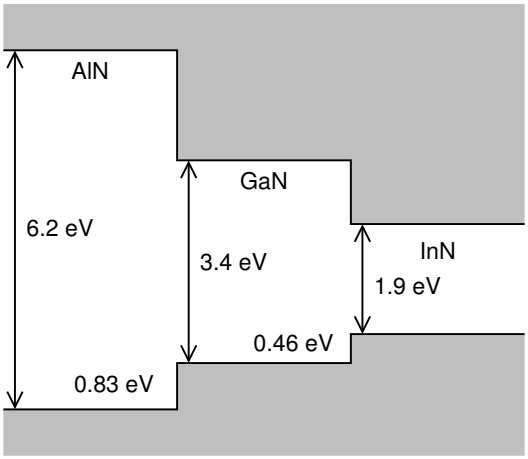

Figure 1.4: The band alignment of the AlN-GaN-InN binary nitrides.

Valence Band Offset				
AlN/GaN	InN/GaN	InN/AlN	Method	Reference
0.8			XPS	[29]
0.5			PL	[30]
1.36			XPS	[31]
0.65			XPS/UPS	[32]
0.83			theory	[33]
0.73	0.70	1.37	theory	[34]
0.54			theory	[35]
0.85	0.2		theory	[36]
0.67			theory	[37]
0.7	0.3		theory	[38]
0.81	0.48	1.25	theory	[39]
	0.95		theory	[40]
	0.58		PL	[41]
0.76	0.54	1.29	average	
28 %	35 %	30 %	$\Delta E_v/\Delta E_g$	

Table 1.2: Valence band offsets as published in literature.

1.2.3 Refractive index

The optical wave in the laser structure is guided along the plane of the quantum well. Accordingly, the propagation is defined by the refractive indices of the individual layers in the structure. In order to achieve stimulated emission, a high overlap of the guided wave with the quantum well is required. This confinement is provided by a waveguide with surrounding cladding layers of lower refractive index, which concentrates the optical field at the center of the waveguide. Relevant for these calculations are the refractive indices at the emission wavelength, i.e. in the short wavelength region of the visible spectrum.

These are contained in Fig. 1.5 for the alloys $In_xGa_{1-x}N$ and $Al_xGa_{1-x}N$ in the concentration range up to 15%. The $Al_xGa_{1-x}N$ data was generated assuming a Sellmeier dispersion law as detailed in Section 2.3.3. For the refractive index of $In_xGa_{1-x}N$, the experimental dispersion curve of GaN was rigidly shifted to lower energies according to the band gap energy difference. In accordance with the band gap energies, $Al_xGa_{1-x}N$ shows a lower refractive index compared to GaN and the index of $In_xGa_{1-x}N$ is higher. For the laser design employing a GaN waveguide this means, that higher confinement and higher overlap with the active region is achieved for higher Al molar fractions in the cladding layers.

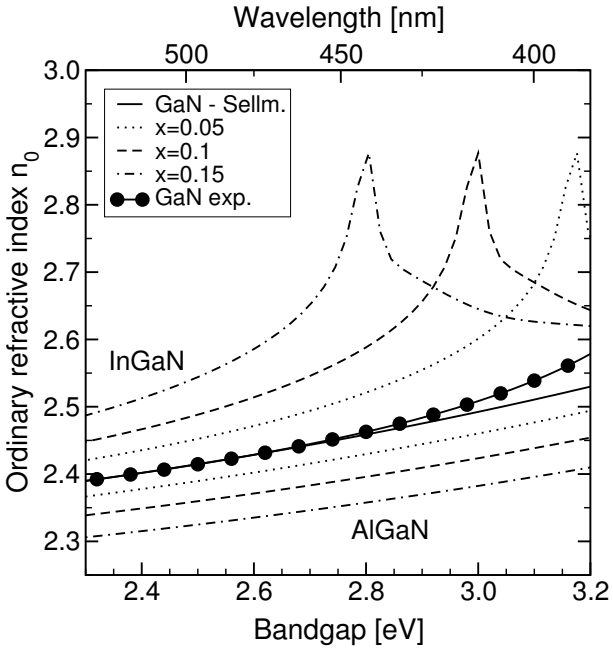

Figure 1.5: The refractive index of $In_xGa_{1-x}N$ and $Al_xGa_{1-x}N$ in dependence on the band gap energy for alloy compositions up to 15%. The experimental data set was measured by A. Kasic, University of Leipzig, Germany.

1.2.4 Typical laser structure

The concept of a separate confinement heterostructure laser is shown in Fig. 1.6 [11]. This type of structure incorporates two separate systems for the confinement of the charge carriers and the propagating light wave [42]. The carrier confinement is provided by the active region having the lowest band gap in the whole structure. This is achieved by the use of $In_xGa_{1-x}N$ at the pn-junction, where the charge carriers are trapped and the formation of a population inversion is enforced (Fig. 1.6 (a)). The optical confinement is defined by the two $Al_xGa_{1-x}N$ cladding layers and the GaN waveguides covering the active region on the p- and n-type doped sides.

The refractive index profile of the structure is sketched in Fig. 1.6 (b). The highest band gap material has the lowest refractive index, such that the refractive index drops towards the $Al_xGa_{1-x}N$ cladding layers. Some additional localization of the optical wave originates from the high refractive index in the active region, but since its volume is small, the main confinement is given by the offset in refractive index at the interfaces of waveguide and cladding layers. For the propagation along the plane of the active region, the electromagnetic wave interferes with the interface under grazing incidence, and therefore undergoes total internal reflection. The optimum waveguide thickness, i.e. the thickness of the two GaN waveguides plus the active region, is dependent on the wavelength of the emitted light and amounts to $\sim \lambda/2$. The light intensity profile of the sketched structure is found in Fig. 1.6 (c), which has its peak intensity at the position of the active region. This provides a high overlap of the light field and the active region containing the inversion of the charge carrier population. Accordingly, the stimulated emission of light is enforced and the threshold current density can be reduced.

For GaN-based laser structures grown on sapphire, a quasi-standard structure has established over the last years, which is depicted in Fig. 1.7 together with the band structure in the vicinity of the active region [10]. The active region consists of $In_xGa_{1-x}N$

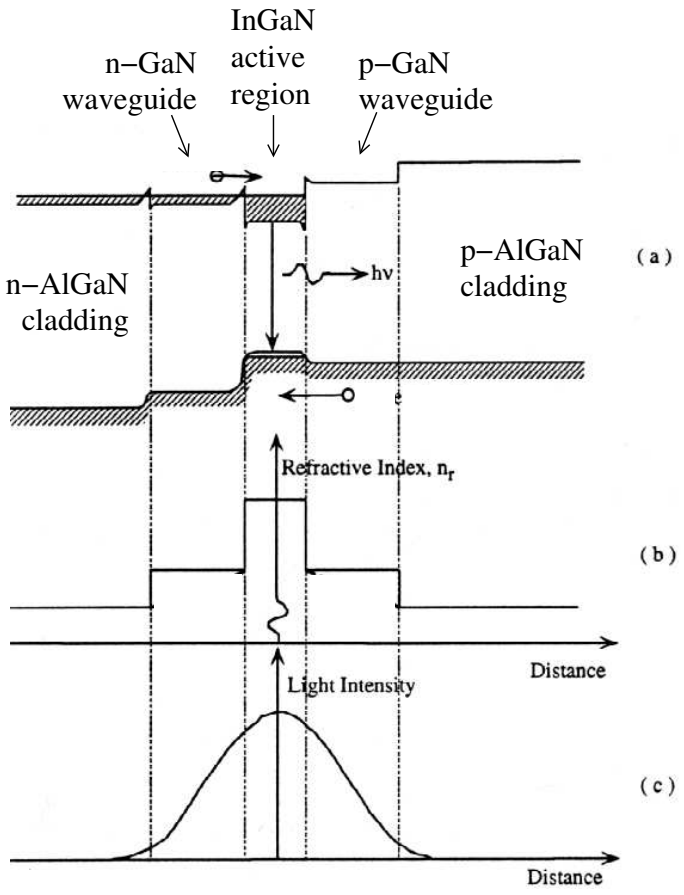

Figure 1.6: Principle of a separate confinement heterostructure laser (a) Band structure of the biased structure (b) Refractive index profile (c) Light intensity profile [11].

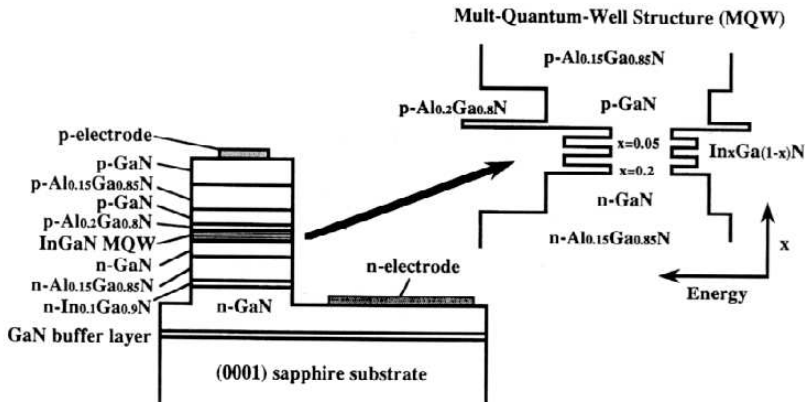

Figure 1.7: The layer structure of a GaN-based laser diode [10].

quantum wells with slightly Si-doped $In_xGa_{1-x}N$ barriers. Commonly, three wells with an In mole fraction of ∼0.14 are used together with barriers containing ∼3% indium. The GaN waveguides have a thickness of 100 nm each, and the cladding layers are ∼400 nm thick with an aluminum molar fraction of 0.1. A peculiarity of GaN-lasers is the p-$Al_xGa_{1-x}N$ blocking layer fabricated on top of the active region. This is required due to the very low hole mobility, which is over an order of magnitude below the one of the electrons. Without the blocking layer, electrons can pass the active region without radiative recombination and recombine non-radiatively in the waveguides. This phenomenon is called current overflow, which reduces the quantum efficiency and causes significant generation of heat. The high conduction band offset of the $Al_xGa_{1-x}N$ makes the blocking layer most efficient for the electrons, preventing the overflow. The thickness of the blocking layer is around 20 nm and the aluminum content is ∼20%. The detrimental effect of the blocking layer is the reduction of the overlap of light wave and active region.

The lower $In_xGa_{1-x}N$ layer is grown to partially compensate the tension in the cladding layers, which allows a higher Al fraction without the formation of macroscopic cracks. The p-GaN layer on top of the structure is needed to achieve a low contact resistivity, since the p-dopability of $Al_xGa_{1-x}N$ is limited. Both layers can be parasitic waveguides and should be as thin as possible. Typical thicknesses are 100 nm.

1.3 Doping

The dopability of the nitrides is essential for the fabrication of optoelectronic devices. Difficulties arise from the high band gap energy, which prevents a shallow acceptor energy level. The n-type doping is commonly achieved by silicon, which incorporates into the lattice on the group-III site, thereby forming a shallow donor with an activation energy of 22 meV for device-relevant doping levels [43]. The solubility of Si into GaN is high, such that doping levels well in excess of 1×10^{19} cm^{-3} are achieved . The doping level is linearly dependent on the molar flow ratio of the precursors $f(\mathrm{SiH_4})/f(\mathrm{TMG})$. For sets of samples grown in Bremen the following dependence of the free electron concentration N_e on the *gas flows* was obtained :

$$N_e[\mathrm{cm}^{-3}] = 2 \times 10^{16}\,\mathrm{cm}^{-3} + 1.41 \times 10^{19}\,\mathrm{cm}^{-3}\,\frac{F(\mathrm{SiH_4})}{F(\mathrm{TMG})} \tag{1.2}$$

The underlying set of samples was grown at 100 Torr with a TMG flow of 47 sccm (95 μmol/min) and silane diluted in hydrogen at a concentration of 10 ppm in hydrogen, but other samples grown at high temperature under different conditions have been found to follow this relation as well within the limits of accuracy. Silane seems to be not harmful to the crystalline perfection of the layers, at least according to x-ray diffraction (XRD). Other demonstrated n-type dopants are GeH_4 and H_2Se. The latter incorporates on the nitrogen site [44]. But since silane is used in industry as the common dopant for GaAs, it is the most important one.

The p-type doping has been most successful for magnesium, which forms a deep acceptor with an activation energy around 140 meV, depending on the doping level [45].

With increasing concentration the close proximity of the magnesium atoms leads to a reduction of the activation energy due to the formation of an impurity band above the valence band edge. At room temperature just ∼1 % of the magnesium atoms are activated, i.e. act as an acceptor. Accordingly, a very high magnesium content on the order of 1×10^{20} cm^{-3} is required to achieve p-type doping levels relevant for devices. For the growth, this means the use of a very high high magnesium flux, which is problematic due to the formation of so-called pyramidal defects. These defects provide a second pathway for the incorporation of magnesium and limit the maximum dopant concentration. The formation process can be quantitatively explained by the segregation of magnesium on the growth surface, as demonstrated by S. Figge and R. Kroeger [1]. In terms of growth parameters, this means an optimum molar flow ratio of the precursors $f(\mathrm{Cp2Mg})/f(\mathrm{TMG})$ to achieve the highest acceptor concentration in conjunction with a high crystalline perfection.

For MOVPE-grown films, the hydrogen from the precursor, the ammonia or reaction products of both passivate the magnesium in the GaN [46]. Here, the hydrogen atom attaches to the magnesium atom and blocks the acceptor bond [47]. In order to transform the Mg-H complex into an acceptor it is necessary to remove the hydrogen from the layer. This has been first observed by Amano *et al.* for the Low Energy Electron Beam Irradiation (LEEBI) treatment of Mg-doped layers [48]. Nakamura *et al.* later showed in annealing experiments under nitrogen and hydrogen atmosphere, that this was caused by the local heating of the layers [10]. Today, the standard procedure for the activation of the magnesium in the layers is the thermal annealing in nitrogen atmosphere at temperatures exceeding ∼600°C. We currently employ a 5 min annealing step at a temperature of ∼850°C.

1.4 Piezoelectricity

Although not necessarily important for the operation of optoelectronic devices due to the typically high current densities, the piezoelectric fields are an important property of the group-III nitrides. It distinguishes the nitrides from the "classic" semiconductors, and has substantial influence on the charge carrier distribution in heterostructures. The origin is the deviation of the GaN unit cell from the ideal wurtzite geometry and the strong ionic character of the III-N bond. Thorough descriptions can be found in Ref. [49] and [12]. The relevant material constants are listed in Table 1.3.
In the absence of external fields, the total polarization in the crystal is the sum the *spontaneous* and the *piezoelectric* polarization. The former is observed in the equilibrium structure due to the deviation of the crystal structure from the ideal hexagonal unit cell and the latter is induced by the deformation of the unit cell upon strain. For an ideal hexagonal structure the spontaneous polarization would be zero, since the positive and negative charges just balance each other. For the deviation from the ideal structure, the sum of all electric dipole moments causes the macroscopic spontaneous polarization [51]. This polarization is usually balanced by mobile surfaces charges, such that

[1] The results were presented on the 2001 Fall Meeting of the Materials Research Society in Boston. A publication will follow.

Parameter	GaN	InN	AlN	Reference
c_0/a_0	1.634	1.627	1.619	[49]
	1.627	1.612	1.601	[12]
u	0.376	0.377	0.380	[49]
Spont. polarization [C/m^2]	-0.029	-0.032	-0.081	[49]
Piezoel. const. e_{33} [C/m^2]	0.73	0.97	1.46	[49]
	1		1.55	[12]
	0.65			[12]
	0.63		1.29	[12]
Piezoel. const. e_{31} [C/m^2]	-0.49	-0.57	-0.60	[49]
	-0.36		-0.58	[12]
	-0.33			[12]
	-0.32		-0.38	[12]
Dielectr. const. ε_r	10.4	15.3	8.5	[11]
	8.9	8.4		[50]

Table 1.3: Unit cell structure parameters, spontaneous polarization and piezoelectric constants of the group-III nitrides.

no static external potential is measured across the crystal. Due to the crystal symmetry the spontaneous polarization is aligned along the [0001] direction, and the positive direction of the polarization is defined to be parallel to the [0001] axis. The spontaneous polarization constants listed in Table 1.3 are negative, thus the polarization points into the plane of the film surface for [0001]-polar material.

The piezoelectric polarization is related to the strain in the film by the piezoelectric tensor. This is a third-rank tensor, which can be reduced for the nitrides to three independent components due to the symmetry of the hexagonal unit cell [51]. The independent components are in matrix notation e_{31}, e_{33} and e_{15}, where the first two describe piezoelectric fields along [0001] and e_{15} is the field caused by shear strain. For details on the matrix notation see Section 2.4.3 and [51]. The relevant relation describing the piezoelectric field along [0001] is

$$P_{\mathrm{pe}} = e_{33}\,\varepsilon_3 + e_{31}\,(\varepsilon_1 + \varepsilon_2). \tag{1.3}$$

The out-of-plane strain is defined as $\varepsilon_3 = (c - c_0)/c_0$ and the in-plane strain is $\varepsilon_1 = \varepsilon_2 = (a - a_0)/a_0$, with the unstrained lattice parameters c_0, a_0 and the strained lattice parameters c and a. The in-plane and the out-of-plane strain are related as

$$\frac{c - c_0}{c_0} = -2\frac{C_{13}}{C_{33}}\,\frac{a - a_0}{a_0}, \tag{1.4}$$

which is explained in Section 2.4.3. C_{13} and C_{33} are the stiffness constants of the crystal.

Then, the polarization can be related to the in-plane strain as

$$P_{\mathrm{pe}} = 2\,\frac{a-a_0}{a_0}\left(e_{31} - e_{33}\frac{C_{13}}{C_{33}}\right). \tag{1.5}$$

The term in brackets on the right side of Eqn. 1.5 is always negative, which means that the polarization is negative as well for tensile strained material, and positive for layers under compression. Accordingly, the piezoelectric polarization is parallel to the spontaneous polarization for the case of tension and antiparallel for compression. The electric fields generated inside the structure are connected to the polarization by the relative dielectric constant of the respective material :

$$E = -\frac{P}{\varepsilon_r(x)\,\varepsilon_0}. \tag{1.6}$$

Since in equilibrium the macroscopic polarization is compensated by surface charges, the important parameter for the numerical treatment of quantum-well structures is the piezoelectric field in the structure. The individual polarizations are sketched in Fig. 1.8. For the case of [0001]-polar material, the compressive strain in the well generates a piezoelectric polarization pointing to the surface. The connected electric field inside the well has the opposite direction and causes the electrons to be confined at the surface side of the well and the holes to be localized at the substrate side. This would be reversed for the case of N-polar material.

The internal field in the quantum well varies with the composition of the well and is a superposition of the external and the internal screening, the piezoelectric and the spontaneous polarization, which makes it hard to apply a closed model. According to literature, the dependence of the internal field F_{int} on the indium content is linear [52, 53] :

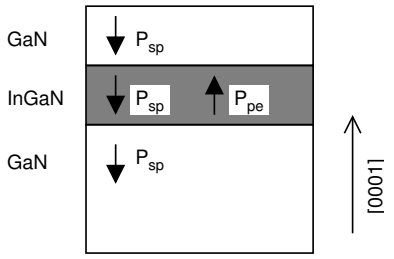

Figure 1.8: The spontaneous and the piezoelectric polarization in a [0001]-polar $In_xGa_{1-x}N$/GaN quantum well.

$$F_{\mathrm{int}} = c_{\mathrm{field}} \cdot x_{\mathrm{In}}. \tag{1.7}$$

The proportionality constant c_{field} is not well known, and literature values scatter from 4.8 MV/cm [52] up to 11 MV/cm [54]. Nevertheless, many publications studying quantum wells with an indium molar fraction of 0.1 can describe their results assuming an internal field of ∼350 keV, which corresponds to a proportionality constant of 3.5 MV/cm [52, 55, 56]. Since this is in good agreement with own results, this value will be assumed for all further considerations.

The impact of the piezoelectric field on the localized states in an $In_xGa_{1-x}N$ quantum well is illustrated in Fig. 1.9 for a well with an indium molar fraction of $x_{\mathrm{In}} = 0.13$ embedded in GaN barrier layers. Plotted is the band structure of this well together with the momentum $\psi\psi^*$ of the electron and the heavy hole wavefunction for a piezoelectric field of 0 kV/cm and 450 kV/cm, respectively. The upper band structure in Fig.1.9 was calculated without any piezoelectric field, such that the electron and the hole are localized in the center of the well. The difference of their energy levels is slightly above the

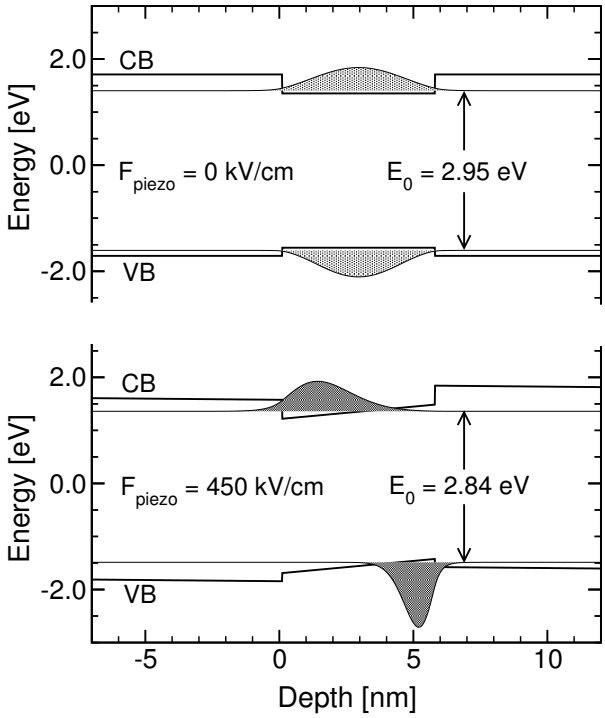

Figure 1.9: Band structure of an $In_xGa_{1-x}N/GaN$ quantum well with and without piezoelectric field. Also shown is the momentum $\psi\psi^*$ of the electron and the heavy hole wavefunctions.

band gap difference due to the quantum confinement. The lower band structure was calculated for a piezoelectric field of 450 kV/cm. In this case the electron and the hole are localized at the opposite sides of the quantum well in the triangular shaped potentials induced by the piezoelectric field. The field reduces the difference of the energy levels of the electron and the hole compared to the field-free structure. This reduction of the transition energy corresponds to a spectral redshift of the luminescence and is called quantum confined Stark effect (QCSE) [57].

The second effect of the piezoelectric field is the reduction of the overlap integral $|\langle\psi_e|\psi_h\rangle|^2$. While the overlap integral is equal to 0.98 without any field present, it is reduced to 0.04 for the piezoelectric field of 450 keV/cm. The transition rate from an initial state to another state is described by Fermi´s golden rule. For a quantum well structure, the transfer matrix element contains the overlap integral, which is a measure for the recombination probability of the electron and the hole [58]. Accordingly, a high overlap integral would correspond to a high transition rate, such that the radiative lifetime decreases and the radiative recombination rate increases. The piezoelectric field present in $In_xGa_{1-x}N$ quantum wells reduces the overlap integral, such that the radiative lifetime of the charge carriers is high [59]. Since a slow radiative recombination increases the probability of the nonradiative recombination, this also limits the radiative efficiency of the $In_xGa_{1-x}N$ quantum wells.

1.5 Lattice and stiffness constants of AlN, InN and GaN

A lot of data has been presented on the lattice parameters of GaN, InN and AlN, but only recently material of sufficient quality became available for reliable measurements.

Lattice parameters

Material	a_0[Å]	c_0[Å]	Method	Reference
GaN	3.189	5.1864	Exp. bulk	[60]
	3.1878	5.185	Exp. homoepitaxy	[60]
	3.1878	5.185	Literature review	[61]
InN	3.5374	5.7027	Experiment	[62]
	3.545	5.703	Literature review	[63]
AlN	3.110	4.980	Experiment	[64]
	3.117	4.982	Theoretical	[65]

Table 1.4: Overview of literature values for the lattice parameters of AlN, InN and GaN.

This section contains an overview of the today most widely accepted values, which are assumed to represent values of ideal crystals. The experimentally determined lattice parameters have been obtained from high resolution XRD, and the investigated samples were either bulk crystals or homoepitaxial layers. The data is listed in Table 1.4. For GaN, the lattice parameters of MOVPE-grown homoepitaxial layers will be used for all further calculations, as published by Leszczynski [60]. For InN the values published by Paszkowicz were chosen [62], determined from microcrystals.

Stiffness constants

Material	C_{11}	C_{12}	C_{13}	C_{33}	C_{44}	$2\,C_{13}/C_{33}$	Method	Reference
GaN	373	141	81	387	94	0.42	Experiment	[66]
	390	145	106	398	105	0.53	Experiment	[67]
	350	140	104	376	101	0.55	Theory	[68]
	367	135	103	405	95	0.51	Theory	[69]
InN	223	115	92	224	84	0.82	Theory	[69]
	271	124	94	200	46	0.94	Theory	[70]
AlN	398	142	112	373	116	0.51	Theory	[69]
	396	137	112	383	127	0.52	Theory	[68]
	410	140	100	390	120	0.51	Experiment	[71]
	411	149	99	389	125	0.51	Experiment	[72]

Table 1.5: Overview of literature values for the stiffness constants of AlN, InN and GaN.

The knowledge of the stiffness constants is required for the understanding of strained structures, which will be discussed in Section 2.4.3 in more detail. These constants of

the nitrides have not been investigated as thoroughly as the lattice parameters, and the scatter of the published data is larger. Experimental values for the stiffness constants, mostly obtained from Brillouin scattering, as well as theoretical calculations have been published. In Table 1.5 the more recent values are presented. The topics are still under discussion, so there might be changes to these values in future. In order to use one consistent set of parameters, the values published by Wright *et al.* [69] were used for all further calculations.

1.6 Further reading

This chapter can not cover all the known properties of the group-III nitrides, and it is limited to the most important aspects to understand optoelectronic devices. To obtain more information some books and review articles are listed below.

Books :

- H.Morkoc, *Nitride Semiconductors and Devices*, Springer Series in Materials Science Springer, New York (1999).
- B.Gil (editor), *Group III Nitride Semiconductor Componds*, Oxford University Press, New York (1998).
- S.Nakamura, G.Fasol, *The blue laser diode*, Springer, Berlin (1997).
- G.B.Stringfellow, *Organometallic Vapor-Phase Epitaxy : Theory and Practice*, Academic Press, New York (1989).

General review :

- S.C.Jain, M.Willander, J.Narayan, R.Van Overstraeten, *III-nitrides: Growth, characterization, and properties*, J Appl. Phys. 87, 975 (2000).
- J.W.Orton and C.T.Foxon, *Group III nitride semiconductors for short wavelength light-emitting devices*, Rep. Prog. Phys. 61, 1 (1998).
- O.Ambacher, *Growth and applications of group-III nitrides*, J. Phys. D : Appl. Phys. 31, 2653 (1998).

Growth :

- H Amano and I Akasaki, *Novel aspects of the growth of nitrides by MOVPE*, J. Phys. : Condens. Matter 13, 6935 (2001).
- N.Grandjean, B.Damilano and J.Massies, *Group-III nitride quantum heterostructures grown by molecular beam epitaxy*, J. Phys. : Condens. Matter 13, 6945 (2001).

Devices and processing :

- T.Mukai, S.Nagahama, N.Iwasa, M.Senoh and T.Yamada, *Nitride light-emitting diodes*, J. Phys. : Condens. Matter 13, 7089 (2001).
- T.Miyajima, T.Tojyo, T.Asano, K.Yanashima, S.Kijima, T.Hino, M.Takeya, S.Uchida, S.Tomiya, K.Funato, T.Asatsuma, T.Kobayashi and M.Ikeda, *GaN-based blue laser diodes*, J. Phys. : Condens. Matter 13, 7099 (2001).
- S.Pearton, J. Zolper, R.Shul and F.Ren, *GaN : Processing, defects, and devices*, J. Appl. Phys. 86, 1 (1999).
- S.Pearton, R.Shul and F.Ren, *A Review of Dry Etching of GaN and Related Materials*, MRS Internet J. Nitride Semicond. Res. 5, 11 (2000).
- S.Pearton, F.Ren, A.Zhang and K.Lee, *Fabrication and performance of GaN electronic devices*, Mat. Sci. Eng. R 30, 55 (2000).

Band structure and parameter sets :

- I.Vurgaftman, J.R.Meyer and L.R.Ram-Mohan, *Band parameters for III V compound semiconductors and their alloys*, J. Appl. Phys. 89, 5815 (2001).
- S.N.Mohammad and H.Morkoc, *Progress and prospects of group-III nitride semiconductors*, Prog. Quant. Electr. 20, 361 (1996).

Chapter 2

Experimental Methods

This chapter provides an overview of some experimental techniques used in this work, and goes into more detail where special aspects important for GaN-based devices are necessary.

2.1 Metalorganic Vapor Phase Epitaxy

The origin of metalorganic vapor phase epitaxy is the work of Manasevit *et al.* in the late 60´s [73, 74]. The method was developed in a period of time when liquid phase epitaxy and vapor phase epitaxy were well established and molecular beam epitaxy was the tool of choice to produce highest quality semiconductor structures. Due to the complex processes involved the evolution process was relatively slow, but today MOVPE is the main production tool for III-V devices. Once a set of parameters is obtained the reproducibility is ensured over a relatively long period of time, and the machine uptime is high.

2.1.1 General

The basic idea of MOVPE is the crystal growth through a chemical reaction, which involves metalorganic molecules containing the metal of interest. The metalorganics have a relatively high vapor pressure, which allows their transport to the substrate using a carrier gas. The growth reaction happens at the interface of the gas phase and the substrate. The environment is commonly based on a mixture of the gases hydrogen and nitrogen, which are the carrier gases for the source materials. In contrast to molecular beam epitaxy the growth is conducted at pressures ranging from 10 hPa to 1000 hPa, and not under ultrahigh vacuum conditions. This makes servicing of the equipment easier, but requires all chemicals and gases involved to be of extremely high purity in order to keep the impurity concentration in the grown sample low.

The structure of the metalorganics is such that organic groups like methane or ethane are bond to the metal atom. The bonds between metal and organic group are the weakest ones in the molecule, such that the temperature required to break these bonds is well below the growth temperature. This ensures the organic groups to be not involved in

the reaction. The growth happens on top of the substrate since this is kept at a high temperature to induce the reaction. The transport of the reagents to the substrate surface occurs through diffusive transport across the boundary layer. This diffusion process is governed by factors like size of the molecules, temperature, pressure, flow velocity and viscosity of the growth atmosphere. Common reactions used are those of trimethylgallium (TMG) and ammonia (NH_3) for the growth of GaN, or triethylgallium (TEG) and arsine (AsH_3) for the growth of GaAs. The description of the growth process can be broken down into thermodynamic, kinetic, hydrodynamic and mass transport aspects. Thermodynamics define the driving force of the reaction, and kinetics prescribe the rate at which the various reactions happen. Hydrodynamics describe the flow transport of the source materials to the substrate and mass transport controls the diffusive transport across the boundary layer. Depending on the growth temperature, three growth regimes can be distinguished :

- At low temperatures, the growth is limited by the kinetics of the reaction, so the growth rate increases with temperature.
- At intermediate temperatures, the reaction proceeds fast enough, but the growth rate is limited by the diffusive transport across the boundary layer, which is mainly independent of temperature.
- At elevated temperatures, desorption due to thermal etching dominates the growth, i.e. the growth rate drops with temperature.

The growth of GaN is usually conducted at 1050°C, which is above its decomposition temperature in vacuum of 850°C [75]. At this temperature, the growth is usually diffusion or desorption limited [76], depending on the pressure and chemistry of the growth atmosphere. In particular, the partial pressures of hydrogen and ammonia are important to control the decomposition.

Molar flows

The chemical reactions involved are quantified by the molar flows of the reactants. They can be derived straightforward for the gaseous sources like ammonia, as the molar flow follows directly from the molar volume of an ideal gas. For metalorganics, the flow calculation is different, since most metalorganics are liquid. They are mixed into the carrier gas in a bubbler, which is a container holding the metalorganic passed by the carrier gas (Fig. 2.1). For low flows the liquid can be treated as being in equilibrium and the concentration of the metalorganic is given by the ratio of the equilibrium vapor pressure p_{eq} above the liquid and the total pressure p_{tot} in the bubbler. The equilibrium vapor pressure is determined

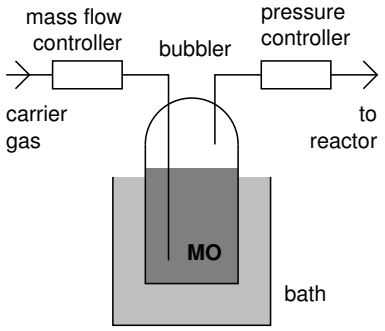

Figure 2.1: Schematic of a metalorganic gas line.

by the temperature of the liquid, i.e. by the bath temperature. The most frequently found relation is [77]

$$\log(\frac{p_{\mathrm{eq}}}{p_0}) = a - \frac{b}{T},$$

with the material specific vapor pressure constants a and b and the temperature measured in Kelvin. Knowing the concentration, the molar flow of the metalorganic then follows to

$$f_{\mathrm{molar}} = \frac{p_{\mathrm{eq}}}{p_{\mathrm{tot}}} \cdot \frac{F_{\mathrm{carrier}}}{22400\ \mathrm{cm}^3/\mathrm{mol}}, \tag{2.1}$$

where F_{carrier} is the carrier gas flow through the bubbler. Since the gas flow is measured in [sccm], the commonly used unit for the molar flow is μmol/min. Concerning the calculation of molar flows, solid sources like trimethylindium can be treated like liquid sources, considering a different temperature dependence. For the operation of solid sources one has to keep in mind that the sublimation from the solid into the gaseous state proceeds significantly slower, which causes the time to obtain a stable molar flow for a preset gas flow to be significantly longer compared to liquid sources. This effect has to be considered in the growth runs, since it inhibits rapid changes of flows for solid source materials

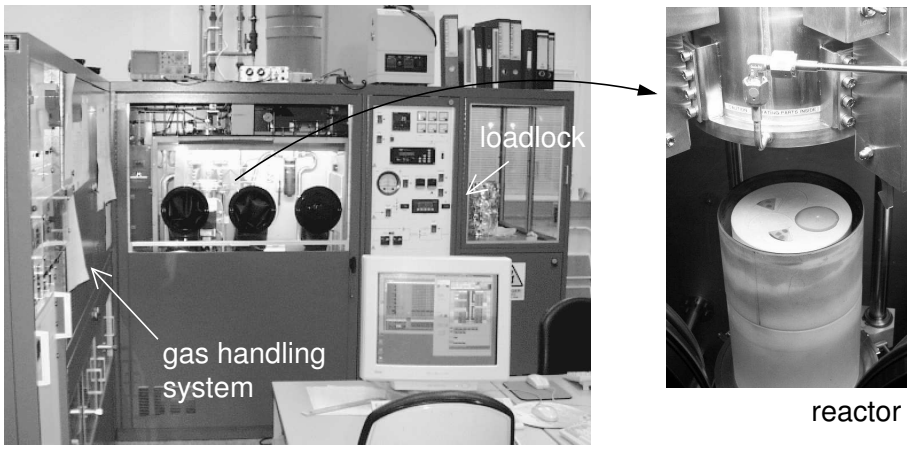

Figure 2.2: The Thomas Swan MOVPE system used in this work.

2.1.2 The Thomas Swan MOVPE system

The reactor used is a $3 \times 2''$ close-spaceded showerhead reactor manufactured by Thomas Swan[1]. The special feature of this system is the showerhead concept, which realizes a vertical gas flow onto the substrates with two separate gas distribution chambers for

[1] Thomas Swan Scientific Equipment Ltd., Buckingway Business Park, Cambridge CB4 5UG, UK

the group-III and the group-V elements, respectively. The gas outlets of the two chambers penetrate each other like two showerheads, providing separate gas flows until few millimeters away from the substrate. This design reduces prereactions significantly and ensures good intermixing of the two flows needed for homogeneous growth. A picture of the entire system is shown in Fig. 2.2.

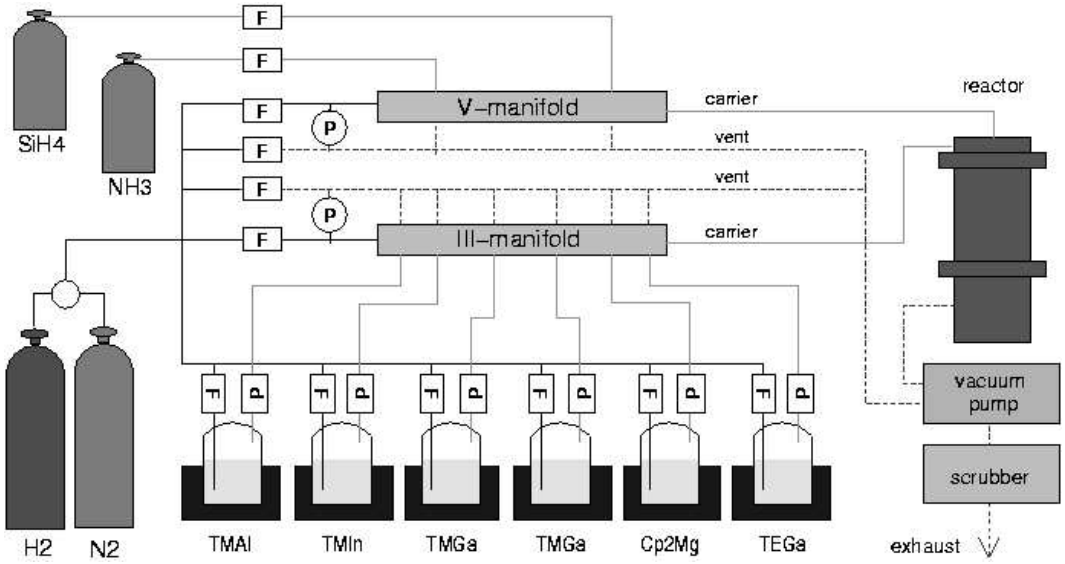

Figure 2.3: Layout of the Thomas Swan MOVPE system including the gas distribution system.

The gas distribution system illustrated in Fig. 2.3 provides six bubbler lines for metalorganics, including a double-dilution line for small metalorganic flows and one Epison-controlled line[2]. Currently, these lines are operated with by Trimethylaluminium, Bis(cyclopentadienyl)magnesium, Trimethylindium, Triethylgallium and two Trimethylgallium sources. One Trimethylgallium bubbler is installed on a double-dilution line for the controlled growth of quantum wells at low growth rates. The group-V source used is ammonia, and the precursor for n-type doping is Silane with a concentration of 10 ppm in hydrogen, which can be further diluted in the gas distribution system. The sources are mixed into the main carrier gas flow in special manifolds, which enable the switching of gases without changing the pressure in the run lines. The latter is accomplished by two dummy lines.

2.2 Molecular Beam Epitaxy

The concept of molecular beam epitaxy (MBE) was invented in 1958 by Günther *et al.*, who proposed the growth of InAs and InSb utilizing different temperatures of the

[2]The Epison is a tool to determine the concentration of the metalorganic precursor in the carrier gas based on the velocity of sound. It basically determines the density of the gas mixture.

sources and the substrate [78]. The experimental realization of the first monocrystalline films was achieved in the late 1960s by Davey and Pankey for the growth of GaAs epilayers [79]. Although mainly used for, it is not restricted to the deposition of semiconductors. It was successfully applied to metals and insulators, and has been used in industry for the production of electronic as well as optoelectronic devices. Furthermore, it is an excellent research tool due to the large number of *in situ* characterization tools available and the good quantitative understanding of the growth process. The former arises from the growth under ultrahigh vacuum (UHV) conditions (10^{-9} Torr), which allows to use electrons as probes for the measurements. Basically, MBE is the controlled evaporation of high-purity materials in a UHV chamber, which deposit on a heated substrate. The UHV corresponds to a mean free path of the atoms far above the dimensions of the chamber, such that all source molecules impinge onto the substrate without the interaction with other molecules. Accordingly, many sources can be used simultaneously, whose molecular beams intersect each other above the substrate and form a mixture of the vaporized elements. This vapor is in contact with the substrate, where the crystallization process takes place. The growth process is determined by the reaction kinetics at the surface, where basically four processes can be distinguished [80] :

- adsorption of the source atoms or molecules on the substrate surface
- surface migration and dissociation of the adsorbed molecules
- incorporation of the atoms into the crystal lattice
- thermal desorption of elements not incorporated

Since the temperatures of the effusion cells normally differ significantly from the temperature of the substrate, the growth proceeds far away from the thermal equilibrium. In order to achieve the thermodynamic equilibrium, the impinging atoms have to exchange energy with the the crystal lattice.

A sketch and a photograph of the MBE chamber is shown in Fig. 2.4. The source materials for the growth of the group-III nitrides are the metals Ga, Al and In as the group-III elements and nitrogen gas as the group-V element. The metals are evaporated in effusion cells, whose temperatures are accurately controlled by proportional-integral-derivative (PID) controllers in order to maintain a stable atomic flux. The nitrogen gas is prepared in a radiofrequency (rf) plasma source, where an rf plasma at 13.56 MHz is used to dissociate the N_2 molecules and provide atomic nitrogen for the growth. For p- and n-type doping effusion cells containing Mg and Si are installed, respectively. In addition, GaAs can be grown in the chamber, for which an As cracker cell is utilized.

The whole MBE complex in Bremen was produced by EPI[3] and consists of two EPI 930 growth chambers and a separate x-ray photoelectron spectroscopy (XPS) chamber. The second MBE besides the described III-V system is used for the growth of II-VI compounds, with the focus on optoelectronic devices. All three chambers are connected via an UHV transfer system, which is linked to one central loadlock. The transfer modules include two degas stations, where the substrates can be thermally cleaned prior

[3]EPI, 1290 Hammond Road, Saint Paul, MN 55110, USA

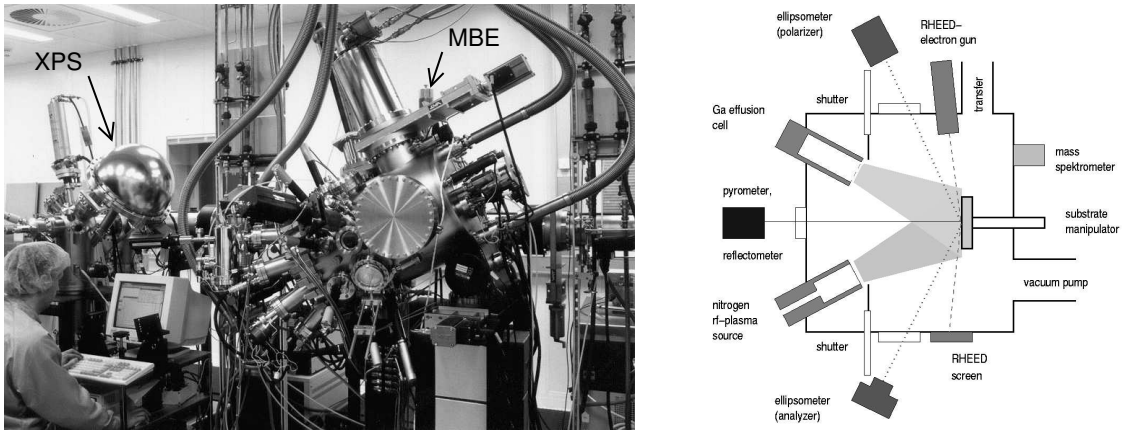

Figure 2.4: The EPI molecular beam epitaxy system installed at the University of Bremen.

to the growth at temperatures up to 1000°C. The growth process can be controlled by computer, which ensures a high reproducibility of the growth runs. The samples are mounted on molybdenum blocks either clamped in indium-free holders or glued to Silicon wafers utilizing indium.

2.3 Reflectometry

The gaseous environment under which MOCVD growth is performed restricts the possibilities of *in situ* measurements significantly compared to vacuum based growth techniques such as MBE. Atoms or electrons cannot be used as probes for the measurement, as their mean free path would be far too low. Thus, techniques established known from MBE like reflection high energy electron deflection (RHEED) or mass spectrometry are ruled out. The only possibility is to use a method which is based on electromagnetic waves, like light or x-rays. Use of the latter requires a sophisticated and expensive setup and is not convenient for everyday use. Therefore, mainly optical methods have been developed for the *in situ* characterization of MOVPE growth.

Reflectometry and ellipsometry are the most popular methods in this context, as they can provide information on the individual layers of a heterostructure, including the bulk properties as well as the interface or surface structure [81]. Furthermore, they are rather robust and inexpensive tools, and the data analysis has reached a very high level. The drawback of both methods is, that they rely on the comparison of the measured data with a model, such that the accuracy falls with the quality of the model applied. A rather surface sensitive method is reflectance anisotropy spectroscopy (RAS), which can even provide information on surface reconstructions [82]. Recently, an optical stress sensor has been developed, which derives the stress state of the layer from the curvature of the substrate. For this, an array of parallel light beams is directed onto the surface, which loses its parallelism after reflection due to the substrate curvature. This allows to

derive the curvature from the change of the relative beam distance [83]. Another very common tool is pyrometry, which allows to determine the actual temperature of the sample based on the radiative emission of a grey body.

The configuration of the optical ports in the Thomas Swan system requires the vertical incidence of light. Therefore, only normal-incidence reflectance is applicable to monitor the growth process.

2.3.1 The basics of reflectometry

Due to the easy implemantation of normal incidence reflectometry, this method has been applied to a wide variety of materials, ranging from semiconductors like silicon [84] or II-VI compounds [85] to metals like tungsten [86]. The basis of all studies is the reflection of light - usually monochromatic - from the surface.

The reflection of light at a single interface is described by the *Fresnel equations*, which are based on the continuity of the tangential components of the electric field **E** and the magnetic field **H** across any boundary. The equations provide the transmission and reflection coefficients of the amplitudes of the electromagnetic field in dependence on the angle of incidence and on the polarization. The full derivation of the equations can be found in [87] or [88]. For a single boundary formed by two materials with complex refractive indices $N_1 = n_1 - ik_1$ and $N_2 = n_2 - ik_2$ the reflection coefficient is the ratio of reflected and incident electric field amplitude E_1^r and E_1^i , respectively. The transmission coefficient is the ratio of transmitted electric field amplitude E_2^t in medium 2 and incident electric field amplitude E_1^i in medium 1. The coefficients are related to the refractive indices following the Fresnel equations. For normal incidence these are

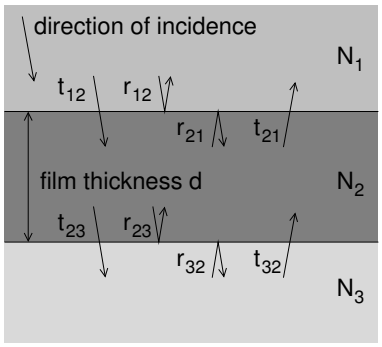

Figure 2.5: Refraction at the boundaries of three media.

$$r_{12} = \frac{E_1^r}{E_1^i} = \frac{N_2 - N_1}{N_1 + N_2} \qquad (2.2) \qquad \text{and} \qquad t_{12} = \frac{E_2^t}{E_1^i} = \frac{2N_1}{N_1 + N_2}, \qquad (2.3)$$

where the direction of incidence is pointing from material 1 to material 2. In order to derive the reflectance of a multilayer structure one first considers the reflectance of a single thin film on a thick substrate, where any reflection from the substrates backside is neglected. The model structure consists of a thin layer with refractive index N_2 and thickness d placed in between two media with refractive indices N_1 and N_3. The various parameters involved in this case are defined in Fig. 2.5. Due to the two interfaces, the incident light is reflected multiple times inside the layer, such that the observed light intensity in a certain direction is a superposition of all transmitted and reflected waves. The resulting reflection and transmission coefficients are derived from the sum of the field amplitudes, which requires to consider the phase shift in addition to the various transmission and reflection coefficients. The phase shift β is proportional to the ratio of

the optical thickness and the wavelength of the light. For normal incidence, β amounts to

$$\beta = \frac{2\pi N_2}{\lambda} d. \tag{2.4}$$

At each reflection a fraction of the light is transmitted through the respective interface, which then contributes to the reflected or transmitted light, respectively. The total reflection coefficient r_{123} follows from the sum of all reflected waves, which resolves to [87] :

$$r_{123} = \frac{r_{12} + r_{23} e^{-2i\beta}}{1 - r_{21} r_{23} e^{-2i\beta}}. \tag{2.5}$$

Similarly, the total transmission through this structure is derived to

$$t_{123} = \frac{t_{12} t_{23} e^{-i\beta}}{1 - t_{21} t_{23} e^{-2i\beta}}. \tag{2.6}$$

In order to determine the reflection coefficients of a multilayer stack, one successively applies these equations to three-media structures, starting from the substrate. First, the reflectivity coefficient at the upper interface of a sample consisting of two layers on a substrate is calculated. This yields the field amplitude inside the uppermost layer, which is not observable. This reflectivity coefficient is then assumed to be the one of a "virtual substrate", such that one can add the next layer and calculate the reflectivity coefficient of the next interface. Repeating these steps until the last medium (which is air) then yields the reflection coefficient of the whole structure. This concept becomes more obvious if one uses the *matrix formalism*, which is described in Appendix A.

Since the reflectance of a material is defined through the intensity ratio of the reflected and incident light, the observable reflectance R for the single layer structure shown in Fig. 2.5 is given by

$$R = r r^* = \frac{r_{12}^2 + 2 r_{12} r_{23} \cos(2\beta) + r_{23}^2}{1 + 2 r_{12} r_{23} \cos(2\beta) + r_{12}^2 r_{23}^2}. \tag{2.7}$$

Absorption has been neglected in Eqn. 2.7, such that the refractive index is real. Knowing the period of the reflectance oscillation and the refractive index of the layer, it is possible to derive the growth rate and the layer thickness from this equation.

2.3.2 Experimental setup on the reactor

The experimental realization on the reactor is constrained by the very narrow viewport due to the showerhead design and the off-center position of the wafer pockets on the susceptor. The former requires the use of a beam splitter to measure the reflected beam. The latter constraint makes a position-dependent measurement unavoidable, as otherwise the average reflectance of all three wafers would be obtained.

Concept

A sketch of the setup installed on the reactor is shown in Fig. 2.6. It employs a reflectance unit which consists of a 670 nm laser diode, a beam splitter and a photo diode. The position resolved measurement is realized by an optical shaft encoder, which monitors the rotation of the susceptor and provides a trigger signal at the edge of each wafer. The trigger signal used for the measurement is manually selected. Furthermore, an analog delay timer allows to shift the trigger signal by up to one second. To circumvent the problem of background radiation, which is superimposed to the measured signal, a differential measurement concept was introduced. It is achieved by measuring the reflection from two spots on the susceptor - one on a specific point on the wafer of interest, and the second on the susceptor next to the wafer. Since the susceptor surface competely scatters the incident light, no reflectance signal can be measured. Therefore, this reference measurement provides the background radiation. The difference of the two intensities yields the reflectance of the sample.

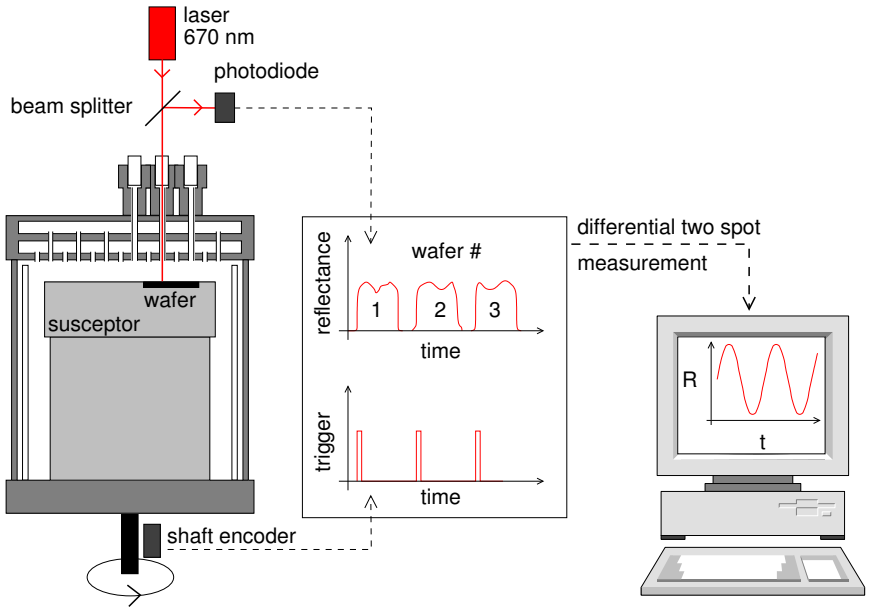

Figure 2.6: Normal incidence reflectometry setup on the reactor.

Experimental realization

The reflectance unit is installed in a shielded box to avoid stray light from the environment. The unit is mounted on a tilt stage and a simple x-y stage for the alignment of the laser. The optical port has been modified to provide a larger diameter, which is now 4 mm. The original probes were replaced by a 1/4-inch quartz rod, which allows to seal the reactor from the environment. The shaft encoder is realized by a light sensor and a cycle wheel mounted on the shaft of the drive motor. This oscillating signal is analyzed by an electronic counter which then periodically generates the trigger signal. The

acquisition of the two intensities is done by analog electronics, consisting of a differential amplifier for the two signals. The voltage on the output resembles the reflectance, which is transmitted to the computer utilizing an A/D converter and a data acquisition program created using the TestPoint toolbox. Details on the electronics are found in Appendix B.

2.3.3 Reflectance during growth of GaN

The reflectance transient recorded during the growth of a multilayer structure is a function of many different variables. It allows one to obtain a lot of information from one growth run, but also requires a good understanding of the effects of the individual variables. The changes due to composition, temperature, growth rate, absorption, surface roughness and macroscopic inhomogeneities are of particular interest for $Al_xIn_yGa_{1-x-y}N$ structures. Each of these will be discussed in the following.

Refractive index

The refractive index of an $Al_xIn_yGa_{1-x-y}N$ layer is a function of the wavelength, the composition and the temperature. Since its knowledge is essential for the design of waveguide structures, several studies have been performed [89, 90, 91, 92, 93, 94, 95]. Most of these reports deal with the optical constants of $Al_xGa_{1-x}N$ and GaN, as these materials are commonly used in waveguide structures and can be grown in thick layers of high crystalline perfection. The growth of $In_xGa_{1-x}N$ requires the use of low growth rates, which hampers the fabrication of thick layers.

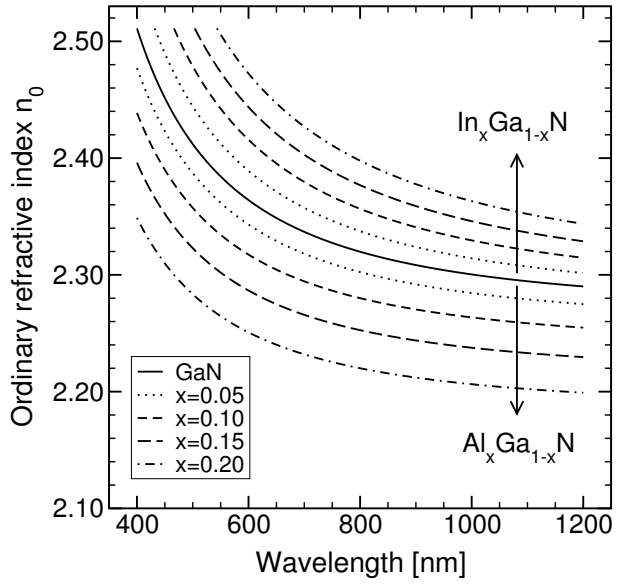

Figure 2.7: The ordinary refractive index of GaN, $In_xGa_{1-x}N$ and $Al_xGa_{1-x}N$ in dependence on the wavelength and the composition in the visible spectral region.

More sophisticated studies investigate the dispersion using a set of samples to deduce a more general picture. For example, Tisch *et al.* developed a model for $Al_xGa_{1-x}N$, describing the temperature and compositional dependence of the refractive index in the

visible spectral region [90]. The study is very careful and the determined values agree with data determined for typical layers grown in Bremen[4]. Bergmann *et al.* applied the Sellmeier dispersion formula extended by a compositional dependence of the fitting parameters to data measured in the spectral region from 457 nm to 980 nm [94]. The derived formula is much simpler compared to the work by Tisch *et al.*, but is capable of generating almost identical values in this spectral region [90]. Therefore, the Sellmeier dispersion formula as described in reference [94] will be used to describe the refractive index of $Al_xGa_{1-x}N$:

$$n(\lambda)^2 = 1 + \frac{A_0\lambda^2}{\lambda^2 - \lambda_0^2} \qquad (2.8) \qquad \text{with} \qquad \begin{aligned} A_0 &= 4.141 - 1.0x - 4.4x^2 \\ \lambda_0 &= (187.4 - 121x)\ \text{nm}. \end{aligned}$$

The dispersion function of $In_xGa_{1-x}N$ has been less investigated, and no comparative study has been published so far. All publications report on the optical constants of single heterostructures, commonly thin $In_xGa_{1-x}N$ grown on GaN. Therefore, an approach was chosen, which was quite successful for AlGaAs/GaAs structures. Based on the assumption of a constant refractive index at the band gap energy of the alloy, the dispersion function of $In_xGa_{1-x}N$ is obtained via the rigid shift of the energy scale by the band gap difference relative to GaN :

$$n_{\text{InGaN}}[E] = n_{\text{GaN}}\left[E - (E_g^{\text{InGaN}} - E_g^{\text{GaN}})\right] \qquad (2.9)$$

Fig. 2.7 contains the dispersion relations of $Al_xGa_{1-x}N$ and $In_xGa_{1-x}N$ derived by Equations 2.8 and 2.9. It should be noted, that GaN is a crystal showing uniaxial bifringence, i.e. it has different optical constants dependent on the polarization of the incident light. One distinguishes between a polarization along the c-axis (extraordinary) and perpendicular to the c-axis (ordinary). The latter is the case for normal incidence, thus, the ordinary refractive index is the relevant one for normal incidence reflectometry.

The temperature dependence of the refractive index is of particular importance for *in situ* measurements as the growth is commonly conducted at ∼1050°C. The reported optical constants are usually determined at room temperature and the high temperature behavior of the dispersion function is not well known for the nitrides. Only studies at low temperatures and up to 600 K have been performed [90, 89]. Therefore, the reflectance of a GaN epilayer was recorded in the reactor after growth during cooling to room temperature. From this data the temperature dependence of the ordinary refractive index n was extracted by comparing the curve to generated data points following the approach described in Appendix A. A linear relation of the refractive index and the temperature was assumed with ν being the temperature coefficient :

$$n_{\text{GaN}}(T) = n_{\text{GaN}}(300\text{K}) + \nu T. \qquad (2.10)$$

The thickness of this layer was determined *ex situ* by secondary electron microscopy (SEM) to avoid the usage of another optical model [5]. The refractive index of the sap-

[4]Measurements by A.Kasic, University of Leipzig, Germany
[5]Measurement by M. Dießelberg, University of Bremen

phire substrate was assumed to be n_{Sapphire}=1.76433 at 670 nm [96] with a temperature dependence of $dn/dT = 13.7\times10^{-6}\mathrm{K}^{-1}$ [96, 97]. The experimental and the generated data are shown in Fig. 2.8.

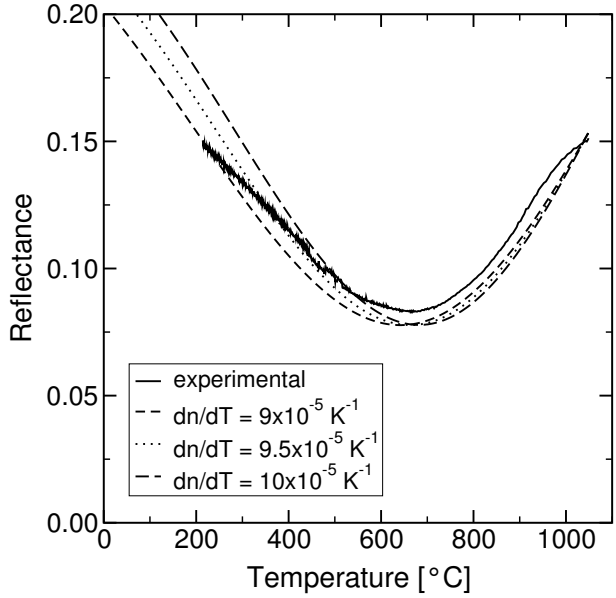

Figure 2.8: The reflectance of a single GaN layer grown on sapphire in dependence on the temperature. Shown are experimental and simulated values.

The best fit is obtained for a slope of ν=9.5$\times10^{-5}\mathrm{K}^{-1}$, corresponding to a difference in the refractive index of 0.1 between the room and the growth temperature. The temperature coefficient was assumed to be valid for the alloys as well, such that the refractive index at 670 nm depends on composition and temperature as described in Equations 2.8, 2.9 and 2.10. In Fig. 2.9 the data used for the following simulations is plotted.

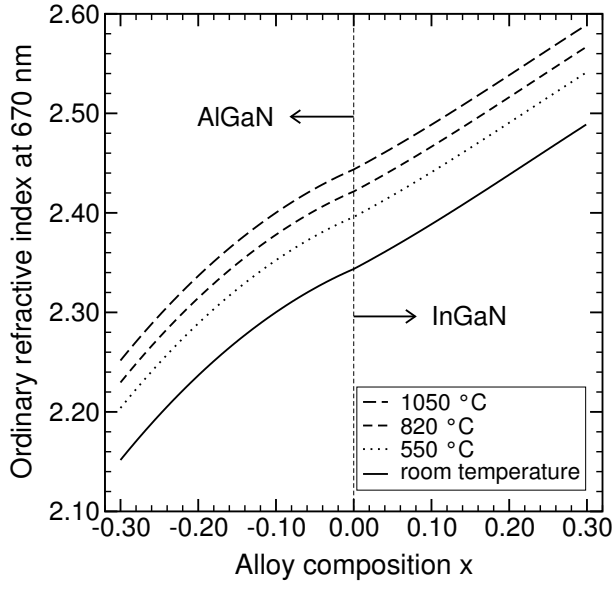

Figure 2.9: The ordinary refractive index at 670 nm for GaN, $\mathrm{In_xGa_{1-x}N}$ and $\mathrm{Al_xGa_{1-x}N}$ in dependence on the composition and the temperature.

The change of the refractive index with the composition of a ternary alloy is directly visible in the reflectance trace during the growth of a heterostructure. As the largest index difference is usually found at the surface, the reflectance is largely determined

by the properties of the topmost layer. Correspondingly, the interference effects during growth mainly stem from the reflections at the interfaces to the sapphire and to the surface.

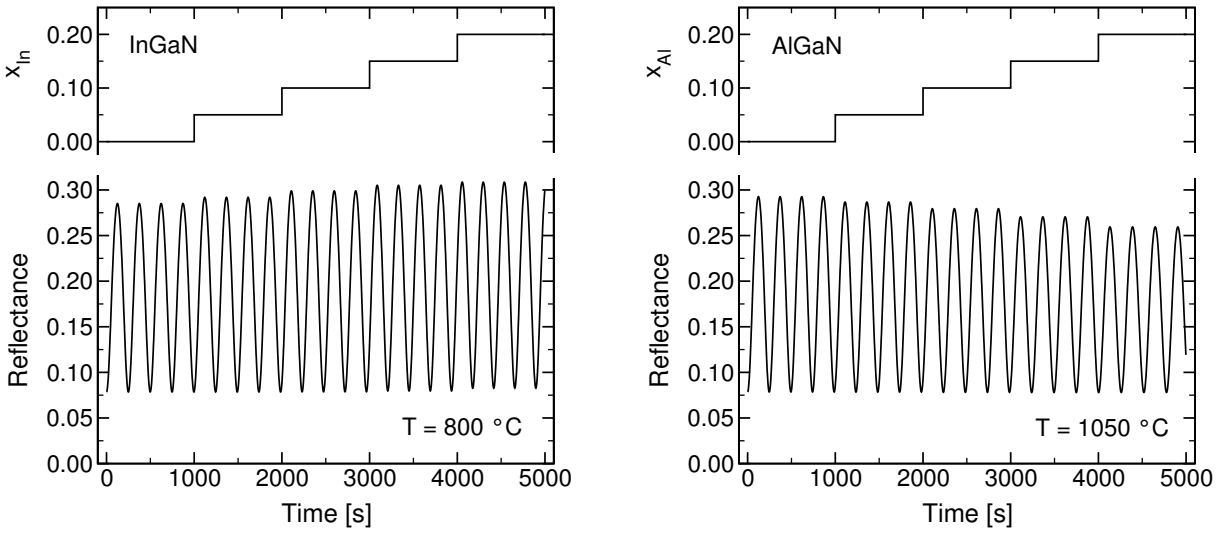

(a) $In_xGa_{1-x}N$-based multilayer structure

(b) $Al_xGa_{1-x}N$-based multilayer structure

Figure 2.10: Simulated reflectance transients of $In_xGa_{1-x}N$- and $Al_xGa_{1-x}N$-based multilayer structures grown on sapphire. In each graph, the composition was varied in steps from $x = 0.0$ to $x = 0.2$.

This can be seen in Fig. 2.10, in which simulated reflectance transients of growing multilayer structures based on $In_xGa_{1-x}N$ and $Al_xGa_{1-x}N$ are plotted. Fig. 2.10(a) demonstrates the impact of a change in the indium content, which corresponds to an increasing refractive index with composition. Accordingly, the reflectance follows the composition in the same manner and the intensity in the oscillation maximum rises by roughly 10% for an indium molar fraction of $x_{In} = 0.2$. The minimum reflectance of the oscillation is less affected by the compositional changes, but it rises with the indium molar fraction. The opposite is the case for an $Al_xGa_{1-x}N$-based heterostructure, in which case the refractive index is reduced with increasing composition and the reflectance decreases accordingly. The major changes happen to the oscillation maxima, whereas the oscillation minima follow the composition just slightly. Similar results were published Ng *et al.* [98].

It should be noted, that the two simulations in Fig. 2.10 were performed for different growth temperatures, namely, 800°C for the $In_xGa_{1-x}N$ structure and 1050°C for the $Al_xGa_{1-x}N$ structure. This allows to estimate the relevance of the measurement temperature from the reflectances of the GaN layers at the beginning of both simulations. A temperature difference of 250 K changes the peak reflectance by 3%. For example, this would correspond to a change in the $Al_xGa_{1-x}N$ composition by $\Delta x_{Al} = 0.05$.

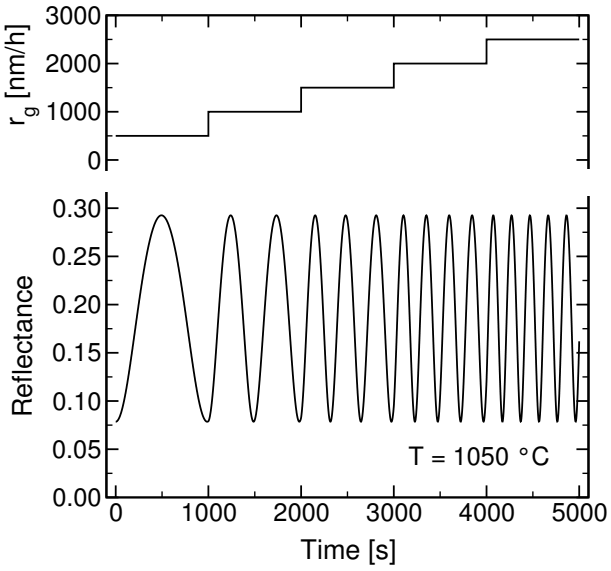

Figure 2.11: Simulated reflectance transient of a growing GaN film on sapphire, where the growth rate was increased from 500 to 2500 nm/h.

Growth rate

As mentioned before, the growth rate r_g and the refractive index N of the layer determine the oscillation period τ_{period} of the reflectance transient. Commonly, the changes in refractive index are small, such that the growth rate is the dominant parameter in this context. Its impact on the reflectance transient is demonstrated in the simulation in Fig. 2.11, where the growth rate was varied from 500 to 2500 nm/h. Although in general the reflectance can only be determined through the simulation of the whole heterostructure, including all layers below the layer of interest, it is possible to extract the growth rate just from the refractive index of the topmost layer and the period of the interference oscillation (see Appendix A). The phase shift in the topmost layer is given by Eqn. 2.4 and Eqn. 2.7 relates the phase shift and the oscillation of the reflectance transient. Since one full oscillation with the period τ_{period} corresponds to a phase shift of 2π, it follows

$$2\pi = 2\beta = 2\,\frac{2\pi n}{\lambda}\,d_{\text{period}} = \frac{4\pi n}{\lambda}\,r_g\,t_{\text{period}}, \tag{2.11}$$

which then yields the growth rate r_g as

$$r_g = \frac{\lambda}{2n}\,\frac{1}{\tau_{\text{period}}} = \frac{d_{\text{period}}}{\tau_{\text{period}}} \quad (2.12) \qquad \text{with} \qquad d_{\text{period}} = \frac{\lambda}{2n}. \quad (2.13)$$

The thickness d_{period} corresponds to the increase in layer thickness during one full oscillation of the reflectance, and amounts to 137 nm for GaN grown at 1050°C. Since the oscillation period τ_{period} is easily obtained during growth without any numerical least-squares fit, Eqn. 2.12 is very useful to extract the growth rate.

Absorption

The large band gap of the nitrides makes absorption at the measurement wavelength of 670 nm usually negligible, which allows to track the growth of very thick layers without

any loss of accuracy. Only for $In_xGa_{1-x}N$ with a very large indium content or for GaN grown at very low temperature, the absorbance is too large to be neglected. In the latter case, the high density of dislocations and point defects is responsible for the absorbance below the band gap. For example, nucleation layers grown at 550°C commonly have a dark, yellowish appearance corresponding to a significant absorption in the visible region.

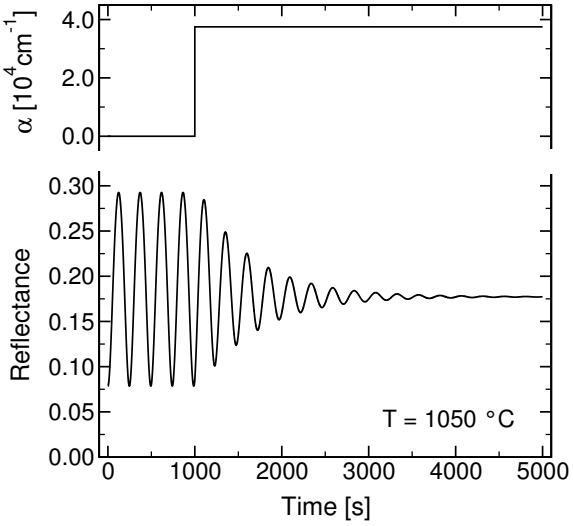

Figure 2.12: Simulated reflectance transient of a GaN film growing on sapphire. After 1000 s the absorption coefficient was set to $\alpha = 3.8 \times 10^4\ \mathrm{cm}^{-1}$.

The general impact of absorption on a reflectance transient is shown in Fig. 2.12, where an extinction coefficient of $k = 0.2$ was assumed after 1000 s of growth. The oscillation is exponentially damped and reaches a reflectance different from the reflectance of sapphire or GaN. Absorption in a layer is introduced into the model through the extinction coefficient k used in the definition of the complex refractive index $N = n - ik$. If the extinction coefficient is different from zero, the damping of the oscillation follows directly from Eqn. 2.5. In this case the reflectance of the sample structure resolves to

$$R = rr^* = \frac{R_{12} + 2Re(r_{12}r_{23}^* e^{i\beta_2' d})e^{-\alpha_2 d} + R_{23}e^{-2\alpha_2 d}}{1 + 2Re(r_{12}r_{23}^* e^{i\beta_2' d})e^{-\alpha_2 d} + R_{12}R_{23}e^{-2\alpha_2 d}}$$

with

$$\alpha_2 = (4\pi/\lambda)k_2 \qquad \text{and} \qquad \beta_2' = (4\pi/\lambda)n_2.$$

In addition to the decay of the amplitude, the superposition of the interference oscillation with the exponential damping reduces the oscillation period in the absorbing material. For large thicknesses compared to the absorption length the reflectance is reduced to $R = R_{12}$, which would be the reflectance of the uppermost layer.

Surface roughness

In general, two kinds of roughness can be distinguished, depending on the scale of the surface features relative to the wavelength of the incident light. The first one is a

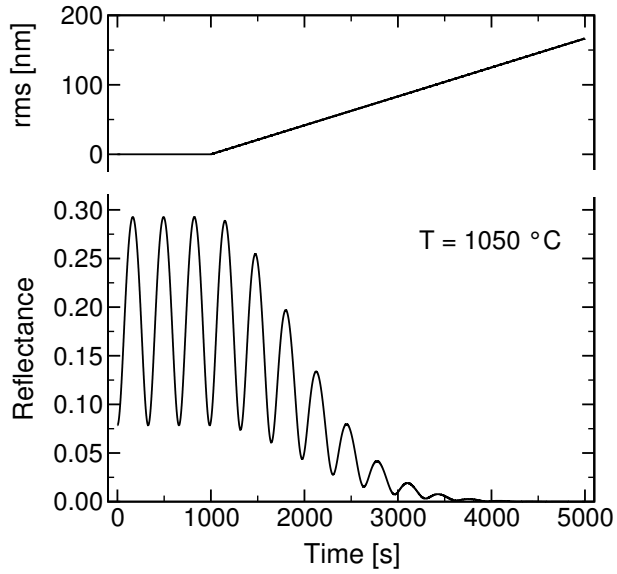

Figure 2.14: Simulated reflectance transient of a growing GaN film on sapphire, where the surface roughness increases with the growth time.

large-scale roughness with features on the scale of a few hundred nanometer. The high-temperature island growth on the recrystallized nucleation layer is an example for this. The second one is a small-scale roughness with a feature size well below the wavelength of the light, like the one seen in Fig. 2.13 The figure contains a cross-section TEM image of a highly Mg-doped GaN layer. The doping causes the formation of pyramidal defects with a diameter of 15 nm, which nucleate on the surface and lead to the diffusive scattering of light.

Including the large-scale roughness quantitatively into the model is difficult, since in this case the specular reflection of light on the individual facets has to be taken into account. In addition, the island diameter and the island height are random, which has to be considered as well. Nevertheless, the impact of surface roughness in general can be studied with a model based on small-scale surface features and a Gaussian distribution of the heights about the mean. The model was developed by Bennett *et al.* [99]. Within the mentioned boundary conditions the reflectance is related to the surface roughness as

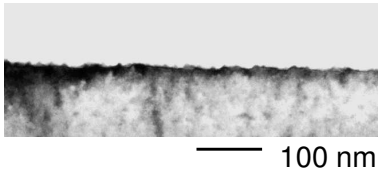

Figure 2.13: TEM image of a Mg-doped GaN layer. Image taken by R.Kroeger, University of Bremen.

$$R = R_0 \exp[-(4\pi\sigma)^2/\lambda^2], \tag{2.14}$$

where R_0 is the specular reflectance of a perfectly smooth surface and σ is the root-mean-square (*rms*) surface roughness. The reflectance decays exponentially with increasing roughness, as is shown in Fig. 2.14. This allows to distinguish the effect of the surface roughness from the layer absorbance, since in the latter case the reflectance approaches a non-zero reflectance. Eqn. 2.14 is capable of describing the high temperature coalescence process for a rather early coalescence, when the average island diameter stays below 100 nm. For larger island diameters of several hundred nanometers the quantitative description fails.

Inhomogeneities in general

The impact of inhomogeneities of various kinds on the reflectance signal can be reduced to an inhomogeneity of the collected light intensity. It is hard to quantify this number without assuming certain microscopic models. It can be a superposition of the inhomogeneities of the thickness, the composition and the roughness inside the laser spot on the surface, which is even more complicated by the finite time of the data acquisition. The time necessary to obtain a stable signal with the used setup is on the order of a few milliseconds, such that the reflectance is the average over a few millimeters on the sample. Since the reflectance profile of this trace is random, its impact cannot be described by a microscopic model.

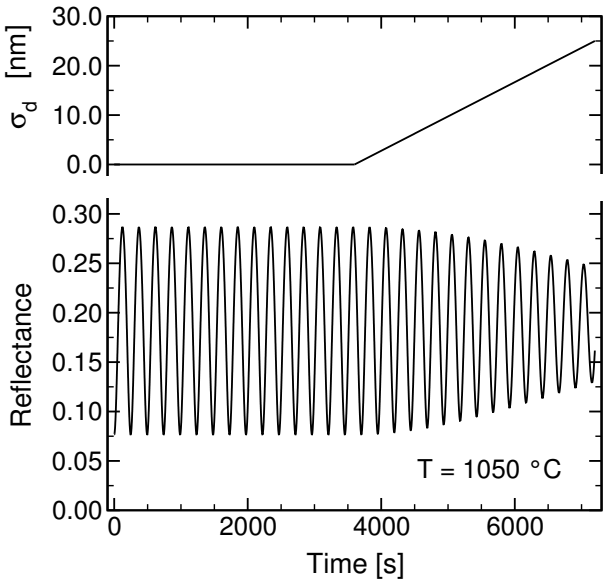

Figure 2.15: Simulated reflectance transient of a growing GaN layer on sapphire, which develops thickness inhomogeneities after one hour of growth.

The main aspect of inhomogeneity is the averaging of the interference oscillations. This leads to a transient, which is somewhat similar to a transient of absorbing material as demonstrated in Fig. 2.15.

Sample transient

As an example, Fig. 2.16 shows the reflectance obtained during the growth run of a laser structure and its simulated counterpart. It is possible to obtain an accurate match using the variables plotted in Fig. 2.16 as well. One can distinguish between composition and roughness effects, and obtain the thicknesses and growth rates of the individual layers. For example, it can be seen that the roughness mainly develops during the growth of the magnesium-doped part of the sample.

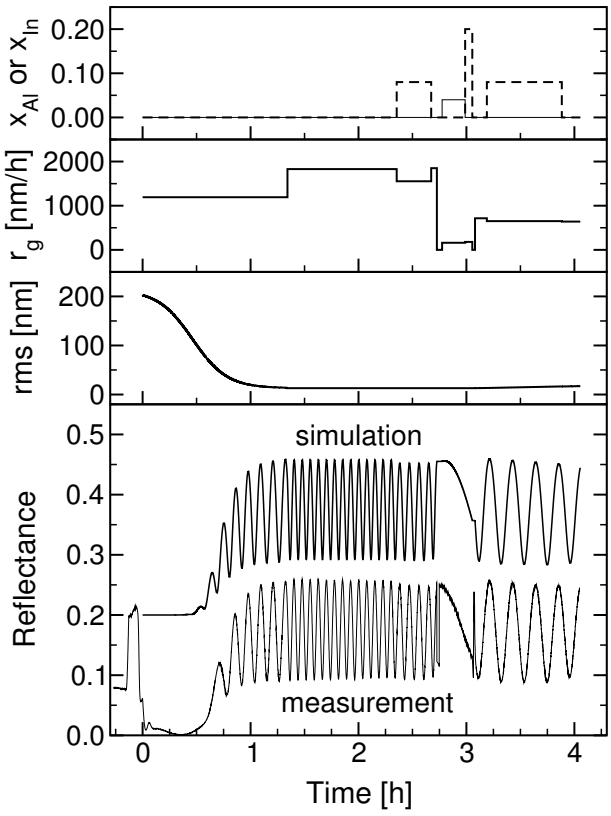

Figure 2.16: The reflectance transient of a laser structure. Shown are the experimental and the simulated data as well as the individual variables used in the simulation.

2.4 X-ray diffraction and strain

2.4.1 Reciprocal space and Ewald construction

Basically, the reciprocal space is the Fourier transformation of the electron density distribution. As the source electrons are localized at the atomic cores, the obtained pattern is directly related to the lattice structure in the sample. Knowing the reciprocal lattice vectors, one can use the Laue condition to understand the interference pattern of the elastically scattered x-rays. This condition says that constructive interference occurs, if the change in wave vector $\vec{q} = \vec{k}_{\text{scattered}} - \vec{k}_{\text{incident}}$ is equal to a vector of the reciprocal lattice. A rather convenient way to illustrate this is the *Ewald construction* shown in Fig. 2.17.

Centered at the beginning of the incoming wave vector $\vec{k}_i$, one draws a sphere in reciprocal space with the radius $1/\lambda$, which is equal to the length of the wave vector. The sphere represents all possible diffraction vectors having the same magnitude and origin as the incident vector $\vec{k}_i$. The sphere is positioned such that the origin of the $\vec{k}$-space coincides with the tip of $\vec{k}_i$. All wave vectors are clearly defined through the angles ω and 2θ, as the orientations of the reciprocal and the real lattice are fixed. All allowed scattered wave vectors $\vec{k}_s$ satisfying the Laue condition end at those points, where the Ewald sphere intersects with lattice points of the reciprocal lattice. The angles ω and 2θ are given by the relative position of the x-ray source, the sample and the detector. Knowing these values, the period d_{hkl} of the diffracting family of lattice planes

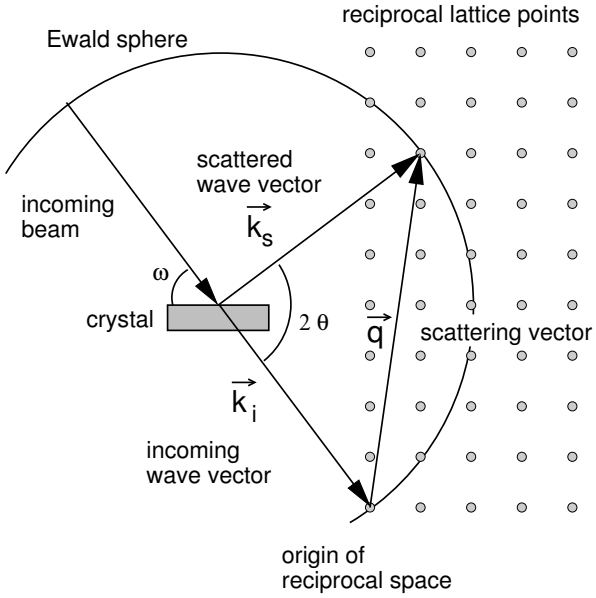

Figure 2.17: X-ray diffraction visualized by the Ewald construction.

is determined from the length of the scattering vector $\vec{q}$:

$$|\vec{q}| = \frac{1}{d_{hkl}} = \frac{2\sin\theta}{\lambda}. \tag{2.15}$$

As the vector $\vec{q}$ can be an integral multiple of the shortest possible reciprocal lattice vector $\vec{q}_0$, it can be replaced by $n \cdot \vec{q}_0$ and one obtains the lattice spacing d in this direction.

$$|n \cdot \vec{q}_0| = \frac{n}{d} = \frac{2\sin\theta}{\lambda}. \tag{2.16}$$

This is *Braggs equation*, which describes the dependence of the scattering angle 2θ on the lattice spacing d along the particular direction. The relation of d to the lattice parameters a and c in a hexagonal unit cell is given via the Miller indices hkl :

$$\left(\frac{1}{d_{\mathrm{hkl}}}\right)^2 = \frac{4}{3} \cdot \frac{h^2 + k^2 + h \cdot k}{a^2} + \frac{l^2}{c^2} \tag{2.17}$$

A good choice for the calculation of the lattice parameters of GaN are the reflections **006** and **204** for the lattice parameters a and c, respectively, or **002** and **105** if the intensity is low. Once the diffraction angles 2θ are obtained, the lattice parameter c can be calculated directly from the symmetric reflection **006** using Eqn. 2.16. The a-axis lattice parameter is then given by Eqn. 2.17, as d_{204} is known from the scattering angle $2\theta_{204}$.

2.4.2 Diffractometer

The diffraction experiments have been performed in two X'Pert diffractometers built by Philips (Philips MRD and X'Pert MRD). A schematic is found in Fig. 2.18. The latter one was extended to allow temperature-dependent measurements, ranging from 10 K to 1200 K. The x-ray source is fixed and provides copper K_α radiation with a wavelength

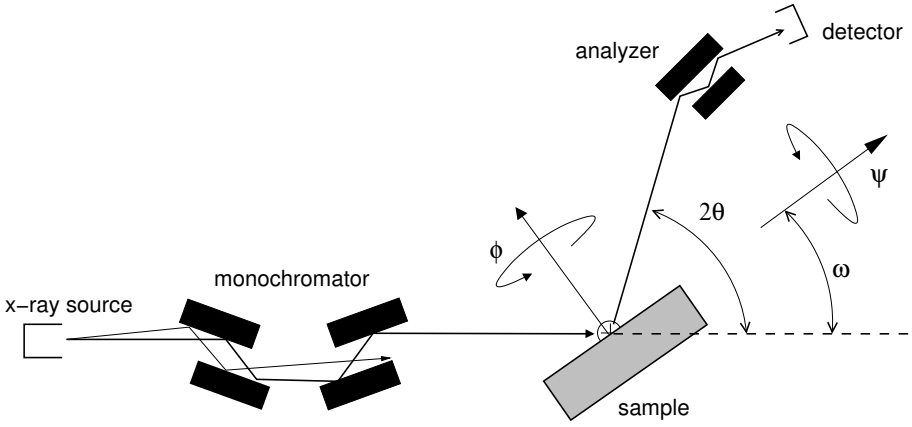

Figure 2.18: Schematic of a high-resolution diffractometer. The various scan angles possible are indicated.

of 1.540553 Å. The beam divergence and the wavelength spread are reduced in a four-crystal monochromator built from germanium single crystals. The sample is mounted on a stage which allows scans along all angles indicated in Fig. 2.18. The precision can be improved by an analyzer crystal placed in front of the detector, which reduces the acceptance angle and thus enhances the resolution in the 2θ direction. The drawback is a significant loss in intensity, making these measurements rather time consuming.

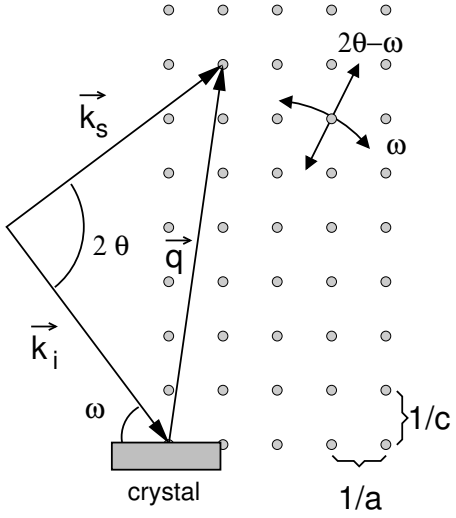

Figure 2.19: Typical scan directions seen in reciprocal space.

The scans of the goniometer are equivalent to movements along certain directions in the reciprocal space of the crystal with respect to the incident wave vector $\vec{k}_i$. The goniometer settings define the scattering vector $\vec{q}$, such that the scans can be translated into movements of $\vec{q}$ in the reciprocal lattice. For example, an ω-scan is represented by a rotation of $\vec{q}$ around the origin, and a 2θ-ω scan corresponds to a elongation of $\vec{q}$ (Fig. 2.19). A combination of these two scan types yields a cross-section of the reciprocal space, from which the strain state of a heterostructure can be derived. For the case of a

pseudomorphic structure containing different alloys the reciprocal lattice parameter $1/a$ would be the same for all layers, whereas for relaxed structures this lattice parameter would differ according to the strain state and the composition.

2.4.3 Elastic Properties

The elastic deformation of a crystal exposed to a stress σ_{ij} can be generally described by *Hooke´s law*. This law is valid for sufficiently small forces, where the elastic limit is not exceeded and the crystal recovers its original shape as soon as the stress is relieved. The strain ε_{kl} describes the change in length $\Delta l/l_0$, with l_0 being the original length and $\Delta l = l - l_0$ the longitudinal increase. Each strain component ε_{kl} is related to all stress components σ_{ij} by :

$$\sigma_{ij} = \sum_{k,l} c_{ijkl}\, \varepsilon_{kl} \qquad \text{with} \qquad i,j,k,l \in \{1,2,3\}, \tag{2.18}$$

where the c_{ijkl} are the stiffness constants of the crystal. The diagonal elements of the strain and stress tensors describe the linear tension and compression of a crystal, whereas the off-axis components describe the shear strains and stresses, respectively. Taking the general symmetry of the stiffness tensor c_{ijkl} in the first two and last two suffixes into account [51], the number of independent components is reduced. This simplification is called *matrix notation* :

Tensor notaion	11	22	33	12,21	13,31	23,32
Matrix notation	1	2	3	4	5	6

Accordingly, Eqn. 2.18 can be rewritten to

$$\sigma_i = \sum_j C_{ij}\, \varepsilon_j \qquad \text{with} \qquad i,j \in \{1,\ldots,6\}. \tag{2.19}$$

The special symmetry of hexagonal crystals allows further simplifications, if the z-axis of coordinate system is aligned along the [0001]-axis of the crystal [51]. In this case one finds $C_{11} = C_{22}$, $C_{13} = C_{23}$, $C_{44} = C_{55}$ and $C_{66} = \frac{1}{2}(C_{11} - C_{22})$. The matrix C_{ij} is symmetric and reads as follows :

$$C_{ij} = \begin{bmatrix} C_{11} & C_{12} & C_{13} & 0 & 0 & 0 \\ C_{12} & C_{11} & C_{13} & 0 & 0 & 0 \\ C_{13} & C_{13} & C_{33} & 0 & 0 & 0 \\ 0 & 0 & 0 & C_{44} & 0 & 0 \\ 0 & 0 & 0 & 0 & C_{44} & 0 \\ 0 & 0 & 0 & 0 & 0 & 0 \end{bmatrix}$$

As the shear stresses can be neglected in many heterostructures, one often finds only the upper left quarter of the matrix for the description of the elastic properties.

Biaxial strain

The most commonly observed strain in GaN-based heterostructures is of biaxial nature, which arises from a mismatch of the relaxed in-plane lattice parameters of the individual layers. If the in-plane lattice parameter is reduced compared to the relaxed one, the strain is *compressive*, if it is enlarged, the strain is *tensile*. As the base material is mostly GaN, $Al_xGa_{1-x}N$ is commonly found to be under tension, whereas $In_xGa_{1-x}N$ is usually under compression (see Fig. 2.20). Thus, the lattice parameters c for $In_xGa_{1-x}N$ and $Al_xGa_{1-x}N$ coherently grown on GaN are enlarged and reduced, respectively.

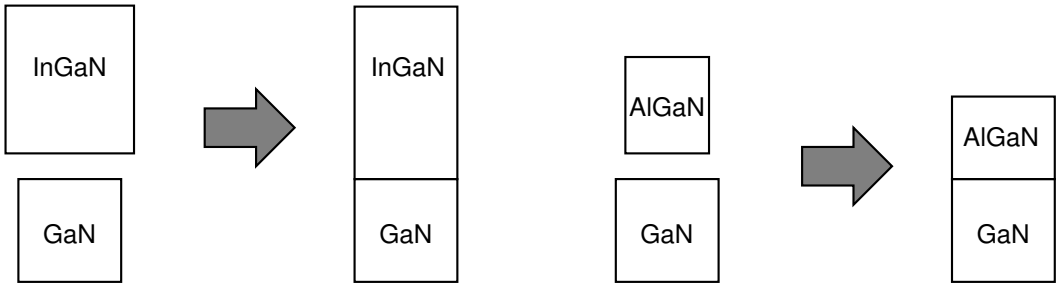

Figure 2.20: Illustration of biaxial strain in GaN-based heterostructures

Pseudomorphically grown heterostructures exhibit the same in-plane lattice parameter for all layers. This means that stresses σ_1 and σ_2 have to be present in the basal plane of the layers, whereas the lattice can relax along the main axis. As hexagonal material has only one in-plane lattice parameter, the boundary conditions for biaxially stressed heterostructures with the [0001] direction parallel to the surface normal are

$$\sigma_1 = \sigma_2 \qquad \text{and} \qquad \sigma_3 = 0. \tag{2.20}$$

Using this in Eqn. 2.19 one finds the relation of the strain in the basal plane and along the main axis

$$\varepsilon_3 = -2\frac{C_{13}}{C_{33}}\,\varepsilon_1 \tag{2.21}$$

$$\Leftrightarrow \frac{c-c_0}{c_0} = -2\frac{C_{13}}{C_{33}}\,\frac{a-a_0}{a_0} \tag{2.22}$$

$$\Leftrightarrow \frac{c-c_0}{c_0} = -\frac{2\nu}{1-\nu}\,\frac{a-a_0}{a_0} \tag{2.23}$$

with ν being the Poisson ratio. The variables a_0 and c_0 are the lattice parameters of the relaxed material, and a and c are those of the strained layers. Eqn. 2.22 allows to derive the composition of an alloy from the biaxially strained lattice parameters, as will be described in more detail for ternary alloys in Section 2.4.4.

Biaxial stress

Using Eqn. 2.21 and Eqn. 2.19 for σ_1, the biaxial in-plane stress can be directly related to the in-plane strain of the layer :

$$\sigma_1 = \left(C_{11} + C_{12} - 2\,\frac{C_{13}}{C_{33}}\,C_{13} \right) \cdot \varepsilon_1. \tag{2.24}$$

As XRD can only access the lattice parameters of the crystal, the derivation of stress values relies on equations like 2.24. Therefore, the stiffness constants and the relaxed lattice parameters of the material play a crucial role and have to be chosen carefully. An overview of the material constants available in literature was given in Section 1.5 on page 13. Inserting the appropriate values for GaN, the relation of stress and strain becomes

$$\sigma_1 = 449.6\ \text{GPa} \times \varepsilon_1. \tag{2.25}$$

2.4.4 How to determine the composition of ternary strained structures

The composition of ternary componds can be determined utilizing *Vegards law*, which assumes a linear dependence of the lattice parameters. The approach is correct, as long as the material is relaxed and the hydrostatic strain due to point defects can be neglected. For $Al_xIn_yGa_{1-x-y}N$, the latter condition is fulfilled, as the changes in lattice parameters due to the compostition are large compared to the effect of point defects. Therefore, for relaxed films it is sufficient to measure only one lattice parameter in order to determine the composition. For the nitrides, one commonly chooses the lattice parameter c as it is measured with little effort from a symmetric reflection (e.g. **002**). In this case the chemical composition of a $Al_xGa_{1-x}N$ or $In_xGa_{1-x}N$ is given by

$$x = \frac{c - c_{\text{GaN}}}{c_{\text{AlN/InN}} - c_{\text{GaN}}}. \tag{2.26}$$

For strained layers the elastic deformation of the unit cell has to be taken into account, such that both lattice parameters c and a have to be determined. From these values the relaxed lattice parameters can be estimated taking the elastic properties of the mixed crystal into account. The relation has been derived in Eqn. 2.23, in which the lattice and the stiffness constants depend on the composition x :

$$(c - c_0(x)) + 2\frac{C_{13}(x)}{C_{33}(x)}\,\frac{c_0(x)}{a_0(x)}\,(a - a_0(x)) = 0 \tag{2.27}$$

Assuming Vegards law to be valid for the lattice parameters as well as for the stiffness constants, one obtains an equation, which cannot be solved analytically. The first possible approximation is to use the Poisson ratio instead of the stiffness constants and to apply Vegards law to it. In this case it is possible to apply an algorithm in order to obtain the correct composition, which has been proposed by Schuster *et al.* [100].

Another simplification of Eqn. 2.27 is possible, if the molar fraction is rather low, i.e. the stiffness constants and the c_0/a_0 ratio are close to those of GaN. In this case one can use values of GaN and keep them constant for all compositions. The solution of Eqn. 2.27 for this case is :

$$x = \frac{(c - c_{\mathrm{GaN}}) + \zeta\,(a - a_{\mathrm{GaN}})}{(c_{\mathrm{AlN/InN}} - c_{\mathrm{GaN}}) + \zeta\,(a_{\mathrm{AlN/InN}} - a_{\mathrm{GaN}})} \qquad (2.28) \qquad \text{with} \qquad \zeta = 2\frac{C_{13}^{\mathrm{GaN}}}{C_{33}^{\mathrm{GaN}}} \cdot \frac{c_0^{\mathrm{GaN}}}{a_0^{\mathrm{GaN}}}$$

The error of this approximation is very small for alloy compositions used in typical devices, namely $x = 0 \ldots 0.2$ for $In_xGa_{1-x}N$ and $x = 0 \ldots 0.3$ for $Al_xGa_{1-x}N$, respectively. This is illustrated in Fig. 2.21, which shows the composition of these two alloys in dependence on the lattice parameter c. As the stiffness constants of AlN and GaN are very similar, the difference between the exact values and the approximation mentioned above is negligible almost over the whole composition range of $Al_xGa_{1-x}N$. For $In_xGa_{1-x}N$ the approximation holds only for small indium molar fractions. The accuracy can be improved, if one uses the lattice and the stiffness constants of $In_{0.1}Ga_{0.9}N$ for the calculation. In this case the relative error for $x < 0.2$ is below 1%, such that the latter approximation was chosen for all further analysis.

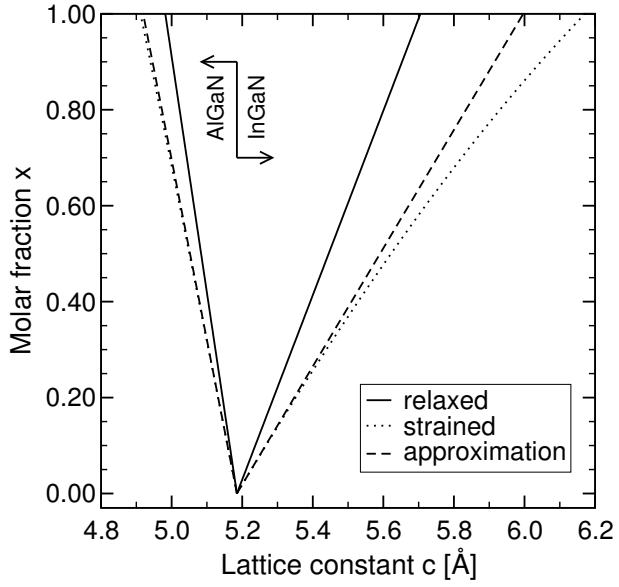

Figure 2.21: The molar fraction of ternary alloys pseudomorphically grown on GaN in dependence on the lattice parameter c. Shown is the relation for relaxed and for strained films and the approximation from Eqn. 2.4.4.

Also shown in Fig. 2.21 is the variation of the lattice parameter c for relaxed material, which is described by Eqn. 2.26. Its use results in significantly higher In or Al contents for the same lattice parameter c compared to the pseudomorphic case. This shows, that the strain in the ternary group-III nitrides may not be neglected for the determination of the composition, not even for low molar fractions x.

2.5 Transmission electron microscopy

This section will briefly outline image generation and dislocations in TEM. More detailed information can be found in Ref. [101].

Image generation

Electrons passing a crystal will strongly interact with the electron shell or the atomic nuclei, i.e. they are scattered. Therefore, to be electron transparent, the samples under investigation have to be extremely thin. Typically thicknesses are on the order of a few hundred atomic layers. Inside the specimen the electrons undergo inelastic and elastic scattering. In the former case the electrons lose energy and cause the generation of x-rays or secondary electrons characteristic for the atomic nuclei. In the latter case the electrons keep their energy but change direction, which is described by Rutherford scattering. This scattering process is dependent on the mass of the nuclei, which causes a mass-dependent contrast in the obtained image and allows to distinguish different alloys or materials.

In crystalline samples the superposition of all individual electron waves leads to interference effects like observed for x-ray diffraction (see Section 2.4.1). Accordingly, an image of the reciprocal lattice is formed behind the specimen. Using an aperture in this image plane, one can select the reflections which will generate the lattice image. For example, this enables one to obtain images of the crystal obtained from one special family of lattice planes. The advantage of such images is the sensitivity to non-isotropic distortions of the lattice, such as those caused by dislocations. One distinguishes bright-field and dark-field images. In the former case the direct beam is used for imaging, and in the latter case one of the diffracted beams is used.

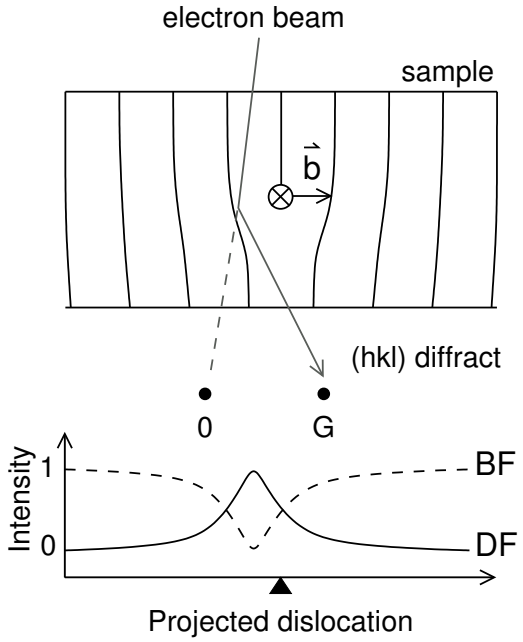

Figure 2.22: Image contrast due to dislocations. The upper drawing illustrates the diffraction of the electrons at the lattice planes. The lower graph depicts the intensity distribution for the **G** reflection [101].

Dislocations in TEM

Dislocations cause a local distortion of the crystal lattice, described by the Burgers vector $\vec{b}$ and the propagation vector $\vec{u}$ along the dislocation line. This is shown in Fig. 2.22 for an edge type threading dislocation seen along the dislocation line. The lattice planes are

bent around the dislocation, resembling a variation of the diffraction conditions across the specimen. To obtain an image of the dislocation, the specimen is slightly tilted, such that only the bent planes around the dislocation fulfill the Bragg condition and diffract into the reciprocal lattice point **G**. The contrast in the image is then caused by this selected family of lattice planes. As the diffracting planes are not precisely at the position of the dislocation, the contrast in the image is slightly displaced with respect to the real position [101].

In the case of a bright field image the dislocation line appears dark, as electrons are scattered into **G**, corresponding to a loss in intensity for the zeroth order peak. The opposite is the case for dark field images. Here, the Bragg condition is fulfilled only in the area of the dislocations and the dislocation lines appear bright. In order to see a dislocation in TEM, the distortion of the lattice has to be along the direction of the diffraction vector $\vec{g}$. This condition is expressed by the *invisibility criterion*, which says that the scalar product $\vec{g} \cdot \vec{b}$ has to be different from zero in order to obtain contrast from a dislocation. As the Burgers vector $\vec{b}$ points along the direction of the distortion, the condition simply requires that the diffracting planes may not be parallel to the distortion. Accordingly, it is possible to determine the dislocation type via the selection of the diffraction vector. For example, in order to see screw type threading dislocations in GaN with a Burgers vector $\vec{b}_s = [0001]$, one has to use a diffraction vector $\vec{g}$ with a component parallel to the c-axis.

Chapter 3

Metalorganic Vapor Phase Epitaxy of GaN

3.1 Chemistry and Thermodynamics

The growth process in general is governed by thermodynamics, reaction kinetics, flow dynamics and chemical composition of the gas phase. Thermodynamics provide the driving force for the reaction, i.e. the conditions of the equilibrium. The reaction kinetics describe the speed of the reaction; and flow dynamics control the transport of the reactants to the surface. The chemical composition of the atmosphere determines the reactions involved in the growth, which includes the pre-reactions as well.

3.1.1 The main reactions to form GaN

The conventional source materials involved in the synthesis of GaN are ammonia, trimethylgallium (TMG) and the carrier gases hydrogen or nitrogen. Many different reactions are involved in the growth process, either directly to form GaN or indirectly for the case of pre-reactions. Starting from the gas phase above the substrate, the main reactions occurring here are the decomposition of the reactants and the formation of various adducts. A detailed description of the gas phase rections is found in [102]. The main reaction is the one between ammonia and TMG, which form a larger molecule :

$$Ga(CH_3)_3 + NH_3 \rightleftharpoons Ga(CH_3)_3{:}NH_3,$$

which is decomposed later at the surface due to the high growth temperature. This decomposition is a multi-step process and provides Ga for the growth reaction to form GaN. The formation of the adduct is the seed for larger complexes, which then appear as particles. The formation velocity of particles is high enough to impair the growth at lower gas velocities, as in this case the particles can deposit on the substrate. In particular, this is problematic for MOVPE growth at atmospheric pressure.

Two main decomposition reactions have to be considered in the gas phase. The first is the decomposition of the mentioned adduct and the second is the parasitic decomposition of NH_3 into H_2 and N_2. The thermal stability of TMG:NH_3 is very low, such

that for typical growth temperatures of 1050°C the adduct can be assumed to be fully decomposed, and does not have to be considered for the growth reaction. Accordingly, the surface reaction for the growth can be described with gaseous Ga as one reactant. The decomposition of ammonia into N_2 and H_2 is a rather slow reaction, despite the instability of ammonia at temperatures exceeding 300°C [103]. Usually, the largest fraction of the introduced ammonia is available for the reaction, although the extent of the decomposition is affected by the growth conditions and the equipment. It is common to introduce a decomposition factor α for thermodynamic calculations [104]:

$$NH_3 \rightleftharpoons (1\text{-}\alpha)\ NH_3 + \frac{\alpha}{2}\ N_2 + \frac{3\alpha}{2}\ H_2.$$

For the used Thomas Swan reactor, the time for the ammonia decomposition prior to the growth reaction is extremely short due to the showerhead concept, which keeps the ammonia at room temperature until 1 cm before the susceptor. This makes the molar fraction α of decomposed ammonia almost negligible. For the growth of GaN, only the reaction at the vapor-solid interface, where gaseous Ga and ammonia react to form GaN and hydrogen, has to be considered :

$$Ga(g) + NH_3(g) \rightleftharpoons GaN(s) + \frac{3}{2}H_2. \tag{3.1}$$

Eqn. 3.1 is the main reaction to be considered for the growth of GaN. As it is reversible, it already points to a difficulty of the growth in a hydrogen atmosphere. An increased hydrogen partial pressure favors the reverse reaction, i.e. the decomposition of GaN.

3.1.2 Thermodynamics

For a chemical system in equilibrium, the rate of the forward reaction equals the rate of the backward reaction [105]. For Eqn. 3.1 this means, that one reaction is continuously forming GaN and one is continuously decomposing it. To describe gas phase reactions quantitatively, the partial pressures of the involved reactants are commonly used, since these are proportional to the respective concentrations. In this case, the reaction rate of a chemical reaction is proportional to the partial pressures of the source reagents. Solids are included in the reaction by their activity, which is often set to one, if the volume of the solid is negligible. Accordingly, the rate of the formation reaction r_{form} is given by $r_{form} = k_{form}\, p(Ga)p(NH_3)$ and the rate of the decomposition reaction r_{decomp} by $r_{decomp} = k_{decomp}\, a(GaN)(p(H_2))^{3/2}$. The rate constants k_{form} and k_{decomp} characterize the reaction kinetics. The equilibrium constant K is then defined as the ratio of the forward and the backward rate constants :

$$K = \frac{k_{form}}{k_{decomp}} = \frac{a(GaN)p(H_2)^{3/2}}{p(NH_3)p(Ga)}. \tag{3.2}$$

The position of the equilibrium is mainly given through the temperature of the system. Koukitu *et al.* have calculated the equilibrium constant K from the free energies of for-

mation of the individual constituents [106]. Table 3.1 contains these values for GaN, InN and AlN.

Reaction	$\log_{10}$K (temperature in K)
$Ga(g) + NH_3(g) \rightleftharpoons GaN(s) + 3/2\ H_2$	$-12.2 + 1.78\times10^4/T + 1.79\ \log_{10}(T)$
$In(g) + NH_3(g) \rightleftharpoons InN(s) + 3/2\ H_2$	$-13.1 + 1.13\times10^4/T + 2.29\ \log_{10}(T)$
$Al(g) + NH_3(g) \rightleftharpoons AlN(s) + 3/2\ H_2$	$-14.2 + 3.17\times10^4/T + 2.33\ \log_{10}(T)$

Table 3.1: The equilibrium constants of the reactions to form GaN, InN and AlN [106].

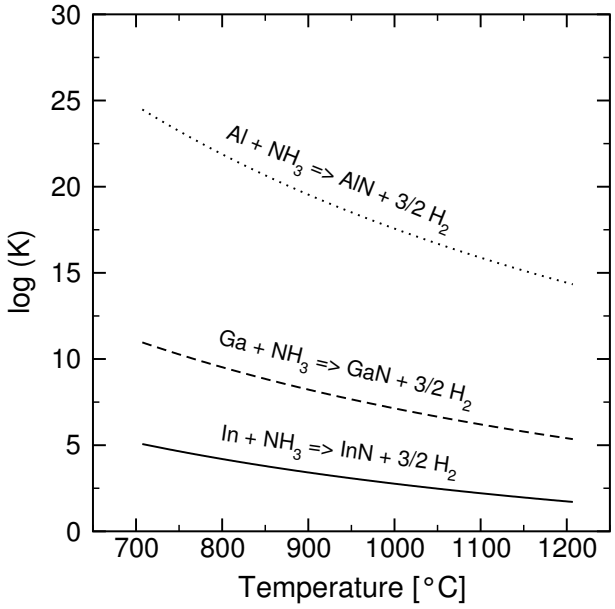

Figure 3.1: The equilibrium constants K versus the temperature for the formation reactions of GaN, InN and AlN [106].

A high equilibrium constant K corresponds to a fast forward or a slow backward reaction, i.e. the equilibrium state would be on the side of the products. The equilibrium constants of the three binary nitrides are shown in Fig. 3.1, in dependence on the temperature. AlN exhibits the highest value of K, i.e. it is the most stable material of these three. For GaN, the equilibrium constant is already lower by orders of magnitude, and InN is again one order below GaN. This illustrates the main problem for the growth of $In_xGa_{1-x}N$. The stability of InN is much lower than that of GaN, which requires the growth of this ternary alloy to be performed at reduced temperatures, typically around 800°C compared to 1050°C for GaN. Similar observations are made for the growth of $Al_xGa_{1-x}N$, where the desorption of Ga atoms from the $Al_xGa_{1-x}N$ surface is enhanced compared to the Al atoms, as the strength of the Al-N bond is higher. This causes the preferential incorporation of Al into the film and needs to be considered for the adjustment of the growth parameters.

3.1.3 Decomposition

The concurrent reaction to the growth process is the decomposition of GaN. Its relevance is evident from the growth regime, which changes from transport-limited to desorption-limited with increasing temperature [76].

Hydrogen and ammonia partial pressure

In contrast to vacuum, the decomposition in an atmosphere involves the chemical reaction of the film with the surrounding gases. These chemical reactions largely determine the temperature dependence of the equilibrium, such that decomposition temperatures ranging from 400 to 1070°C were reported ([107, 108, 109, 107] and references therein). Experiments performed in an inert atmosphere like N_2 or He yielded a higher decomposition temperature compared to experiments performed in hydrogen. This shows that the effect of hydrogen is significant, as it supports the reverse synthesis reaction, namely

$$\mathrm{GaN(s)} + \frac{3}{2}\mathrm{H_2} \rightleftharpoons \mathrm{Ga(g)} + \mathrm{NH_3(g)}. \tag{3.3}$$

The existence of this reformation reaction has been demonstrated experimentally by measuring the ammonia concentration in the exhaust gas of an annealing furnace flowing hydrogen gas over GaN [110]. In some cases, Ga droplets were observed on the GaN surface, indicating that the vapor pressure of Ga over GaN can even exceed that of liquid Ga [107, 111]. Applying the principle of Le Chatelier, one finds the inverse of Eqn. 3.2 for the equilibrium constant :

$$\mathrm{K_{decomposition}} = \frac{\mathrm{p(NH_3)p(Ga)}}{\mathrm{a(GaN)p(H_2)^{3/2}}} = \frac{\mathrm{p(NH_3)p(Ga)}}{\mathrm{p(H_2)^{3/2}}} \tag{3.4}$$

Since GaN is a solid, its activity a is set to one. If the partial pressure of hydrogen is increased in Eqn. 3.4, the concentration of the reaction products has to increase as well to keep $\mathrm{K_{decomposition}}$ constant. Therefore, the system evades by forming more products, namely, decomposing GaN, and enhances the forward (decomposition) reaction [112, 113]. The opposite is the case for an increased partial pressure of ammonia, which supports the reverse reaction path. In this case the concentration of the products is increased, and the system reacts by forming more GaN and reducing the decomposition. This can be seen in the data presented in Fig. 3.2, where the decomposition rate of GaN in a mixed H_2/NH_3 atmosphere is plotted in dependence on the ammonia partial pressure together with the equilibrium partial pressure of Ga over this surface.

In this experiment the decomposition of GaN was monitored through the interference oscillations due to the decrease in thickness. The decomposition rate was determined as described in Section 2.3. The difficulty of this experiment laid in the increasing roughness of the surface, which diminishes the reflectance and the oscillation amplitude. To some extent, this can be taken care of by including roughness in the reflectance model, but to determine the decomposition rates accurately, it is necessary to perform several decomposition runs with different samples.

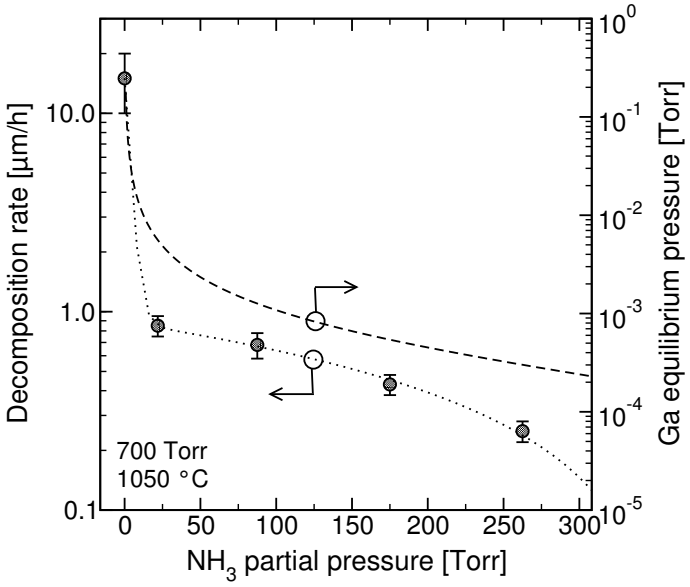

Figure 3.2: Decomposition rate and equilibrium partial pressure of Ga in a mixed H_2/NH_3 atmosphere in dependence on the partial pressure of ammonia.The dotted line is a guide to the eye.

Ammonia significantly increases the stability of the GaN surface against decomposition, as just a few percent of ammonia in the atmosphere are sufficient to reduce the decomposition rate by an order of magnitude, i.e. from 15 μm/h to 1 μm/h. This can be qualitatively understood using a thermodynamic argument similar to the approaches of Koukitu or Duan [104, 114]. The interface reaction dominating the decomposition at the interface is assumed to be the reaction in 3.3, whereas all other reactions are neglected. The respective equilibrium state is given by Eqn. 3.4 with the equilibrium constant from Table 3.1. The partial pressures used in the equations are the equilibrium partial pressures p_i of the chemical reaction. Then, the equilibrium partial pressure of Ga over the surface is

$$p(\mathrm{Ga}) = \frac{p(\mathrm{H_2})^{3/2}}{\mathrm{K}\, p(\mathrm{NH_3})}. \tag{3.5}$$

This value can be understood as the thermodynamic driving force for the decomposition reaction, as the Ga in the atmosphere is continuously removed by the gas flow in the reactor. If the Ga equilibrium pressure over the surface is high, but the actual partial pressure is lower, then the decomposition reaction is enhanced proportional to the deviation from the equilibrium. The corresponding curve is plotted in Fig. 3.2. It can be seen that the deviation from the equilibrium is diverging with the ammonia partial pressure going to zero, which equals a divergence of the etch rate.

A more quantitative model for this feature is obtained from the analysis of the rate equations to form Ga in the gas phase. Assuming Eqn. 3.3 to be the dominant reaction pathway, the rate equation for gaseous Ga is the sum of the two terms describing the decomposition and formation of GaN,

$$\frac{\mathrm{d}}{\mathrm{dt}} p(\mathrm{Ga}) = k_{\mathrm{decomp}} p(\mathrm{H2})^{3/2} - k_{\mathrm{form}} p(\mathrm{NH_3}) p(\mathrm{Ga}), \tag{3.6}$$

where k_{decomp} and k_{form} are the rate constants of the decomposition and the formation

reaction of GaN. The solution of this inhomogeneous differential equation is

$$p(\mathrm{Ga}) = \frac{p(\mathrm{H_2})^{3/2}}{Kp(\mathrm{NH_3})} + \left(p_0(\mathrm{Ga}) - \frac{p(\mathrm{H_2})^{3/2}}{Kp(\mathrm{NH_3})} \right) \exp\left[-k_{\mathrm{form}} p(\mathrm{NH_3}) t\right]. \tag{3.7}$$

Eqn. 3.7 describes the evolution of the Ga partial pressure in dependence on the time, starting from an initial pressure $p_0(\mathrm{Ga})$ for $t = 0$. The two fractions are equal to the equilibrium partial pressures of Ga, $p_{\mathrm{eq}}(\mathrm{Ga})$, for these ammonia and hydrogen partial pressures as derived in Eqn. 3.5. Naming the deviation of the initial partial pressure $p_0(\mathrm{Ga})$ from the equilibrium partial pressure $p_{\mathrm{eq}}(\mathrm{Ga})$ by $\Delta p = p_0(\mathrm{Ga}) - p_{\mathrm{eq}}(\mathrm{Ga})$, the Eqn. 3.7 reads :

$$p(\mathrm{Ga}) = p_{\mathrm{eq}}(\mathrm{Ga}) + \Delta p \cdot \exp\left[-k_{\mathrm{form}} p(\mathrm{NH_3}) t\right] \tag{3.8}$$

As the partial pressures p_i are connected to the molar quantities n_i as

$$p_i = \frac{n_i}{n_{\mathrm{tot}}} p_{\mathrm{tot}}, \tag{3.9}$$

the partial pressures can be directly related to the decomposition rates. The variables n_{tot} and p_{tot} are the total molar quantity and the total pressure, respectively. Both can be assumed to be constant for typical reactor conditions, as the equilibrium partial pressure of gallium is orders of magnitude below the partial pressures of ammonia and hydrogen (see Fig. 3.2), except for input partial pressures of ammonia approaching zero. In this case the equilibrium equation would require the Ga partial pressure to diverge. As this is not relevant for growth, the following discussion is restricted to ammonia pressures above 25 Torr. The time derivative of the partial pressure of Ga in the atmosphere is proportional to the decomposition rate of the GaN. The decomposition rate r_{decomp} of GaN in a mixed H_2/NH_3 atmosphere then reads

$$r_{\mathrm{decomp}} \propto \frac{d}{dt} p(\mathrm{Ga})\Big|_{t=t_0} = -k_{\mathrm{form}} p(\mathrm{NH_3}) \left(p_0(\mathrm{Ga}) - \frac{p(\mathrm{H_2})^{3/2}}{\mathrm{K}p(\mathrm{NH_3})} \right) \exp[-k_{\mathrm{form}} p(\mathrm{NH_3}) t_0]. \tag{3.10}$$

The time constant t_0 in Eqn. 3.10 characterizes the time needed to transport the Ga from the sample surface across the boundary layer into the gas phase, i.e. it defines the Ga partial pressure, which can build up in the boundary layer. To describe the experimental values, the time constant t_0 is assumed to be constant for all conditions employed. This is not necessarily true, as the viscosity and the diffusion processes can change and affect the reaction kinetics. Assuming the initial Ga partial pressure of the atmosphere to be zero, i.e. $p_0(\mathrm{Ga}) = 0\,\mathrm{Torr}$, and using $p_{\mathrm{tot}} = p_{\mathrm{H2}} + p_{\mathrm{NH3}}$, the dependence of the decomposition rate on the ammonia partial pressure is obtained as

$$r_{\mathrm{decomp}} = c_0 \left(p_{\mathrm{tot}} - p(\mathrm{NH_3})\right)^{3/2} \exp\left(-c_1 p(\mathrm{NH_3})\right). \tag{3.11}$$

The two parameters c_0 and c_1 are fitting constants. The fit of Eqn. 3.11 to the experimental data is shown in Fig. 3.3.

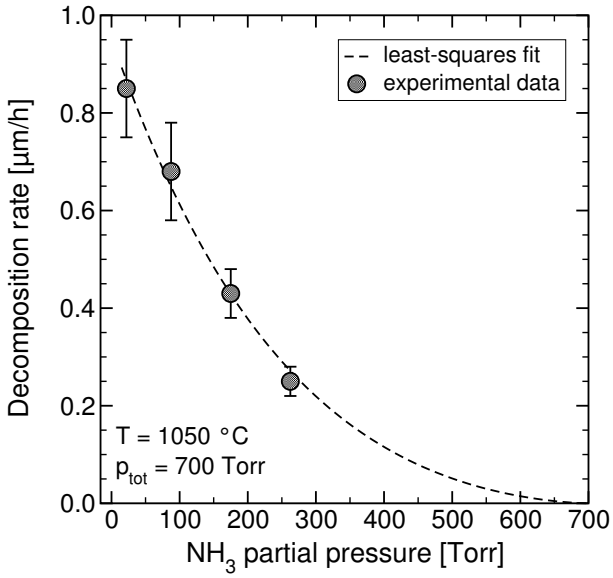

Figure 3.3: The decomposition rate of GaN in dependence on the ammonia partial pressure in a mixed H_2/N_2 atmosphere. The dashed line is a least squares fit of Eqn. 3.11 to the experimental values.

It can be seen, that the model reasonably describes the decomposition of GaN with varying ammonia content of the atmosphere. The decomposition is strongest for low ammonia partial pressures, but for typical gas phase compositions with 30% - 40% of ammonia the decomposition has still to be considered.

Total pressure

The impact the total pressure on a gas-phase reaction depends on its nature. If the total molar quantity remains unchanged, the pressure will not affect the equilibrium. However, if the number of moles in the gas phase changes upon the reaction, then the equilibrium constant can vary as well. For GaN this is the case, as it is a heterogeneous reaction. The phase changes from gaseous to solid for the case of growth and from solid to gaseous (or liquid in the case of Ga droplets) for the decomposition reaction. This means that the equilibrium constant K becomes a function of the total pressure. Restricting the reaction to the surface, the surface structure and reaction kinetics might play a role as well in the pressure dependence of K. For example, it has been observed, that during the decomposition of GaN in hydrogen Ga droplets are easier formed at atmospheric pressure compared to low pressure [111]. As the Ga stored in these droplets does not contribute to the partial pressure in the gas phase, the equilibrium constant is modified as well.

For a mixed growth H_2/N_2 atmosphere, the decomposition rate was shown to increase from 70 nm/h to 350 nm/h if the total pressure is raised from 20 to 300 Torr [107]. In that report, the growth rate decreased by almost exactly by the same amount, which indicates that pre-reactions can be neglected for this pressure range. In order to study the impact of the total pressure on the equilibrium, the equilibrium partial pressure of Ga was measured in dependence on the total pressure. This was achieved by recording the reflectance while changing the TMG flow. If one starts from a rather low flow, then the surface is first unstable, i.e. it decomposes, then it stabilizes and finally growth starts due to the enhanced forward reaction. Thus, the equilibrium partial pres-

sure of Ga is found at the turning point of the reflectance. This is also in agreement with Eqn. 3.10, as the decomposition rate is zero for an input partial pressure of Ga equal to the equilibrium partial pressure.

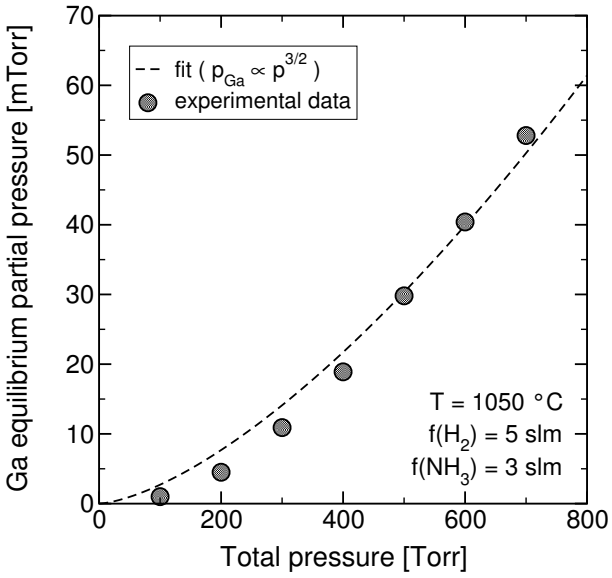

Figure 3.4: Variation of the equilibrium partial pressure of gallium with the total pressure. The dashed line is a least-squares fit based on the assumption that the partial pressure of Ga is proportional to the partial pressure of hydrogen.

The variation of the equilibrium partial pressure with the total pressure of the reaction is shown in Fig. 3.4. The gas flows of hydrogen and ammonia were kept constant at 5 slm and 3 slm, respectively, and the total pressure was varied from 100 Torr to 700 Torr. At a reactor pressure of 100 Torr the growth initiated at the lowest Ga flow possible, such that the equilibrium pressure must be below 5 mTorr in this case. Fig. 3.4 shows that the Ga pressure increases by an order of magnitude, when the total pressure is raised from low pressure to atmospheric pressure. The experimental values approximately follow the total pressure raised to the power 3/2. This can be understood as the decomposition in hydrogen, since the hydrogen partial pressure enters the equilibrium equations at exactly this power (Eqn. 3.4 on page 46). This interpretation was proposed by Mayumi *et al.* for the decomposition in a mixed atmosphere containing an inert gas and hydrogen [112, 113].

The equilibrium constant K was calculated from the measured partial pressures using Eqn. 3.2, assuming ammonia and hydrogen to follow the total pressure of the system linearly. The obtained values are depicted in Fig. 3.5 on a logarithmic scale. The equilibrium constant is found to be consistently below the theoretically expected value presented by Koukitu *et al.* [106], but it might approach this value for low pressures. For rising pressure, K decreases, corresponding to the observed lower stability of the solid phase. However, it is unclear, to which extent this result is quantitative, since the Ga partial pressure in the boundary layer, which determines the reaction with the solid, is probably not equal to the measured input partial pressure, but below this value. Pre-reactions, changes in the flow pattern or in the diffusion across the boundary layer might be responsible for this. These are sensitive to the total pressure, but the extent is unknown. Thus, the obtained equilibrium constant K should not be understood quantitatively, but can serve as a qualitative measure of the equilibrium, particularly since the

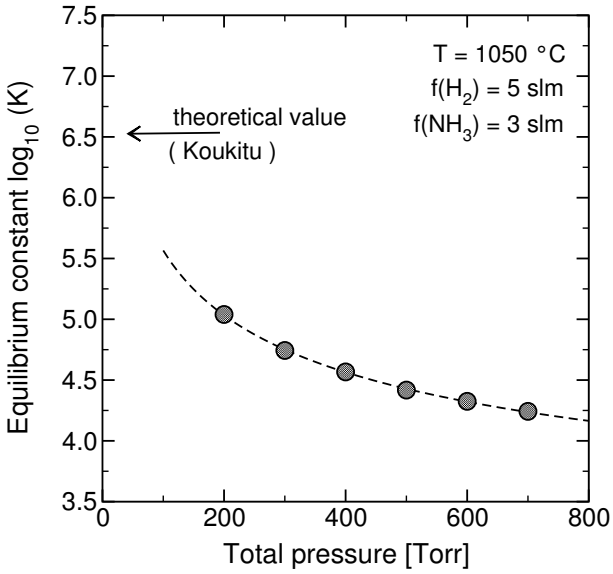

Figure 3.5: The equilibrium constant K as determined from the Ga equilibrium pressures in dependence on the total pressure.

results are in accordance with observations from several other groups.

3.2 Growth of GaN films

3.2.1 The main substrates

Since GaN single crystals of sufficient size are not available up to now almost the whole engineering work has been based on the heteroepitaxy. It is possible to grow GaN on many different substrates like silicon (111), silicon carbide or zinc oxide, but the most successfully used ones are 4H- or 6H-SiC (0001) and (0001)-oriented sapphire. The choice of sapphire as a substrate is due to its hexagonal symmetry in the (0001) plane and its stability at temperatures exceeding 1000°C, which is necessary for MOVPE-grown films of high perfection. 4H- and 6H-SiC exhibit the same features and have even a smaller lattice mismatch to GaN and a higher thermal conductivity. Furthermore, they can be conductive, making device design easier. The drawback of SiC are its small thermal expansion coefficient and the difficulty to stabilize one polytype. The former leads to tension in the nitride layers at room temperature unless the growth process uses an AlN or $Al_xGa_{1-x}N$ buffer layer. The latter makes the substrates rather expensive, since over 200 polytypes have been identified up to now. Most of these polytypes are based on a hexagonal lattice, which makes it difficult to maintain one certain stacking order along the growth direction [0001]. Mainly due to the pricing sapphire came to be the main substrate used for GaN epitaxy. Since sapphire was used for almost all growth runs in this work, it will be focused on in the remainder of this section. The epitaxial relationship of GaN grown on sapphire is

$$[0001]\ \text{GaN} \parallel [0001]\ \text{sapphire} \qquad \text{and} \qquad [01\bar{1}0]\ \text{GaN} \parallel [11\bar{2}0]\ \text{sapphire}.$$

This corresponds to a rotation of the GaN crystal by 30° relative to the sapphire, and a lattice mismatch in the basal plane of ∼16.1%, if one calculates the mismatch with

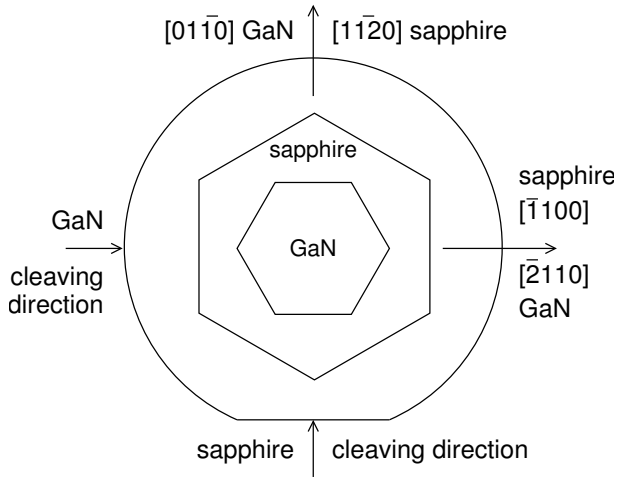

Figure 3.6: Orientation of the unit cells of GaN and sapphire with respect to a typical wafer [96].

respect to the Al sublattice of the sapphire. This mismatch is by far too large to allow direct coherent growth of GaN, since the critical thickness is on the order of a few nanometers [115]. The origin of the rotational mismatch is the rotation of the hexagonal aluminum sublattice in the substrate relative to the sapphire unit cell as seen in Fig. 3.6. It causes the cleaving planes of sapphire and GaN to be misaligned as well. This makes it very difficult to obtain smooth facets by cleaving, which is a severe problem for the production of laser diodes.

The thermal mismatch of sapphire and GaN is large as well. The in-plane thermal expansion coefficients are $\alpha_{GaN} = 5 \times 10^{-6}K^{-1}$ and $\alpha_{Sapphire} \approx 8 \times 10^{-6}K^{-1}$ for GaN and sapphire, respectively [61, 116, 96]. The thermal expansion coefficient of sapphire strongly depends on the temperature; the value mentioned here is valid for a temperature of 800 K. The larger expansion coefficient of sapphire compared to GaN leads to compressive strain at room temperature, since epitaxial GaN grows under little tensile strain at growth temperature [83, 117]. It has the advantage that cracking of GaN layers due to tension is rarely observed.

3.2.2 Growth onto sapphire

The first attempts to deposit GaN onto sapphire employed a single-step method, namely growing the material directly onto nitridated [0001]-oriented sapphire [118, 5]. The obtained material showed the mentioned epitaxial relation to the substrate. For the use of halide vapor phase epitaxy (HVPE) the film was purely grown in the hexagonal phase [5], but the surface was not specular. Hexagonal features like pyramids or prisms appeared on the surface like those observed for too thin nucleation layers [10].

One major step in the GaN heteroepitaxy was the introduction of the so-called two-step process, which employs the deposition of a nucleation layer (NL) at temperatures far below the growth temperature commonly used for GaN. This procedure was first reported by Amano *et al.* in 1986, who deposited an AlN NL with a thickness of 50-100 nm prior to the growth of GaN at high temperature [48]. The NL had two effects on the resulting GaN film : First, it reduced the threading dislocation density and second, it generated a specular, smooth surface of the high-temperature GaN without any protru-

sions. In successive studies the optimized thickness and deposition temperature of the NL came out to be ∼50 nm and ∼500-600°C, respectively [119]. The NL completely wets the sapphire and provides nucleation centers for the GaN grown at high temperature (HT-GaN). This forces the HT-GaN to grow in a three-dimensional island mode, where the islands grow almost dislocation-free and finally coalesce to form a compact layer. Mass-transport provides a homogeneous thickness during the coalescence of the individual islands, such that the resulting film has a smooth and featureless surface. Later in 1991, Nakamura modified the process by using a low temperature (LT) GaN NL instead of AlN, which mainly resulted in an improvement of the electrical properties of the GaN film [10].

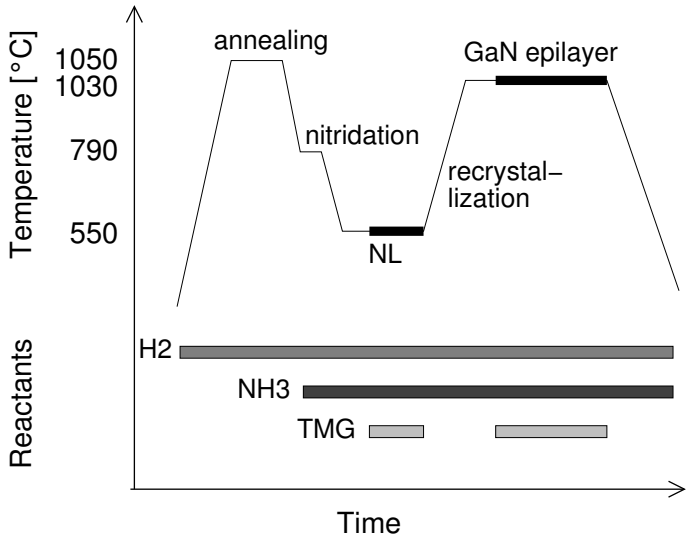

Figure 3.7: Schematic of the "two-step" growth process employed for the deposition of GaN onto sapphire.

A schematic of the growth process similar to the one employed in Bremen is depicted in Fig. 3.7. It can be seen that the "two-step" process is rather a multi-step process, as several subsequent steps with different impact have to be optimized separately. First, the substrate is cleaned in a hydrogen atmosphere at a temperature exceeding the main layer growth temperature, then the sapphire is nitridated with ammonia, followed by the LT deposition of the NL. During the successive temperature ramp to the growth temperature the NL recrystallizes, i.e. it changes its crystalline structure, and is then overgrown at high temperature. After growth, the layer is cooled to room temperature under a flow of ammonia to stabilize the surface. The individual steps will be discussed in the following sections.

Substrate annealing

The first step in the growth cycle is the *in situ* preparation of the substrate by exposing the sapphire at high temperature. This is performed in a hydrogen atmosphere, which removes oxygen from the surface, stabilizes an aluminum-terminated surface and is supposed to produce a high density of kink sites on the steps of the sapphire [120]. The aluminum represents the reference lattice for the GaN growth and thus provides the in-plane orientation of the GaN. The kinked step structure should increase the nucleation site density and improve the homogeneity of the NL. Furthermore, the annealing

cleans the surface from remaining organic substances and improves the flatness of the substrate [121]. The temperature of the anneal is mainly given by the intended growth temperature of the HT-GaN. It should be above this temperature to remove all contaminations in the reactor, which could possibly deposit on the NL before the HT-GaN starts. Many groups anneal the substrate approx. 20°C above the growth temperature of the HT-GaN [121, 98, 10].

The detrimental effect of the annealing step is the possibility of material deposition on the sapphire prior to the NL. These deposits strongly distort the nucleation and the epilayer growth process and commonly lead to discontinuous films or large-scale protrusions. For example, if the degassing step is performed at atmospheric pressure, then the decomposition of GaN on the susceptor and on the reactor walls proceeds extremely rapid (see Section 3.1.3 and [107]). This leads to the formation of liquid Ga droplets on the susceptor, as the Ga remaining after decomposition is not transported away fast enough. These droplets are very stable, such that during the successive nitridation step the droplets are converted into large polycrystalline GaN islands. These hinder the coalescence process in their surrounding and lead to a discontinuous film. To circumvent this problem, the degas step should be performed at a lower reactor pressure up to 200 Torr in order to reduce the GaN decomposition rate. Furthermore, the whole reactor should be thermally cleaned in a hydrogen atmosphere in between two successive growth runs. The latter was evaluated in detail by Marc Dießelberg with the focus on the improvement of the surface structure and the reduction of particle density [122].

Nitridation

The nitridation step following the substrate annealing has the purpose of generating a thin layer of AlN on the sapphire. This happens through the replacement of oxygen atoms by nitrogen atoms underneath the top aluminum layer. It might be that the polarity of the GaN is determined by the nitridation, but this has not been shown yet. The nitridation is caused by ammonia, which is supplied for a short time prior to the start of the NL growth. Since the nitridation interacts with the NL growth, the recrystallization and the epilayer growth, the ideal nitridation conditions depend on the whole deposition sequence. In principle, the thickness of the AlN layer raises with the nitridation temperature and with the duration of the nitridation step.

Nevertheless, an extensive nitridation seems to be detrimental to the epilayer quality. Thick AlN forces the NL material to develop a larger fraction of hexagonal material after the recrystallization, which inhibits the lateral overgrowth at high temperature starting from nucleation sites [123]. The studied layer had an edge type threading dislocation density of 10^{10} cm^{-2} compared to 10^{8} cm^{-2} for a shorter nitridation [124]. To some extent this trend was confirmed in own experiments, although the impact was not as drastic.

Nucleation layer

The initial nucleation of GaN on the nitridated sapphire is performed at a relatively low temperature around 550°C in order to obtain a thin and homogeneous layer on the sur-

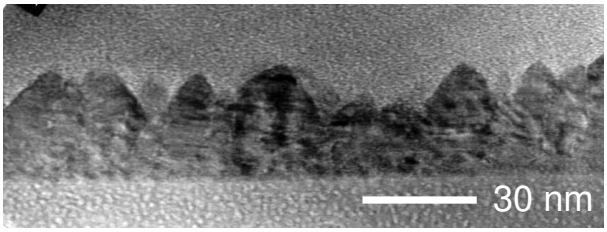

Figure 3.8: Cross-sectional TEM image of an as-grown NL. Image taken by H. Selke, University of Bremen.

face. At elevated temperatures the GaN tends to grow in large islands, which develop into columnar hexagonal grains of uneven height. At low temperatures the mobility of the source atoms is too low to form larger islands, such that the layer thickness is homogeneous across the whole substrate. The as-grown NL consists of a mixture of amorphous, cubic [111] and hexagonal [0001] GaN, with the fractions depending on the growth conditions. Usually, the cubic and the hexagonal parts are dominant. For NL grown at atmospheric pressure a cubic fraction of 0.56 was determined by grazing incidence XRD [125, 126]. The GaN NL grows in a Volmer-Weber growth mode due to the lattice mismatch between GaN and sapphire and the low growth temperature. It develops pointed grains with a diameter of approx. 15-50 nm as seen in Fig. 3.8.

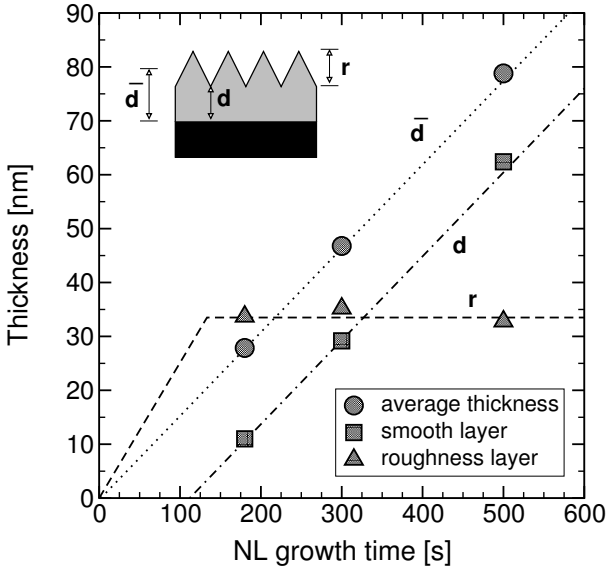

Figure 3.9: Analysis of the NL growth process by spectral ellipsometry. Shown is the average thickness of the NL together with the thicknesses of the homogeneous and the discontinuous layers as illustrated in the inset. The data is plotted versus the growth time.

The nucleation process was observed by ellipsometry as shown in Fig. 3.9. The graph shows the model parameter used to fit ellipsometry spectra of NLs of different thickness. The spectra were recorded *ex situ* at an incident angle of 75°, close to the Brewster angle. A Woollam M44 ellipsometer was used for this experiment, which can acquire data in the spectral range of 2.0 eV to 4.5 eV. Details on ellipsometry can be found in Ref. [127]. The data was fitted using a two-layer model on sapphire. The lower layer was smooth GaN, whereas the upper layer was assumed to be a discontinuous layer as illustrated in the inset of Fig. 3.9 to include the surface roughness. The roughness was modeled using an effective medium approximation. This is based on the assumption, that the scale of the roughness is much smaller than the wavelength of the light. In this case the polarization is insensitive to the individual facets and the roughness can be ap-

proximated by a layer with an average refractive index obtained from the layer material and the ambient. Accordingly, the refractive index is given by the fraction of GaN in the roughness layer, which was assumed to be 50%. The two layer thicknesses, the angle of incidence and the band gap were used as the fitting variables. The latter two were identical for all samples. The results are summarized in Fig. 3.9.

Two main observations were made. First, the bandedge was broadened and shifted below that of hexagonal GaN, which is expected for largely cubic material. Second, the thickness r of the roughness layer was found to be $\sim$33 nm for all growth times, and the thickness of the homogeneous layer d was found to increase linearly with an extrapolated offset of 100 s in the growth time, i.e. it is supposed to be zero for growth times below 100 s. Plotting the average thickness $\overline{d} = d + 1/2r$ versus the growth time one finds a straight line through the origin, which demonstrates that the growth starts immediately and that the growth rate is constant. Fig. 3.9 suggests that the nucleation starts from small isolated islands, which are distributed homogeneously across the whole substrate. This happens at an average thickness of about 15 nm, which is just below the optimized NL thickness reported by many researchers [10, 128, 129]. Although the optimum thickness presumably depends on the whole process sequence, in particular on the recrystallization, most groups seem to end up with a thickness just large enough to wet the whole substrate surface.

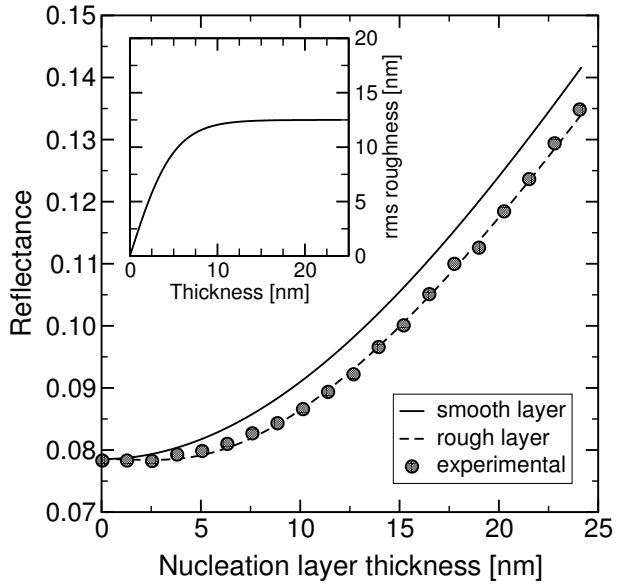

Figure 3.10: Reflectance during NL deposition versus the layer thickness. Shown are theoretical as well as theoretical values. The *rms* roughness used to fit the experimental data is shown inset.

The three-dimensional growth of the NL also affects the reflectance transient recorded during growth as the roughness of the surface reduces the reflectance due to incoherent scattering as described in Section 6. When the growth starts, the GaN forms islands, i.e. the roughness increases together with the layer thickness. These two contrary effects keep the reflectance constant for a short time as depicted in Fig. 3.10. Compared to the theoretically expected curve for a smooth layer, the experimental values are delayed. Assuming the *rms* roughness to evolve as shown in the inset of Fig. 3.10, the experimental values can be fitted accurately. Occasionally, the delay of reflectance is entitled "nucleation delay". Presumably this effect is not a delay of nucleation, but rather a

change in the surface roughness due to parameters like the sapphire nitridation [130].

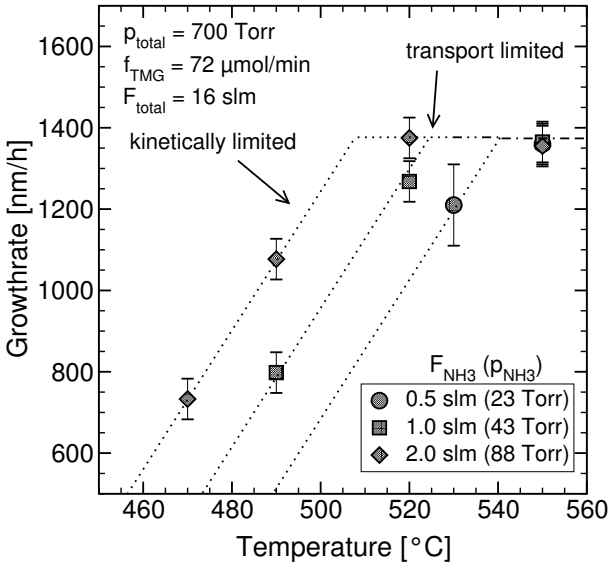

Figure 3.11: The growth rate of NL material in dependence on the growth temperature. Shown are data sets for different partial pressures of ammonia.

The growth of the NL happens close to the transition from kinetically limited growth to transport limited growth. This is shown in Fig. 3.11, which displays the growth rate of GaN in dependence on the growth temperature for differnet gas phase compositions. The growth mode transition is directly visible, since for kinetically limited growth the growth rate raises with the temperature, whereas it is constant as soon as the transport limited growth regime is reached. For an ammonia partial pressure of 88 Torr this transition happens at 510°C, whereas it is shifted to higher temperatures for lower ammonia partial pressures. In the kinetically limited growth regime the growth rate is limited by the partial pressure of ammonia, whereas it is defined by the TMG flow in the transport limited regime.

At lower pressures, the transport across the boundary layer is faster, such that the transport limited regime starts at higher temperatures (not shown). For example, at a total pressure of 100 Torr instead of 700 Torr as in Fig. 3.11, the transition temperature is shifted to 530°C compared to 510°C, which confirms the proposed change of the growth mode. To establish reproducible growth conditions for the NL, it is advisable to select a growth temperature in the transport limited regime. The gas flows and the pressures can be controlled and reproduced more precise than the temperature, which can easily deviate by a few degrees from run to run and depends on the susceptor emissivity. A change of the growth temperature in the kinetically limited regime would directly affect the NL thickness and accordingly change the whole epilayer growth process, which makes it unstable.

Recrystallization

The recrystallization step is the annealing of the as-grown NL before the high-temperature growth starts. Commonly, it is performed at the same ammonia and hydrogen flows as used for the successive HT growth. During the recrystallization two processes happen. On the one hand, the GaN is being decomposed mainly due to the hydrogen in the gas

phase, and on the other hand, mass transport on the surface changes the crystal structure. The latter can be understood as an Ostwald ripening process, which refers to the coarsening of an ensemble of differently sized islands due to the diffusion of atoms between the islands. Larger islands will grow in size at the expense of smaller ones that decay and eventually disappear, since these smaller islands are less stable than the larger ones due to a larger fraction of edge atoms. A careful study of the NL transformation was performed by Wu *et al.* [123, 125]. They showed that the as-grown NL consists of grains with mixed cubic/hexagonal stacking sequence, which is transformed to partly hexagonal material upon high-temperature annealing. The cubic fraction drops from ∼0.56 in the as-grown NL to ∼0.17 after annealing [126]. Specially the surface of the grains was transformed into hexagonal material in their study, which shows that this process is driven by mass transport. The average grain diameter in the layer increases approximately by a factor of two, with some larger, exposed grains, which contain a larger fraction of hexagonal material.

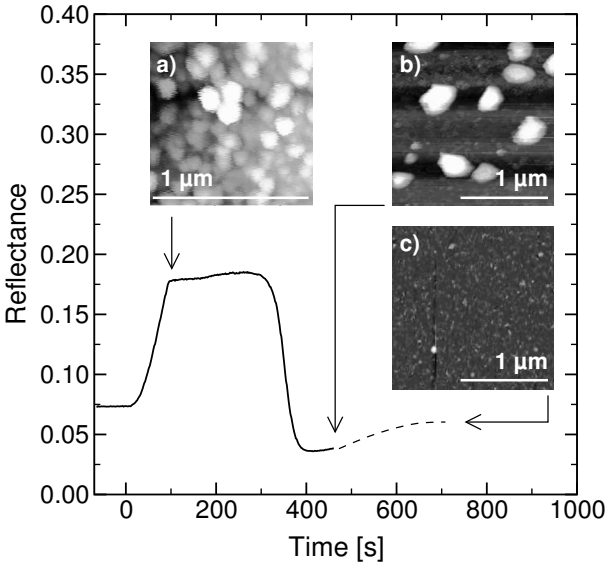

Figure 3.12: Change of the NL surface morphology upon annealing and its impact on the reflectance. The experiment was performed at a total pressure of 700 Torr and an ammonia partial pressure of 175 Torr.

This change in morphology is directly accessible by atomic force microscopy, as seen in Fig. 3.12. It illustrates the evolution of the NL morphology during recrystallization together with the reflectance transient. The annealing was done at atmospheric pressure (700 Torr) in an atmosphere with a hydrogen partial pressure of 350 Torr. Due to the high reactor pressure the decomposition of GaN is enhanced compared to low-pressure conditions, such that the NL is fully removed after a few minutes at 1050°C as seen in the AFM image in Fig. 3.12(c). For intermediate recrystallization times the NL develops larger, presumably hexagonal islands with a diameter of ∼300 nm and a height of ∼100 nm (Fig. 3.12 b). These grains act as nucleation centers for the following high temperature growth, during which the nucleation layer is laterally overgrown. The probably most useful way to optimize the recrystallization is the variation of the temperature ramp and the time delay prior to the HT overgrowth using the gas mixture of the main epilayer growth conditions. This avoids the change of the temperature and the flow pattern at the growth start. In general, a high total pressure enhances the decomposition and hence requires a shorter recrystallization time. To some extent, this

can be balanced by a raised ammonia flow, but typically the nucleation site density is lower for an atmospheric pressure process.

High temperature island growth

The lateral overgrowth of the recrystallized NL has been studied since the introduction of the two-step process [131, 128, 123]. It is characterized by an island growth mechanism starting from the larger hexagonal grains in the recrystallized NL. First, the islands start to develop a trapezoidal shape with the preferred crystallographic facets. The lateral growth proceeds over the $\{10\bar{1}1\}$ planes, and the vertical growth evolves through the (0001) plane [132, 133]. The reason for this is the low stability of the $\{10\bar{1}1\}$ facet. This causes all other lateral facets to grow themselves away, leaving the $\{10\bar{1}1\}$ facets behind. This is also evident in epitaxial lateral overgrowth (ELO), where the $\{10\bar{1}1\}$ facets develop as soon as the SiO_2 mask is patterned along the $\langle 11\bar{2}0\rangle$ direction or if stripes along the $\langle 10\bar{1}0\rangle$ direction are overgrown utilizing a high ammonia partial pressure [128, 134]. The latter condition enhances the growth of all facets leaving the $\{10\bar{1}1\}$ family as the least stable surface [128].

The overgrowth process and the accompanying formation of the dislocation structure was studied in detail by Wu *et al.* [132, 123, 120]. During NL overgrowth the individual islands grow almost dislocation free, as was shown by TEM [123, 135]. The stacking disorder between NL and HT-island is accommodated by stacking faults with Frank and Shockley partial dislocations [123, 120]. These partial dislocations mark the boundaries of the stacking faults, where Shockley partials accommodate differences in stacking sequence of neighboring regions and Frank partials balance the tilt disorder in the interface of high-temperature GaN and NL [123]. The partial dislocations have the line direction in the (0001) plane and a Burgers vector with in-plane component. Since they are bound to stacking faults, they do not thread through the film, but stay in the (0001) glide plane [120]. The strain state during overgrowth is still unclear, but since a misfit dislocation network forms at the interface of buffer layer and sapphire, it is probable, that the NL can release some of the thermal strain imposed during the ramp to growth temperature. Accordingly, the HT-island can grow free of thermal strain, which will be assumed for the further discussion. It should be noted, that the misfit dislocation network can not release the intrinsic strain in the buffer layer originating from the high density of point defects. This is only possible during the recrystallization process, which involves the mass transport over the open surface.

With the overgrowth velocity depending on the set of growth parameters, the lateral growth proceeds until the neighboring islands meet and coalesce to form a smooth film. This smoothing process is presumably supported by mass transport from higher to lower islands, which leads to a homogeneous film thickness across the whole sample. The formation of dislocations in the layer is caused by the misalignment of the islands relative to each other and to the substrate. As was shown by grazing incidence x-ray diffraction, the twist in the annealed NL is significant and amounts to roughly 1.4° [126]. This causes the individual islands to be misoriented relative to each other as well, such that from geometrical constraints it is necessary to form edge type threading dislocations with line direction along [0001] at the coalescence fronts. Edge type thread-

ing dislocations accommodate the in-plane twist in the layer and screw type threading dislocations form to adapt the out-of-plane tilt of the islands. Three types of threading dislocations were found in hexagonal GaN: pure screw (Burgers vector $\vec{b}_s = [0001]$), mixed-character ($\vec{b}_m = 1/3\langle 11\bar{2}3\rangle$), and pure edge ($\vec{b}_e = 1/3\langle 11\bar{2}0\rangle$) threading dislocations. The pure edge type threading dislocation density was found to dominate under all sets of MOVPE growth parameters [136].

Dislocations cannot terminate in a perfect layer, thus they commonly form dislocation loops, where the Burgers vector is preserved and the line direction varies. For edge type threading dislocations along [0001] this means a transformation to a screw type threading dislocation running along the sapphire-GaN interface, which again compensates the rotation of the grain relative to the substrate. Accordingly, screw type threading dislocations along [0001] change into an edge type threading dislocation in the plane of the sapphire-GaN interface, compensating the tilt of the grain relative to the substrate. It is possible that dislocations join and form a mixed dislocation, which is rather often observed for GaN. Experimental evidence for the described dislocation structure in fully coalesced films was given by Wu *et al.* [120, 123]. They demonstrated the alignment of edge-component threading dislocations in plan-view TEM micrographs of films having a high threading dislocation density. In this case the dislocation density was sufficiently high to reveal the grain structure. For samples with lower dislocation density like those presented in the plan-view TEM images in Fig. 4.6, the large dislocation spacing gives the impression of a random distribution.

3.3 Reduction of threading dislocation densities

As discussed in Section 3.2.2, the majority of the threading dislocations form during the coalescence of the high-temperature islands. Therefore, in order to reduce the dislocation density in the layer, it is necessary to control the coalescence process. A prolonged coalescence generally corresponds to a low threading dislocation density, in which mainly the threading dislocations with edge component are affected. Different approaches are possible, like the optimization of the growth parameters [137], a Si pretreatment of the sapphire [138], low-temperature or SiN interlayers [139] or the epitaxial lateral overgrowth [140]. In the following two approaches will be discussed in more detail, as they can be applied *in situ*. First, the different growth parameters will be evaluated in view of their impact on the coalescence, and second, the first results obtained for SiN interlayers will be presented.

3.3.1 Growth parameters

Almost all steps in the described growth scheme affect the coalescence process to some extent. This allows to obtain growth modes ranging from an immediate two-dimensional growth to a stable island growth. The set of parameters discussed here are the most efficient ones for the Thomas Swan reactor, which allow to deposit smooth films on sapphire with a threading dislocation density as low as 1×10^8 cm^{-2}.

Nucleation layer

The impact of the NL growth on the quality of the epilayer has been widely investigated in literature, in which different properties have been chosen as the figure of merit [129, 141, 130, 142]. Mostly, the NL thickness, the growth rate, the molar V/III ratio or the growth temperature were varied. The outcome of these studies was, that the second important parameter besides the NL thickness is the molar V/III ratio. The best epilayers were reported for a lower molar V/III ratio.

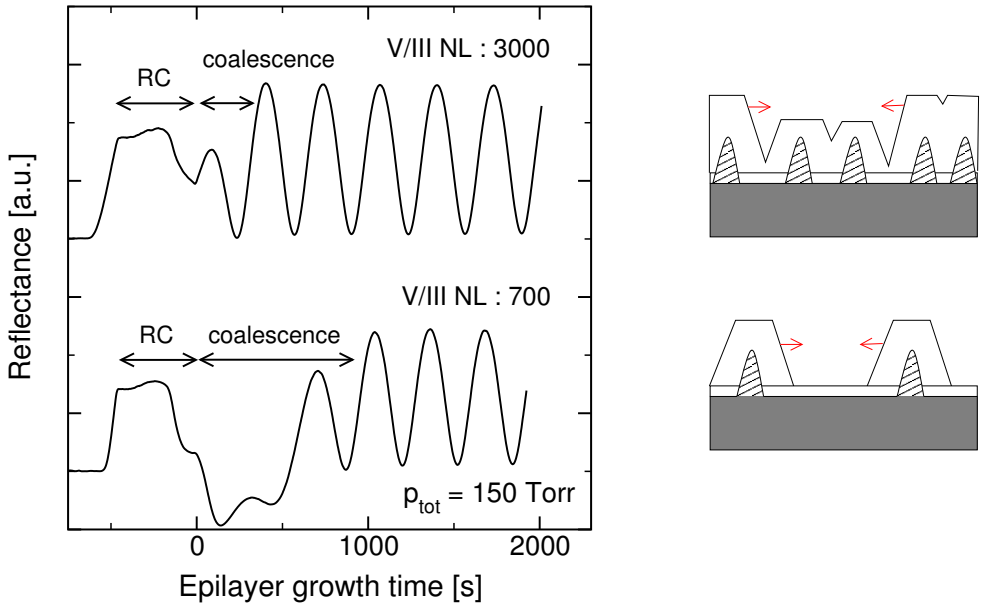

Figure 3.13: Reflectance transients of two GaN films grown on sapphire employing NLs with different molar V/III ratio. The overgrowth process is illustrated in the two drawings on the right.

This effect is demonstrated in Fig. 3.13, which compares the reflectance transients of two samples grown under identical conditions except for the TMG flow during NL growth, corresponding to molar V/III ratios of 700 and 3000 for the two samples, respectively. The high temperature island growth mode is significantly elongated for the sample with the lower V/III ratio. Furthermore, the roughening of the NL during recrystallization is enhanced for this sample. Thus, for a low molar V/III ratio the nucleation site density is reduced and the thermal stability of the NL during recrystallization is lower. This confirms the results of Keller *et al.*, who compared AFM images of annealed NLs grown under different TMG flows [141]. In their study, the samples with an increased TMG flow, i.e. a low V/III ratio, exhibited a larger average grain diameter. This reduces the nucleation site density and causes the subsequent high temperature growth to develop fewer, but larger islands. Since these grow almost dislocation-free, the coalesced film has a reduced threading dislocation density as well.

Total pressure

Most research groups optimized their growth scheme either for atmospheric pressure (700 - 800 Torr) or for low pressure (75-150 Torr). It is rather uncommon to use an intermediate pressure, although there is no obvious reason for this. The growth process of GaN is very sensitive to a change of the reactor pressure, which is caused by the decomposition of GaN in a hydrogen-containing atmosphere. This decomposition reaction is strongly enhanced at higher pressures, as was discussed in Section 3.1.3.

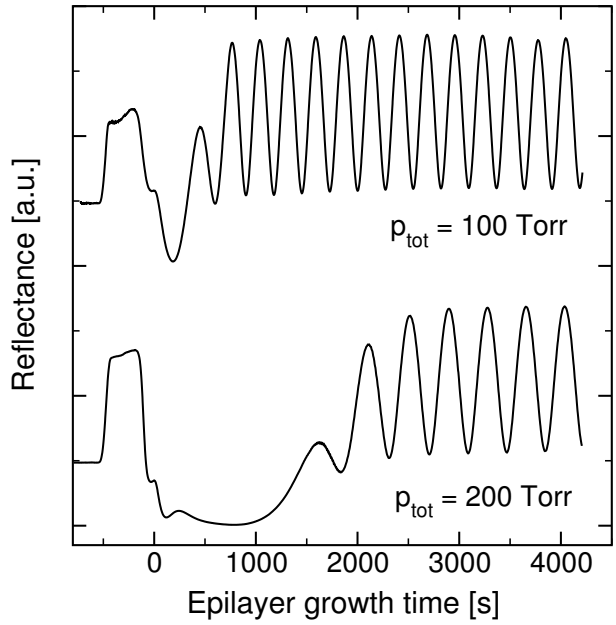

Figure 3.14: The reflectance transients of two samples grown under identical conditions except for the total pressure.

Fig. 3.14 shows the reflectance transients of two samples grown under identical conditions except for the total pressure. A doubling of the pressure from 100 Torr to 200 Torr caused a remarkable delay of the island coalescence process. The enhanced decomposition at 200 Torr supports the island selection process during the recrystallization and the high temperature growth, thus, it generates larger dislocation-free islands. The increase in pressure reduced the dislocation density by almost one order of magnitude from $\sim 6 \times 10^9$ cm^{-2} to $\sim 1 \times 10^9$ cm^{-2}. If the total pressure is raised further to 700 Torr, the selectivity is even high enough to obtain an average island diameter of 4 μm. It might be possible, that the growth pressure additionally changes the ratio of the lateral and the vertical growth rate because of the different stabilities of the growth facets. For example, the less stable $\{10\bar{1}1\}$ facet could be stronger affected by the total pressure than the (0001) facet, which would reduce the lateral growth rate and enhance the island selectivity. However, for selected uncoalesced samples investigated by AFM, the lateral growth rate was approximately equal to the vertical growth rate.

The drawback of the growth at a higher pressure is the reduction of the growth rate due to the increased etching and the change in the flow pattern. This manifests itself in the elongated oscillation period of the sample grown at 200 Torr, which had a growth rate of 1.3 μm/h compared to 1.8 μm/h for the sample grown at 100 Torr. Presumably, the higher etch rate directly counteracted the growth rate. The flow pattern changes due

to the reduced gas velocity at a higher pressure, as the total gas flows were kept constant during the two growth runs in Fig. 3.14. It has three effects - first, the boundary layer thickness increases, second, the diffusion is reduced, and third, more pre-reactions can occur due to the lower gas velocity. All this reduce the growth rate by keeping the reactants away from the surface.

Hydrogen and ammonia partial pressure

Unless inert gases are used for the growth, the sum of the ammonia and the hydrogen partial pressure is almost equal to the total pressure. Thus, it is usually not possible to vary these two partial pressures independently at a constant total pressure. Since the two gases have the opposite influence on the surface stability, the ratio of the ammonia and the hydrogen partial pressure is the parameter governing the growth process. Ammonia in general stabilizes the GaN surface, whereas hydrogen supports its decomposition (see Section 3.1.3). This allows one to use the gas phase composition for the control of the coalescence process.

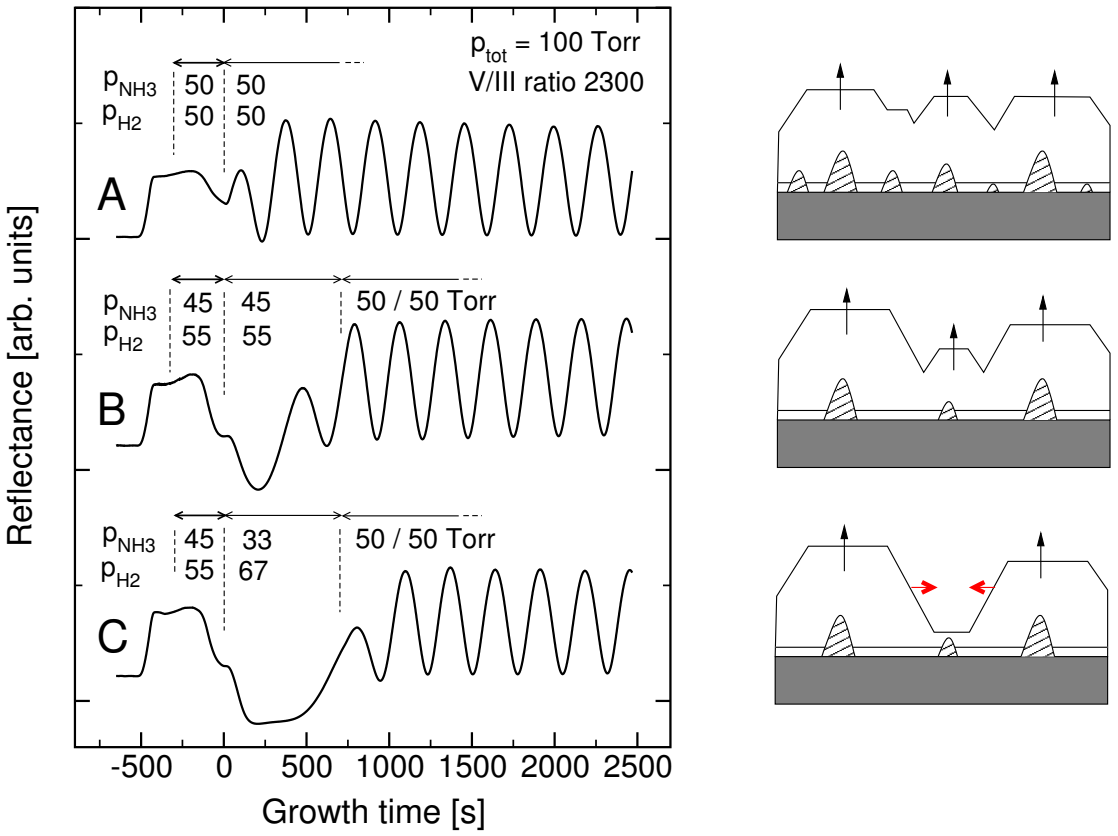

Figure 3.15: The reflectance transients of three GaN films grown under identical conditions except for the NH_3/H_2 ratio during recrystallization and initial high-temperature growth. The growth processes are illustrated in the drawings on the right.

Fig. 3.15 demonstrates this possibility for the low pressure growth at 100 Torr. In order

to separate the influence of the NH_3/H_2 ratio from the molar V/III ratio, all growth runs were conducted under the same molar V/III ratio of 2300 by adjusting the TMG flow accordingly. For sample A, the recrystallization and the high temperature growth were performed at equal partial pressures of ammonia and hydrogen. This is a rather stabilizing atmosphere for the GaN growth, as the recrystallization of the NL proceeds slowly and the island growth mode is completed after a GaN thickness of roughly 100 nm. Raising the hydrogen partial pressure to 55 Torr during the recrystallization and the initial growth at high temperature (sample B) already delays the coalescence thickness to ∼200 nm. It should be noted that the growth rate is reduced during the initial HT growth as the TMG flow was lowered to maintain a constant V/III ratio. In this case, the increased hydrogen partial pressure leads to a faster roughening of the NL during recrystallization, which represents a stronger selection of nucleation sites for the HT overgrowth. Furthermore, the selectivity during the overgrowth is enhanced, which in conjunction with the lower nucleation site density caused the elongation of the island growth mode.

To separate the effect of the hydrogen on the recrystallization from the influence on the island growth mode, sample C was grown under the identical recrystallization conditions like sample B, but the hydrogen flow was increased further during the initial HT growth. This doubled the coalescence thickness again to ∼400 nm. Therefore, the hydrogen partial pressure during the initial island growth seems to be the main effect.

Optimized growth parameters for low and atmospheric pressure MOVPE

Although not discussed in this work, extensive studies on AP grown GaN were performed, which was motivated by the excellent results reported in the literature [133, 10]. The samples obtained at AP exhibited a relatively low density of dislocations, which can be expected from the aspects discussed before. However, the contamination of the reactor with deposits on the reactor walls and on the showerhead required extensive mechanical cleaning of the whole system in very short cycles, which in turn affected the reproducibility substantially. A good compromise was found at a total pressure of 200 Torr combined with a raised hydrogen flow during initial HT growth. This provides samples with a similar quality as those grown at 700 Torr, while the reactor uptime and the run-to-run reproducibility are high.

3.3.2 SiN micromasking

The use of SiN as a micromask on GaN to reduce the dislocation density in the subsequently grown film was first reported by Tanaka *et al.* [143], although Si was already used before as an antisurfactant for the growth of GaN quantum dots on $Al_xGa_{1-x}N$ [144, 145]. GaN and $Al_xGa_{1-x}N$ form a quasi lattice matched system. The small lattice mismatch inhibits to obtain a Volmer-Weber growth mode for low concentrations of aluminum. Thus, the dot formation is only observed for GaN grown on AlN. The predeposition of ∼1 ML of SiN on the GaN surface forces the growth mode to switch from a step-flow to a three-dimensional growth [145], which enables to grow GaN quantum dots in an $Al_xGa_{1-x}N$ (x=0.15) matrix. This transition is explained by a reduction of the

sticking coefficient of the precursors on the SiN. The SiN forms a mask with nano-holes, though which the quantum dots start to grow. No growth on the masked regions was observed [143].

If the growth is continued, the SiN is laterally overgrown. It was observed by TEM, that many threading dislocations change their line direction at the SiN layer. The preferential incorporation of Si at the dislocation cores could be the reason for this, as nitrogen dangling bonds are available at these sites. This means that the SiN deposition is enhanced at the dislocations. Then the core sites are overgrown and the dislocations are bent into the (0001) plane, where they can annihilate with dislocations having an opposite Burgers vector. This bending into the $\langle 10\bar{1}0 \rangle$ direction occurs, if a threading dislocation intersects with the inclined $\{10\bar{1}1\}$ facet of a HT island [146, 147]. As a result, the dislocations form dislocation loops, which do not continue in the growth direction. If the GaN nucleation starts at an uncovered dislocation core, the dislocation is not terminated.

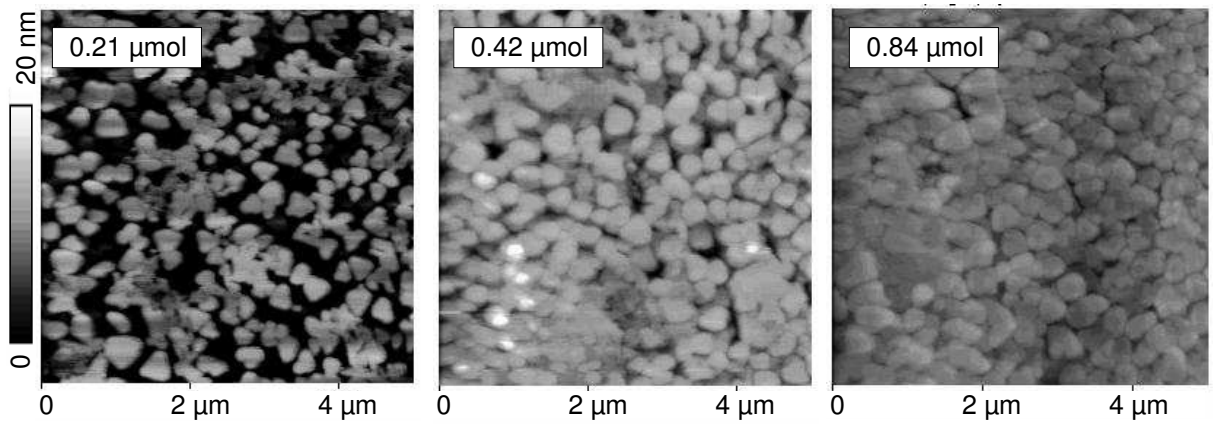

Figure 3.16: The growth of SiN islands on GaN illustrated by AFM images. The given numbers correspond to the overall amount of Si supplied during SiN deposition. Samples grown by S. Figge, University Bremen.

SiN deposition

To study the evolution of the micromask, the SiN was grown on GaN films by supplying ammonia and silane to the surface at the growth temperature. The silane was the same source as used for the n-type doping, i.e. it is delivered in a concentration of 10 ppm diluted in hydrogen. The lattice mismatch of Si_3N_4 to GaN amounts to 10% [148]. This induces an island growth mode of the SiN which might nucleate at the dislocation cores. The evolution of the SiN coverage is seen in Fig. 3.16, where AFM images of samples with different growth times of SiN are displayed. The growth starts in a three-dimensional manner and is followed by a mainly lateral expansion of the SiN islands. Assuming that each island corresponds to a single dislocation, the dislocation density in the underlying film should be $\sim 1 \times 10^9 \mathrm{cm}^{-2}$. This would be in good agree-

ment with the expected dislocation density from the set of growth parameters used, according to previous measurements of similar films.

Island coalescence and lateral overgrowth

The overgrowth of the SiN happens in a three-dimensional island growth mode, which starts from the holes in the SiN, where the underlying GaN has still an open surface. The corresponding roughening of the surface is directly evident in the reflectance transients shown in Fig. 3.17. In this experiment, two samples were grown under identical conditions, but with different thicknesses of the SiN interlayer.

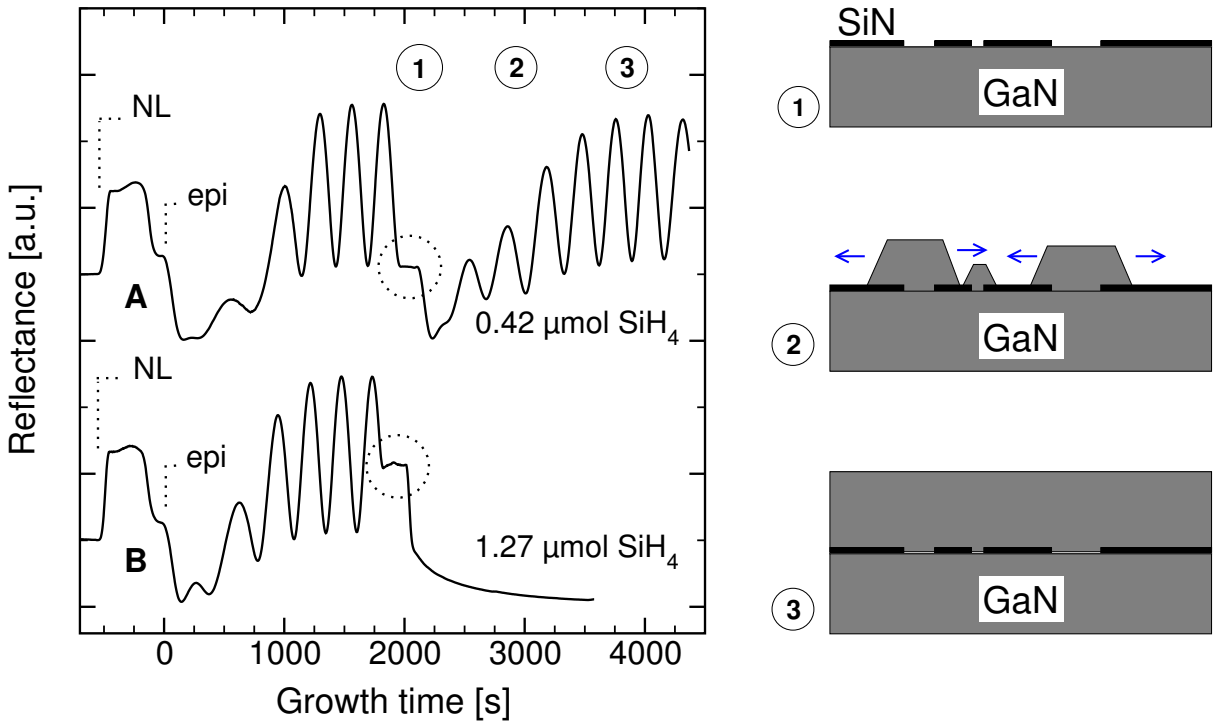

Figure 3.17: Reflectance transients for GaN grown on SiN interlayers of different thickness. The proposed growth mode for sample A is illustrated at the right.

After the deposition of the SiN, the HT island growth is initiated and the reflectance decreases. If the density of the nucleation sites in the SiN is sufficient, then the islands coalesce again and the smooth surface is recovered. This is the case for the sample A in Fig. 3.17, which was exposed to 0.42 μmol of SiH_4. The coalescence on the SiN micromask is finished after additional ~750 nm of GaN. If the the SiN layer is too thick, like for the sample B, which was dosed with 1.72 μmol of SiH_4, then the spacing of the openings in the mask is too large. It causes the GaN to grow in large islands, which do not coalesce within reasonable time.

These differences are evident in the cross-sectional TEM images of Fig. 3.18. Sample A has developed a smooth surface and most of the threading dislocations annihilate at the SiN interface. In comparison, sample B with the triple dose of SiH_4 shows large

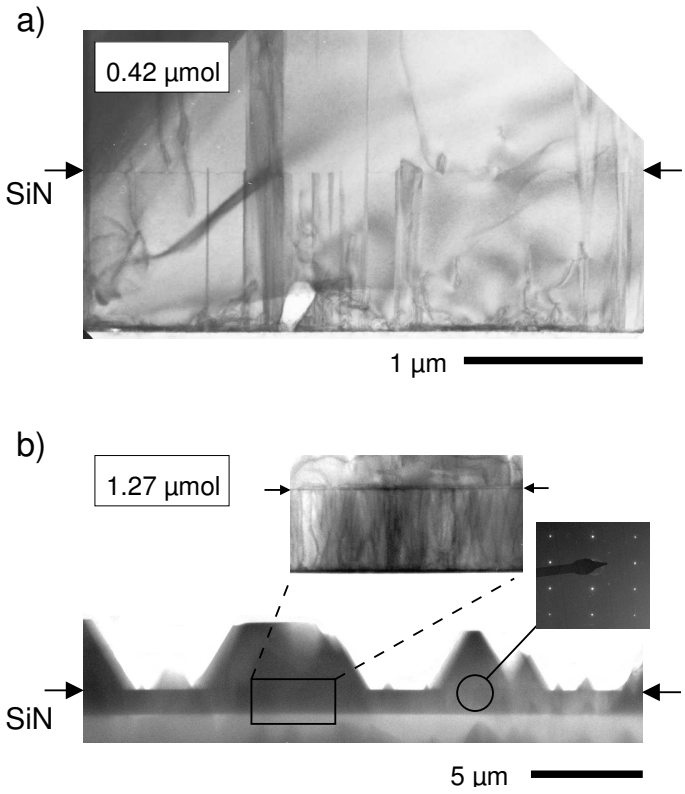

Figure 3.18: Cross-sectional TEM images of the samples from Fig. 3.17. a) sample exposed to 0.42 μmol of SiH_4, bright-field image along $\langle 10\bar{1}0 \rangle$, b) sample exposed to 1.27 μmol of SiH_4, bright-field image along $\langle 11\bar{2}0 \rangle$ together with a diffraction image from the SiN interface region. Images taken by R. Kroeger, University of Bremen.

islands with a diameter exceeding 1 μm. The threading dislocations are terminated as well and the epitaxial relation of the islands relative to the template is maintained, as seen in the diffraction image from the interface of the template and the island. It should be noted, that the height of the islands by far exceeds that of the underlying GaN film in spite of an identical set of growth conditions and a similar growth time. This illustrates the low sticking coefficient of the precursors on the SiN, which enhances the incorporation of material into the islands. A rough estimate of the deposited volume showed the average deposition rate to be constant. The comparison of the samples A and B demonstrates, that the the SiN thickness has to be carefully adjusted in order to reproducibly obtain epilayers with a low dislocation density. Once this is done, the process captivates by its simplicity and the possibility to use it *in situ*.

It remains unclear, if the overgrowth step can change the strain in the layer. The GaN overgrows SiN, which has been successfully used as a masking material for lateral epitaxial overgrowth [149]. In that publication, strong variations of the local strain were observed according to micro-Raman mappings. It might be, that this also applies to the *in situ* treatment. Furthermore, misfit dislocations are generated, which might release strain at this interface. However, assuming a random nucleation of the islands, the average strain release from the misfit dislocations would be zero at first sight, since an equal number of Burgers vectors $+\vec{b}$ and $-\vec{b}$ would be formed.

Chapter 4

High temperature island coalescence

The island growth mode obtained during the overgrowth of the NL at high temperature is one of the key steps to control the final epilayer properties. As the microstructure of the epilayer is defined duringthis step, many important parameters like photoluminescence characteristics, strain or threading dislocation density are affected. Possible growth parameters to modify the high temperature island growth mode were presented in Chapter 3. This chapter will treat the correlation of the coalescence process, the threading dislocation density and the strain in more detail.

4.1 Microstructure of layers as seen by X-ray diffraction

4.1.1 The model of mosaic crystals

The reciprocal lattice of a crystal is defined through the periodicity of the atoms inside it. Accordingly, the broadening of the reciprocal lattice points is inversely proportional to the volume of the undisturbed lattice. As described in Section 3.2.2, the high-temperature islands grow almost free of threading dislocations. Due to the misorientation of the islands, threading dislocations with edge component form along the coalescence boundaries of neighboring islands to compensate for the relative in-plane twist. In a first approximation, this pattern of dislocations can be regarded as the boundary of perfect grains, which are tilted and twisted with respect to each other. This model is called the model of moasic crystals and has been widely used for the description of semiconductor structures. It is illustrated in Fig. 4.1. A set of four parameters is used to describe the mosaicity in the sample. The in-plane and out-of-plane rotation of the grains is quantified by the twist and the tilt, respectively. The average grain dimensions are measured by the lateral and the vertical coherence length. The definition of twist used in this context is the full width at half maximum (FWHM) of the distribution function of the individual in-plane rotation angles. Accordingly, the tilt is the FWHM of the out-of-plane rotation angles. The lateral and vertical coherence lengths are defined as the average values of the grain diameter and the grain height, respectively. For smooth GaN layers, the vertical coherence length is commonly equal to the film thickness, as the threading dislocations propagate along the [0001] direction.

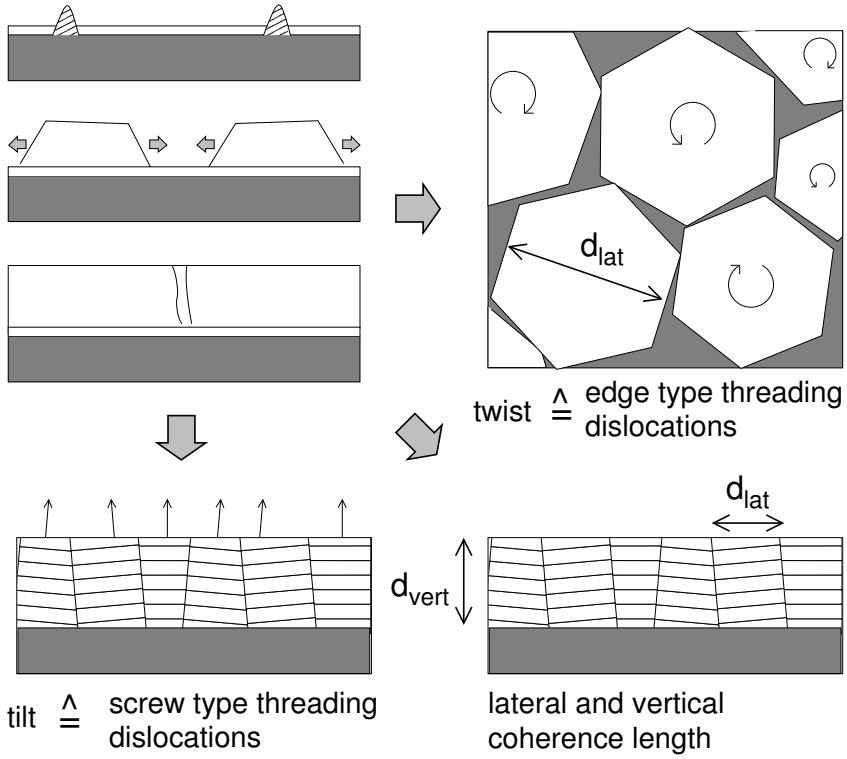

Figure 4.1: Illustration of the mosaic model used for textured crystals. The individual islands are twisted and tilted, therefore edge, mixed and screw type threading dislocations form in the layer.

The typical distribution of dislocations in GaN layers grown by MOVPE was found to be in accordance with this model. TEM revealed the sub-boundary structure, which is visible as an array of edge type threading dislocations in plan-view TEM [133]. These dislocations are the dominant type in GaN as shown by Hino *et al.* [136]. Using a novel etching technique they reported that for most films ∼89% of the threading dislocations were edge type, ∼9% were mixed type and only ∼2% were screw type. This is in agreement with the process of island coalescence and grain boundary formation. The twist is the dominant misorientation, thus, the edge and mixed dislocations are major in number. The mixed dislocations contain a Burgers vector component along [0001], and can compensate for the tilt across the grain boundaries. Pure screw type dislocations occur randomly in the subgrains, caused by the tilt of the grains relative to the substrate. The tilt is commonly smaller than the twist, therefore, only few pure screw dislocations are formed. On this background, it is interesting to note, that Hino *et al.* found the photoluminescence to drop with an increase of the *screw and mixed* threading dislocation density [136]. This suggests that only these dislocations are responsible for the non-radiative recombination in the material, although they are the minor dislocation type [136].

4.1.2 Broadening of reciprocal lattic points

Based on the model of mosaic crystals, it is possible to understand the broadening of reciprocal lattice points (RLP). This then allows one to use XRD to quantify the individual dislocation densities, as the broadening is directly connected to a geometric misfit.

Finite size broadening

The spatial limitation of coherently scattering material is defined by the network of threading dislocations, separating undisturbed grains. As the reciprocal lattice is a Fourier transform of the electron density distribution in the crystal lattice, a limitation in real space will broaden the reciprocal lattice points inversely proportional to the dimension of the diffracting grain. This broadening applies to all dimensions of the grains, i.e. for GaN layers, the average lateral grain diameter causes the in-plane broadening of the RLPs and the film thickness corresponds to the RLP broadening along q_z-direction. The mathematical description of the finite size broadening is given by the Scherrer equation, which relates the coherence length d, the scattering angle Θ and the broadening along 2Θ [150] :

$$d = \frac{0.9\lambda}{\mathrm{FWHM}_{2\Theta}\cos\Theta} \tag{4.1}$$

The formula is translated into reciprocal lattice units by using the definition of the diffraction vector $\vec{q}$:

$$|\vec{q}| = q = 2\sin\Theta\frac{1}{\lambda}$$

The differential then yields an expression for Δq

$$\Delta q = 2\Delta\Theta\cos\Theta\frac{1}{\lambda},$$

which is used in Eqn. 4.1 to convert it to reciprocal lattice units :

$$\Delta q = \frac{0.9}{d}.$$

Since d is constant for all RLPs, the broadening along a certain direction in reciprocal space is the same for all RLPs.

This change of the reciprocal lattice due to finite size broadening is illustrated in Fig. 4.2. As the lateral restriction d is provided by the average grain diameter, the in-plane broadening of the RLPs is isotropic in the q_{xy}-plane. Thus, the RLPs are circularly widened in-plane as shown in Fig. 4.2 (a). Commonly, the film thickness is not equal to the in-plane grain diameter, such that the out-of-plane broadening differs. This is shown in Fig. 4.2 (b). In cross-sectional view, the RLPs appear as ellipsoids, with the lateral and the vertical broadenings following the inverse lateral and vertical coherence length, respectively.

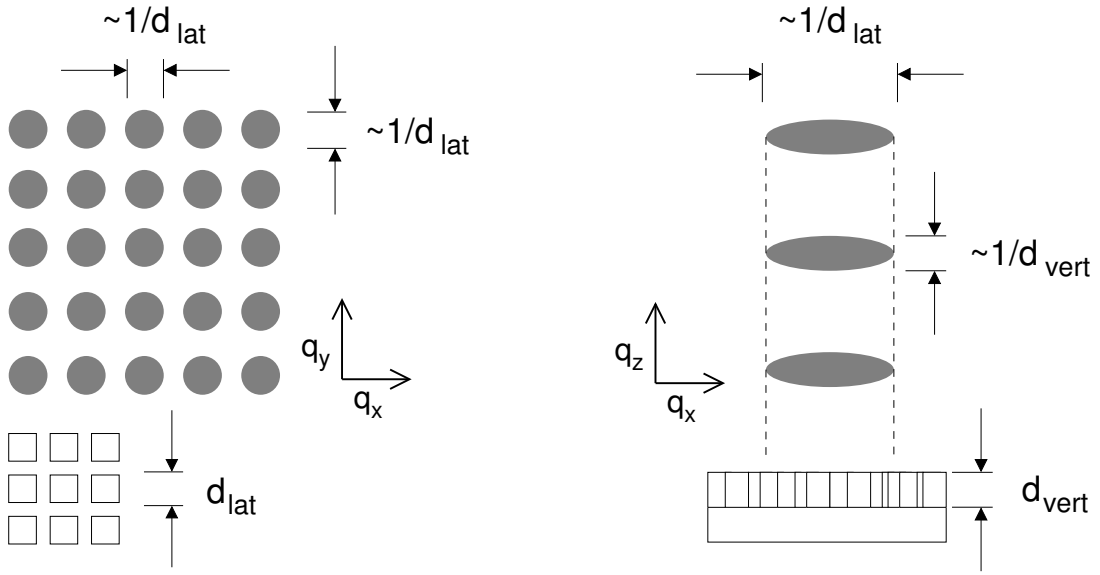

(a) lateral coherence length

(b) vertical coherence length

Figure 4.2: The impact of finite size broadening on the reciprocal lattice of the film.

Tilt and twist broadening

Besides the two coherence lengths, tilt and twist are the other two parameters of the model for mosaic crystals. These describe the in-plane and out-of-plane rotation of the grains, such that the reciprocal lattice can be thought of as the superposition of all the reciprocal lattices from the individual, misaligned grains.

Fig. 4.3 (a) demonstrates the modification to the reciprocal lattice in the q_{xy}-plane, caused by the twist of the grains. The rotational misfit causes the broadening of a RLP to be proportional to its distance from the origin of the reciprocal space, and the direction of the broadening to be perpendicular to the diffraction vector $\vec{q}$. The cross-sectional view in Fig. 4.3 b) illustrates the effect of the tilt in the layer. Here, the broadening and its direction behaves similar.

Superposition

Commonly, one finds a superposition of the four described broadening effects. They need to be separated in order to use them for the calculation of dislocation densities. The superposition is illustrated in Fig. 4.4 for the broadening of the symmetric lattice points **00*l*** due to a finite grain diameter and a tilt. The broadening in reciprocal space increases for higher order RLPs due to the tilt in the layer, but it is offset by a constant caused by the finite diameter of the grains.

The latter is determined by the extrapolation of the RLP broadening to $q_z = 0$. This is done in a so-called Williamson-Hall plot as sketched in Fig. 4.4 (b). Here, the FWHM

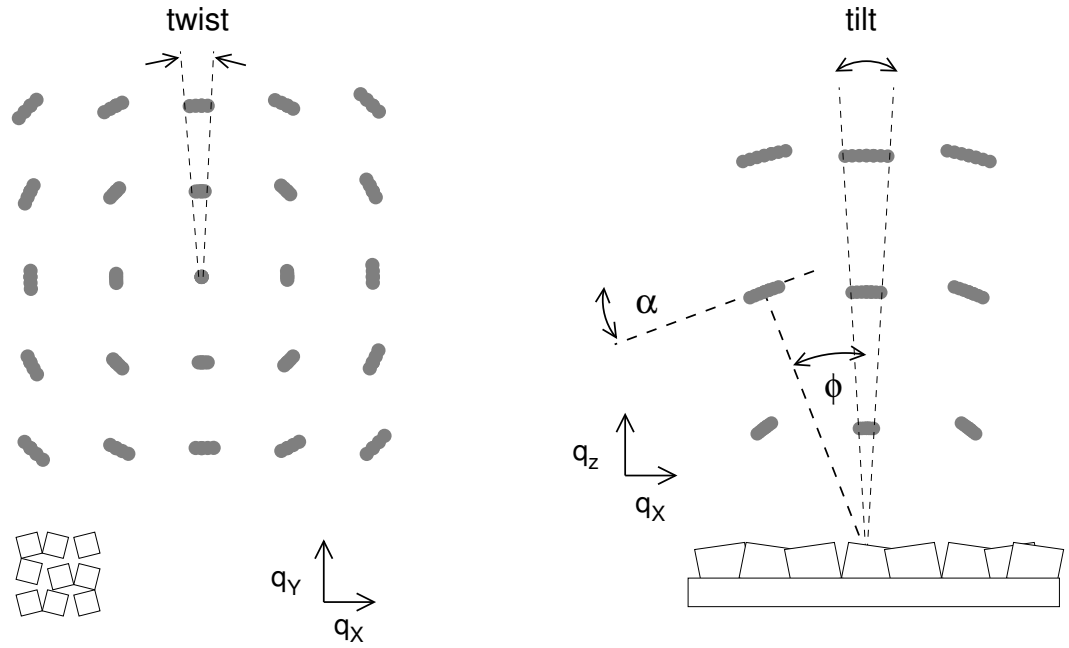

(a) twist **(b)** tilt

Figure 4.3: Modification of the reciprocal lattice due to twist and tilt. The lattice can be understood as a superposition of several reciprocal lattices slightly rotated relative to each other.

of the RLPs measured in units of the reciprocal space is plotted versus their position in reciprocal space. The slope of the resulting straight line then yields the tilt in the layer and the intersection with the y-axis provides the lateral coherence length.

Visibility of dislocations

Dislocations are distortions of the crystal lattice. Depending on the type of dislocation, different families of lattice planes are affected. The distortion is described by the Burgers vector, which points along the direction of the distortion, as illustrated in Fig. 4.5. For GaN, three types of dislocations were identified, with Burgers vectors of different orientation as described in Section 3.2.2. The screw type threading dislocations have a Burgers vector $\vec{b}_s = [0001]$, thus the periodicity of the lattice is disturbed only in the [0001] direction. In contrast to this, edge type threading dislocations create an in-plane distortion of the lattice due to their Burgers vector $\vec{b}_e = 1/3\langle 11\bar{2}0\rangle$. Mixed dislocation affect the in-plane as well as the out-of plane periodicity, because their Burgers vector $\vec{b}_m = 1/3\langle 11\bar{2}3\rangle$ has components along both directions. XRD can only provide information about the lattice periodicity in one direction, namely the direction corresponding to the actually measured RLP. Therefore, if the Burgers vector of a dislocation has a

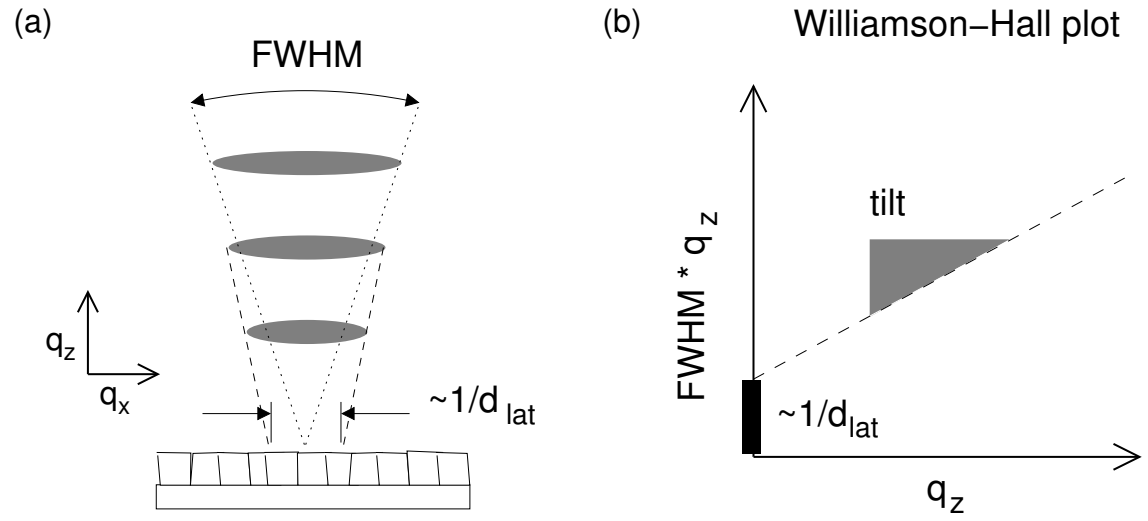

Figure 4.4: a) The superposition of tilt broadening and finite size broadening illustrated for the symmetric RLPs. b) Williamson-Hall plot to separate the two effects.

component along the diffraction vector, then the RLP is broadened as well, according to the scalar product $\vec{q} \cdot \vec{b}$. For $\vec{q} \cdot \vec{b} = 0$, then the distortion happens perpendicular to the diffraction vector, and the particular RLP is insensitive to this type of dislocation (compare invisibility criterion for TEM in Section 2.5).

The most important consequence for GaN is the insensitivity of the **00*l*** reflections to edge type threading dislocations, as demonstrated by Heying *et al.*, who compared the symmetric and asymmetric XRD scans of samples with different dislocation structures [151]. Accordingly, in-plane reflections are insensitive to screw dislocations, and mixed dislocations affect symmetric as well as asymmetric reflections (see Fig. 4.5). In order to compare the structural properties of GaN, it is therefore necessary to study symmetric as well as asymmetric reflections [152]. Moreover, two lateral coherence lengths have to be defined, one for mixed and screw type threading dislocations and one for edge and mixed type threading dislocations. This is important to keep in mind for the quantification of twist and tilt utilizing Williamson-Hall plots.

4.2 Dislocation densities determined by XRD

The advantage of x-ray diffraction is its non-destructivity and the fast generation of data, making it one of the most efficient tools for growth optimization. Even without deep knowledge of this technique it is possible to create good figures of merit for growth optimization, namely the FWHMs of a symmetric ω-scan and an asymmetric ϕ-scan. The former provides some information about the screw type threading dislocation density and the latter about the edge type threading dislocation density. However, XRD can be much more quantitative, if accurate models are being used. This will be discussed in more depth.

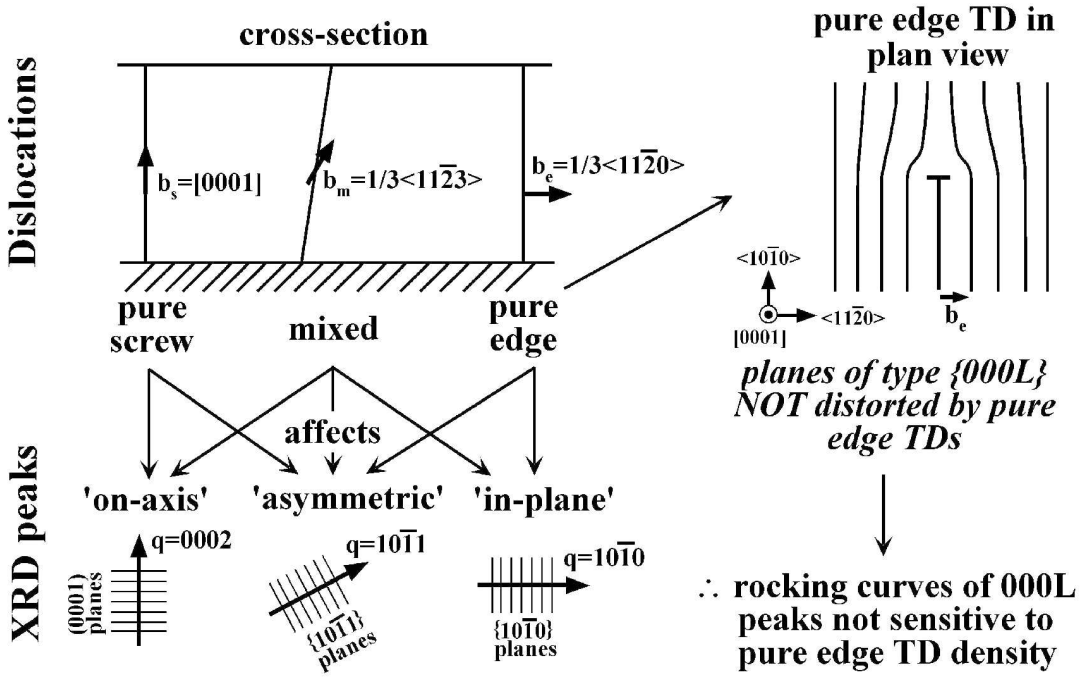

Figure 4.5: Influences of pure-screw, mixed-character, and pure-edge threading dislocations in GaN/sapphire films on rocking curve full-width at half-maximum values. The left portion of the schematic is in cross-section, while the upper-right portion is in plan-view [128].

4.2.1 Established models for the quantification of dislocation densities

The correlation of XRD and microstructure has been the subject of several publications and books (e.g. [153, 150]). However, the application of quantitative models to GaN films happened only recently, among which two main approaches can be distinguished [154]. One approach analyzes the *local* lattice distortion due to the strain field of the individual dislocations and uses it to quantify the broadening of the RLPs in the radial scan direction [155]. The second approach is based on the model of mosaic crystals and uses the tilt and the twist in the layer to calculate the dislocation density from geometrical arguments. If one assumes, that all dislocations with a screw component are related to edge-type misfit dislocations in the interface to accommodate the tilt α in the layer, then the screw type threading dislocation density N_s is given by [156]

$$N_s = \frac{\alpha^2}{4.35 b_s^2}. \tag{4.2}$$

Here, $b_s=|\vec{b}_s|$ is the length of the Burgers vector and amounts to b_s=5.185 Å for GaN [60]. It should be noted, that the equation assumes a fully random spatial distribution of the dislocations. For screw type threading dislocations in GaN, this condition can be regarded as fulfilled according to experimental results.

Eqn. 4.2 can also be applied to the measured twist β in order to calculate the edge

type threading dislocation density. Again, this is based on the assumption that the geometric misfit is exactly compensated by the edge dislocations, and that the distribution is random. Using the corresponding Burgers vector equal to one a-axis lattice constant (b_e=3.189 Å), the edge type threading dislocation density N_e follows to

$$N_e = \frac{\beta^2}{4.35 b_e^2}. \tag{4.3}$$

Equations 4.2 and 4.3 have been successfully used to access dislocation densities in MBE-grown material within reasonable limits of accuracy [154, 157]. If the dislocations are localized at the grain boundaries, which is more applicable to MOVPE-grown GaN, another formula can be used, which was originally developed for material with small-angle grain boundaries [120, 154] :

$$N_e = \frac{\beta}{2.1\ b_e\ d_{\mathrm{lat}}} \tag{4.4}$$

Eqn. 4.4 also uses the twist β and the length of the Burgers vector b_e, but takes the lateral coherence length d_{lat} into account, which is given by the average grain diameter (compare Section 4.1.2). For MBE-grown films on sapphire, the dislocation densities obtained from Eqn. 4.4 significantly underestimated the actual values as verified by TEM [154].

4.2.2 Coalescence thickness and island diameter

The samples investigated in this study were grown using different sets of growth parameters in order to achieve a wide variation of the dislocation structure. Out of the set of parameters presented in Chapter 3, primarily the total pressure and the V/III ratio during the NL growth were changed to vary the coalescence process. This allowed one to obtain samples with edge type threading dislocation densities ranging from $\sim 4 \times 10^9$ cm^{-2} down to $\sim 7 \times 10^7$ cm^{-2} as proved by plan-view TEM (see Fig. 4.6).

From these images, it is reasonable to assume, that the average island diameter during the growth at high temperature increased. This is also evident from the reflectance transients of these samples which are displayed in Fig. 4.6 as well. For sample 1 with the highest dislocation density, the three-dimensional growth mode sustained only for a short period, whereas for sample 3 with the lowest dislocation density the extended drop of the reflectance indicates an elongated island growth mode. This picture was verified by AFM images of selected uncoalesced films. These images also revealed the lateral and vertical growth rate to be approximately equal, i.e. the base diameter was roughly twice the height of the islands. This finding is also in agreement with TEM images presented by Wu *et al.* [132]. In the following the growth rate ratio is assumed to be unity, which should be justified at least for the set of samples under investigation. The correlation of reflectance transient and dislocation pattern visible in Fig. 4.6 can then be exploited to estimate an average grain diameter for the model of mosaic crystals. The average spacing of the edge type threading dislocations, as seen in the TEM images, scales with the film thickness at which the HT islands coalesce. Since the process of coalescence is visible in the reflectance transients, the corresponding film thickness can

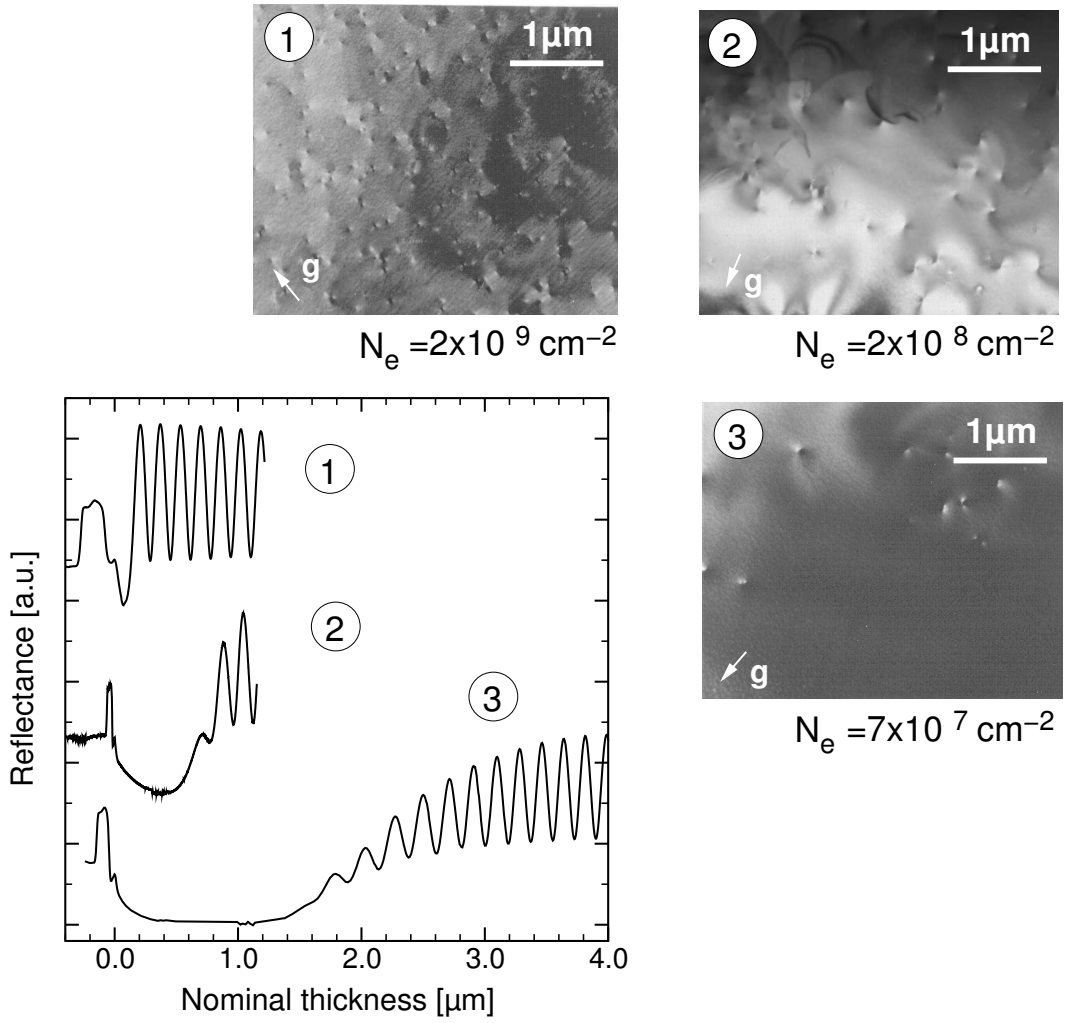

Figure 4.6: Reflectance transients of three GaN layers with different coalescence speeds and corresponding plan-view TEM images.

be determined as well. The ratio of lateral to vertical growth rate then yields the island diameter at coalescence.

To quantify the reflectance of a coalescing film, the model presented in Section 6 can not be used, since the average island diameter is on the same order as the wavelength used for the measurement. Therefore, a simple geometrical approach is used, which is based on the assumption, that only the (0001) facets of the growing HT islands reflect the light in the normal direction. In particular, this is justified for the late stages of the coalescence process, when large fractions of the surface are already smooth. The lateral growth of the islands proceeds via the $\{10\bar{1}1\}$ facets, who scatter the incident light by an angle of $\sim 120^\circ$ and do not contribute to the reflectance. At coalescence, the island geometry can then assumed to be similar to Fig. 4.7 (a). The base diameter of the islands is twice their height, such that the reflectance R of this structure is defined by the fraction of the total (0001) surface $A_{(0001)}$ inside the laser spot

$$R = \frac{A_{(0001)}}{A_{spot}} R_{max},$$

where R_{max} denotes the reflectance of a smooth layer. For later stages of the coalescence, the (0001) surface area increases, and the reflectance rises accordingly. At the point where the film thickness is equal to the average grain diameter, the grain shape is assumed to be as drawn in Fig. 4.7 b). The relative reflectance r is then given, assuming a hexagonal shape of the (0001) facet :

$$r = \frac{R}{R_{max}} = \frac{A_{(0001)}}{A_{base}} = \frac{2\sqrt{3}(1-\frac{a}{c})^2 h^2}{\frac{\sqrt{3}}{2} d^2}, \qquad (4.5)$$

where a and c are the lattice constants of GaN. As the film thickness h and grain diameter d are identical, Eqn. 4.5 results in

$$r = 4\left(1 - \frac{3.1878\text{Å}}{5.185\text{Å}}\right)^2 \approx 0.6. \qquad (4.6)$$

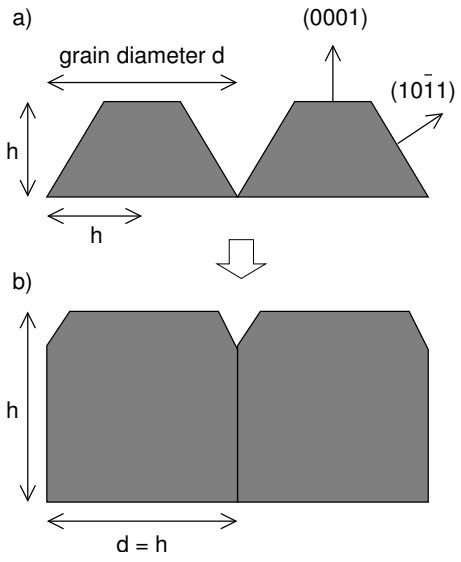

Figure 4.7: Assumed island geometry during the HT island coalescence.

Thus, the film thickness at a reflectance of 60% of the maximum value has been taken as a measure for the average grain diameter. Two approaches were applied to determine this thickness. For the more accurate one, the film thickness was measured after growth utilizing either optical transmission or ellipsometry, and the thickness of the two-dimensionally grown part of the film was subtracted. For the second approach, a constant growth rate throughout the whole film was assumed , such that the thickness at $r = 0.6$ is given by the growth time and the growth rate. Interestingly, no significant differences between the two methods were found. This indicates a constant growth rate, i.e. a constant volume of material being deposited per time.

4.2.3 Screw and mixed type threading dislocations

As described before, the threading dislocations with a Burgers vector component along [0001] affect the symmetric **00*l*** reflections. These reflections are broadened along q_{xy} mainly due to tilt and finite in-plane size, i.e. the broadening can be accessed via ω-scans. The two broadening effects are separated in a Williamson-Hall plot. Due to the small peak width, the scans were acquired with an analyzer crystal to minimize the apparatus function.

Fig. 4.8 contains this plot for samples with different grain diameters. The data sets are each fitted by a straight line to obtain the slope and the intersection with the y-axis. The former yields the tilt in the layer and the latter allows to determine the lateral coherence length as seen by the symmetric reflections. For all samples, the slope and the

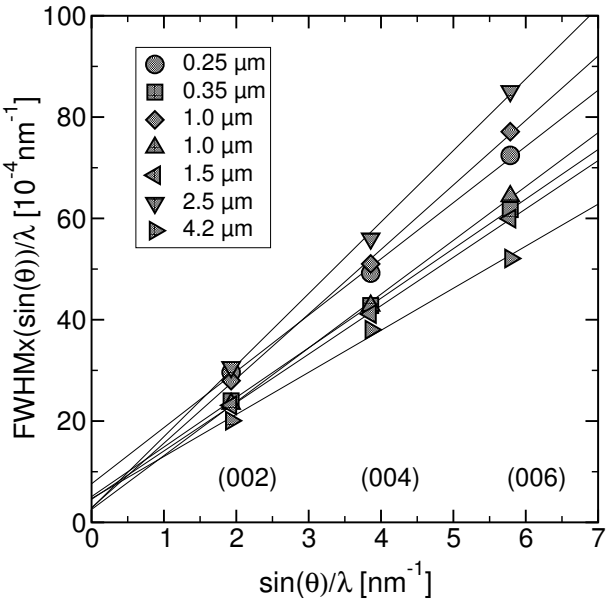

Figure 4.8: Williamson-Hall plot for samples of different average grain diameter comparing the FWHM of the symmetric reflections. The measurements were done in collaboration with R. Chierchia, University of Bremen.

y-axis offset are very similar. The tilt broadening clearly exceeds the finite size broadening, indicating a low density of the screw/mixed dislocations. It is remarkable to note, that in spite of the change in grain diameter by an order of magnitude, the tilt as well as the lateral coherence length seem to not vary significantly. Converting the tilt into a threading dislocation density using Eqn. 4.2, the grey circles in Fig. 4.9 are obtained.

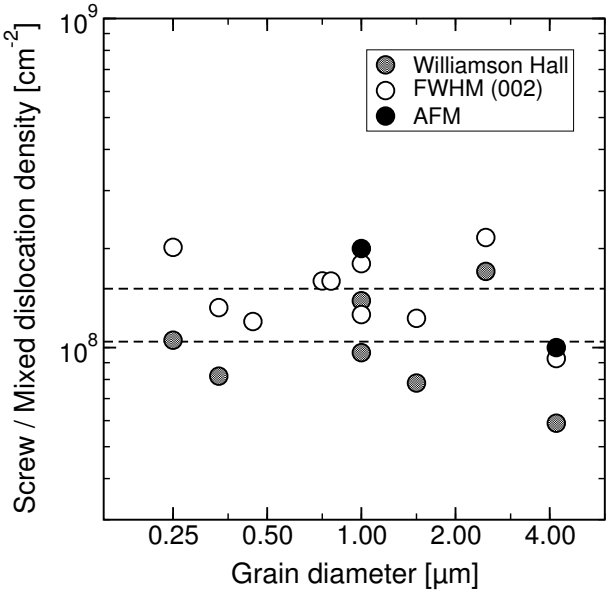

Figure 4.9: The screw type threading dislocation density in dependence on the grain diameter as calculated from the Williamson-Hall plot, from the FWHM of the **002** reflection and from AFM measurements, respectively.

As suspected, the screw and mixed type threading dislocation density obtained from this method is roughly constant, although there might be a slight drop with increasing grain diameter. It scatters around 10^8 cm^{-2}, which was confirmed for two samples by analyzing AFM images. The latter method is based on the fact, that threading dislocations with a Burgers vector component along [0001] pin atomic steps as soon as they intersect with the free surface [158]. Edge type threading dislocations do not have a

component along this direction - thus, they do not interfere with the step structure of the surface. Surface depressions due to these dislocations are sometimes visible, but they can be clearly distinguished, as they appear independently from the steps.

Also plotted in Fig. 4.9 are the calculated dislocation densities, if the **002**-FWHM is taken as the tilt value of the structure. This approximation is possible, since the FWHM of the reflections mainly originates from the tilt and not from the finite size of the grains. The dislocation densities determined this way are slightly larger than the values extracted from the Williamson-Hall plot, but the differences are small. The error could be reduced further by using the FWHM of higher order reflections, e.g. the **004**-peak, but due to the good agreement of the values from AFM and from the **002**-FWHM, the latter peak should be preferred. Therefore, for the ease of use, the screw type threading dislocation density can be estimated using the FWHM of a symmetric reflection and the formula proposed by Dunn *et al.* [156] :

$$N_{\text{screw}} \approx \frac{(\text{FWHM}_{001})^2}{4.35 \cdot b_s^2} = 8.55 \cdot 10^{13} (\text{FWHM}_{001})^2 [\text{cm}^{-2}]. \tag{4.7}$$

As the **002**-peak is rather intense, and can be easily accessed, it is recommended to analyze the ω-scan of this reflection. The FWHM values has to be inserted in units of radians.

4.2.4 Edge and mixed type threading dislocations

Within the model of mosaic crystals, the edge and mixed type threading dislocation density can be quantified from the twist in the layer. Symmetric reflections are insensitive to edge type threading dislocations, as illustrated in Fig. 4.5, therefore, one has to access in-plane reflections and make a Williamson-Hall plot to separate the finite size from the twist broadening. In normal diffraction geometry, these reflections are not accessible. They could be measured in transmission or edge geometry, but those are non-standard, and not suitable for everyday use. In order to use the standard diffraction geometry, the first step is to get an estimate of the FWHM of an in-plane reflection. This can be done by acquiring ω-scans of asymmetric reflections with varying inclination angle of the corresponding lattice planes relative to the (0001) surface, and extrapolating these to an inclination angle of 90°. The method has been evaluated in great detail by H. Heinke *et al.* and V. Srikant *et al.* [157, 159, 152]. The scans have to be done in skew symmetric geometry, as otherwise the twist can not be attained. It is also possible to use ϕ-scans in asymmetric diffraction geometry, but one has to be aware that the apparatus function is usually extremely broad in this case, as the slit in front of the detector is commonly oriented parallel to the scan direction [157].

The experiment was done for selected samples of varying grain diameter as shown in Fig. 4.10. The FWHM of the various reflections is plotted against the inclination angle of the respective lattice planes. For higher inclination angle, the peaks get more sensitive to the edge type threading dislocation distribution and the twist in the layer. In the figure, the differences in the microstructure become visible. For films with small grains, the FWHM increases significantly with the inclination angle, whereas for the samples with the largest grain diameter, the FWHM is roughly constant. The transition between

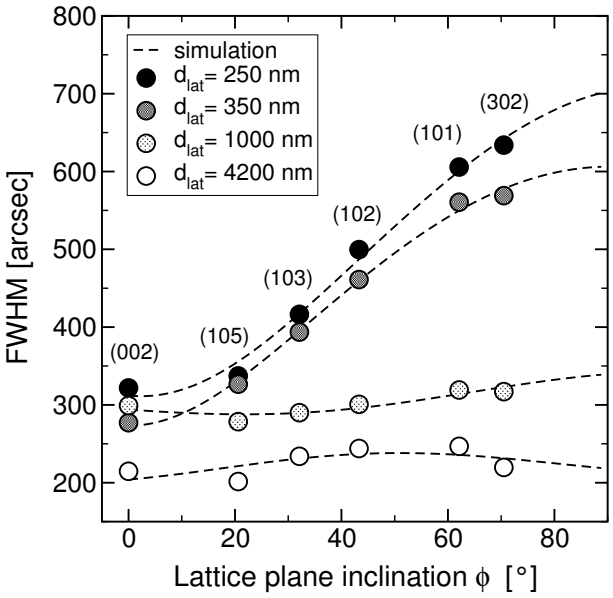

Figure 4.10: FWHM of ω-scans in dependence on the lattice inclination angle for samples with different grain diameter. Measurements and simulations were done by R. Chierchia, University of Bremen.

these two extreme cases is gradual. The first approximation is to determine the twist by extrapolating the profile width of these scans to 90° and assuming the broadening due to the finite size effects to be negligible. These simulations were done taking an interdependence of tilt and twist into account as described in reference [152] and appear as dashed lines in Fig. 4.10. The study has been performed by H. Heinke and R. Chierchia for several GaN films, apart from the series discussed here. For most films the determined twist exceeded the FWHM of the **302** reflection by approximately 14% [157, 116].

However, as the change in the FWHM can be caused by the twist as well as the finite size broadening, the effect of the latter should not be neglected for low grain sizes. In particular for those peaks having a large inclination angle, the finite grain size can be expected to have a large influence, as the product $\vec{g} \cdot \vec{b}$ is close to unity. An estimate of the finite size effect can be gained from the Scherrer equation, which is plotted for the **302** peak in Fig. 4.11.

Here, the coherence length was set equal to the average grain diameter, which is justified in the context of the model of mosaic crystals. The inclination angle for this reflection is 70.5°, such that screw type dislocations are basically invisible and the relevant microstructure is determined by the edge and mixed type threading dislocations. Assuming the grains to be decorated by the latter dislocations, the coherence length can be taken equal to the grain diameter from reflectometry. The related broadening is given by the Scherrer equation 4.1. Fig. 4.11 demonstrates, that for smaller grain diameters the coherence length can make up to ∼50 % of the broadening of the **302** reflection, and therefore, should be taken into account for the extraction of the twist. Following this approach for all investigated samples, the twist is found to decrease with the grain diameter, but by far not as significant as suggested by the peak widths in Fig. 4.10. The experimental proof of this effect requires to determine the peak widths for a series of in-plane reflections in order to draw a Williamson-Hall plot. This is currently under investigation.

Including the finite size broadening in Eqn. 4.4 yields the following equation for the

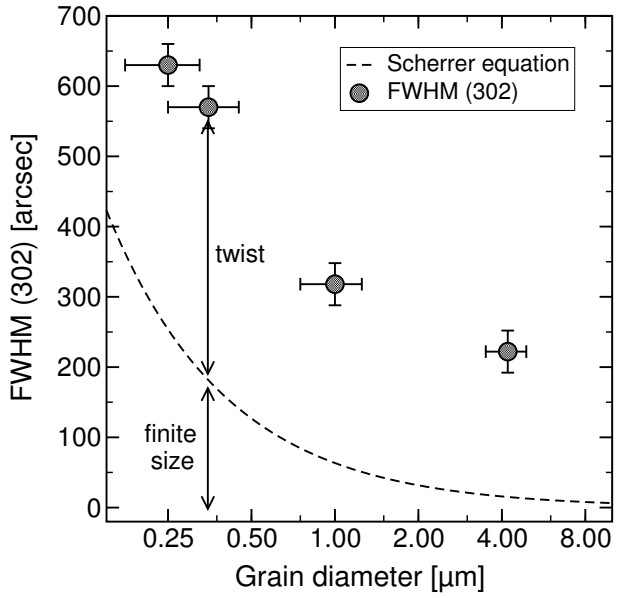

Figure 4.11: The FWHM of the **302** reflection for samples with different grain diameter. The dashed line is the broadening due to the finite grain size as estimated from the Scherrer equation.

edge and mixed type threading dislocation density N_{e} :

$$N_{\mathrm{e}} = \frac{1.14}{2.1\, b_e\, d_{\mathrm{lat}}} \left(\mathrm{FWHM}_{302} - \frac{0.9\lambda}{d_{\mathrm{lat}} \cos\theta} \right). \tag{4.8}$$

Here, the extrapolation of the twist from the **302**-FWHM is already considered by the factor of 1.14 as explained before. The FWHM is measured in radians, b_e is the length of the edge type Burgers vector (0.31878 nm [60]), d_{lat} is the grain diameter, λ is the wavelength of the x-rays and θ is the diffraction angle of the **302** reflection.

At this point, three different models are possible to extract an edge and mixed type threading dislocation density from the ω-scan profile width of the **302** peak :

1. extrapolation of the twist as sketched in Fig. 4.10 and assuming a random dislocation distribution (Eqn. 4.3)

2. extrapolation of the twist as sketched in Fig. 4.10 and assuming a correlated dislocation arrangement (Eqn. 4.4)

3. correction of the **302**-FWHM for the finite size broadening, extrapolation of the twist and assuming a correlated dislocation distribution (Eqn. 4.4)

The edge and mixed type threading dislocation density obtained from the first two cases is plotted in Fig. 4.12 and compared to the data obtained from the plan-view TEM images shown in Fig. 4.6 on page 77. As can be expected, the random model significantly overestimates this dislocation density, whereas the model of correlated edge and mixed type threading dislocations already provides a reasonable estimate. Only for lower grain diameter the calculated dislocation density deviates to higher values, which is caused by the finite size effect. The data from the third case is shown in Fig. 4.13 together with the screw / mixed type threading dislocation density.

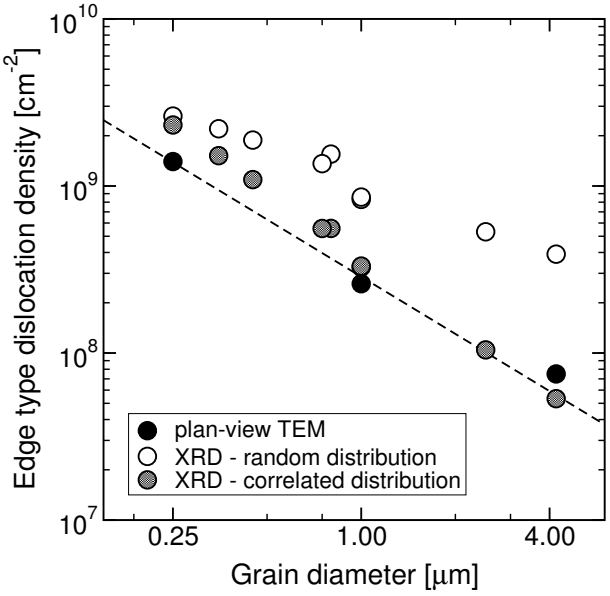

Figure 4.12: The edge type threading dislocation density versus the grain diameter as determined by plan-view TEM images and XRD, assuming a random or correlated dislocation distribution, respectively. The dashed line is a least-squares fit to the TEM data.

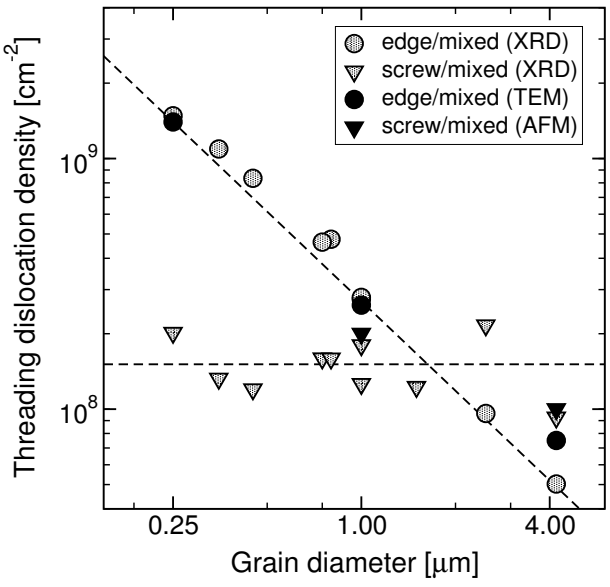

Figure 4.13: The threading dislocation densities as determined by TEM, AFM and XRD using Eqn. 4.8 in dependence of the grain diameter. The dashed lines are least-squares fits to the TEM and AFM data, respectively.

Eqn. 4.8 provides the best estimation of the edge and mixed type threading dislocation density determined by TEM. The figure illustrates the evolution of the threading dislocation structure with the average grain diameter. The edge and mixed type threading dislocation density dominates for almost all samples, but drops for larger grain diameters. The screw and mixed dislocation density is roughly constant around 1×10^8 cm^{-2}. The comparison of the XRD data with dislocation densities obtained from plan-view TEM and AFM demonstrates, that the model of mosaic crystals is well suited to utilize XRD as a tool to quantify the film perfection.

4.3 Strain state of GaN grown on sapphire

The compressive strain measured at room temperature for GaN layers on sapphire shows significant variations in literature, depending on the chosen growth conditions (e.g. [160]). No explanation has been given so far for this phenomenon. In this section, the possibility of the high temperature island coalescence being the responsible factor will be discussed. Part of it is published in [117].

4.3.1 Strain in dependence on the grain diameter

The *a*- and *c*-lattice parameters for all layers discussed in the previous section were determined from triple-axis analyzer scans of the **002**- and **114**-reflections, respectively. The lattice parameters are displayed in the inset of Fig. 4.14, exhibiting a strong dependence on the average grain diameter. The lattice parameters vary almost linearly for low sizes, and approach a constant value for larger diameters. The determined lattice constants compare well to reported literature values for heteroepitaxial GaN [161, 160]. Here, only undoped films grown on GaN nucleation layers under similar deposition conditions were considered.

Taking the lattice constant $a = 3.1878$ Å for a nominally unstrained GaN film [60], the strain is obtained as seen in Fig. 4.14. All layers are found to be under biaxial compression in the c-plane, which is expected due to the thermal mismatch to the sapphire. The interesting point is, that the compression increases with the grain diameter and shows an asymptotic behavior for the largest grain sizes. The maximum value of the in-plane strain is approximately $\varepsilon_{xx} = -1.5 \times 10^{-3}$. Most of the literature values fall within the limits visible in Fig. 4.14 and the inset. In particular, almost no higher compressive strain values are reported.

4.3.2 Strain components

The strain in GaN layers can be divided into an extrinsic and an intrinsic strain component. Normally, these components do not interfere, such that the strain and the stress state are linear superpositions of these components :

$$\varepsilon_1^{\text{tot}} = \varepsilon_1^{\text{extr}} + \varepsilon_1^{\text{intr}} \tag{4.9}$$

$$\sigma_1^{\text{tot}} = \sigma_1^{\text{extr}} + \sigma_1^{\text{intr}} \tag{4.10}$$

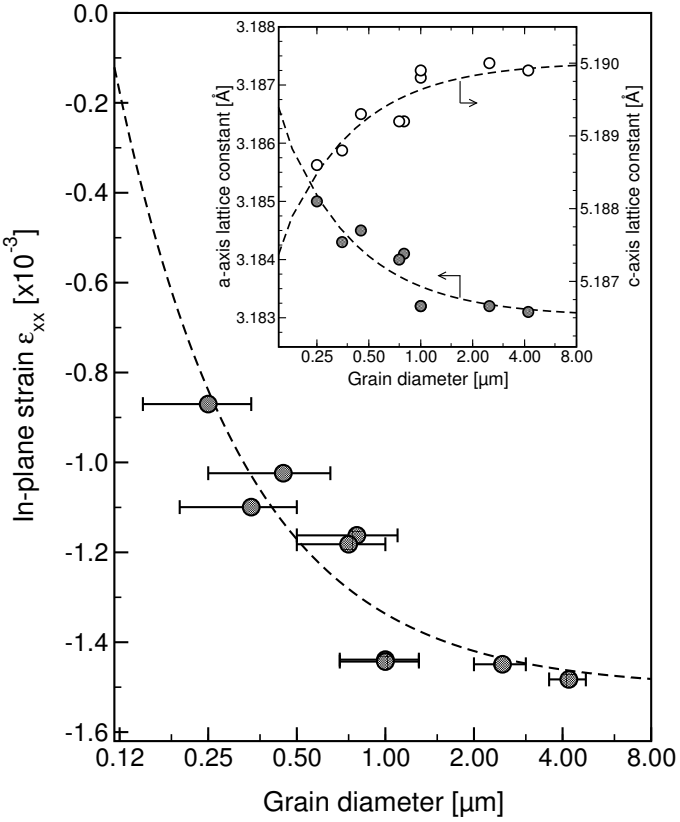

Figure 4.14: The change of the in-plane strain with the grain diameter. The inset shows the according variation of the *a*- and *c*-axis lattice parameters.

Extrinsic strain is imposed upon the layer through external load like the thermal expansion mismatch. In contrast, intrinsic strain develops during the growth of the layer. This is well known from other material systems and can be caused by a change in the microstructure, like point defects, island coalescence, grain growth or surface stress [162].

Extrinsic, thermal strain

The mismatch of the thermal expansion coefficients of GaN and sapphire causes the film to be compressively strained during cooling to room temperature. If no intrinsic strain is generated, the film would grow strain-free at high temperature. When the temperature is reduced after growth, the sapphire in-plane lattice parameter shrinks faster than that of the GaN and the film becomes compressively strained. This thermal strain ε_{th} follows from the integration over the temperature as

$$\varepsilon_{\text{th}} = \int_{T_0}^{T} (\alpha_{\text{GaN}} - \alpha_{\text{sapphire}}) dT. \tag{4.11}$$

Here, the in-plane expansion coefficients of the GaN and the sapphire are labeled α_{GaN} and α_{sapphire}, respectively. The thermal expansion of sapphire is usually assumed to follow the equation [163]

$$\frac{\Delta a}{a_0} = -0.00176 + 5.431 \times 10^{-6} T + 2.15 \times 10^{-9} T^2 - 2.81 \times 10^{-13} T^3, \tag{4.12}$$

with the temperature measured in Kelvin and a_0 is the in-plane lattice parameter at room temperature [164]. The expansion coefficient of GaN is still under investigation, and problematic due to the lack of ideal GaN single crystals. However, the results obtained recently do not scatter significantly [61, 116]. The according lattice parameter at room temperature and growth temperature are listed in Table 4.1.

Temperature [K]	293	1343
a_{sapphire} [Å]	4.7578	4.7993
$\Delta a/a_0$	0	+ 0.873 %
a_{GaN} [Å]	3.1878	3.2048
$\Delta a/a_0$	0	+ 0.535 %

Table 4.1: In-plane lattice parameters and strain of GaN and sapphire at room and growth temperature, respectively.

The strain difference of 0.338 % translates in an expected compressive thermal stress of 1.5 ± 0.7 GPa, if Eqn. 2.25 on page 39 and the corresponding elastic constants are used. The uncertainty of this value is large, though, due to inconsistencies in the literature values for the thermal expansion coefficients of GaN and sapphire and the lattice parameter of unstrained GaN.

Intrinsic strain : Experimental observations

In spite of its compressive mismatch to sapphire, the GaN is found to be under tension in the c-plane at growth temperature, if a GaN nucleation layer is used. This was demonstrated by Hearne *et al.*, who performed *in situ* measurements employing a multiple-beam optical stress sensor [83]. Hearnes data is plotted in Fig. 4.15. The measured quantity is the product of stress σ and the film thickness t, which determines the sample curvature. The layer thickness is obtained from the period of the intensity oscillations due to interference, such that the stress in the layer is equal to the slope of this line. The increase of $(\sigma \cdot t)$ with time indicates the in-plane tension at growth temperature. The annealing experiment in Fig. 4.15 additionally demonstrates, that plastic relaxation in GaN does not occur. This was further supported by the comparison of the strain states at growth and room temperature, where the latter were determined by XRD. This study revealed a constant compressive stress of $\sigma_1^{\text{extr}} = (-0.66 \pm 0.1)$ GPa due to the thermal mismatch. Therefore, the variations in strain have to be attributed to variations of the intrinsic, or growth stress.

The origin of the strain remained unclear. The simplest explanation would be the pseudomorphic growth of the GaN on the thermally tensile strained NL, since the NL is usually deposited around ~ 550°C and would be under tension at growth temperature, assuming that it is strain-free during its deposition. However, the high-temperature growth on AlN nucleation layers was found to happen under tension as well, in spite of the expected compressive lattice mismatch of AlN and GaN [83]. As seen in Fig. 4.15, the strain at growth temperature does not change upon annealing or thermal cycling,

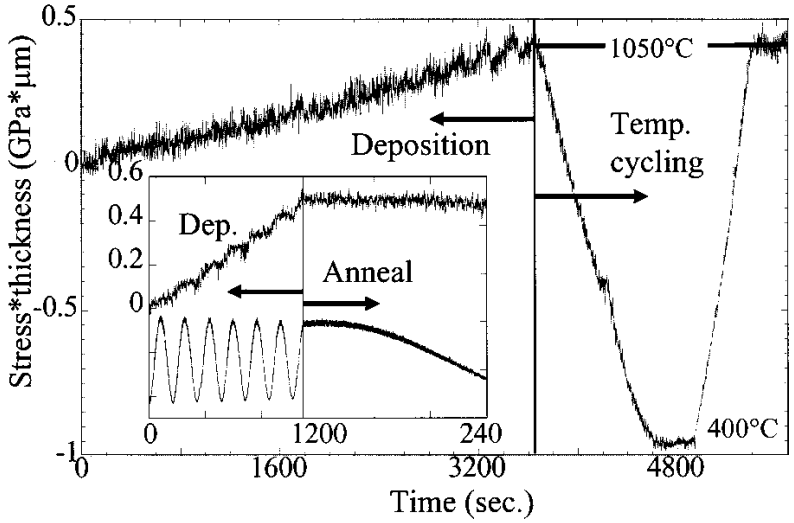

Figure 4.15: Stress thickness vs. time during growth and subsequent thermal cycling of a 2.2 μm GaN film from 1050 to 450 to 1050°C. The stress thickness and reflected intensity for annealing of a 2.2 μm GaN film for 30 min at 1050°C is shown inset [83].

which excludes according variations in the microstructure like grain growth. Island coalescence was partially excluded by Hearne *et al.*, because the tension was observed from the earliest stages of growth. However, this might have been caused by the HT island growth mode with a very early coalescence.

On the background of Hearne's work two possible origins of the intrinsic strain remain. The first is the pseudomorphic growth on a NL with enlarged lattice constant due to point defects and the second is the tension due to HT island coalescence. These will be detailed in the following two sections.

Intrinsic tensile strain : The pseudomorphic growth on the NL

As discussed in Section 3.2.2, the dislocation structure of the NL is suitable to accommodate the stacking mismatch to the HT GaN, but it does not relieve macroscopic strain. Therefore, the HT islands have to grow pseudomorphic on the NL. Annealing experiments showed the relaxation process of a GaN nucleation layer deposited at 505°C onto sapphire to be almost complete after annealing for ∼150 s at 1050°C [165]. When heating the layer to high temperature, the tension in the layer develops until approx. 750°C, and as soon as recrystallization and mass transport start, the strain is beginning to be relieved and the lattice structure of hexagonal GaN is observed. Unfortunately, the paper of Yi *et al.* only discusses symmetric reflections quantitatively, such that the fraction of the hydrostatic strain due to dislocations remains unknown. The main conclusion from this work is the rapid relief of strain as soon as mass transport sets in. A misfit dislocation network is generated at the sapphire-GaN interface, which allows the nucleation layer to relax at high temperature. This rules out the assumption of thermally induced tension in the HT islands, since the overgrowth happens on a much longer timescale,

i.e. GaN layers should grow strain-free at high temperature.

However, it is still unclear, if the supercell structure of misfit dislocations found in high-resolution TEM images of the sapphire interface generates any residual strain. Reports in literature state additional $\langle 10\bar{1}0 \rangle$ substrate half-planes about every 6-8 GaN planes, which either corresponds to tension or compression at growth temperature, depending on the period reported [120, 166, 167]. It has to be kept in mind, that TEM can only provide a very local analysis, therefore, it is not yet possible to derive a final conlusion. Accordingly, the nucleation layer is assumed to be free of thermal strain at the growth temperature within this following discussion.

A possible origin of the tension could by the change in defect structure. The as-grown NL is far from equilibrium and highly defective, such that it has an enlarged unit cell. Since the thermal strain is relieved during annealing, the enlarged unit cell is retained even at the growth temperature. This would cause the initial HT islands to grow under tension. During the recrystallization process, the dislocation density in the NL is reduced and, accordingly, the volume of the NL unit cell would shrink. Thus, with ongoing HT growth the tension in the HT islands is more and more relieved. Since the recrystallization process requires an open surface for the phase transition from cubic to hexagonal [125], the local strain state is conserved in the overgrown areas. In total, this would lead to a net tension at growth temperature, which is dependent on the average HT island size. The time scale of the phase transition during recrystallization is on the same order as the overgrowth process, so it might be a possible source of intrinsic tensile strain.

Intrinsic tensile strain : The high-temperature island coalescence

The process outlined before can explain the observed strain state, although the data published so far rather point to a strain generation process independent of the NL structure. Assuming the isolated HT islands to grow strain-free, a possible process would be the gap closure during the coalescence of islands at the growth temperature as proposed by Finegan and Hoffman [168]. The measurements presented in Ref. [83] do not exclude this possibility, since the coalescence in the presented experiments happened early, i.e. the tension would be generated at the earliest stages of growth as well. The island coalescence allows the film to reduce its surface energy, such that it is energetically favorable to close the gap between two randomly placed islands by elastic deformation at the expense of elastic energy. As the HT GaN islands are bonded to the substrate, this would cause tensile stress, with the magnitude depending on the grain diameter.

This process is sketched in Fig. 4.16. If the two neighboring islands are too close to insert an additional unit cell, the gap is closed elastically. The strain generated within an island then depends on the island diameter d and the gap width Δ :

$$\varepsilon_{\parallel}^{\mathrm{intr}} = \frac{\Delta}{d} \tag{4.13}$$

If the islands would not be bonded to the substrate, then this in-plane strain would be homogeneous across the whole layer, as suggested in Fig. 4.16. For immobile islands, the strain distribution has to show the same average value, but will vary across the

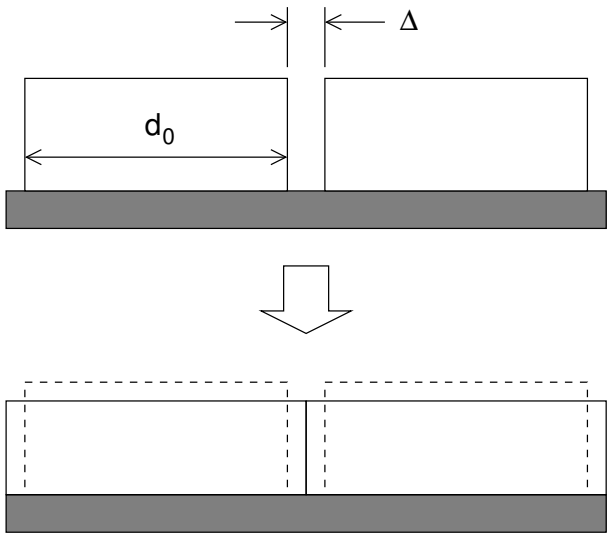

Figure 4.16: Formation of intrinsic tensile strain due to the gap closure of neighboring islands by elastic deformation.

island by approximately $\pm\varepsilon_{\perp}^{intr}$. The tension is then highest at the boundaries and lowest in the grain centers.

The development of strain in MOVPE-grown GaN due to the coalescence process can be understood if one takes into account, that the individual grains growing on the NL are misaligned in distance and twist with respect to each other. This leads to the formation of either low-angle grain boundaries, if the angle between the grains is large, or to almost dislocation-free interfaces, if the mismatch is small. As the net strain of a grain boundary at equilibrium is zero [169], it is not yet clear, if the grain boundaries itself can contribute to the average tensile stress in the film. However, if the angle between two adjacent grains is sufficiently small, the TD density along their interface is nearly zero, and the closure failure due to the random position has to be compensated by elastic deformation. This always leads to tensile strain, with the gap spacing ranging from zero to a. From an energetic point of view, the maximum gap at which the system still reduces its free energy, amounts to 1 nm [170]. This would correspond to as much as three a-axis lattice parameters in GaN.

A more recent analysis of the coalescence process was presented by Sheldon *et al.*, who developed a model for the coalescence process of three-dimensional islands as illustrated in Fig. 4.17 [171]. The model quantitatively describes the increase of tensile strain with proceeding coalescence, i.e. with the buildup of the grain boundary. At the point of coalescence, the tension is small, since the grain-boundary area is small as well due to the shape of the islands. With ongoing coalescence, the grain boundaries grow and accordingly the tension increases until it approaches the maximum value for the case of a closed, smooth film. This upper bound of the tensile strain follows energetic constraints and is given by Eqn. 4.13 [170, 171, 172]. Therefore, the strain state of the coalesced films can be described by the simple gap closure model proposed by Finegan and Hoffman [168].

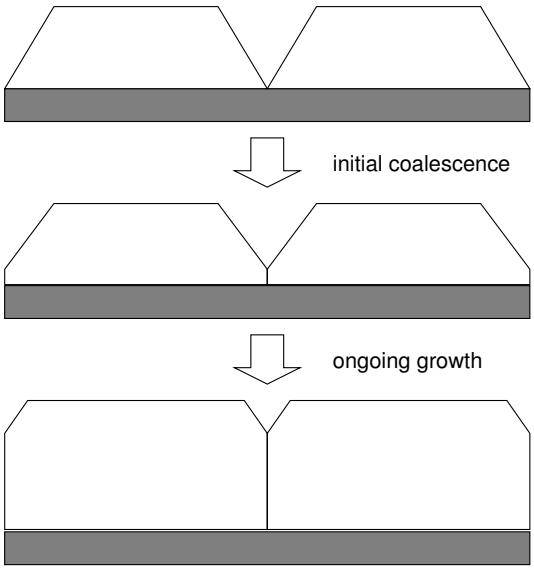

Figure 4.17: Island coalescence as described by Sheldon *et al.* [171].

4.3.3 Quantitative discussion of coalescence-related strain

The model of tension due to island coalescence is well suited for a quantitative discussion of the strain state, such that the experimental data from Fig. 4.14 can be theoretically verified. Since the strain state was measured at room temperature, the intrinsic as well as the extrinsic strain will have to be considered.

Intrinsic strain in a coalesced film

The basic assumption is that the microstructure of the film consists of hexagonal grains and that the grain diameters follow a Gaussian distribution peaking at the average grain diameter d_0. The standard deviation was estimated from AFM images and set to $d_0/2$. The intrinsic tensile stress is taken into account by assuming that the grains of diameter d in the coalesced film are separated by gaps of a constant width Δ. The average strain inside a grain is then given by Eqn. 4.13. Integrating over the Gaussian distributed grain diameters, the average intrinsic strain in the whole layer can be written as

$$\varepsilon_1^{\mathrm{intr}}(d_0) = \frac{\int_0^\infty \frac{\sqrt{3}}{2} d^2 e^{-\frac{(d-d_0)^2}{2\sigma^2}} \frac{\Delta}{d}\, dd}{\int_0^\infty \frac{\sqrt{3}}{2} d^2 e^{-\frac{(d-d_0)^2}{2\sigma^2}}\, dd} = \frac{2\sqrt{2}+4\sqrt{\pi}}{4\sqrt{2}+5\sqrt{\pi}} \cdot \frac{\Delta}{d_0} \approx 0.683 \cdot \frac{\Delta}{d_0}. \tag{4.14}$$

From Eqn. 2.25 the corresponding stress is obtained as

$$\sigma_1^{\mathrm{intr}}(d_0) = 0.683 \times (c_{11} + c_{12} - 2c_{13}^2/c_{33}) \times \varepsilon_1^{\mathrm{intr}}(d_0) = 307.1\ \mathrm{GPa}\ \times \frac{\Delta}{d_0}. \tag{4.15}$$

It should be emphasized that Equations 4.14 and 4.15 are based on a constant gap spacing. It causes the reduction of the elastic modulus, since the strain is inversely depen-

dent on the grain diameter, such that larger grains are less affected. As the strain has to be weighted via the grain area to obtain the average value in the film, the contribution of large grains is dominant and the effective strain is reduced.

Extrinsic, thermal stress

An estimate of the extrinsic, thermal strain can be achieved by the extrapolation of the lattice parameter a towards a vanishing edge/mixed type threading dislocation density. This yields the value of a perfect GaN layer on sapphire and allows the calculation of the extrinsic stress originating only from the thermal mismatch.

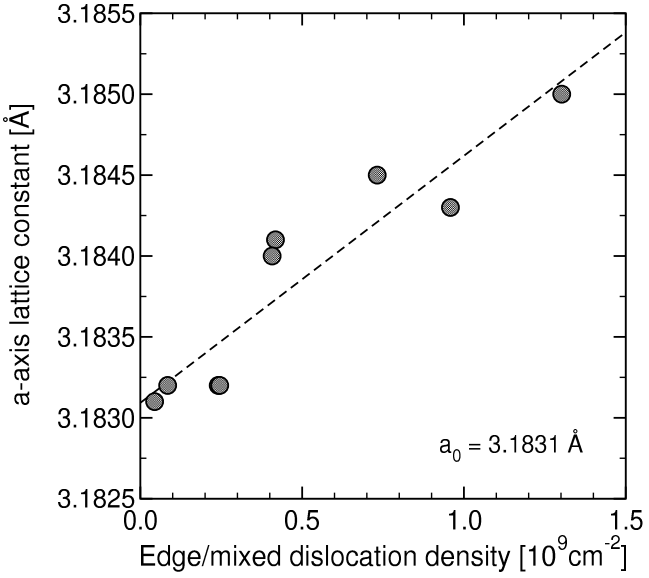

Figure 4.18: Lattice parameter a versus the density of edge/mixed type threading dislocations. The dashed line is a least-squares fit based on a linear relation.

The according graph is shown in Fig. 4.18. The dislocation density is inversely dependent on the grain diameter d_0 like the intrinsic strain. Therefore, the assumption of a linear dependence is justified for the relation shown in Fig. 4.18. In this case a dislocation-free layer on sapphire (without grains) should show an a-axis lattice parameter of 3.1831 Å at room temperature. Taking the a-axis lattice parameter of homoepitaxial GaN as the value for unstrained material [60] and Eqn. 2.25, the extrinsic, thermal stress amounts to

$$\sigma_1^{\mathrm{extr}} = 449.6\,\mathrm{GPa} \times \frac{3.1831\mathrm{Å} - 3.1878\mathrm{Å}}{3.1878\mathrm{Å}} = -0.66 \pm 0.10\,\mathrm{GPa}. \tag{4.16}$$

This is exactly the same value as published by Hearne *et al.* utilizing *in situ* stress measurements as discussed before [83]. For comparison, the calculated thermal stress estimated in section 4.3.2 from the thermal expansion coefficients of sapphire and GaN amounts to $\sigma_1^{\mathrm{extr}} = -1.5 \pm 0.7$ GPa. This difference could be caused by differences in the literature values for thermal expansion and the lattice constants of strain-free GaN. An additional hydrostatic strain component not yet considered in this model might be responsible, too.

Experimental data

The experimentally determined stresses for all samples are shown in Fig. 4.19. The extrinsic, thermal stress overcompensates the intrinsic tensile stress, resulting in a total compressive stress which strongly depends on the high temperature island size at coalescence.

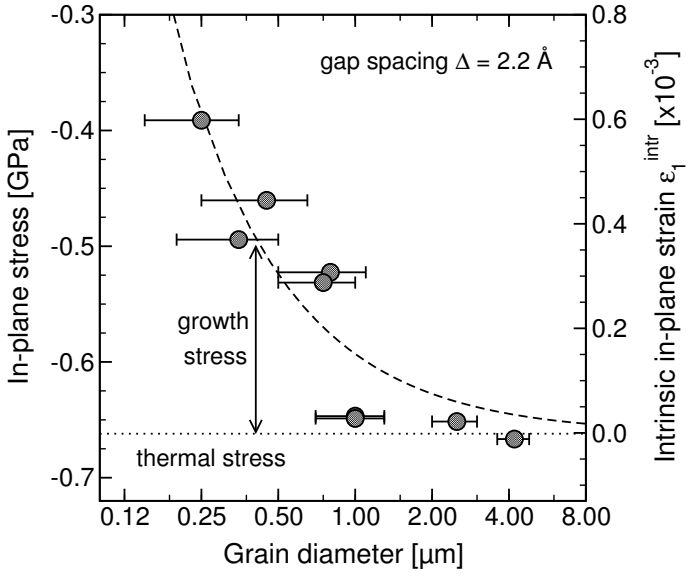

Figure 4.19: In-plane stress and intrinsic strain in the GaN layers in dependence on the grain diameter. The dashed line is the theoretically expected sum of intrinsic and extrinsic stress assuming an average gap size of 2.2 Å.

For large grain diameters an asymptotic behavior is observed, approaching the value of the thermal stress. The curve obtained from the model discussed in the previous section is plotted in Fig. 4.19 as well. For this fit, the thermal stress determined in Eqn. 4.16 and the intrinsic stress from Eqn. 4.15 were used :

$$\sigma_1^{\mathrm{tot}}(d_0) = \sigma_1^{\mathrm{extr}} + \sigma_1^{\mathrm{intr}}(d_0) = -0.66\,\mathrm{GPa} + 307.1\,\mathrm{GPa} \times \frac{\Delta}{d_0} \tag{4.17}$$

For the least-squares fit, the gap width was the only variable parameter, which was determined to $\Delta = (2.2 \pm 1.0)$ Å. This value is below the length of the Burgers vector of the edge type TDs, which accumulate along the grain boundaries in GaN layers [173]. Furthermore, it fits to the discussion in Section 4.3.2 as it is smaller than the lattice parameter a. The average intrinsic strain for the respective grain diameter is also visible in Fig. 4.17.

Since the intrinsic, tensile strain is assumed to be highest in the region of the coalescence boundaries, the strain distribution in the film should be inhomogeneous across the layer as sketched in Fig. 4.20. Close to the sapphire interface, the local strain strongly varies with position, whereas it is more homogeneous at the film surface. This local variation of strain is called heterogeneous or micro-strain. The magnitude of the heterogeneous strain in a sample can be estimated from a Williamson-Hall plot, which analyzes

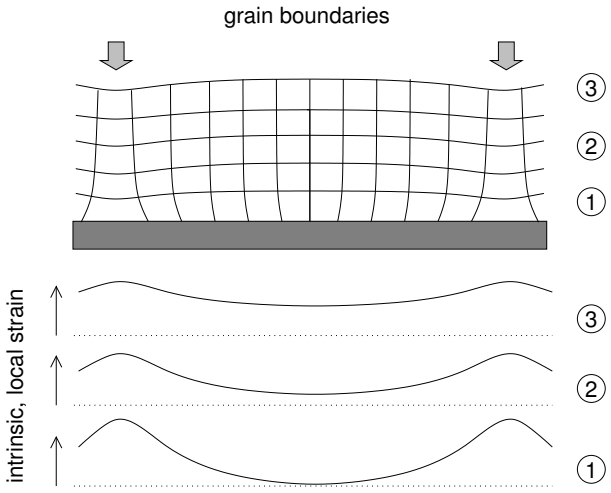

Figure 4.20: Heterogeneous strain due to the gap closure process.

the 2θ-broadening of the symmetric **00*l*** reflections. This plot is depicted in Fig. 4.21(a) for three layers of different thickness, which were grown under identical conditions, i.e. whose coalescence thickness of 700 nm was the same. In reciprocal space, the finite size broadening along q_z is constant for all reflections and follows the reciprocal film thickness according to the Scherrer equation, whereas the heterogeneous strain broadening linearly increases with q_z due to the local variation in the c-axis lattice constant. Therefore, the slope of the linear fit of the broadening yields the heterogeneous strain and the y-axis offset provides the broadening arising from from the vertical coherence length [153].

For film thicknesses close to the average grain diameter, the heterogeneous strain should be on the order of the intrinsic strain, as the center of the grains is less distorted than the grain boundary regions. Films that are much thicker than the coalescence thickness can elastically smooth out the strain variations, therefore the heterogeneous strain should roughly follow the inverse film thickness. This is seen in Fig. 4.21(b), where the heterogeneous strain of the three samples is plotted against the film thickness. As expected from the strain distribution described above, the heterogeneous strain decreases with the film thickness and is roughly proportional to the ratio of grain diameter and film thickness. The dashed line is the expected thickness dependence assuming the grain diameter of 700 nm and the heterogeneous strain just after coalescence to be equal to the intrinsic strain. For this grain diameter the latter amounts to $\varepsilon_{\perp}^{\mathrm{intr}}=2.1\times10^{-4}$, which is on the same order as the experimentally observed heterogeneous strain in the thinnest film (compare Fig. 4.19). This finding supports that the tensile strain during growth develops as a result of island coalescence.

4.3.4 Verification by temperature-dependent XRD

The various strain components in a heteroepitaxial film can be directly accessed by temperature-dependent X-ray diffraction. The variation of the temperature allows to control the external strain in the layer. From the comparison of the strained material to nominally unstrained reference material one can then separate the strain components. The reference values used for heteroepitaxial GaN are the lattice parameters published

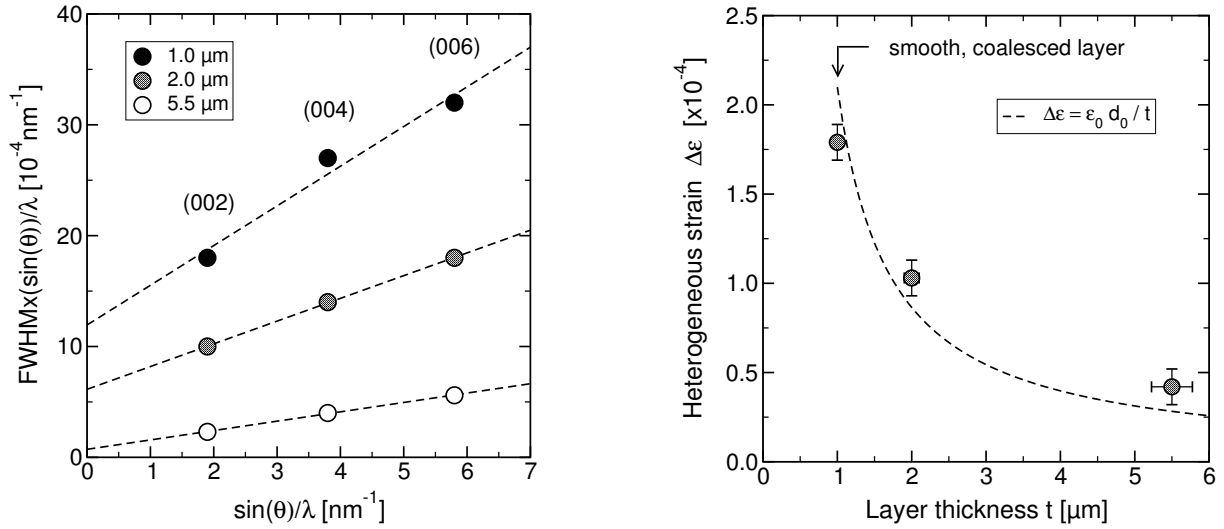

(a) Williamson-Hall plot

(b) Thickness dependence

Figure 4.21: The heterogeneous strain in GaN films with equal grain diameter, but varying thickness. The dashed line in (b) describes the expected decay of the heterogeneous strain for this grain diameter. Data measured by R.Chierchia, University of Bremen.

by Leszczynski *et al.* [60] and the semiempirical model for the thermal expansion of GaN published by Wang and Reeber [61].

The principle is sketched in Fig. 4.22 for GaN. The strain components, which can be distinguished, are the extrinsic thermal, the intrinsic hydrostatic and the intrinsic growth strain. For GaN, the latter would be the biaxial, tensile strain originating from the HT island coalescence. As seen Fig. 4.22 (a), the variation in temperature varies the biaxial, thermal strain in the layer, therefore the c/a-ratio of the unit cell changes. The sapphire expands faster than the GaN unit cell with increasing temperature, and accordingly the c/a-ratio drops. From the comparison to the reference material, the temperature T_0 is obtained, at which biaxial thermal and biaxial growth strain compensate each other, and the hydrostatic strain is the only component distorting the unit cell. Knowing the hydrostatic component, the growth strain component is extracted from the strain state at growth temperature as illustrated in Fig. 4.22 (b). Based on the assumption of a temperature-independent hydrostatic strain, the difference of the measured and the hydrostatic strain yields the growth strain, since the extrinsic, thermal strain is zero at the growth temperature. Finally, the thermal strain at room temperature is known, because the other two intrinsic components are independent of temperature. Accordingly, the strain at room temperature can be corrected for the growth and the hydrostatic strain.

The described experiment was performed by R. Chierchia using a temperature-controlled sample holder mounted in a high-resolution x-ray diffractometer. The accessible temperatures range from room temperature to 1250°C, which would allow to measure

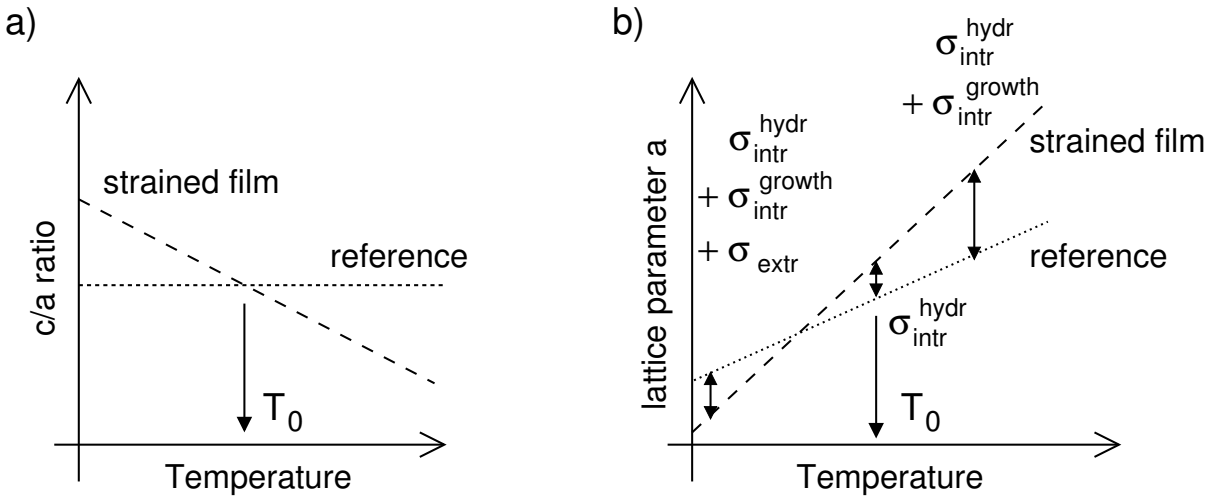

Figure 4.22: The separation of the strain components utilizing temperature dependent XRD.

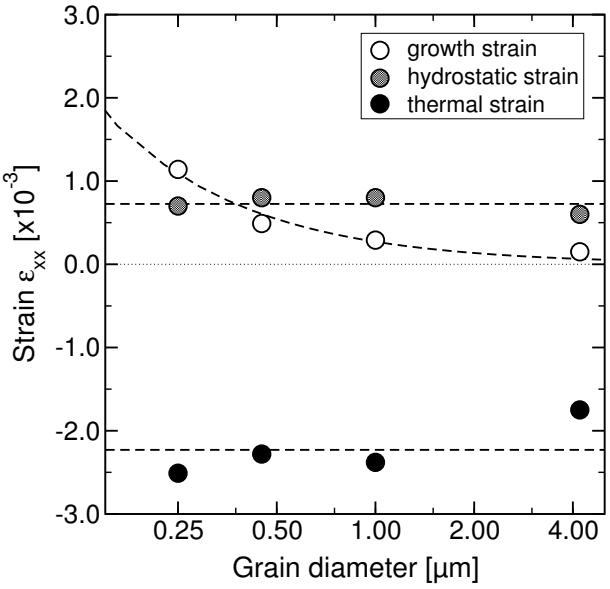

Figure 4.23: The separated strain components for layers of different grain diameter. Data measured by R. Chierchia, University of Bremen.

at the growth temperature. However, to avoid the decomposition of the GaN film, the temperatures were restricted to a maximum of 750°C and the lattice constants were extrapolated to the growth temperature of 1050°C. The measurements were done for four samples with grain diameters between 0.25 μm and 4.2 μm. The extracted strain components of the four samples are plotted in Fig. 4.23 in dependence of the grain diameter. It can be seen, that the extrinsic thermal and the intrinsic hydrostatic strain components are constant, whereas the intrinsic growth strain drops with the inverse grain diameter. Besides the compressive thermal strain one finds the two intrinsic strain components to be tensile. This is in accordance with the measurements done at room temperature and supports the model of tension due to high temperature island coalescence.

4.4 Formation of thermally induced stress

As discussed before, GaN grown on sapphire by MOVPE is under tension at growth temperature, depending on the used set of growth parameters. However, at room temperature the strain is compressive due to the compensation by the larger thermal compressice strain. In order to demonstrate this build-up of thermal compressive strain and its relation to the film coalescence, films with different thicknesses and correspondingly different stages of coalescence were compared [1]. The same growth process yielding a coalescence thickness of ∼700 nm was used for all samples and interrupted at different stages of the growth. The process was a compromise of a late coalescence and a fast epilayer growth, as the HT growth start was performed at 700 Torr to provide widely spaced islands and then the growth was continued at 150 Torr to increase the growth rate. The change was done after a nominal deposition of 140 nm GaN at 700 Torr. Five samples were grown with intended epilayer thicknesses of 0.14 μm (A), 0.5 μm (B), 1.0 μm (C), 2.0 μm (D) and 5.6 μm (E).

The reflectance transient of sample E is depicted in Fig. 4.24. The transients of the other samples were almost identical and can be deduced from the indicated marks in the graph. The first rise in the reflectance is the deposition of the NL with a nominal thickness of ∼25 nm, followed by the recrystallization. After starting with the HT epilayer growth the reflectance drops to zero indicating a significant surface roughening. After the deposition of nominally 300 nm the signal rises again due to the proceeding film coalescence and intensity oscillations due to interference occur after a thickness of roughly 500 nm. At ∼1 μm the oscillation starts to become constant in amplitude indicating two-dimensional growth. The different stages of the growth are illustrated by the AFM images in Fig. 4.24. Sample A shows the state directly after the initial 700 Torr growth step, where the islands are separated from each other and of unequal height. This indicates that only few nucleation sites were provided by the recrystallized NL. After the deposition of 500 nm of GaN (sample (B)) the islands start to coalesce and overgrow each other, beginning to level out the height differences, and at 1 μm a compact layer is obtained (C). Further growth decreases the roughness and provides a smooth surface with monoatomic steps (E).

[1] This study was done in collaboration with S.Einfeldt and S.Figge. The data was published in Ref. [174]

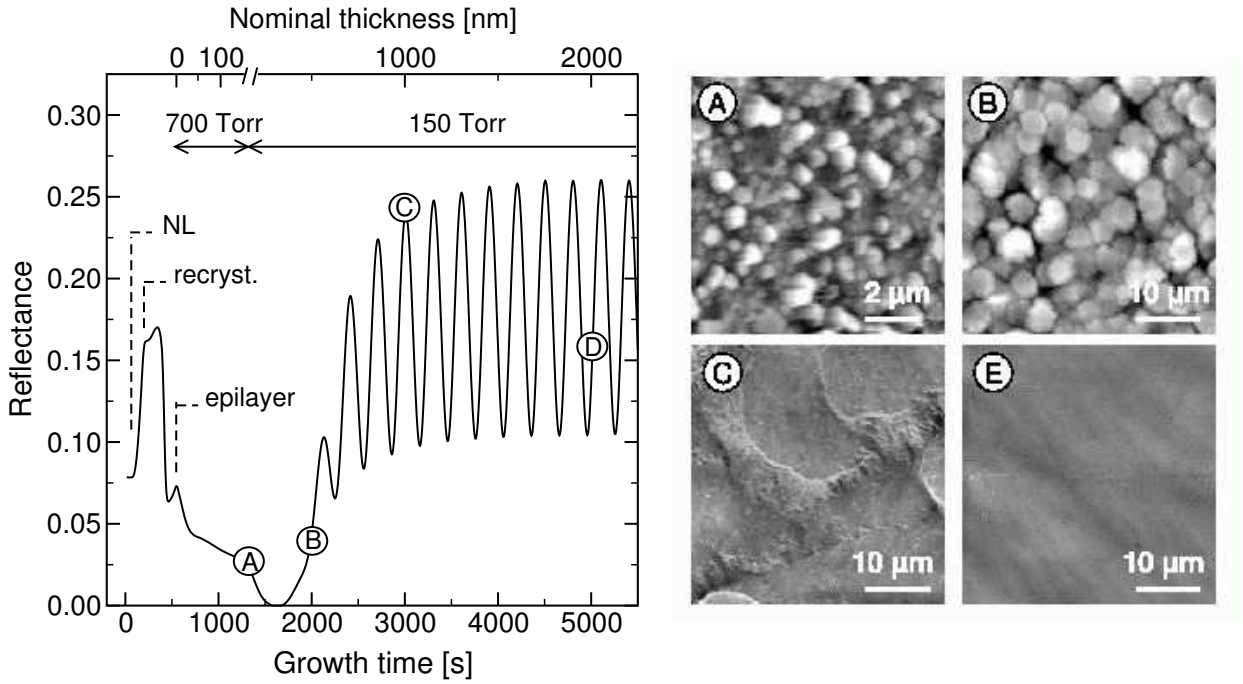

Figure 4.24: The reflectance transient of a GaN layer (left) and AFM images corresponding to different stages of growth (right) as marked.

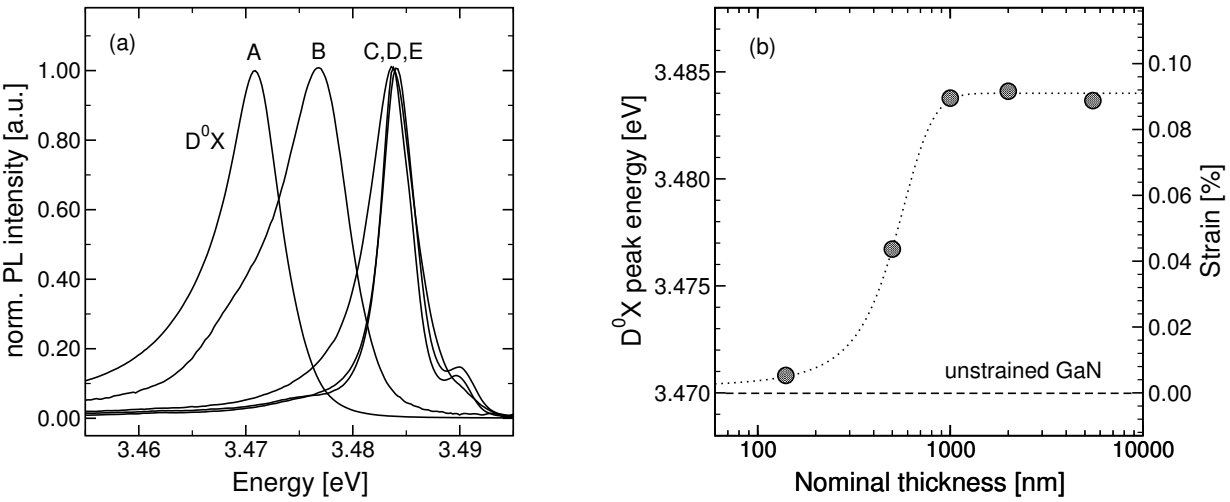

Figure 4.25: The change of strain upon coalescence. a) PL spectra taken at 4 K. b) The strain as extracted from the peak position in dependence on the layer thickness.

The relation of film coalescence and biaxial, thermal stress after growth can be directly observed in the photoluminescence (PL) of the samples. The PL spectra taken at 4 K are shown in Fig. 4.25 (a). The dominant feature of all spectra is the recombination of excitons bound to neutral donors (D^0X). As the energetic position of this peak closely follows the deformation of the unit cell, it is a good measure for the average strain in the layer. Biaxial compressive strain causes a blueshift of the peak, whereas tension results in a redshift. The strain ε_{zz} can then be calculated using the deformation potentials for GaN, which link the strain of the unit cell to the energetic shift of the exciton line [160, 175]. In the following, a deformation potential of 15.4 eV was used as described in Ref. [160]. The D^0X peak positions of all samples in dependence on their thickness is plotted in Fig. 4.25 (b). It can be seen that the peak shifts to higher energies with the thickness as long as the film is not compact. For thicknesses exceeding 1 μm, the peak position remains constant. Sample A has a peak position of 3.471 eV which is very close to the value of epitaxial GaN films grown on GaN bulk crystals [176]. Thus, the thermally induced strain for this uncoalesced film can be assumed to be very small. As the coalescence proceeds, the compressive strain increases approximately linearly until the maximum strain is reached for sample C, where the coalescence process is complete. The compact layers C, D and E exhibit the same D^0X peak energy of 3.484 eV, according to a c-axis strain of $\varepsilon_{zz} = 8.4 \times 10^{-4}$. It should be stressed that the strain is constant for those layers and is *not* relieved with increasing thickness.

The increase of the thermally induced strain with coalescence is explained by the possibility of the individual islands to elastically relax via their free surfaces. In uncoalesced films, the islands are small enough to allow the unit cell to assume the shape of almost unstrained GaN, yielding the D^0X peak position of 3.471 eV. Remaining local stresses are then compensated by a deformation of the substrate in this region. For compact layers this relaxation mechanism is no longer possible, causing the increased biaxial, compressive strain which is independent of the thickness. The only way to elastically relieve strain in this case is to bend the whole substrate [177]. This might be the case for sample E, where the D^0X peak energy is a little lower. However, this small deviation is within the accuracy of the measurement.

Chapter 5

InGaN quantum wells

This chapter will treat $In_xGa_{1-x}N$-based multiple quantum wells (MQWs), which are used in the active region of light-emitting devices. Besides the growth of these structures, the photoluminescence will be discussed and compared to numerical simulations.

5.1 Growth by molecular beam epitaxy

The main subject of this thesis is the growth of the group-III nitrides and related structures utilizing MOVPE. A second technique capable of growing structures of high structural perfection is molecular beam epitaxy (MBE), which was applied to produce InGaN-based quantum-well structures.

5.1.1 Growth parameter

The growth by MBE is based on different boundary conditions compared to MOVPE, as the growth is performed far away from the thermodynamic equilibrium. For example, it puts a limit on the maximum growth temperature, which is around 850°C. The advantage of MBE is the well-defined growth process, which gives the possibility to treat the growth kinetics numerically. Most of this theoretical work has been published by Neugebauer *et al.* and Northrup *et al.* (see [13, 178, 179] and references therein). Accordingly, the growth process itself is better understood in comparison to MOVPE.

One of most relevant growth parameters for the MBE of the group-III nitrides is the flux ratio of gallium and nitrogen. These are determined via the beam equivalent pressure (BEP), as obtained from the beam flux monitor. To extract the atomic flux, the BEP has to be corrected for the atomic mass of the actual element [80]. Fig. 5.1 contains a cross-section TEM image of a multilayer structure, where the individual layers were grown under decreasing Ga/N flux ratio. In order to be able to see the sections in TEM, they are separated by thin layers of $Al_xGa_{1-x}N$, which has a lower scattering contrast compared to GaN. The growth temperature of the multilayer sequence was 650°C, since this was the common growth temperature of the quantum well region. As long as the growth is performed under Ga-rich conditions, no additional defects are formed, but as soon as the growth is performed N-rich, the formation of stacking faults is ob-

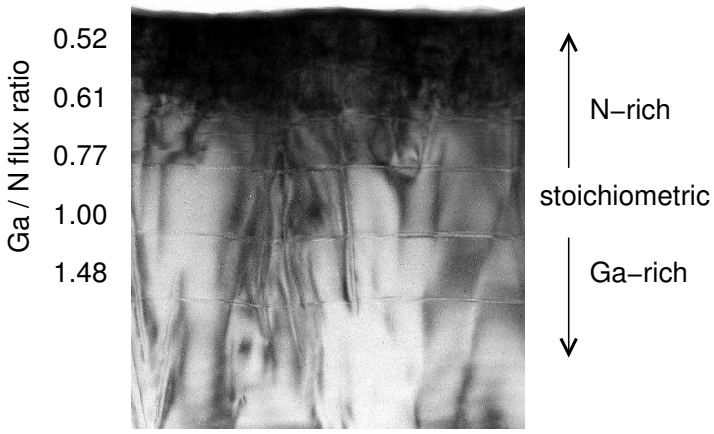

Figure 5.1: Cross-section TEM image of a multilayer structure with varying Ga/N flux ratio. The growth temperature was 650°C and the Ga/N ratio was varied by adjusting the N-flux. Image taken by H.Selke, University of Bremen.

served. This is in accordance with the results reported by Tarsa *et al.*, who investigated the growth on MOVPE-grown GaN templates [180]. Although the polarity is different in this case, the formation mechanism is probably similar. The reduced surface mobility of the Ga adatoms under N-rich conditions raises the probability of the Ga atoms to be incorporated on a *fcc* site, which would be the nucleation center of a stacking fault. Accordingly, the stacking fault density increases with lower Ga/N ratio, as seen in Fig. 5.1. Compared to the study of Tarsa *et al.*, which was performed on Ga-polar material, the transition seems to happen not as abrupt for the N-polar surface investigated here [180]. This might be explained by the lower diffusion barrier for Ga adatoms on the N-polar surface, which provides a higher Ga diffusion length compared to the Ga-polar surface even under N-rich conditions [13]. Changing from Ga-rich to N-rich growth conditions, the diffusion barrier was predicted to rise from 0.6 to 1.8 eV for the (0001) surface, while it increases from 0.2 to 1.0 eV for the $(000\bar{1})$ surface [13]. The lower diffusion barrier of the N-polar surface delays the stacking fault formation, but does not suppress it as seen is Fig. 5.1. Therefore, stacking faults can only be avoided under Ga- or group-III-rich growth conditions.

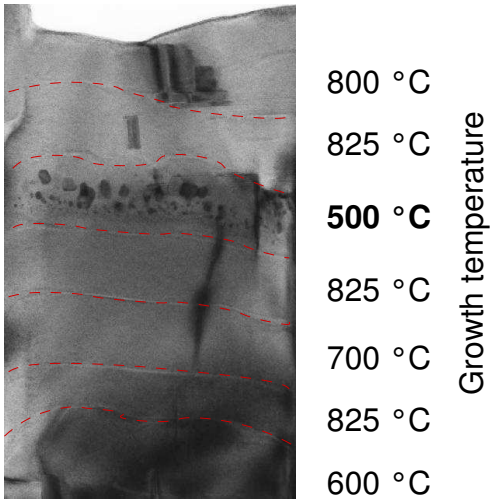

Figure 5.2: Cross-section TEM image of a multilayer structure, where the growth temperature was varied. Image taken by H.Selke, University of Bremen.

The second growth parameter influencing the surface diffusion is the growth temperature, since it provides the kinetic energy for the surface diffusion. The change of the

microstructure with growth temperature is depicted in Fig. 5.2, which contains a cross-section TEM image of a multilayer stack of layers grown at different temperatures. The polarity of this film is $(000\bar{1})$ due to the direct deposition onto sapphire. The growth conditions were kept in the Ga-rich regime for all layers, such that the formation of stacking faults is suppressed as far as possible. Only at very low temperatures of $\sim$500°C, large cubic inclusions are observed. Presumably, two effects are responsible for this - on the one hand, the cubic phase is stabilized at low temperatures, and on the other hand, the low surface mobility of the atoms enhances the formation of stacking faults, which act as nucleation centers for cubic material. Thus, low temperatures of $\sim$600°C are possible for MBE without the formation of extended defects, as long as the growth is performed in the Ga-rich regime. To obtain a smooth surface, the growth temperature should be chosen as high as possible.

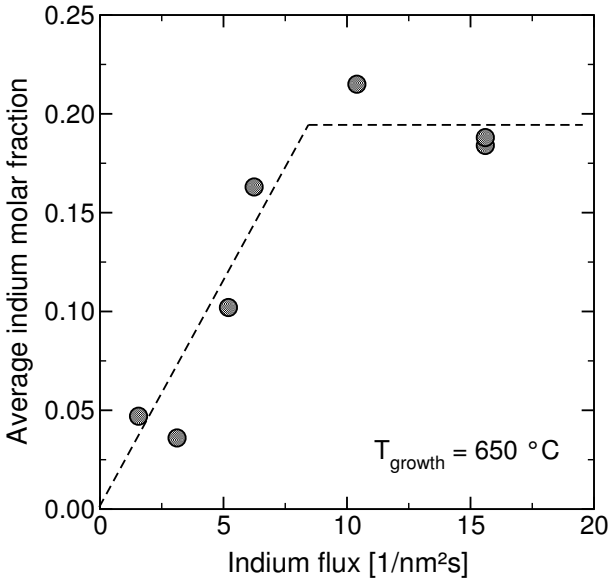

Figure 5.3: The indium molar fraction in the solid in dependence on the impingent In flux. The fluxes of Ga and N were kept constant [181].

An aspect essential for the growth of the ternary $In_xGa_{1-x}N$ is the ratio of the individual atomic fluxes [181, 182]. The main aspect is illustrated in Fig. 5.3, which contains the indium molar fraction in 600 nm thick $In_xGa_{1-x}N$ films deposited on [0001] sapphire. For all samples the growth parameters except for the indium flux were kept constant, i.e. the growth temperature was 650°C, and the Ga and N fluxes were 6.5 $nm^{-2}s^{-1}$ and 8.3 $nm^{-2}s^{-1}$, respectively. The In flux was varied between 1.6 and 16 $nm^{-2}s^{-1}$. The composition was then determined from high-resolution x-ray diffraction as described in Section 2.4.4. For low In fluxes the In molar fraction in the film increases linearly as expected, where the slope corresponds to an In sticking coefficient of $s_{In} = 0.16$, caused by the low binding energy of InN [75]. In contrast to this, the Ga sticking coefficient can be assumed to be unity at the chosen growth temperature, since the N flux exceeds the Ga flux and the decomposition of GaN in vacuum starts at 830°C [75]. Consequently, for In fluxes above 8.3 $nm^{-2}s^{-1}$, the In molar fraction is limited to a value of $x_{In} \sim 0.2$ (see Fig. 5.3), as higher In contents would require the formation of InN bonds in expense of GaN bonds. This again is unlikely to occur due to the low stability of the In-N bond.

Thus, the maximum possible In content is defined by the difference of N and Ga flux as

$$x_{\max} = 1 - \frac{f_{Ga}}{f_N}. \tag{5.1}$$

Eqn. 5.1 requires the Ga flux to be lower than the N flux during the MBE of $In_xGa_{1-x}N$ in order to incorporate any indium. The effect was first presented by Riechert *et al.*, who later extended the findings into a quantitative model for the ternary nitrides [183, 184].

To summarize, the MBE growth for high-quality $In_xGa_{1-x}N$ is subject to the following boundary conditions :

- the group-III flux has to exceed the nitrogen flux
- the Ga flux has to be below the nitrogen flux
- the growth temperature should be as high as possible

This implies, that during growth of multi-quantum-well structures the conditions for GaN barrier and $In_xGa_{1-x}N$ well differ significantly. While the barrier growth requires $f_{Ga} > f_N$, the growth of the well needs the opposite, namely $f_N > f_{Ga}$. This can either be accomplished by using two Ga sources or by the variation of the N flux. As the MBE system in Bremen provides only one Ga source, the latter approach was chosen. The required changes in the nitrogen flux were realized by changing the RF power supplied to the plasma source. In order to ensure reproducible conditions, the RF generator was controlled via the computer within the growth recipe.

The growth temperature should be as high as possible to enhance the surface mobility of adsorbed atoms, but is limited by the intended indium content of the film. As a higher growth temperature enhances the desorption of indium from the surface, it also reduces the incorporation of indium into the film and limits the maximum indium content for a given incident flux [184]. Typical deposition temperatures are in the range of 650 to 680°C.

5.1.2 Surface cleaning

For the epitaxy onto GaN templates, for example grown by MOVPE, it is necessary to prepare a clean surface prior to growth. This arises from the contamination of the surface with organic substances and from the formation of a surface oxide, when the material is in contact with air. To remove the organics, the templates are successively cleaned in the solvents Trichloroethylene, Acetone and Methanol, each time for 5 min in an ultrasonic bath or in boiling solvent. Finally, the sample is rinsed in deionized water. This a very common sequence for the preparation of substrates, which has been successfully applied to several materials. Inside the vacuum system but outside the growth chamber, the template is degassed for one hour at 600°C on a separate degas station.

Compared to the untreated template, this thermal annealing step already removes part of the surface oxide as shown by x-ray photoelectron spectroscopy (XPS) analyzing

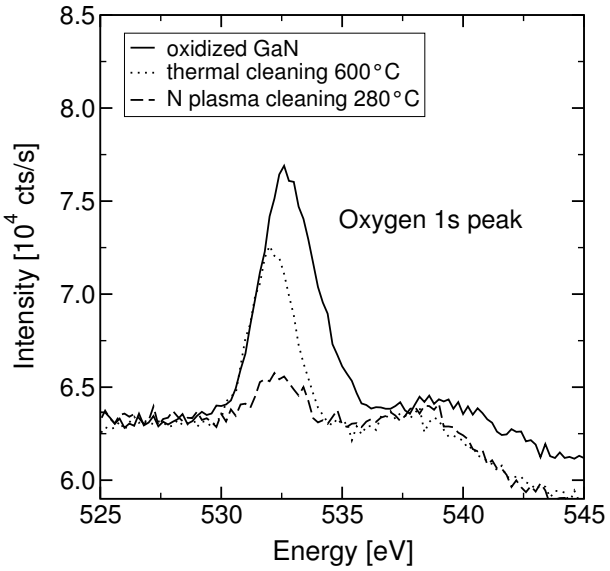

Figure 5.4: XPS spectra of the oxygen 1s peak for a GaN film after different surface treatments.

the oxygen *1s* peak. These spectra are depicted in Fig. 5.4 for one GaN layer after different treatment steps. The initial state after the solvent cleaning reveals a strong oxygen signal, caused by the surface oxidation in air. After the thermal cleaning, the signal already decreased by ∼30%, but did not vanish. Most of the remaining oxide is removed by a nitrogen plasma treatment performed at low temperature, as shown in Fig. 5.4 as well. The GaN was exposed to a nitrogen plasma (300 W, F_{N2}=1.3 sccm) in the growth chamber for 30 min at 280°C. The low temperature is necessary to avoid the roughening of the surface, which happens at higher temperatures. The sequence of these three steps has become the standard preparation procedure for the quasi-homoepitaxy on GaN templates.

5.1.3 Quantum well structures grown on different templates

This section will discuss the properties of similar multiple quantum-well structures grown by MBE onto different template layers, under the conditions as described before [1]. Compared will be a structure grown on an atomically smooth GaN template layer produced by MOVPE and a similar structure deposited directly on sapphire using MBE only. The samples contain three $In_xGa_{1-x}N$ quantum wells separated by undoped GaN barriers, with an indium content in the well of approximately 12 %. The quantum wells were grown on GaN of ∼1200 nm thickness and were capped by a 50 nm thick GaN layer. As a reference, a fully MOVPE-grown structure will be used. The precise values are listed in Table 5.1. The thicknesses given for the first two samples are intended thicknesses, i.e. they are based on previous growth rate calibrations and the growth time. The MOVPE sample is part of a quantum-well thickness series, where the individual thicknesses should be more accurate.

[1] Part of this section is published in [185].

Structure	Template	Well thickness	Barrier thickness	In content
3× MQW, MBE	MBE	2.4 nm	6.4 nm	14.1±0.5 %
3× MQW, MBE	MOVPE	2.7 nm	6.8 nm	11.5±0.5 %
10× MQW, MOVPE	MOVPE	2.4 nm	6.2 nm	10.0±0.4 %

Table 5.1: The structure of the MQWs used for comparison.

Structural analysis

Fig. 5.5 shows the 2θ-ω scans of the **002** reflections obtained by high-resolution X-ray diffraction (HRXRD) using an analyzer crystal in front of the detector. Both samples show clear peaks of the GaN bulk layer and the InGaN MQW region superimposed by thickness interference fringes. The fine structure is caused by reflections between surface and MQW region, giving a distance of 65±5 nm, whereas the broader envelope structure originates from the periodicity of the MQW region. The two satellite peaks of the MQW are labeled, corresponding to a period of 9.5±0.5 nm for the structure grown on the MOVPE template and 8.8±0.5 nm for the fully MBE-grown sample.

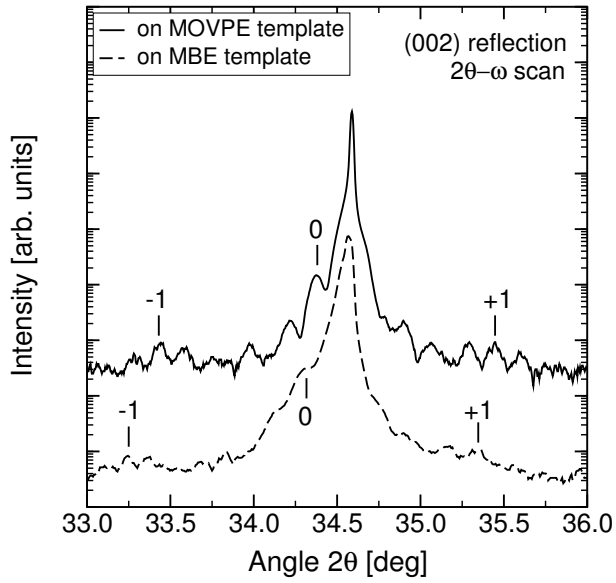

Figure 5.5: 2θ-ω scans of the **002** reflections for MQW structures grown on MBE and MOVPE templates.

First, the interference fringes are significantly more pronounced for the MQW grown on the MOVPE template. Thus, the interface flatness, the homogeneity of the indium content and/or of the strain state in the well region is suggested to be superior for this sample compared to the fully MBE grown structure. Nevertheless, HRXRD reciprocal space mappings for the **105** reflections of GaN and $In_xGa_{1-x}N$ revealed the wells to be pseudomorphic in both cases. The FWHM values of the ω-scans for both the GaN **002** and **302** reflections, which are not shown here, are surprisingly similar for both samples. At first sight this should be attributed to a comparable density of extended defects.

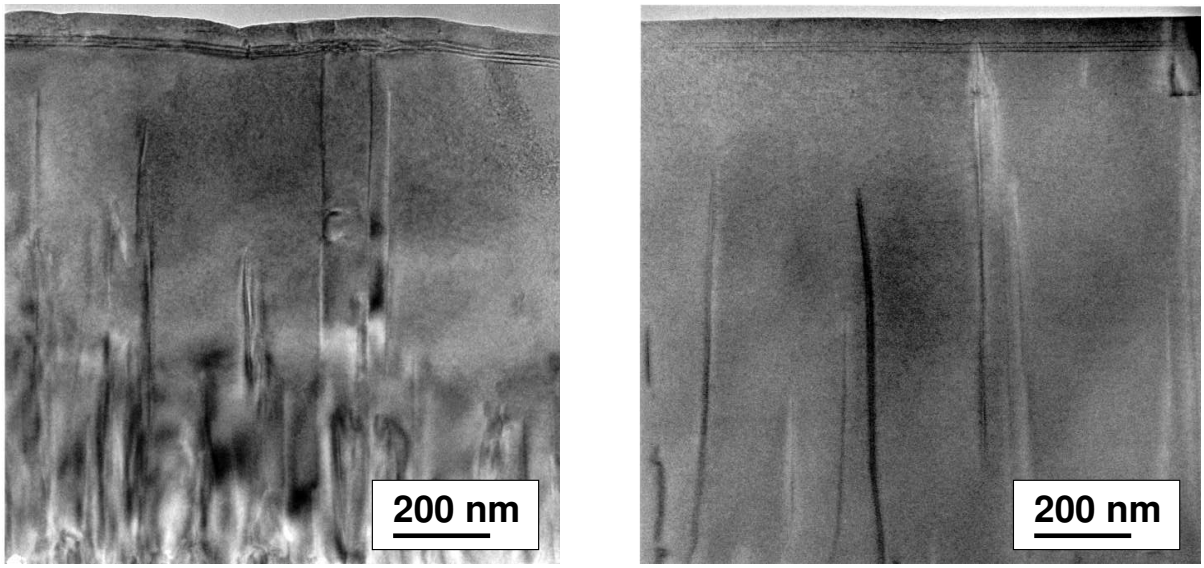

(a) MQW grown on MBE template

(b) MQW grown on MOVPE template

Figure 5.6: Cross-section TEM images of MBE-grown quantum well structures deposited on different templates. Image taken by H.Selke, University of Bremen.

This is evident from the cross-section TEM images displayed in Fig. 5.6. The bulk volume of the layers, which governs the broadening of the diffraction peaks, shows similar dislocation densities in both samples. Significant differences are found for the surface structures, which are also visible in atomic force microscopy (not shown). While the MOVPE template is smooth even after overgrowth by MBE, the fully MBE-grown structure exhibits a high surface roughness by far exceeding the atomic scale. Typical root-mean-square (*rms*) values are 0.9 nm for the overgrown MOVPE layers and 9 nm for the MBE templates. This is typical for MBE-material directly grown on sapphire, even for samples of low threading dislocation density. It is problematic, since the quantum wells themself are distorted by this surface morphology. For the structure on the MOVPE template, the interface between MBE- and MOVPE-grown part is still slightly visible. It is probably caused by the special treatment of this template, which was cutted prior to the growth using a diamond saw. During this procedure, the surface was heavily contaminated. In more recent, cleaved samples, the interface is mostly invisible, indicating the efficient cleaning procedure.

Luminescence

Photoluminescence spectra of the discussed samples are displayed in Fig. 5.7. Compared are the two MBE-grown structures and the MOVPE-grown sample used as a reference. The latter is a sample from the undoped thickness series, which will be discussed later in this chapter in Section 5.4. In addition to the experimental data, the

theoretically expected emission energies from these wells is shown, as indicated by arrows. These theoretical values were generated with the program 1DPoisson [2], which is described in more detail in Section 5.3.2 and Appendix C. The program numerically solves Poisson´s and Schrödinger´s equation for a given semiconductor heterostructure. For quantum wells, it can provide the wavefunctions and the energy levels of the localized states. The theoretical emission energy is then given by the lowest energy difference of the electron and the hole states. All spectra are redshifted with respect to the theoretically expected peak energies, which can be caused by local fluctuations of the thickness, the strain or the composition. All those effects cause a Stokes-like redshift of the emission energy relative to the absorption. For this set of samples, it is unclear, which of these is the main origin. Since the MBE of $In_xGa_{1-x}N$ has to be performed at low temperatures, the spiral growth mode is enhanced and the surface mobility of adsorbed atoms is reduced. The former causes thickness fluctuations and the latter might cause compositional fluctuations.

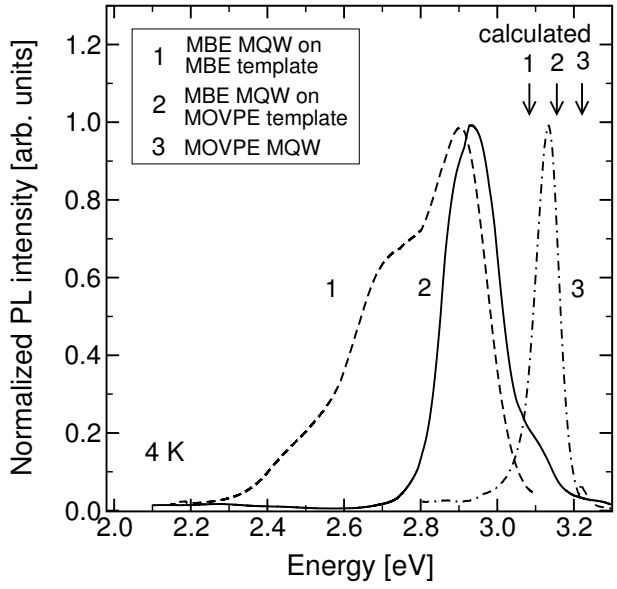

Figure 5.7: Low-temperature photoluminescence spectra of the quantum-well structures under discussion. Compared are the spectra of the MBE-grown samples on different templates and a fully MOVPE-grown structure.

The impact of the inferior structural quality of the fully MBE-grown sample is directly seen in the fact, that its spectrum in Fig. 5.7 is broadened compared to the spectra of the other samples. The broadening far exceeds the expected effect due to the slight difference in composition. Furthermore, the emission shows a pronounced tail with two shoulders at approx. 150 meV and 400 meV below the main peak. Therefore, it is reasonable to assume that the tail does not mainly originate from compositional or thickness fluctuations. It could be caused by defect-related emission with fixed energy levels or simply be the superposition of quantum wells of defined, but different width. The former assignment also fits to commonly observed defect related luminescence in GaN, which peaks with a similar energy offset relative to the band gap [186]. The luminescence of the MBE-grown MQW on the MOVPE template exhibits no additional emission on the low energy side, although the growth conditions of the well regions

[2] programmed by G.L. Snyder, University of Notre Dame, e-mail: snider.7@nd.edu

were almost identical and the densities of extended defects are similar. Consequently, the type of defect responsible for the deep emission in the fully MBE-grown structure remains unclear at this stage. Nevertheless, although the PL of the sample grown on the MOVPE template is narrower than that of the sample completely grown by MBE, its FWHM still exceeds that of the pure MOVPE structure by a factor of three. To some extent, this difference could be reduced by further growth optimization, i.e. paying attention to the stability of the temperature and to the growth interruptions. The lowest FWHM obtained for MBE-grown quantum wells was 90 meV at a peak emission of 2.9 eV, which is just average for MOVPE.

Spatially resolved cathodoluminescence (CL) measurements exhibit fluctuations in intensity and spectral distribution of the luminescence on a typical lateral length scale of $\sim$1 μm for both discussed MBE samples. Wavelength and intensity mappings together with local spectra and a histogram of the local peak emission energies are depicted in Fig. 5.8. While the MQW grown on the MOVPE template is marked by a single peak, at least two peaks of varying intensity can be distinguished in the spectra of the fully MBE-grown structure. The energetically lower one might be attributed to defect related transitions as already discussed above for the photoluminescence. From a more qualitative point of view, the sample grown on the MOVPE template shows similar features in CL like typical MOVPE structures [187]. The spatial variation of intensity and wavelength is not abrupt and the local emission spectra are governed by one dominant peak. The statistical analysis of the local peak position also shown in Fig. 5.8 yields a typical variation of 40 meV and $\sim$90 meV for the MQW grown on MOVPE and MBE template, respectively. Using these values as a figure of merit for fluctuations of the local indium content, the local strain state and the quantum-well thickness, a superior homogeneity is evident for the growth on MOVPE templates.

5.1.4 Summary

Due to the low number of samples, it is presumptuous to speculate on the origin of the differences between MBE- and MOVPE-grown quantum-well structures. However, it was possible to demonstrate the improvement of the structural perfection and the photoluminescence spectra with the use of MOVPE-grown templates. For sure, this is related to the superior surface smoothness of these templates, but it might possible as well, that the different polarity contributes to the improvement. This could be verified by utilizing MOVPE-grown GaN templates, whose polarity was inverted by an interlayer of magnesium [188]. This should provide a smooth, N-polar film, which allows to perform comparative studies of polarity-related effects during growth of $In_xGa_{1-x}N$-based quantum wells.

Although the studies described at the beginning of this section resulted in a reproducible procedure for surface preparation, the homoepitaxy by MBE still has to be optimized. In particular, the occurrence of large pits in the grown material has to be avoided, since closed, smooth films are the basis of all more advanced studies. Currently, this can only be prevented by using indium as a surfactant. In order to grow more complicated structures, the surfactant-free growth should be understood in more detail.

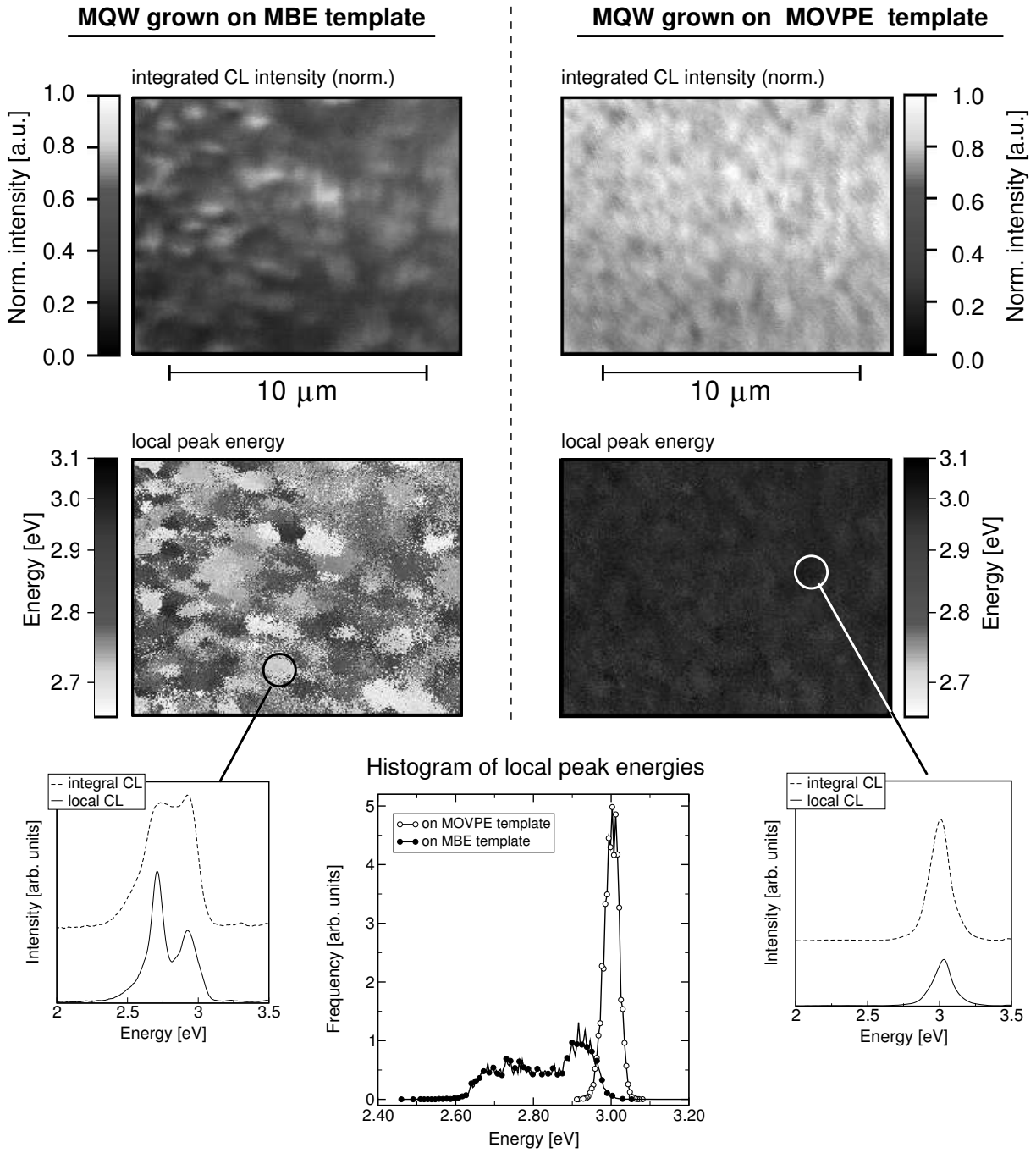

Figure 5.8: Comparative cathodoluminescence analysis of the MBE-grown quantum wells. Shown are the mappings of the local intensity and the local peak wavelength. Below the mappings the integrated and representative local spectra are displayed together with the histogram of the local peak energies. Data acquired by F. Bertram, University of Magdeburg, Germany.

5.2 Growth by MOVPE

The MOVPE of $In_xGa_{1-x}N$ is hampered as well by the low stability of the In-N bond. Desorption experiments under vacuum showed the decomposition of InN to start at 630°C compared to 850°C for GaN [75]. It requires the growth conditions of $In_xGa_{1-x}N$ to differ significantly from the established parameter set used for GaN.

5.2.1 Thermodynamics

The aspects to be considered in the design of the growth process for $In_xGa_{1-x}N$ can best be estimated from the equilibrium equations for the formation of InN and GaN using the equilibrium constants from Table 3.1. For a temperature of 1050°C these equations are :

$$K_{InN} = \frac{a(InN)\,p(H_2)^{3/2}}{p(NH_3)p(In)} = 274 \qquad K_{GaN} = \frac{a(GaN)\,p(H_2)^{3/2}}{p(NH_3)p(Ga)} = 3.8 \times 10^6 \tag{5.2}$$

First, at the common growth temperature of GaN, the stability of the InN compound is orders of magnitude below the stability of GaN. This means, the equilibrium state of the InN reaction is significantly shifted to the source side, namely, to gaseous indium and ammonia. Since decomposition is already important for the growth of GaN, as discussed in Section 3.1.3, it can be expected that the growth of $In_xGa_{1-x}N$ can not be performed at the normal growth temperature of 1050°C. Accordingly, the commonly used temperatures reported in literature are roughly 250 K below that of GaN. Most researchers report deposition temperatures in the range of 750 to 850°C [10, 189, 190].

The second important aspect of Eqn. 5.2 is the choice of the carrier gas for the deposition of $In_xGa_{1-x}N$. An increase in the hydrogen partial pressure forces the decomposition of InN, therefore, nitrogen should be used as the carrier gas. The deposition of $In_xGa_{1-x}N$ from the viewpoint of thermodynamics was discussed in more detail by Koukitu *et al.*, who concluded, that the incorporation of indium is hindered by the hydrogen partial pressure coming from the thermal decomposition of the ammonia [191]. Experimentally, the incorporation of indium into $In_xGa_{1-x}N$ was reported to be very sensitive to the partial pressure of hydrogen during growth [190]. Introducing a hydrogen flow of only 20 sccm into a total flow of ∼5 slm reduced the indium molar fraction from 0.12 to 0.05. Nevertheless, the deposition under hydrogen is possible, but the resulting material quality is inferior compared to $In_xGa_{1-x}N$ deposited with a nitrogen carrier.

5.2.2 Growth temperature

The probably most important parameter for the growth of $In_xGa_{1-x}N$ is the growth temperature. It allows one to control the composition as well as the growth rate, and determines the luminescence properties of corresponding quantum wells to a large extent.

The change of the growth rates of GaN and $In_xGa_{1-x}N$ with the temperature is depicted in Fig. 5.9. The growth rates were determined for $In_xGa_{1-x}N$/GaN MQWs grown

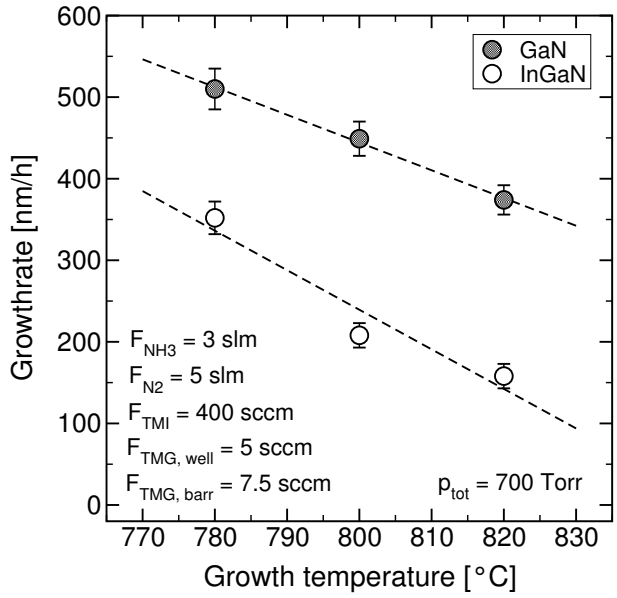

Figure 5.9: The growth rates of GaN and $In_xGa_{1-x}N$ versus growth temperature as determined by *in situ* reflectance and XRD. The dashed lines are least-square fits based on a linear relation.

at atmospheric pressure, where the thickness ratio of the wells and barriers was obtained from reflectometry. The period resulted from the MQW satellite peaks in XRD $\omega - 2\theta$-scans of the **002** reflection. If should be noted, that the TMG flows were different for the well and the barrier layers. With increasing temperature, both growth rates drop, indicating that either desorption or pre-reactions increase. As the TMG flows were small compared to the flows normally used during high-temperature deposition of GaN, the onset of desorption is probably observed. For the case of $In_xGa_{1-x}N$, the slope of the linear fit in Fig. 5.9 is higher, which underlines the destabilization of the surface due to the presence of indium. Besides the direct decomposition of InN at the surface, the indium atoms are also assumed to enhance the desorption probability of Ga atoms bonded to InN clusters.

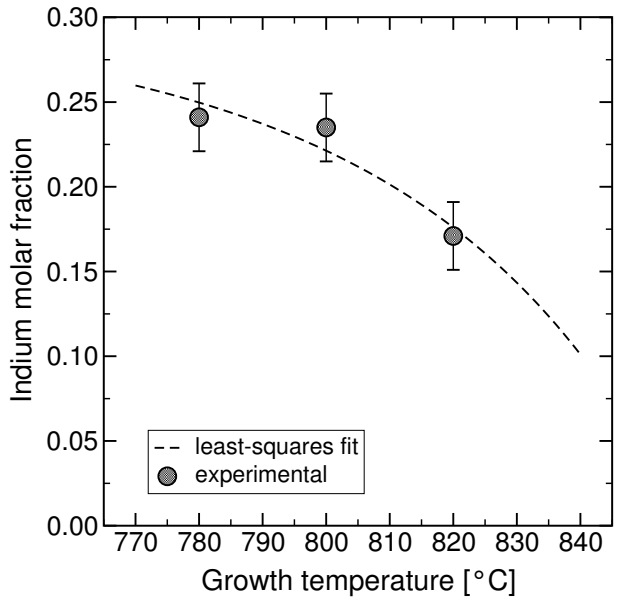

Figure 5.10: In molar fraction of $In_xGa_{1-x}N$ MQWs grown at different temperatures. The dashed line is a least-squares fit of Eqn. 5.3.

The loss of indium atoms from the growing surface directly affects the composition of the wells in the MQWs as seen in Fig. 5.10. With increasing growth temperature, the indium molar fraction decreases, which is in accordance with the enhanced In desorption rate. The dashed line in the graph was generated from the driving forces for the formation of GaN and InN. These are proportional to the deviation of the input partial pressures from their equilibrium values following the discussion in section 3.1.3. Correspondingly, the indium molar fraction x(In) is given by the input partial pressures p_0 and the equilibrium partial pressures p_{eq} [191] :

$$x(\mathrm{In}) = \frac{p_0(\mathrm{In}) - p_{eq}(\mathrm{In})}{(p_0(\mathrm{In}) - p_{eq}(\mathrm{In})) + (p_0(\mathrm{Ga}) - p_{eq}(\mathrm{Ga}))} \tag{5.3}$$

For the equilibrium pressures, the theoretical temperature dependence of the equilibrium constants was assumed (see Table 3.1 on page 45). The partial pressure of hydrogen was used as one fitting constant, and assumed to be independent of temperature. The second one was the ratio of the indium and gallium partial pressure, since the extent of pre-reactions and thermal desorption is unknown. The fit yields a reasonable description of the data within the experimental errors, and it is in accordance with data from literature, concerning the maximum possible growth temperature for indium incorporation [10].

Growth temperature	Well thickness	Barrier thickness	In content
780°C	5.1 nm	8.5 nm	0.24
800°C	3.0 nm	7.5 nm	0.23
820°C	2.2 nm	6.3 nm	0.17

Table 5.2: Structural parameters of $10\times In_xGa_{1-x}N/GaN$ MQWs grown under identical conditions except for the growth temperature.

Due to the changes in the growth rate and in composition, the samples differ in well thickness and indium content, which makes it hard to compare their material quality. The structural data of the three samples are summarized in the Table 5.2.

It is possible to get a qualitative impression of the sample perfection from the photoluminescence spectra contained in Fig. 5.11. The peak energies of the three luminescence spectra differ clearly. As expected from the composition, the sample with the lowest indium concentration exhibits the highest peak energy. The differences in the peak position are further enhanced by the varying well thicknesses of the samples, since thicker wells always have a lower emission energy (compare Section 1.4). An indication of the material quality is gained from the FWHM and the peak intensity. Although the MQW grown at 820°C has the thinnest quantum well of 2.2 nm, it shows the brightest luminescence. Usually, wells with a thickness around 3-4 nm are expected to show the strongest emission. Furthermore, the FWHM for this MQW is diminished by more than a factor of two compared to the other samples. It points towards a lower perfection

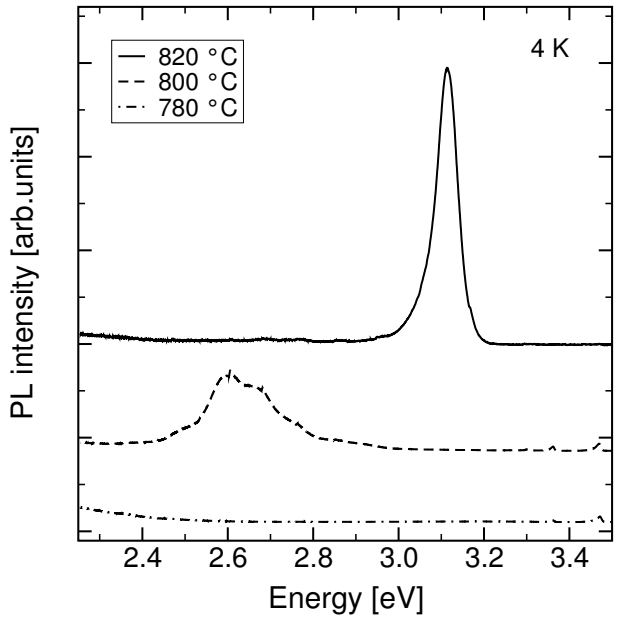

Figure 5.11: PL spectra of $In_xGa_{1-x}N/GaN$ MQWs grown at different temperatures.

of the $In_xGa_{1-x}N$, as soon as the growth temperature is reduced, which would be the origin of the lower radiative efficiencies.

The reduction in brightness is accompanied by a change of the sample color, at least for those samples investigated so far. Films with a yellowish appearance never showed a bright luminescence in the blue-violet spectral region as expected from the composition. Mostly, their luminescence was dominated by deep-level emission in the yellow spectral region, which is also in accordance with observations by Nakamura *et al.* [10]. The growth temperature for all quantum wells discussed in the following was usually 820°C.

5.2.3 Growth rate

The growth rate for the deposition of $In_xGa_{1-x}N$ quantum wells is commonly chosen relatively low compared to the normal growth rates of GaN. Commonly, reported values are on the order of 100 to 200 nm/h, as higher growth rates cause an increased surface roughness and deep-level luminescence [192, 193, 10]. The samples investigated in this study were grown at atmospheric pressure and at a temperature of 820°C. The growth rate of the quantum well was varied by adjusting the TMG and TMI flows and keeping their flow ratio constant. The structural data in Table 5.3 was obtained from the MQW satellite peaks in XRD and the thickness ratio from *in situ* reflectance.

These samples only characterize the regime of low growth rates. However, other MQWs grown at a lower temperature or at a higher growth rate confirmed the observations known from literature, namely, a lower growth temperature reduces the maximum possible growth rate [192, 10]. From the structural data it is seen, that the indium content rises with growth rate. This can be explained with the reduction of the In loss from the growing surface, as the indium atoms are trapped by the growing film [194, 192]. The desorption process is governed by the temperature, which provides a finite time constant for the desorption, independent of the growth rate. An increase in growth rate

QW growth rate	Well thickness	Barrier thickness	In content
158 nm/h	3.0 nm	6.3 nm	0.107
117 nm/h	3.3 nm	6.0 nm	0.075
72 nm/h	4.0 nm	6.4 nm	0.060

Table 5.3: Structural parameters of $10\times In_xGa_{1-x}N/GaN$ MQWs grown with different growth rates of the well regions. The growth rate of the barriers was held constant at 180 nm/h.

reduces the time available for the desorption process, and the amount of incorporated indium raises with growth rate.

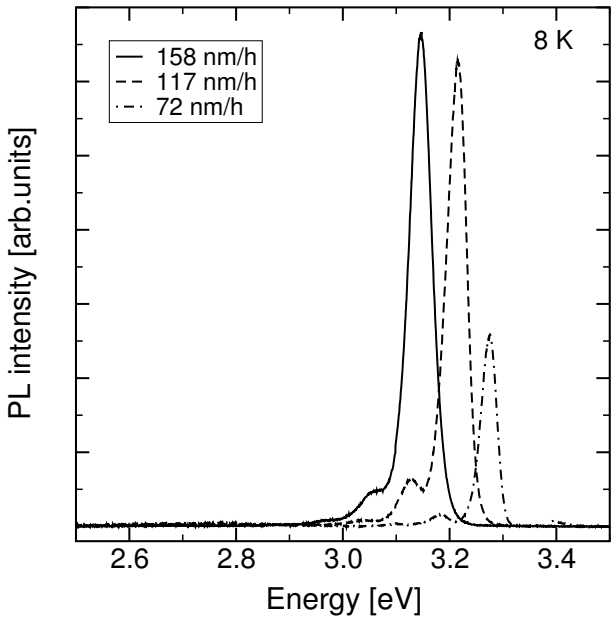

Figure 5.12: Photoluminescence of MQWs grown with different quantum well growth rates.

The photoluminescence spectra of these samples are depicted in Fig. 5.12. Again, the peak positions vary according to the quantum well thickness and the indium content. The sample grown at the lowest growth rate shows the highest peak energy and a the lowest peak intensity. Presumably, the latter fact might be caused by the low indium content, which enhances the nonradiative recombination in the barrier layers. Most important is the absence of deep-level luminescence within this range of growth rates. The differences between the samples with respect to the FWHM and the peak intensity are not major, although the variation in the peak intensity was more significant at room temperature. In this case, again the sample with the highest indium molar fraction showed the highest intensity, which can be attributed to the lower thermal emission of charge carriers into the barrier layers.

5.2.4 Carrier gas

To study the influence of the carrier gas on the optical and structural properties of $In_xGa_{1-x}N$/GaN MQW structures, two samples were grown under identical conditions except for the main carrier gas, which was nitrogen in the one and hydrogen in the other case. Interestingly, the growth rates did not change significantly upon the change of the carrier gas, such that the MQW period and the well thickness of bath samples are comparable.

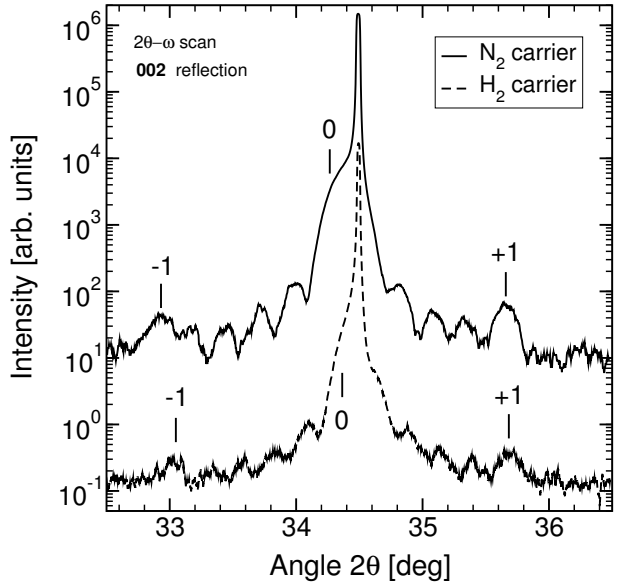

Figure 5.13: $2\theta - \omega$ scans of two samples grown with nitrogen and hydrogen carrier gas, respectively.

The structural analysis was again done by HRXRD, where reciprocal space mapping (RSM) of the **105** reflection were taken to verify the strain state, and symmetric $2\theta - \omega$ scans were done to study the periodicity and the interface perfection (see Fig. 5.13). The RSMs revealed both structures to be fully strained, which was expected for the low indium molar fractions of $\sim$0.08 and $\sim$0.05 for the nitrogen and the hydrogen carrier, respectively. The reduction of the indium content is clearly caused by the hydrogen, which destabilizes the growth of $In_xGa_{1-x}N$ as described in Section 5.2.1. From the $2\theta - \omega$-scans in Fig. 5.13 the period was estimated to be $\sim$7 nm. The well thickness can only be estimated from the growth rates, and should be around $\sim$2.9 nm for both samples. Fig. 5.13 also shows that the periodicity in the MQW is distorted upon the change of the carrier from nitrogen to hydrogen. This is seen in the loss of contrast in the superlattice fringes, which points to a stronger variation of well and barrier thickness.

This thickness variation probably also manifests in the photoluminescence spectra of the two samples shown in Fig. 5.14. The difference in peak energy is in line with the determined indium contents, since the MQW grown under hydrogen emits at 3.3 eV, whereas the one grown with nitrogen carrier peaks at 3.17 eV. The spectra differ significantly in FWHM and peak intensity. The MQW grown in hydrogen atmosphere shows a lower intensity and has a broader emission compared to the sample grown under nitrogen. Taking the XRD results into account, this is probably caused by larger fluctuations of the well thickness or of the composition, which generates spatial variations of the local emission.

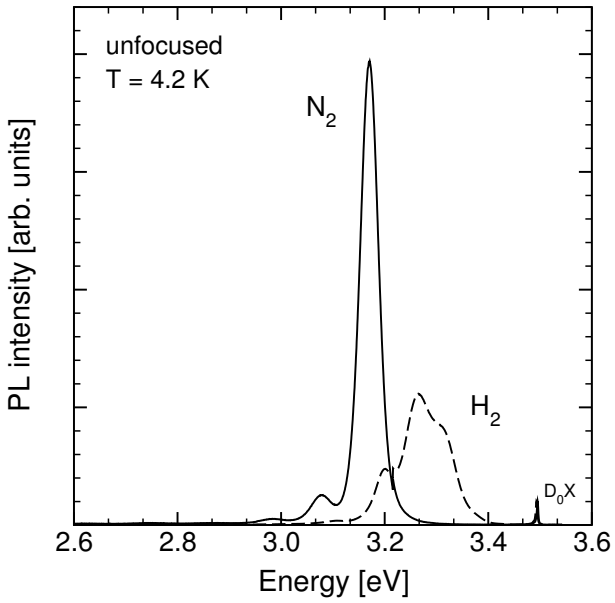

Figure 5.14: Photoluminescence spectra of two MQWs grown under identical conditions except for the carrier gas.

5.3 MQW barrier doping

The doping of $In_xGa_{1-x}N$ structures to improve their optical properties has been investigated since the beginning of using $In_xGa_{1-x}N$ for optoelectronic devices [195]. Publications systematically investigating the effect of Si doping of quantum well structures and superlattices appeared later, among which many were initiated by the groups at the University of California at Santa Barbara, USA (UCSB) [196, 197, 198, 189]. For thick layers, it was found that Si doping enhances the luminescence intensity by an order of magnitude already at low levels of dopant concentration [10, 195]. The doping of the active region in optoelectronic devices is also a common technique to raise the output power [199]. $In_xGa_{1-x}N/In_xGa_{1-x}N$ MQW structures showed an increased room temperature photoluminescence intensity upon doping the whole structure with silicon [196]. Again, the main improvement was observed for low doping levels around 1×10^{18} cm^{-3}, and for higher Si concentrations the PL intensity saturated. The effect of doping the barrier only was demonstrated to have the same effect like the doping of the whole structure, particularly for the emission at room temperature [197]. With increasing doping level, the Stokes-like shift of the absorption and the emission was reduced. This was accompanied by a drop of the radiative recombination lifetime at low temperature [198]. It was qualitatively argued, that the localization is reduced and the piezoelectric field gets screened due to the doping, such that the overlap of electron and hole wavefunctions increases [197, 198]. The Si doping can also modify the growth at low temperature, as it might initiate a layer-by-layer growth mode [200]. This can reduce the interface roughness and compositional fluctuations of the well. Both are seen as possible centers for the localization of charge carriers and can affect the emission properties [189, 198]. However, the relative impact of these effects upon doping has not yet been quantified.

5.3.1 Structural properties

The MQWs investigated consist of a 10× $In_xGa_{1-x}N$/GaN layer structure. The well thickness was estimated from the sample series discussed in Section 5.4, as this allowed to separate the barrier thickness from the period of the MQW and to accurately determine the QW growth rate. One undoped and four doped samples were grown on a 1 μm thick undoped GaN template, which was the same for all structures. Silane was used for the doping of the barrier layers, whereas the wells were nominally undoped. The growth was performed at 820°C with nitrogen as the carrier gas. The doping levels were extrapolated from calibration samples grown at a higher temperature, as the doping level should directly follow the molar SiH_4/TMG ratio and not depend on the temperature. The intended doping levels of the doped structures were 8.0×10^{17} cm^{-3}, 2.8×10^{18} cm^{-3}, 8.0×10^{18} cm^{-3} and 2.8×10^{19} cm^{-3}. Following previous measurements, the undoped sample was assumed to have a background electron concentration of 2.0×10^{16} cm^{-3} at room temperature.

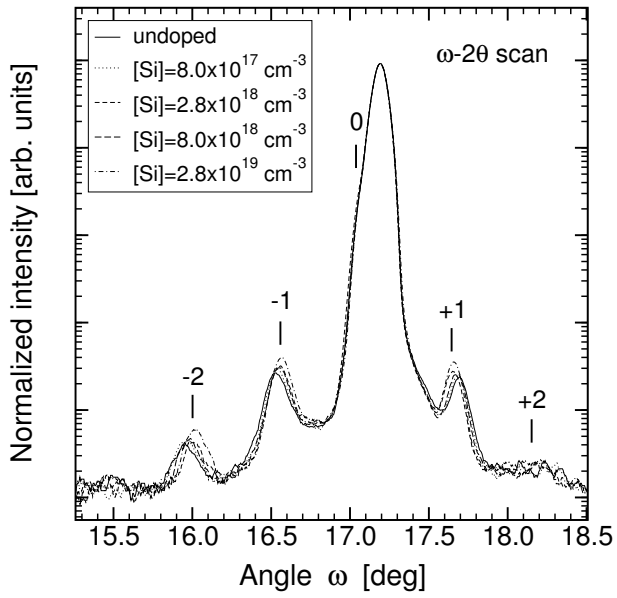

Figure 5.15: XRD $\omega - 2\theta$ scans of MQW structures with varying Si doping level in the barrier. The scans were done with slit to raise the satellite intensities.

The structural properties were extracted from HRXRD scans and RSMs. The $\omega - 2\theta$ scans of the **002** reflection displayed in Fig. 5.15 were performed to obtain the MQW period and to compare the peak intensities of the satellites. The average composition was determined from $2\theta - \omega$ scans with an analyzer crystal in front of the detector, assuming a fully strained MQW. The latter was verified for selected samples in RSMs of the **105** reflection. The $\omega - 2\theta$ scans in Fig. 5.15 are normalized with respect to the intensity of the GaN peak. With increasing doping level, the MQW signature gains in contrast and the spacing of the satellite peaks is reduced.

The structural data gained from the XRD analysis are plotted in Figs. 5.16(a) to 5.16(c). From the MQW satellite spacings, the MQW periods are obtained using the following equation [150] :

$$d_{\text{period}} = \frac{(n_i - n_j)\,\lambda}{2\,(\sin\theta_i - \sin\theta_j)} \tag{5.4}$$

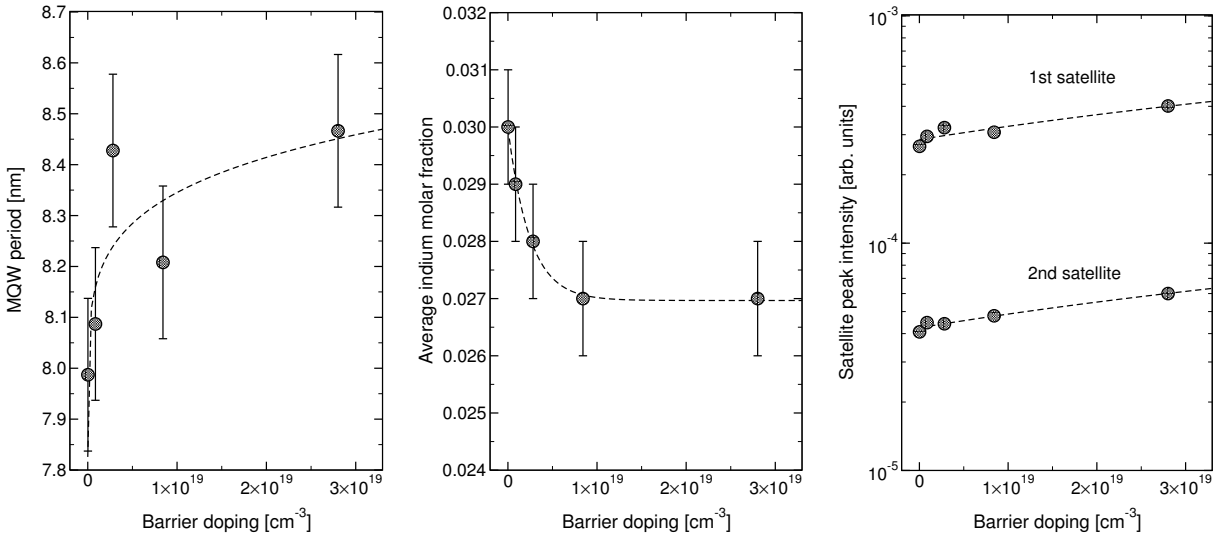

(a) MQW period **(b)** Average In content **(c)** Satellite intensity

Figure 5.16: Structural data of MQWs in dependence on the Si concentration in the GaN barriers. The data was generated from the XRD analysis of the samples. The dashed lines are guides to the eye.

Here, θ_i and θ_j are the diffraction angles of the ith and jth MQW satellites, and $n_i(n_j)$ is the diffraction order of the corresponding peak. The periods are displayed in Fig. 5.16(a), showing an increase of the MQW period with the Si concentration. Presumably, this results from an increase in the growth rate of the low-temperature GaN:Si barriers, as the average indium content in the MQW drops as well. The latter effect is depicted in Fig. 5.16(b), where the composition was determined from the **002** reflection. The peak position of the 0th MQW peak used for this analysis provides the *average* lattice constant. Therefore, it depends on the thickness ratio of well and barrier as well as on the QW composition. It is reasonable to assume identical growth conditions for all quantum wells and ascribe the observed changes in the MQW period to the barrier layer growth. A good agreement of the experimental data in Figs. 5.16(a) and 5.16(b) is found for a well width of 2.4 nm with an indium molar fraction of $x_{\mathrm{In}} = 0.1$, which will be used for the following simulations.

Another important aspect of the XRD studies is the rise of the satellite peak intensities with the dopant concentration as shown in Fig. 5.16(c). It is caused by a higher perfection of the MQW structure, i.e. a smaller variation of the individual barrier and well thicknesses and smoother interfaces. This is in accordance with an XRD study by Cho *et al.*, who showed the satellite FWHM to decrease with the Si concentration [198]. Furthermore, the growth of undoped GaN onto Si-doped GaN at 810°C was demonstrated to change from a step-flow towards a layer-by-layer growth mode [200], which should cause a better thickness homogeneity of the quantum well. The surface roughness of the GaN barrier itself decreases significantly as shown in AFM studies of GaN grown

at low temperature on GaN templates [189]. In this study, the *rms* roughness dropped from 0.49 nm to 0.22 nm upon a Si doping level of 3×10^{19}cm^{-3}. Besides an increase in the terrace width upon doping, the spiral growth mode of the undoped GaN seems to be suppressed. This would cause a significant reduction of thickness fluctuations in the MQW region and, consequently, change the localization of charge carriers.

5.3.2 Optical properties

The change of the Si concentration in the barrier layer is accompanied by a strong variation of the photoluminescence characteristics. Apart from the change in the surface, the thickness and the interface perfection, the Si doping provides charge carriers to partially screen the piezoelectric fields in the quantum wells. The intention of the following studies is to estimate, to which extent the reduction of the piezoelectric fields is responsible for the changes in luminescence.

Experimental results : Photoluminescence peak position

The photoluminescence was measured at room temperature under unfocused beam conditions in order to avoid the generation of a large charge carrier density, which might screen the piezoelectric field. To extract the peak position and the intensity as accurately as possible, the spectra were fitted with a Gaussian taking interference oscillations into account.

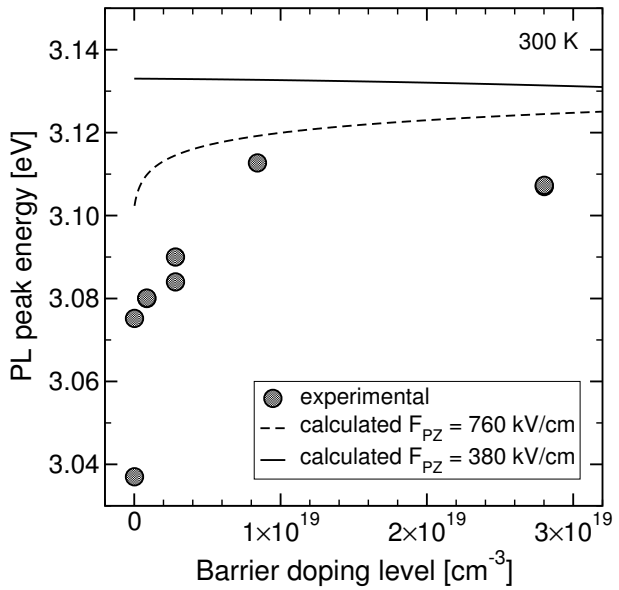

Figure 5.17: The PL peak position versus the Si doping of the GaN barriers. Also shown are theoretical results taking different piezoelectric fields into account.

The variation of the PL peak position with the Si doping level is shown in Fig. 5.17. With increasing dopant concentration, the peak shifts to higher energies, which is particularly strong for low concentrations. The blueshift agrees with the observations of Chichibu *et al.* [201]. Additionally, these authors measured photoluminescence excitation (PLE) and time resolved PL, which revealed a sharper absorption edge and a decrease in the radiative decay time with increasing Si doping. They explained these findings with the

effective screening of the internal field, but did not take the changes in the morphology into account. All results could be understood as well on the basis of a different carrier localization due to a more homogeneous well width. The fluctuation of the well thickness generates localization centers causing a redshift of the emission due to the piezoelectric fields and the quantum confinement (compare Section 1.4). A larger thickness corresponds to a lower transition energy and, as most of the photoluminescence signal originates from the areas of the lowest energy, the PL peak is redshifted. In contrast to this, the PLE signal provides information about the average thickness. A more homogeneous thickness would cause a higher absorption coefficient and a sharper absorption edge. The same effect would have a variation of the composition in the quantum well. Thus, the conclusion, that a reduction of the piezoelectric field is the only reason responsible for the observed findings, has to be taken with care. Probably, the superposition of both effects, namely an improved interface and thickness perfection in combination with a reduction of the piezoelectric field, has to be considered for Si.doped MQWs.

Simulation of band structures

The quantum wells were simulated using the software for the calculation of one-dimensional bandstructures mentioned before [202, 203]. Piezoelectric fields were included through the introduction of δ-charges at the interfaces of the quantum well. The structures were simulated for a temperature of 300 K, such that the total carrier concentration almost equals the dopant concentration. The program was tested to provide consistent results for all structures under investigation. The quantitative values might be a subject of change, if more accurate material constants for the nitrides are known, but the trends discussed here should not be affected. A description of the used material constants and of the simulation procedure is found in Appendix C.

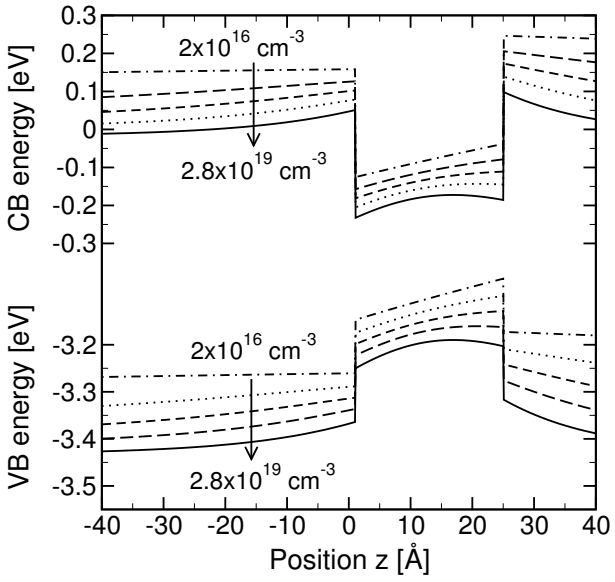

Figure 5.18: The simulated conduction band (CB) and valence band (VB) structure of single quantum wells for different Si doping levels of the barrier. The Si concentrations were chosen identical to those of the MQWs discussed in this section, namely 2.0×10^{16} cm^{-3} for the undoped structure and 8.0×10^{17} cm^{-3}, 2.8×10^{18} cm^{-3}, 8.0×10^{18} cm^{-3} and 2.8×10^{19} cm^{-3} for the Si-doped structures.

The impact of the Si doping on the band structure is shown in Fig. 5.18 assuming a well thickness of 2.4 nm and a piezoelectric field of 380 kV/cm, which is in good agreement

with corresponding values reported in literature for an In molar fraction of $x_{\mathrm{In}} = 0.1$ [56, 201, 53, 55]. The change of the bandstructure inside the quantum well upon doping is caused by the expected screening of the internal field. The tilt of the band edges is partially compensated, and the bands become more horizontal inside the well. However, a major effect is only obtained for Si concentrations exceeding 1×10^{18} cm^{-3}. For low doping levels, the bands inside the well remain almost unchanged.

Comparison of peak energies from simulation and experiment

For thin quantum wells, where the exciton Bohr radius a_B is larger than the quantum well thickness L_z, the piezoelectric fields should have almost no effect on the emission energy, as the quantum confinement dominates the positions of the energy levels in the conduction and the valence band [201]. The exciton Bohr radius in GaN amounts to $a_B = 3.6$ nm [50], which exceeds the well thickness of the discussed samples by 30 %. Therefore, the screening effect should not be dominant in this case, and the emission peak energy should be independent of the doping level. This is seen in the calculated values shown in Fig. 5.17 on page 118, which were obtained for an internal field of 380 kV/cm.

However, for very large fields in the well, a blueshift with increasing doping level can be expected. This happens as soon as the tilt of the valence band due to the piezoelectric field exceeds the valence band offset ΔE_v. In this case the hole is localized in the triangular shaped potential at the QW interface, which is defined by the tilted band inside the well and the valence band edge. Any reduction of the field strength then generates a blueshift of the luminescence peak. The piezoelectric field necessary to obtain a shift similar to the observed one is as large as ∼780 kV/cm, as shown in Fig. 5.17 as well. This is rather large compared to literature data [56, 201, 53, 55]. For an indium molar fraction of 0.1, the reported values scatter around 350 kV/cm. As will be discussed later in Section 5.4, this field fits reasonably well to the PL peak energies obtained for an undoped and a doped set of samples, where the quantum well thickness was varied. For an internal field of 780 kV/cm, theoretical and experimental data in these thickness series diverge, therefore this field is not suitable to explain the behavior of the luminescence in this MQW barrier doping series.

It means, that the PL peak shift with doping observed in Fig. 5.17 has to have another origin. A possibility would be the reduction of fluctuations of the QW thickness due to the doping. An increased thickness variation in undoped samples would provide localization centers formed by areas of larger well thickness, since a larger well width corresponds to a lower emission energy. Accordingly, the observed PL peak is redshifted with respect to the theoretical value. An increased Si doping during barrier growth smoothens the interfaces and reduces the well thickness fluctuations [189], such that the Stokes-like redshift decreases. Furthermore, the reduced localization and the enhanced emission from areas of lower thickness would reduce the decay time of the PL intensity, which is in agreement with literature [201, 57]. An increased fluctuation of the indium content for the case of undoped quantum wells cannot be fully excluded, since it would generate similar effects. An origin might be the preferential incorporation of In atoms at the atomic steps, which are affected by the Si doping. However, since

the growth parameters of the $In_xGa_{1-x}N$ wells were kept constant in this series, a significant modification of the compositional homogeneity is not as probable as a change of the growth mode and interface perfection.

Experimental results: Photoluminescence peak intensity

The peak intensity of the room-temperature photoluminescence is much more sensitive to the barrier doping level than is the peak position, as seen in Fig. 5.19. The lowest Si concentration in the barriers was 8×10^{17} cm^{-3}, which already rises the peak intensity by an order of magnitude. Further doping lead to an additional increase of 50%, thus, the main effect is already obtained for low dopant concentrations.

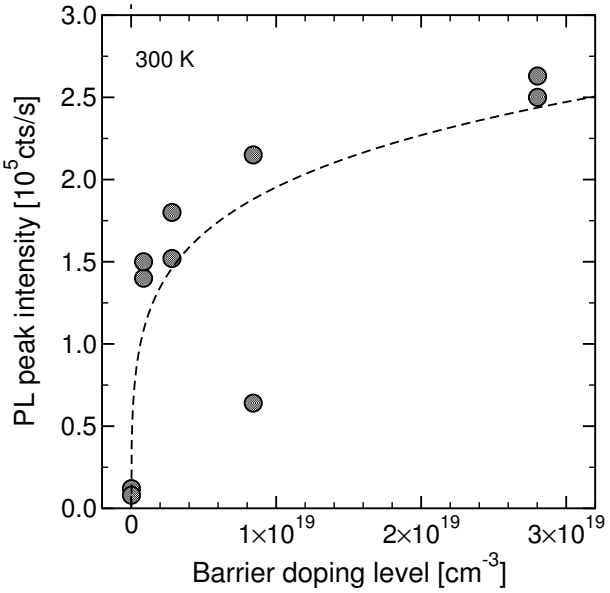

Figure 5.19: PL peak intensity of MQWs in dependence on the Si doping level of the barrier. The dashed line is a guide to the eye.

Very often, this increase is ascribed to the reduction of the piezoelectric field [201, 187], such that the quantum confined Stark effect is partly compensated and the overlap integral of electron and hole wavefunction increases. The latter would enhance the oscillator strength for the radiative recombination of the electron and the hole, and the PL intensity should improve. However, this effect should only be significant for well widths exceeding the exciton Bohr radius of 3.6 nm. In MQWs with a lower well thickness, like in the set of samples investigated, the quantum confinement should govern the shape and the overlap of the wavefunctions. Accordingly, for very thin, homogeneous wells, the impact of barrier doping should be negligible. This would be different for thin, inhomogeneous wells with QW thickness fluctuations, where the localization centers are formed by the sections of larger well width. Since the luminescence originates from these sections of larger thickness, the Si doping might strongly influence the luminescence intensity.

The band structures of an undoped and a doped structure are compared in Fig. 5.20 together with the momentum $\Psi\Psi^*$ of the electron and hole wavefunctions. Only very few localized states are found in the conduction band due to the low effective electron mass of $0.22m_0$, where m_0 is the mass of the free electron. The light and the heavy hole

in the valence band experience stronger localization, since their effective mass is higher by a factor of roughly 3-6.

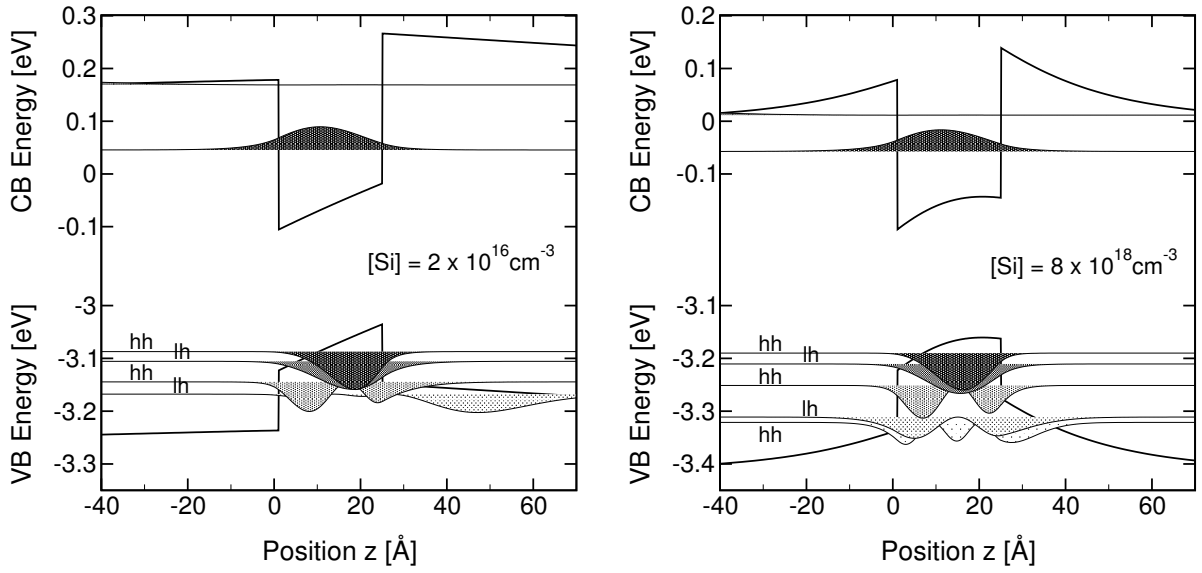

(a) Undoped barriers

(b) Si-doped barriers

Figure 5.20: Simulated band structures of $In_xGa_{1-x}N$ quantum wells with different Si doping level of the GaN barrier layers. Also plotted is the momentum $\Psi\Psi^*$ of the ground and the first excited states of the electron, the light hole and the heavy hole. The QW thickness is 2.4 nm, the In molar fraction is 0.1 and the piezoelectric field is 380 kV/cm for an undoped structure.

Fig. 5.20(a) shows the calculated band structure of the undoped quantum well. Only the ground state of the electron is localized in the well region. In the valence band, the ground as well as the first excited states of the heavy and the light hole are localized, where the lowest state is occupied by the heavy hole. Upon n-type doping of the barriers with a Si concentration of $8.0 \times 10^{18}\text{cm}^{-3}$, the band structure is modified as seen in Fig. 5.20(b). The screening of the piezoelectric field has two effects : First, the potential drop across the well is reduced and second, the triangular shaped potentials at the well interfaces are widened. The former generates a blueshift of the luminescence due to the reduction of the quantum confined Stark effect. The latter causes a redshift, since the quantum confinement energy is lower in the widened triangular potential. For this low well thickness, the two effects just balance each other, such that the PL peak energy remains unchanged (see Fig. 5.17).

Furthermore, the relative positions of the electron and hole remain almost unchanged, i.e. the width of the wavefunctions as well as the positions of the maxima are almost constant. Only for the higher order states of the heavy and the light hole significant changes are observed, which experience an enhanced localization in the doped structure. Another possibility for the rise in peak intensity upon the doping could therefore

be the improved localization of the holes in the well region, which is induced by the changed slope of the valence band. Since the high effective mass reduces the hole mobility, the QW efficiency is limited by the hole diffusion into the well. The structure of the valence band in the doped quantum well generates a driving force, which supports the diffusion of the holes into the well region, such that the radiative recombination rate increases. It might be possible to verify this hypothesis in time-resolved PL measurements, where one compares the excitation into the barriers and into the quantum wells.

Probably, the intensity increase is not caused by the rising overlap integral of the electron and the hole wavefunctions, which are shown in Fig. 5.21. Assuming the radiative recombination of electron and hole to happen from the states with the lowest energy, the momentum $\Psi\Psi^*$ of the electron and the heavy hole wavefunctions are plotted for the various doping levels.

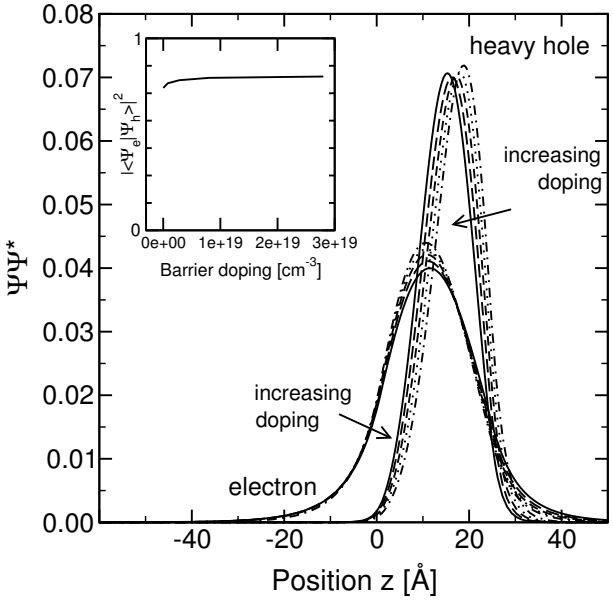

Figure 5.21: The momentum $\Psi\Psi^*$ of the electron and the heavy hole wavefunctions for different barrier doping levels. The overlap integral $|\langle\Psi_e|\Psi_h\rangle|^2$ is shown inset.

With doping, both wavefunctions shift towards the center of the well, while the main shift is observed for the hole. Additionally, the FWHM of both wavefunctions slightly increases due to the broadened potential inside the well. From the two wavefunctions, the electron-hole overlap integral $|\langle\Psi_e|\Psi_h\rangle|^2$ is calculated, which is shown in the inset of Fig. 5.21 in dependence on the barrier doping level. The overlap is already large for low or no doping in the barriers, such that the calculated increase is by far not as big as the luminescence increase observed in Fig. 5.19. Accordingly, the reduction of the piezoelectric field cannot fully explain the experimental findings for thin wells. This is different for thicker quantum wells with $L_z > a_B$, as will be shown in Section 5.4. Therefore, another effect induced by the Si doping of the barriers has to be responsible for the PL improvement as there might be :

- A reduction of the well thickness inhomogeneity eliminates localization centers formed by areas of larger well thickness. As the overlap integral in thinner wells is higher, the radiative intensity in more homogeneous wells would increase, i.e. the emission originates from larger areas in the well.

- The screening of the internal field should be more efficient at larger well width. This would increase the overlap integral in the localization centers formed by areas of larger well thickness. Accordingly, the radiative recombination rate should rise.

- The increasing charge carrier density with Si doping might block the localized states of the threading dislocations, which act as nonradiative recombination centers [204]. In particular, this effect should be relevant at low doping levels [205].

- The improved interface perfection upon doping enhances the diffusion across the interface, such that the charge carrier density in the quantum well is higher. This effect is only relevant for the excitation of the PL via the GaN barrier layers.

- The stronger localization of the holes with doping in combination with the change of the band structure leads to a raised hole density in the well region. As holes are the minority charge carriers, the diffusion and light emission is governed by this density in the well. Again, this effect is only relevant for the excitation of the PL via the GaN barriers.

Which of these is responsible, cannot be said from the experiments done so far. Also, literature does not give an answer, but the most discussed reasons are thickness and compositional fluctuations. Presumably, the reduction and the screening of thickness fluctuations are the main reasons. It can be enhanced by the occupation of the localized states of the threading dislocations. This will be detailed in Section 5.5.

5.4 Quantum well thickness

The primary aim of this study was the optimization of the quantum well thickness in the $In_xGa_{1-x}N$/GaN active region of optoelectronic devices. In combination with the doping series discussed in the previous section, it allowed to estimate the influence of the piezoelectric field in MQW structures with doped and undoped GaN barriers.

5.4.1 Structural properties

The growth conditions of all samples were identical, except for the Si doping level in the GaN barrier layers. The first set of samples was grown without any Si doping, and the second set was grown with Si-doped barriers. Within each series, the $In_xGa_{1-x}N$ quantum well thickness was varied from $\sim$1 nm to $\sim$5 nm. The Si doping level in the second set was chosen to be 8.0×10^{18} cm^{-3}. The growth temperature was 820°C, the growth pressure was 700 Torr and the growth rate was adjusted to 140 nm/h. The molar TMI/TMG input flow ratio was set to five, which is needed at this high growth temperature to obtain a significant incorporation of indium. The structures consisted out of 10 $In_xGa_{1-x}N$ quantum wells of different thickness embedded in $\sim$6.5 nm thick barriers. The thickness ratio was chosen to ensure sufficient separation of the quantum wells, such that the coupling of the wave functions of neighboring wells is suppressed.

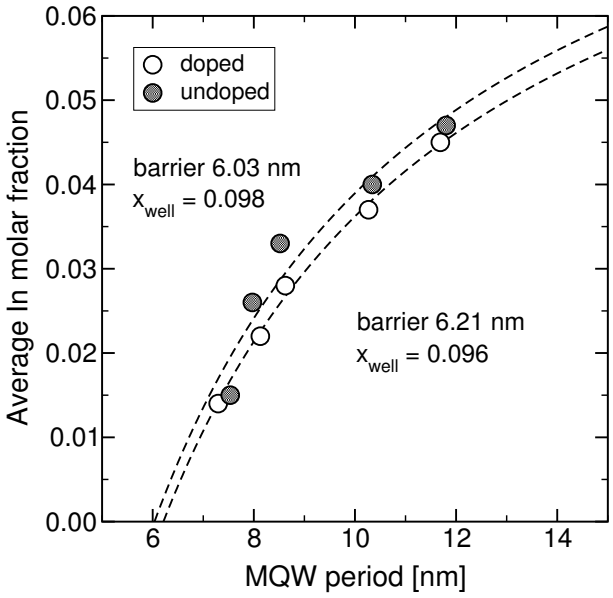

Figure 5.22: The average In molar fraction in dependence on the MQW period. Shown are the data sets for samples with doped and undoped GaN barriers, respectively. The dashed lines are least-squares fits assuming a constant barrier width and a constant In content of the QW within each set of samples.

The structural analysis was done by HRXRD investigating the **002** reflection. The period was obtained from $\omega - 2\theta$ scans with slit in front of the detector, and the average indium content was extracted from analyzer scans assuming coherently grown structures. For the samples with the largest well thickness this strain state was verified by a RSM of the **105** reflection. Fig. 5.22 contains the structural data of the doped and the undoped set of samples, where the average composition is plotted against the MQW period. From this plot the barrier thickness and the indium content in the wells can be separated, as the average indium molar fraction of the structure is given by :

$$\bar{x}_{\mathrm{In}} = x_{\mathrm{well}} \cdot \frac{d_{\mathrm{period}} - d_{\mathrm{barrier}}}{d_{\mathrm{period}}}. \tag{5.5}$$

Using x_{well} and d_{barrier} as fitting constants, the experimental values are well reproduced. The errors of the barrier thickness and the well composition are $\Delta d_{\mathrm{barr}} = 0.1$ nm and $\Delta x_{\mathrm{In}} = 0.005$, respectively. In agreement with the doping series discussed before, the barrier thickness of the doped MQWs is a little larger compared to the undoped structures. This effect is not large, but relevant in order to extract the correct well composition. The determined In molar fraction of the quantum wells is identical for the two series within the limits of accuracy.

Another possibility to extract the barrier thickness would be to plot the MQW period against the $In_xGa_{1-x}N$ growth time and extrapolate it to zero. The barrier thicknesses from such a plot are 6.58 nm and 6.56 nm for the undoped and the doped series, respectively. These are clearly larger compared to the values from Eqn. 5.5 and correspondingly suggest too high In fractions in the wells. It generates significant inconsistencies in the comparison with the luminescence data, such that this analysis provides wrong data. The real well thickness exceeds the intended thickness by a constant offset. This offset amounts to roughly 0.3 nm, which is on the order of a (Ga-N) bilayer. It might be generated by segregation of indium on the surface during the growth of the quantum well, which is then incorporated during the successive barrier growth, or by outdiffu-

sion of indium into the barriers. The whole analysis is consistent taking this effect into account, which was done before by using the barrier thickness as a fitting constant in Eqn. 5.5. Accordingly, the structural parameters contained in Fig. 5.22 will be used for the following simulations of the band structures.

5.4.2 Optical properties

To compare the optical properties, the photoluminescence of the samples was acquired at room temperature and 4.2 K. Unfocused beam conditions were used to avoid additional screening of the internal fields.

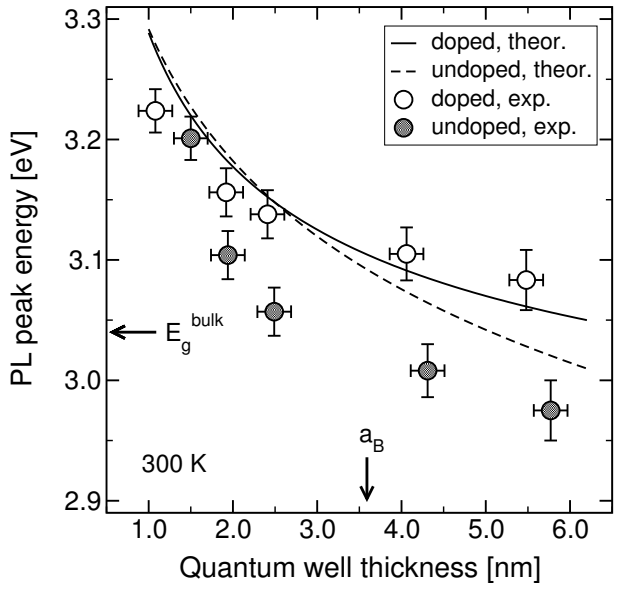

Figure 5.23: Thickness dependence of the photoluminescence peak energy in dependence on the quantum well thickness. Also shown are the theoretical peak positions for a piezoelectric field of 360 kV/cm

Fig. 5.23 contains the PL peak energy in dependence on the quantum well thickness. For both sets of samples the luminescence peak energy is redshifted with increasing well width. This redshift is more pronounced for the samples with undoped GaN barrier. For comparison, bulk strained $In_xGa_{1-x}N$ with an indium content of 9.7% assumed for these samples has a band gap of 3.04 eV, which is amongst of the experimental values [26]. This indicates that the luminescence peak energy is defined by the quantum confinement as well as the quantum confined Stark effect. For thicknesses below the exciton Bohr radius, the dominant factor is the blueshift with respect to the bulk value originating from the quantum confinement. For thicknesses on the order of or exceeding this value, the redshift due to the QCSE gains influence.

This is directly evident from the two calculated curves depicted in Fig. 5.23 as well. The theoretical peak position was obtained from the difference of the energy levels of the electron and the heavy hole. The input parameters for the simulation were an indium molar fraction of 0.097, a piezoelectric field of 360 kV/cm and Si doping concentrations of 2×10^{16} cm^{-3} and 8×10^{18} cm^{-3} for the barrier layers of the undoped and the doped structure, respectively. The doping concentration in the undoped MQWs was assumed to be equal to the background electron concentration of typical undoped GaN films. The two curves coincide for low QW thicknesses, and diverge for thicknesses exceeding

~3 nm. This supports the concept of dominant quantum confinement for the low well thicknesses and the importance of the QCSE for the higher well widths. The theoretical curve can reproduce the experimental values of the samples with doped barrier reasonably well, whereas the peak positions found for the undoped structures are redshifted by 50-100 meV with respect to the calculated curve. This indicates an enhanced localization of the charge carriers in the undoped structures, originating from thickness or compositional fluctuations. In the context of the arguments used so far (see Section 5.3), a reduced thickness homogeneity in the undoped structures is more probable than compositional fluctuations.

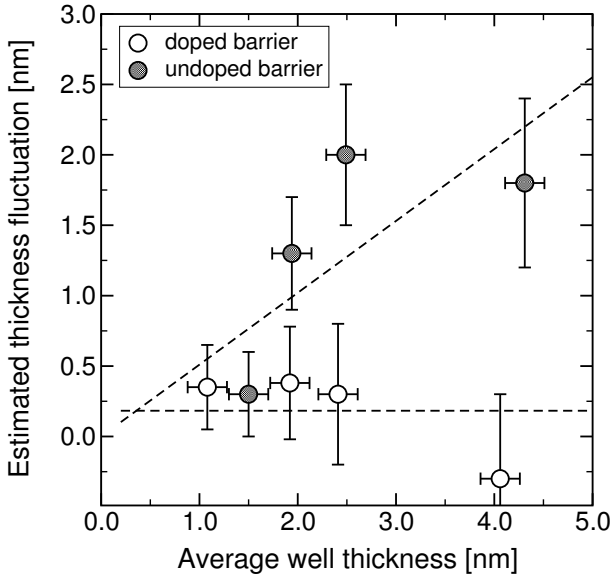

Figure 5.24: The estimated average QW thickness inhomogeneity obtained from the comparison of the experimental and the theoretical data in Fig. 5.23. The dashed lines are linear least-squares fits.

The average QW thickness in such a localization center can be estimated from the comparison of the experimental data with the theoretical curve in Fig. 5.23. For example, the PL peak energy of the nominally 1.1 nm thick doped MQW corresponds to a theoretical thickness of 1.45 nm. This would be the value of the average thickness fluctuation which dominates the radiative emission. The estimated QW thickness fluctuations for both sample series are shown in Fig. 5.24. The doped samples show a constant fluctuation around ~0.35 nm, which is on the order of a (Ga-N) bilayer. This might be caused by thickness variations arising from the atomic step structure of the surfaces. In contrast to this, for the undoped MQWs, the thickness variation increases with well thickness, and amounts to roughly 50% of the quantum well thickness. This observation is in qualitative agreement with the AFM studies by Keller *et al.* [189].

The second parameter to obtain a high quantum efficiency besides the Si doping level of the barriers is the correct choice of the quantum well thickness as seen in Fig. 5.25. The two graphs contain the photoluminescence peak intensities of the doped and the undoped MQWs, measured at room temperature and 4.2 K. For both sets of samples, the optimum well thickness is around 3.5 nm, which is close to the exciton Bohr radius. The intensity variation with the deviation from the optimum thickness is similar as well, although at room temperature the loss in intensity seems to be a bit more pronounced for the undoped MQWs. At room temperature, the luminescence yield from doping

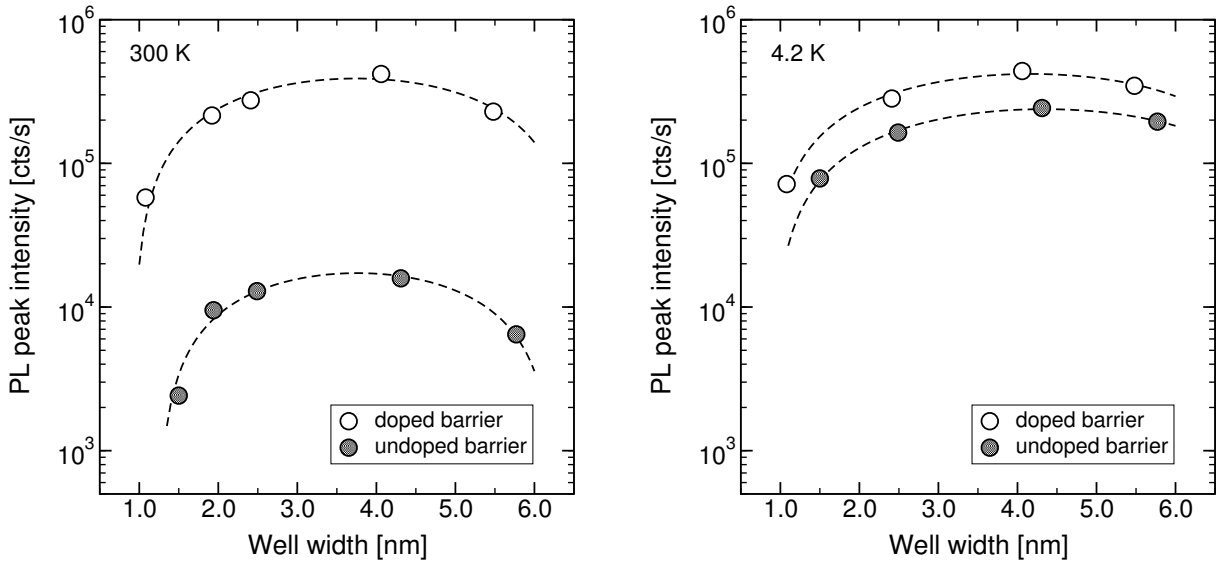

(a) Room temperature (300 K)

(b) Low temperature (4.2 K)

Figure 5.25: Variation of the PL peak intensity with the quantum well thickness measured at room temperature and 4.2 K. Compared are MQWs with doped and undoped GaN barriers.

amounts to more than an order of magnitude, whereas at 4.2 K, the intensity difference is reduced to a factor of roughly two. Although the intensities can not be exactly compared, since the data sets were collected in two separate sessions, it can be stated, that a reduction of the measurement temperature mainly enhances the luminescence intensity of quantum wells with undoped barriers, whereas structures with Si-doped barriers are much less affected. This behavior can be understood if one takes the cross-section of the nonradiative centers into account. The intensity of the photoluminescence increases with a lower cross-section of the nonradiative centers. The latter can be reduced by a faster radiative recombination, by the full occupation of the localized states of the nonradiative centers or by a lower diffusion length of the minority charge carriers. The first two aspects are presumably true for Si doped samples, since the doping increases the overlap integral of the electron and the hole wavefunctions and the increased electron density might occupy the localized states at the nonradiative centers, assuming these are formed by threading dislocations [205, 206]. As the radiative recombination time of a localized state is generally high, the full occupation of these states with electrons would eventually block these nonradiative centers. Therefore, the Si doped structures show a very high radiative efficiency at room temperature, whereas the radiative efficiency of the undoped samples is low. At 4.2 K, the diffusion length of the charge carriers is reduced, such that the cross-section of the nonradiative centers is diminished. This process is efficiently raises the PL intensity of the undoped MQWs, whereas the luminescence yield of the doped samples is less affected. Accordingly, the difference in the PL intensity of the doped and the undoped MQWs is high at room temperature and

low at 4.2 K.

The PL intensity variation with well thickness is a superposition of two effects. On the one hand, the intensity follows the overlap integral of the electron and the hole wavefunction, and on the other hand, the intensity is reduced by the diffusion of charge carriers into nonradiative recombination centers like threading dislocations [136, 207]. The overlap integral is determined by the well thickness and the strength of the piezoelectric field. The result of this calculation shown in Fig. 5.26 for the doped and the undoped quantum wells. The plot contains the overlap integral in dependence on the QW thickness, assuming the same set of parameters as for the data in Fig. 5.23.

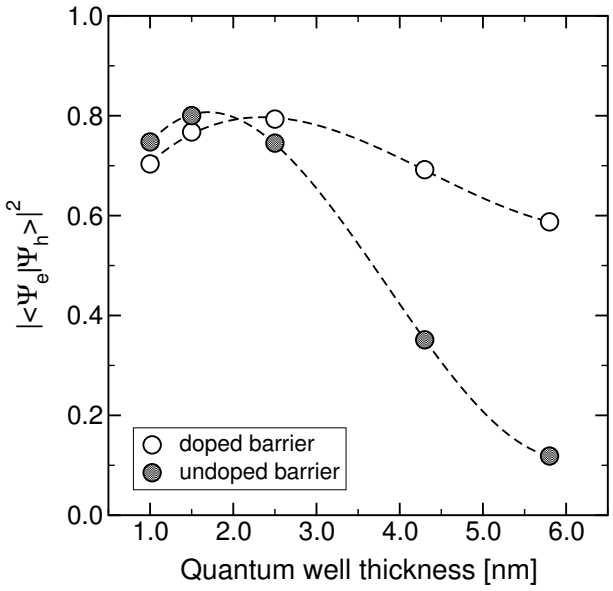

Figure 5.26: The overlap integral in dependence on the well thickness. The dashed lines are guides to the eye.

As can be expected from the shown variation of the peak energies, the piezoelectric fields are of minor influence for the QW thicknesses below the exciton Bohr radius. In this case, the overlap integral is almost identical for samples with doped and undoped barrier. For larger QW thicknesses, the electrons and holes are primarily localized at the opposite sides of the well in the triangular shaped potentials formed by the band offest to the barriers and the tilted bands in the well. Now, the internal field significantly influences the wavefunction overlap, since it spatially separates the two wavefunctions. Doping of the barriers partially compensates the field and the overlap integral increases compared to the undoped case. Therefore, for QW thicknesses exceeding the exciton Bohr radius, the overlap integral is reduced with increasing well thickness for undoped barriers, whereas it is much less affected in samples with doped barriers. This also implies, that thickness fluctuations in doped structures are more efficient recombination centers compared to undoped ones. For example, if the QW thickness variations amount to 1 nm in a 3 nm thick well, then the localization centers are formed by the sections of 4 nm thickness. In the undoped structure, the overlap integral at 4 nm amounts to 0.4, whereas it is 0.7 in the doped structure. Accordingly, the radiative recombination in the localization center is more efficient for the case of the MQW with doped barriers. This will be discussed in the next section in more detail.

5.5 Localization in quantum wells and luminescence efficiency

The aim of this section is to explain the previous findings within a consistent qualitative model for localization in quantum wells, in particular to understand the enormous influence of the barrier doping on the room-temperature photoluminescence intensity. The reduction of the piezoelectric field upon barrier doping can not be the only reason, at least for thin quantum wells with $L_z < a_B$, as shown before in Fig. 5.21 on page 123.

5.5.1 Potential localization centers

The measured photoluminescence intensity is determined by the ratio of two concurrent processes, the radiative and the nonradiative recobination of charge carriers. Nonradiative recombination centers can be dislocations or point defects. For the case of GaN, for example threading dislocations were identified as one such center [136, 207]. To raise the luminescence intensity, one can increase the radiative recombination rate or decrease the nonradiative recombination rate. The radiative recombination rate follows the overlap integral of the electron and hole wavefunction in the quantum well [59], since the latter quantifies the probability of the electron transition from the conduction band into the valence band according to Fermi´s golden rule. The piezoelectric field in GaN-based structures is the main reason for the reduction of the overlap integral. Thus, in order to raise the radiative recombination rate, one possibility is the screening of the internal field. This can be achieved by doping the barriers with silicon or by adjusting the doping profile around the well. The same happens for very high excitation densities, which generates a very high charge carrier density in the well.

The reduction of the nonradiative recombination rate can be achieved by a reduction of the according centers, or by the localization of the charge carriers in the quantum well at dislocation-free local potential minima. This hinders the charge carriers to diffuse into a nonradiative center, such that the probability of radiative recombination is increased. For $In_xGa_{1-x}N/GaN$ quantum-well structures, different possible sources for local potential minima exist :

- compositional fluctuations
- quantum-well thickness fluctuations
- strain fluctuations

Basically, the impact of these local fluctuations for localized charge carriers is the same. The carriers can lower their energy at the expense of a lower electron-hole overlap. For a local increase of the indium molar fraction, the local band gap is decreased and the piezoelectric field is increased. The former lowers the energy of the carriers and the latter raises the separation of the electron and the hole. For a local increase in the well width, a local potential minimum is formed by the diminished quantum confinement in

combination with the quantum confined Stark effect. The reduction of the overlap integral is induced by the localization of the electron and hole at the opposite sides of the quantum well, such that a larger width corresponds to a lower overlap (see Fig. 5.26). Strain fluctuations could provide localization centers by the accompanying variation of the piezoelectric field. The localization centers are the fully strained sections of the quantum well, as the energy of the charge carriers is lowest in this case. However, this partial release of the strain should be visible in RSMs of reflections with in-plane component. This is not the case for samples of high structural perfection, such that strain fluctuations can be excluded. In order to be efficient, the spacing of the localization centers should be on the order of the diffusion length, which has been estimated from cathodoluminescence mappings to be in the range of 60 nm to 200 nm [208, 57, 209, 204].

5.5.2 Compositional fluctuations in quantum wells

Compositional fluctuations in $In_xGa_{1-x}N$ have been used as the main explanation for the exceptionally high quantum efficiency of optoelectronic devices, as they were experimentally observed in bulk layers as well as quantum wells (i.e. [210, 211]). It was proposed, that the driving force behind this inhomogeneity is the large lattice mismatch of InN and GaN, leading to a miscibility gap for higher indium contents [212]. The scale of the reported fluctuations is still under discussion, but in quantum wells of high structural perfection, the diameter of the In-rich clusters are reported to be on the order of 15 nm [210]. Those observations are based on the analysis of TEM images, which provokes the question, whether the fluctuations were produced by the ion milling during the specimen preparation. From extended X-ray absorption fine structure studies, evidence for some clustering on an atomic scale was found, and in this case the samples were as-grown [213]. Although the samples investigated were thick films, it can not be excluded, that fluctuations are present in $In_xGa_{1-x}N$/GaN quantum-well structures.

In spite of this it is doubtful, that they form the major localization center in quantum wells, in particular in view of the observed changes of the photoluminescence upon barrier doping. The impact of compositional fluctuations can be estimated from the transition energies and the overlap integral in quantum wells plotted in dependence on the indium molar fraction of the quantum well. This was done in Fig. 5.27, which contains these values as obtained from calculations of the bandstructure. The well width used was 2.3 nm, and the piezoelectric field was assumed to linearly follow the composition as observed experimentally [52]. The variation of the band gap with composition was based on the work by McCluskey *et al.* [26], and the Si concentration in the GaN barrier of the doped MQWs was set to 8×10^{18} cm^{-3} as before.

As seen in Fig. 5.27(a) the variation of the peak energy depends very sensitively on the indium molar fraction of the well, which can be expected from the large bowing parameter [26]. It should be noted, that the transition energies of the doped and the undoped structures are plotted. Due to the low quantum-well thickness the two data sets coincide almost perfectly. This means, that the PL peak energy is *not* expected to change with the barrier doping, if the same microstructure of the compositional fluctuations is assumed. Should the compositional fluctuations be responsible for the variation of the luminescence peak energy, then the doping has to change the fluctuation

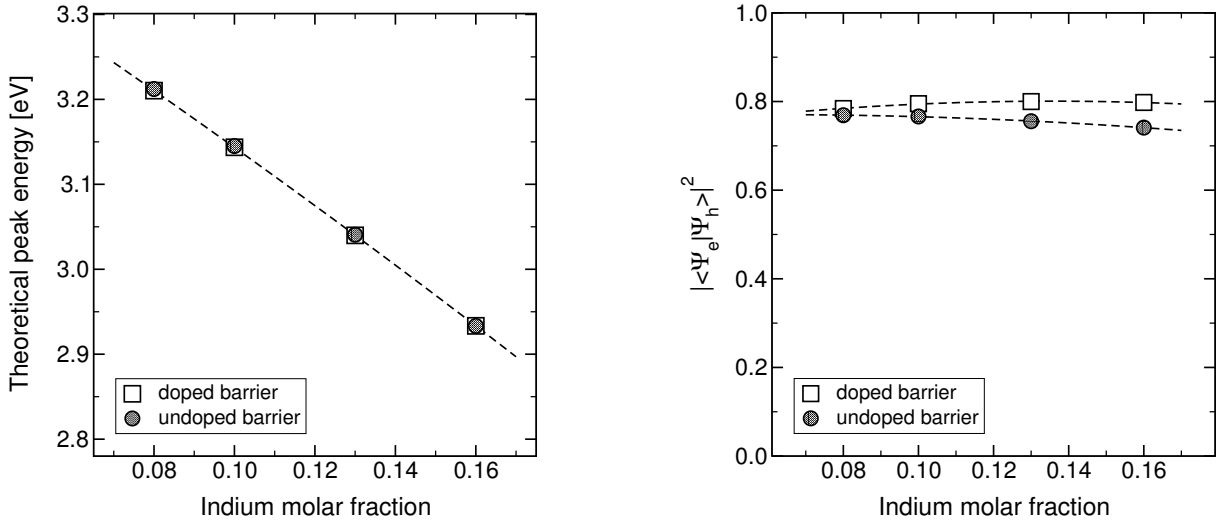

(a) Photoluminescence peak energy

(b) Overlap integral

Figure 5.27: The theoretical photoluminescence peak energy and the overlap integral for varying quantum-well *composition*. The well width was assumed to be 2.3 nm. The Si doping levels were 2×10^{16} cm^{-3} and 8×10^{18} cm^{-3} for the undoped and the doped structure, respectively. The piezoelectric field was varied linearly with the In molar fraction of the well.

structure itself, i.e. the fluctuations have to be reduced upon Si doping to explain the observed blueshift seen in Fig. 5.17 on page 118. A reduction of the indium fluctuation would mean a reduction of the localization and should correspond to a lower intensity, since the nonradiative recombination rate is increased. This is not observed. It could be circumvented by a much higher recombination rate in the doped structures, but if one calculates the overlap integral for different compositions as shown in Fig. 5.27(b), one again finds almost no significant changes, neither by doping nor by a variation of the composition. Thus, the PL decay times should not change much, if the structures contain doped barriers, which is again in contradiction to literature [197].

Furthermore, one can make a *very* rough estimate of the compositional fluctuations from the FWHM of the low-temperature photoluminescence as described in [54]. This analysis yields an upper limit of the variation of the indium content in the quantum well. For the undoped QW thickness series described in Section 5.4 one finds a relative variation of $\pm 8\%$, such that the indium molar fraction of the wells amounts to $x_{In} = 0.097 \pm 0.007$. Since the estimate provides an upper limit, this is comparable to alloys in other III-V material systems.

5.5.3 Thickness fluctuations

The fluctuation of the QW thickness is presumably caused by the spiral growth mode of GaN at low growth temperatures [214, 189]. This changes towards a more two-

dimensional growth mode as soon as the GaN is doped with silicon or the growth is performed on Si-doped material [200, 189]. It might be layer-by-layer growth or step flow growth. The according transition in the surface structure is seen in the AFM images in Fig. 5.28, which were taken from Ref. [189].

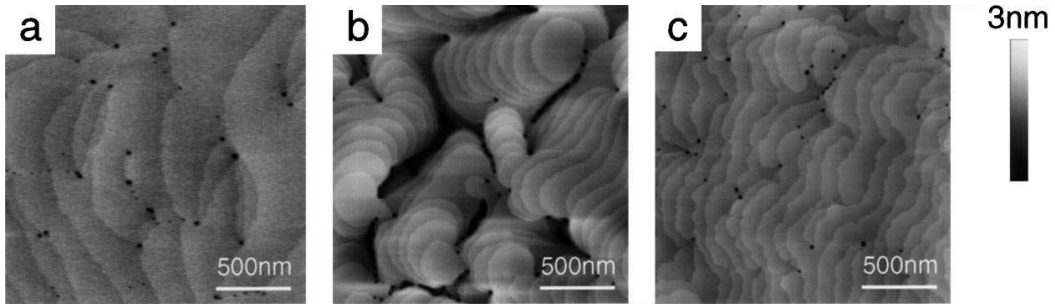

Figure 5.28: AFM images of a) underlying GaN grown at high temperature (∼1050°C), b) 7 nm undoped GaN grown at 800°C, (c) 7 nm GaN grown at 800°C, but doped with $\sim 2 \times 10^{19}$ cm^{-3} silicon. Images taken from Ref. [189].

The underlying high-temperature GaN in Fig. 5.28(a) shows the well-known smooth surface structure with atomic steps. Undoped GaN grown on this material at low temperature (800°C) develops strong thickness fluctuations with a typical lateral scale of 500 nm, as seen in Fig. 5.28(b). Upon doping the low-temperature layer with silicon, the surface roughness significantly decreases and gets close to the value of the high-temperature GaN (Fig. 5.28(c)). This starts at doping levels around 2×10^{18} cm^{-3} but is distinct only at high levels around 2×10^{19} cm^{-3} [189]. Therefore, thickness fluctuations on a lateral scale of 500 nm can be assumed to be present in undoped material. For the samples investigated in this work, the concept of a reduced thickness fluctuation with doping coincides with the rising satellite intensities in Fig. 5.16(c) and the estimated thickness variation of 50% for the undoped structures compared to 0.3 nm for highly doped structures (see Fig. 5.24). The importance of the quantum well thickness for the luminescence was discussed in the previous section, such that those results can now be viewed under the aspect of well thickness fluctuations.

Similar to the discussion of the compositional fluctuations, the graphs in Fig. 5.29 contain the peak position and the overlap integral versus the QW thickness. The graphs were already shown before, and are included here for completeness. Comparing the peak energy in Fig. 5.29(a), it is seen that QW thickness variations on the order of one monolayer can already generate a potential drop around 15 meV, specially for thin wells. Therefore, QW thickness fluctuations on the order of more than 1 nm as seen in the AFM images in Fig. 5.28 can generate localization centers with an energy difference of ∼100 meV. This can explain the red shift of the experimental data with respect to the theoretical values. In addition, the overlap integral depicted in Fig. 5.29(b) is very sensitive to the local thickness and the barrier doping level. For undoped structures, the overlap integral drops quickly with QW thickness, i.e. in the localization centers. Therefore, the radiative recombination of charge carriers is relatively slow compared to samples with doped barriers. For doped barriers, the internal field is screened and the overlap

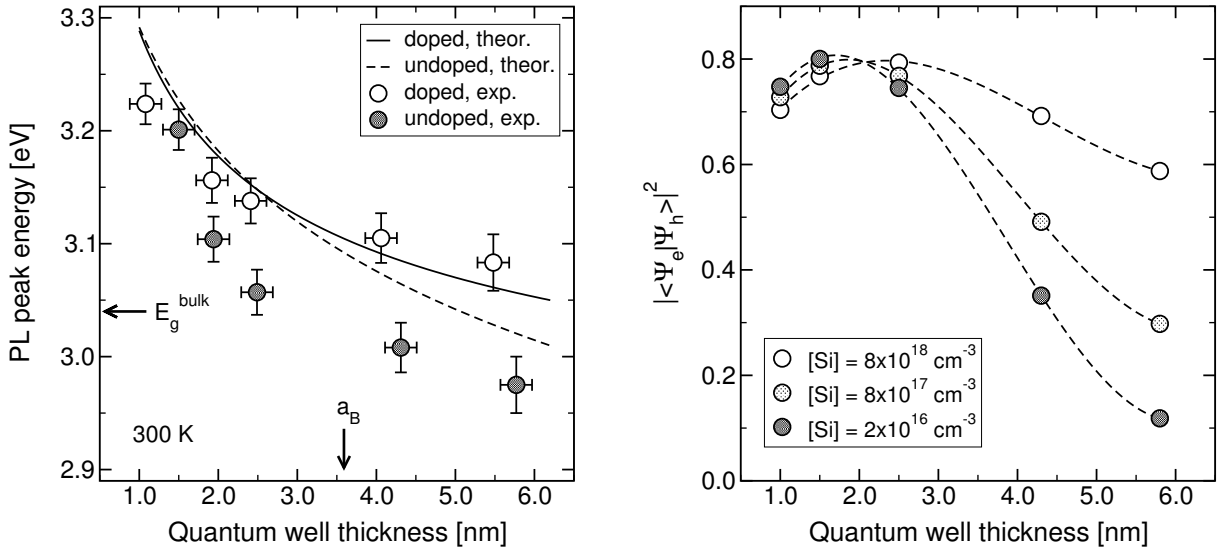

(a) photoluminescence peak energy

(b) overlap integral

Figure 5.29: The theoretical photoluminescence peak energy and the overlap integral for varying quantum-well *thickness*. The indium molar fraction in the well was assumed to be 0.097.

integral is much larger. Thus, the recombination is fast an the decay time of the PL intensity drops with doping, which is in accordance with literature [197]. And since a fast radiative recombination prevents the diffusion of the charge carriers into nonradiative recombination centers, the luminescence intensity has to increase accordingly.

The improved interface perfection and well thickness homogeneity with Si doping should reduce the localization in the quantum wells, but the much faster radiative recombination limits the diffusion length drastically, such that the nonradiative recombination rate decreases. Additionally, thickness fluctuations with the height of one (Ga-N) bilayer will always be present in the quantum wells, due to the natural stepped surface structure of GaN. These represent localization centers with a depth of 5-30 meV, depending on the average well thickness, and will always limit the diffusion of charge carriers. And the surface improvement is significant only at high doping levels, whereas the screening already starts at lower doping level, in particular for well thicknesses clearly exceeding the exciton Bohr radius.

The microstructure of the luminescence can be resolved in cathodoluminescence intensity mappings. An example for InGaN/InGaN multiple quantum-well structures is shown in Fig. 5.30, which contains CL mappings for two identical structures except for the barrier doping. The images were taken from Ref. [187]. The mapping in Fig. 5.30(a) depicts the undoped structure. It shows an inhomogeneous luminescence intensity with a feature size of ∼500 nm, which is on the lateral scale of typical thickness variations. The mapping in Fig. 5.30(b) originates from a structure employing doped barriers. Again, the luminescence intensity fluctuates on a scale of ∼500 nm, but the density

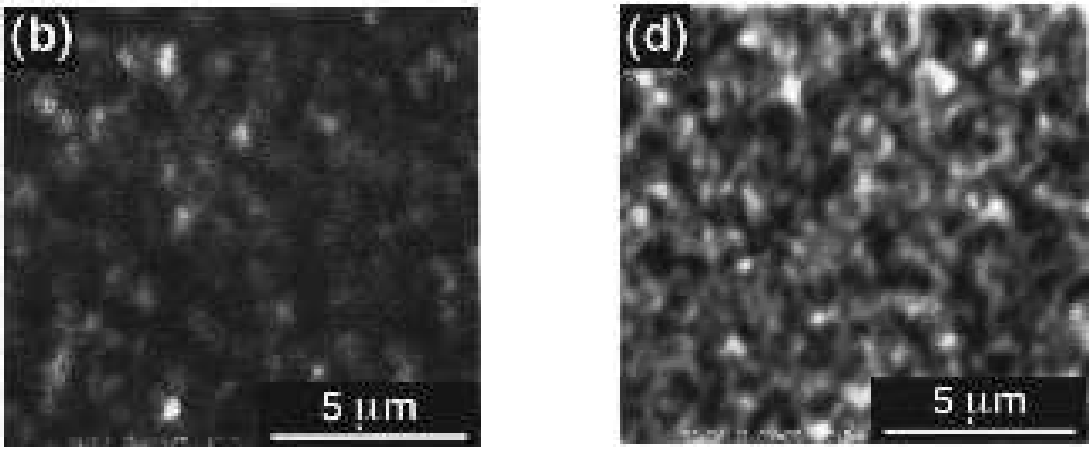

(a) undoped barrier **(b)** doped barrier

Figure 5.30: Cathodoluminescence intensity mappings of 3 nm $In_{0.2}Ga_{0.8}N$/ 5 nm $In_{0.02}Ga_{0.98}N$ multiple quantum-well structures. The Si doping of the barrier layers has strong influence on the microstructure of the luminescence. Images taken from Ref. [187].

of the bright spots has increased. This would be consistent with the partial screening of the internal field, which mainly affects areas of higher well width. Accordingly, the potential structure for the localization did not change significantly, whereas the recombination is much faster and the localization centers gain in efficiency. The scale of the intensity fluctuations seen in CL is typical for $In_xGa_{1-x}N$ quantum-well structures grown on heteroepitaxial GaN and found throughout the literature [208, 57]. In contrast to this, quantum-well structures grown on the wings of lateral epitaxial overgrowth (LEO) templates show almost no intensity fluctuations [206, 204]. This is probably caused by the suppressed low-temperature spiral growth mode in these areas, since no screw-component threading dislocations are available to initiate this growth mode.

5.5.4 Summary : Why the efficiency of quantum wells improves upon silicon doping of the barriers

The experiments, literature references and calculations presented so far point towards a light emission mechanism, which is governed by quantum well thickness fluctuations superimposed by the internal piezoelectric field. The screening of the internal field alone can not explain the experimental observations, and compositional fluctuations can be ruled out as well (see Section 5.5.2). Fluctuations in thickness are visible in AFM images (Fig. 5.28), and get reduced with the Si doping of the barriers (Fig. 5.16(c) and [198]). They are generated due to the spiral growth mode at low temperature [214, 189], such that they are prominent for the low-temperature growth on heteroepitaxial GaN, whereas they are less pronounced for low-temperature material grown on LEO tem-

plates due to the lack of screw-component dislocations [209, 204, 215]. Segments of higher well thickness are local potential minima in doped as well as in undoped structures (Fig. 5.29(a)). Due to the exciton Bohr radius of 3.6 nm, the piezoelectric field is less important in sections of lower thickness and dominant in sections of larger thickness. It causes a redshift due to the quantum confined Stark effect and reduces the overlap integral of electron and hole wavefunction (Fig. 5.29(b), 5.29(a) and [201]). The screening of this field due to doping is most efficient in the areas of higher well thickness, thereby locally raising the overlap integral and the radiative recombination rate in the localization centers (Fig. 5.29(b) and [198]). Therefore, the Si doping makes the localization centers formed by sections of larger well thickness much more efficient. It reduces the diffusion length and accordingly the fraction of nonradiative recombination. It raises the localization of the hole and it improves the perfection of the quantum-well thickness and the interfaces. Furthermore, the increased electron density induced by the Si doping might block the localized states of the threading dislocations, which act as nonradiative centers [204, 206, 205].

This concept could be verified by a set of quantum-well structures with different Si doping levels of the barriers, which are grown on LEO templates. Since thickness fluctuations caused by the spiral growth mode at low growth temperature are lower on the wing regions of this material, the increase in photoluminescence intensity due to doping should be much less pronounced.

" There is something fascinating about science. One gets such wholesale returns of conjecture out of such a trifling investment of fact. "

Mark Twain (1835-1910)

Summary

This thesis accompanied a large part of the research work related to the epitaxy of group-III nitrides at the University of Bremen. Since the objective of the institute is the development of optoelectronic devices, most of the research is aimed at the realization of laser structures. Molecular Beam Epitaxy (MBE) was the first growth method investigated in Bremen, which started in 1996 with the installation of the two MBE chambers by EPI and the initial set-up of the cleanroom facilities. The second system acquired was the Metalorganic Vapor Phase Epitaxy (MOVPE) reactor by Thomas Swan, whose installation started in 1999. The development of the initial growth processes utilizing the MOVPE were largely connected to the research within this thesis. To monitor the growth process *in situ*, a reflectometry setup was developed. It measures the reflectance of laser light from the growing surface under normal incidence. Due to the promising initial results, the equipment was improved to provide a position-resolved signal, which is additionally corrected for the thermal background radiation. A simulation program based on the Jones matrix formalism was written to understand the data more quantitatively.

The mainly used substrate was sapphire, such that the common approach of the high-temperature growth of GaN onto a recrystallized GaN nucleation layer (NL) was chosen. In order to obtain a stable process and to understand the evolution of the growth, the growth sequence was broken down into the individual steps, which were investigated separately. The initial step is the annealing of the substrate in a hydrogen atmosphere. It was found to be mandatory to perform this step at lower pressures around 100 Torr to avoid the contamination of the substrate surface with deposits from the reactor walls or the susceptor. Although not discussed in detail, the nitridation of the substrate should be kept short, which is in accordance with Ref. [124]. The deposition of the nucleation layer at low temperature was shown to be an island growth mode arising from the large lattice mismatch and the low temperature. The typical growth temperature around 550°C is close to the transition temperature from kinetically limited growth to transport limited growth. Since the transport limited growth is more reproducible, the growth conditions should be chosen accordingly. The minimum thickness of the NL was found to be ∼25 nm, which corresponds to a homogeneous coverage of the substrate. The recrystallization of the NL during the ramp to high temperature (∼1050°C) as well as the successive island growth mode are largely determined by the composition of the reactor atmosphere and the total pressure in the reactor. This is caused by the instability of GaN in a hydrogen-containing environment at high temperatures, which is intensified at atmospheric pressure. The surface can be partially stabilized by the ammonia partial pressure in the reactor. According experiments were discussed

on the background of a thermodynamic description of the decomposition reaction. In particular, a rate equation model was developed to understand the dependence of the equilibrium partial pressure of Ga on the chemistry of the atmosphere.

Since the edge-component threading dislocations develop as a consequence of the island coalescence at high temperature, their density can be controlled via the island growth mode. In general, a low threading dislocation density in the layer is obtained for growth processes showing an elongated island growth mode, i.e. for a large diameter of the high-temperature islands, as those grow free of dislocations. To optimize the growth process, one has to distinguish between growth at low pressure (LP, ∼100 Torr) and at atmospheric pressure (AP, ∼700 Torr), as the decomposition of GaN in hydrogen increases severely with the reactor pressure. In order to obtain low threading dislocation density films at LP, the goal is to *increase* the average grain diameter. This is achieved by a reduced ammonia partial pressure during all stages of growth. A NL grown at a low molar V/III ratio provides fewer potential nucleation sites, and the raised hydrogen partial pressure during the recrystallization and the initial high temperature growth enhances the island selection. Depending on the chosen set of parameters, the possible average grain diameter can be up to 1 μm. In contrast to this, the growth at AP has to compensate the strong decomposition, thus the goal is to *stabilize* the GaN film. This is done by raising the ammonia partial pressure in all steps. A high V/III ratio during NL growth generates a high nucleation site density, and an increased ammonia pressure during the recrystallization and the initial HT growth compensates the decomposition and selection to some extent. The lowest average grain diameter obtained in these films was approximately 0.7 μm, and the largest one amounted to roughly 4 μm. Samples with even larger island diameter did not coalesce within reasonable growth times.

Another method to reduce the threading dislocation density is the usage of a SiN interlayer, as proposed by Tanaka *et al.* [143]. The SiN is deposited *in situ* using ammonia and silane as the source materials. It forms a micromask on the GaN layer, thereby inducing a second island growth mode. During the overgrowth of the mask, many dislocations change their line direction and propagate in the (0001) plane, where they can annihilate with dislocations of opposite Burgers vector. The SiN was demonstrated to grow in flat, triangular shaped islands with a high lateral growth rate. Presumably, the nucleation of the successive GaN starts in the holes between these islands, which would explain the sensitivity of the island growth mode to the SiN deposition time. The average island diameter increases with a longer treatment of the surface with silane and ammonia, which would correspond to a larger spacing of the nucleation sites. It seems, that no or only few threading dislocations form during the coalescence of the islands, such that the threading dislocation density at the surface can be reduced by more than an order of magnitude.

Extending the work of H.Heinke, a model was developed to measure the threading dislocation density of MOVPE-grown GaN films utilizing x-ray diffraction (XRD). It uses the concept of mosaic crystals, which describes the microstructure of the smooth layer as many dislocation-free, but tilted and twisted crystals. Since the average grain dimensions provide the lateral and the vertical coherence lengths, it is possible to understand the broadening of reciprocal lattice points (RLP) due to different microstructures. While the FWHM of the **002** reflection is mainly caused by the tilt in the layer,

the **302** RLP is broadened due to twist and finite size effects. Accordingly, the rocking curve FWHMs of the **002** and the **302** RLPs are used as the input parameters together with the average grain diameter in the film, which can be estimated from reflectometry. The latter measures the film thickness at island coalescence, such that the average grain diameter follows from the island geometry. It was shown by plan-view TEM images, that the edge- and screw-type threading dislocation densities can be determined within reasonable limits of accuracy utilizing XRD and the model of mosaic crystals.

The strain state at room temperature of the studied GaN layers was found to correlate with the island diameter at coalescence as well. Due to the thermal mismatch to the substrate, GaN grown on sapphire is compressively strained at room temperature. This compressive strain is partly compensated by an intrinsic, tensile strain, which decreases with an increasing diameter at coalescence. Two models were proposed to explain the formation of tensile strain during growth at high temperature. The first is based on the pseudomorphic growth on a highly defective NL, and the second describes the tension as a consequence of the gap closure during island coalescence. The gap is closed elastically, which then causes the observed tensile strain. The latter model was investigated quantitatively, which provided an average gap spacing of 2.2 Å. Since the intrinsic strain originates at the grain boundaries, the local strain distribution is expected to be inhomogeneous across the layer. This inhomogeneity is measured by the heterogeneous strain. It was found to be released elastically with the inverse film thickness and to be of the same magnitude as the intrinsic, coalescence-related strain. Both findings support that the tensile strain during growth develops as a result of island coalescence.

An essential element of light emitting devices is the $In_xGa_{1-x}N$-based quantum well (QW), which is used in the active region. Corresponding structures were grown by MBE as well as by MOVPE. Within the MBE studies, it was possible to demonstrate the improvement of the structural perfection and the photoluminescence spectra of the QWs with the use of MOVPE-grown templates. For sure, this is related to the superior surface smoothness of these templates, but it it might be possible as well, that the different polarity contributes to the improvement. In order to prepare the surface of the template, a plasma cleaning procedure was proposed, which removes the oxidized surface layer. The boundary conditions for the QW growth are given by the formation of stacking faults and cubic inclusions, which require group-III rich growth conditions and a growth temperature above $\sim$600°C. Furthermore, in order to incorporate any indium, the Ga-flux has to be below the N-flux.

The MOVPE of $In_xGa_{1-x}N$ requires the usage of a nitrogen atmosphere due to the instability of InN in hydrogen. The most important growth parameters with regard to the quantum efficiency of QW structures are the growth temperature and the growth rate. The photoluminescence (PL) was studied for different QW thicknesses and for different Si doping levels of the GaN barriers. In accordance with literature, the optimum QW thickness was found to be $\sim$3.5 nm for doped as well as for undoped MQW structures. The Si doping of the barriers was demonstrated to enhance the PL intensity at room temperature substantially, whereas the improvement is less pronounced at 4 K. The increase is accompanied by a blueshift of the PL peak energy. The QW structures were simulated numerically, taking the piezoelectric field in the well into account. The experiments, literature references and calculations presented point towards a light

emission mechanism, which is governed by quantum well thickness fluctuations superimposed by the internal piezoelectric field. The screening of the piezoelectric field alone can not explain the experimental observations, and compositional fluctuations can be ruled out as well. Segments of higher well thickness are local potential minima in doped as well as in undoped structures. Due to the exciton Bohr radius of 3.6 nm, the piezoelectric field is less important in sections of lower thickness and dominant in sections of larger thickness. The screening of this field due to doping is most efficient in the areas of higher well thickness, thereby locally raising the overlap integral and the radiative recombination rate in the localization centers. Therefore, the Si doping makes the localization centers formed by sections of larger well thickness much more efficient. This reduces the diffusion length and accordingly the fraction of nonradiative recombination in MQW structures with Si doped barriers. Furthermore, the increased electron density induced by the Si doping can block the localized states of the threading dislocations, which act as nonradiative centers [204, 205]. In particular, this effect might be relevant for the changes observed for low doping levels.

Together with S. Figge, C. Zellweger and C. Petter, the first GaN laser grown in Bremen was realized. S. Figge optimized the p-type doping, C. Zellweger processed the devices and C. Petter developed the dielectric mirrors. The key issues to achieve the lasing were the design of the active region with optimized growth parameters of the wells, the barriers and the $Al_xGa_{1-x}N$ blocking layer, the p-type doping without pyramidal defects, and the device processing including the wet etching of the facets, electrically stable contacts and the application of dielectric mirrors. The spectra and an L-I curve are shown in Fig. S.1 on the facing page together with a photograph of the operating device.

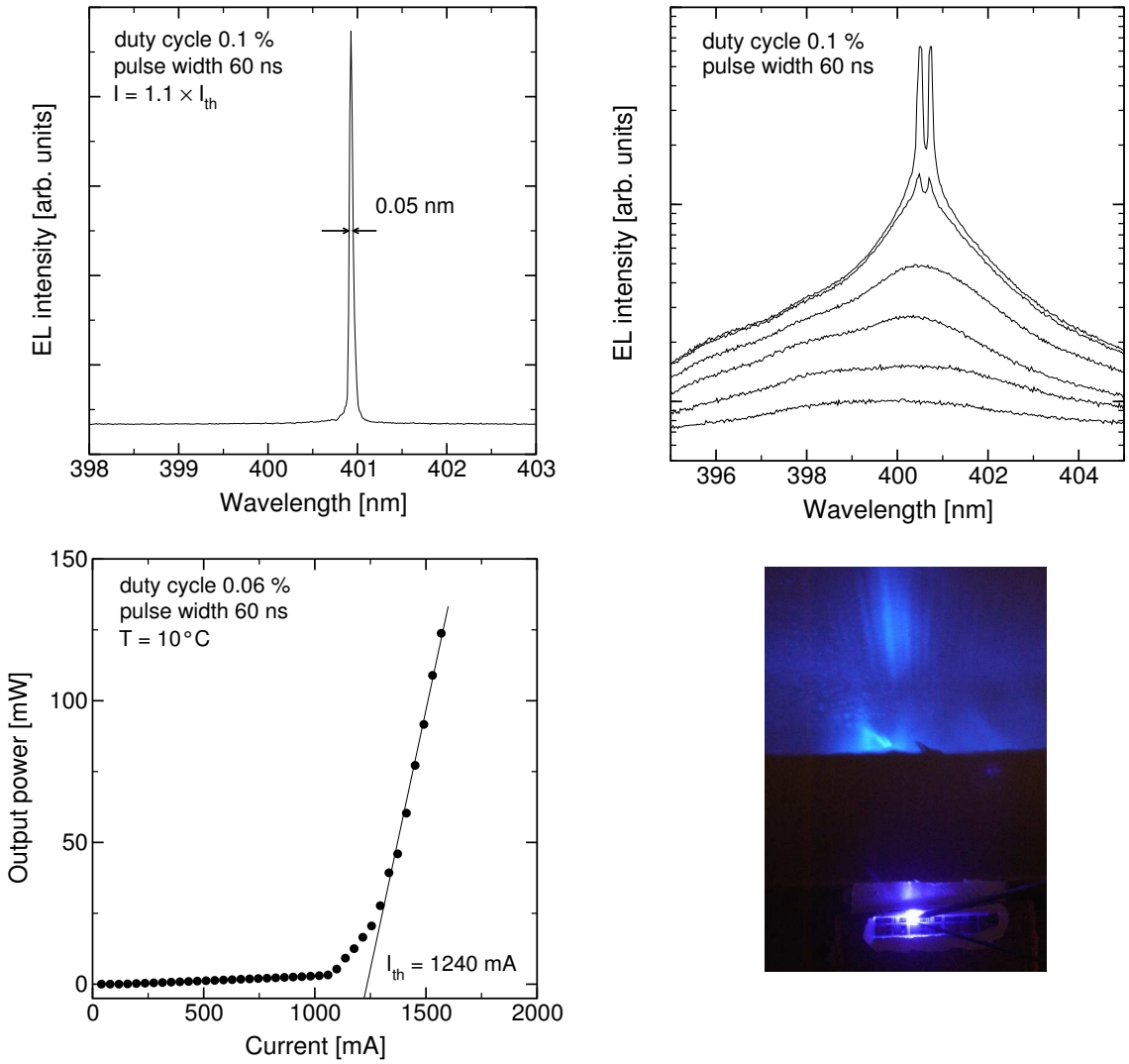

Figure S.1 : Spectra and L-I curve of the first GaN laser diode grown in Bremen.

Appendix A

Jones' matrix formalism

Another way of describing the normal incidence reflectance of a multilayer structure is a matrix formalism where each interface and each layer is described by an interface and a layer matrix, respectively. These are 2×2 matrices linking the electric field amplitude outside the uppermost layer with the electric field at the semi-infinite substrate [127]. Each layer with complex refractive index $N_i = n_i - ik_i$ is characterized by a layer matrix

$$L_i = \begin{bmatrix} \exp(i2\pi N_i d/\lambda) & 0 \\ 0 & \exp(-i2\pi N_i d/\lambda) \end{bmatrix}, \tag{A.1}$$

describing the wave propagation and an interface matrix

$$I_i = \frac{1}{2N_{i-1}} \begin{bmatrix} N_{i-1}+N_i & N_{i-1}-N_i \\ N_{i-1}-N_i & N_{i-1}+N_i \end{bmatrix}, \tag{A.2}$$

which links the layer i with layer $i-1$ above it. Assuming the sample to consist of n layers, the field amplitudes in the vacuum are connected to the amplitudes at the substrate through a product of all matrices :

$$\begin{bmatrix} E_f \\ E_b \end{bmatrix}_{surface} = I_1 L_1 I_2 L_2 \cdots I_n L_n I_{sub} \begin{bmatrix} E_f \\ 0 \end{bmatrix}_{substrate} \tag{A.3}$$

$$= I_1 L_1 I_2 L_2 \cdots I_n L_n \begin{bmatrix} E'_f \\ E'_b \end{bmatrix}_{substrate}. \tag{A.4}$$

The complex electric field amplitudes E are labeled according to the propagation - E_f corresponding to the forward direction into the sample and E_b to the backward direction. Furthermore, it is assumed that the backward electric field amplitude in the substrate is zero as no light comes from inside the semi-infinite substrate. In equation A.4 the interface matrix of the nth layer has been multiplied with the substrate amplitude field vector. Therefore, the primed terms are the field amplitudes inside the nth layer at the interface with the substrate. As there is no difference between a substrate-layer and a layer-layer interface, equation A.4 describes the optical properties of a layered structure on top of a generalized substrate, which could be a multi-layer structure as

well. This has been used for the virtual substrate model, where all matrix multiplications from I_2 to the substrate electric field vector have been performed, resulting in an expression of a single-layer structure on a virtual substrate [216] :

$$\begin{bmatrix} E_f \\ E_b \end{bmatrix}_{surface} = I_1 L_1 \begin{bmatrix} E_f'' \\ E_b'' \end{bmatrix}_{vs} . \tag{A.5}$$

This is an equivalent expression of equations 2.5 and 2.6, which will be shown for a three-layer structure as used before. The lower interface is taken care of by using the electric field in the layer 2 at the lower interface like for the virtual substrate approach before. The upper interface is treated by using the interface matrix I_2 which then yields the electric field amplitude in layer 1 right at the interface :

$$\begin{bmatrix} E_f^1 \\ E_b^1 \end{bmatrix} = L_1 I_2 L_2 \begin{bmatrix} E_f^2 \\ E_b^2 \end{bmatrix} .$$

As the field at the interface is of interest, layer 1 has a thickness of zero, thus L_1 is an identity matrix. Then the matrix equation reads

$$\begin{aligned} \begin{bmatrix} E_f^1 \\ E_b^1 \end{bmatrix} &= \frac{1}{2N_1} \begin{bmatrix} N_1+N_2 & N_1-N_2 \\ N_1-N_2 & N_1+N_2 \end{bmatrix} \begin{bmatrix} \exp(i\beta) & 0 \\ 0 & \exp(-i\beta) \end{bmatrix} \begin{bmatrix} E_f^2 \\ E_b^2 \end{bmatrix} \\ &= \frac{1}{t_{12}} \begin{bmatrix} 1 & r_{12} \\ r_{12} & 1 \end{bmatrix} \begin{bmatrix} \exp(i\beta) & 0 \\ 0 & \exp(-i\beta) \end{bmatrix} \begin{bmatrix} E_f^2 \\ E_b^2 \end{bmatrix} \\ &= \frac{1}{t_{12}} \begin{bmatrix} \exp(i\beta) & r_{12}\exp(-i\beta) \\ r_{12}\exp(i\beta) & \exp(-i\beta) \end{bmatrix} \begin{bmatrix} E_f^2 \\ E_b^2 \end{bmatrix} . \end{aligned}$$

The reflectivity coefficient is calculated from the electric field ratio as shown in equation 2.2 on page 23 :

$$r_{123} = \frac{E_b^1}{E_f^1} = \frac{r_{12}e^{i\beta}E_f^2 + e^{-i\beta}E_b^2}{e^{i\beta}E_f^2 + r_{12}e^{-i\beta}E_b^2},$$

with $r_{23} = (E_b^2)/(E_f^2)$ and $r_{12} = -r_{21}$, this is equivalent to equation 2.5 on page 24 :

$$r_{123} = \frac{r_{12} + r_{23}e^{-2i\beta}}{1 - r_{21}r_{23}e^{-2i\beta}}.$$

Since the matrix approach provides a clearer scheme how to calculate reflectances this formalism was used for the program to simulate the reflectance transients to quantify the data obtained during growth.

Appendix B

Reflectometer electronics

B.1 Operation principle

The difficulties of accurate *in situ* reflectance measurements are the background radiation due to the susceptor temperature and the sample inhomogeneity. The former offsets the measured intensity depending on the growth temperature, and the latter reduces the reflectance oscillations, since the reflectance intensity is averaged. The problems can be circumvented by spatially resolved data acquisition, i.e. measurements only on certain spots on the susceptor. The difference of the light intensities collected on spots on the sample and on the susceptor is proportional to the reflectance of the sample surface, assuming the same background radiation in both spots. Using the reflected light intensity of the bare sapphire prior to the growth start as a reference, the real reflectance can then be extracted.

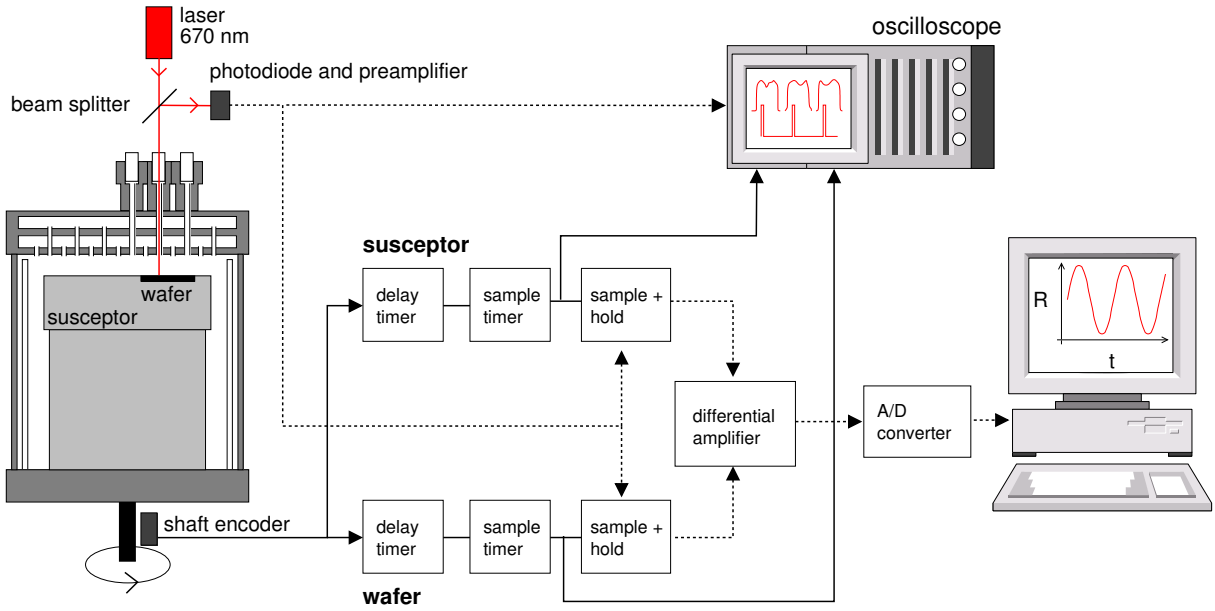

Figure B.1: Flow diagram of the reflectometer electronics.

The flow diagram of the reflectometer electronics is contained in Fig. B.1. A laser operating at 670 nm is used as a light source and the light intensity is measured over a beam splitter using a photodiode with preamplifier. Parallel to this, the position of the susceptor is tracked by an optical shaft encoder, which generates a trigger signal after each full rotation of the susceptor. This trigger signal starts two analog delay lines, which define the time offest of the two measurements. Each delay timer again starts a sample timer, whose time constant is equal for both the sample and the susceptor measurement. The sample timer activate a sample-and-hold integrated circuits, which collect the incoming signal during the defined periods and afterwards hold the two signals at the output. The difference of the two signals is then extracted in a differential amplifier with a gain of one, and transferred to the computer via an analog/digital converter. To adjust the measurement points, the two trigger signals as well as the actual intensity are monitored by an oscilloscope.

B.2 Circuits

The following figures contain the circuits of the individual reflectometer boards. I will not explain all details of the electronics, but the sections according to the flow diagram in Fig. B.1 are marked. The reflectometer contains four modules as listed in the following table.

board	units	figure
optical sensor	photodiode preamplifier	B.2
shaft encoder	light sensor counter	B.3
analysis electronics	2 delay timer 2 sample timer 2 sample and hold units differential amplifier	B.4
A/D converter	A/D converter	(not shown)

The sensor head mounted on the MOVPE showerhead contains a biased BPX 61 photodiode and two inverting amplifiers with offset correction (see Fig. B.2 on page 148). The preamplifier was integrated into the sensor to reduce the noise level of the signal and use a simpler shielding from external fields.

The shaft encoder in Fig. B.3 on page 148 is based on a concept I proposed, but the electronics were developed by A. Gesierich, who worked in our group as a student assistant. Besides the driving electronics of the light sensor a preamplifier and a Schmitt trigger is included to improve the signal shape. The counter to gain the postion information was realized in a programmable gate-array logic. One rotation of the susceptor equals 24 counts, such that a trigger signal is generated every eight counts corresponding to the spacing of two neighboring wafer pockets. Out of the three signals generated

within one full rotation, the wafer of interest is selected with a switch. Thus, a trigger signal at the output is generated after each full rotation of the susceptor.

The signal analysis board in Fig. B.4 on page 149 is founded on the analog timer chip NE555, which allows to define a continuous offset relative to the trigger signal from the shaft encoder. The sampling timer is also an NE555, with a fixed timing during which the sample and hold ICs LF 398 are activated. The high-pass filters between the timer ICs are required to obtain the correct signal shape for starting the ICs. The differential amplifier is an OPA 27A, which is a common low-noise operational amplifier. Furthermore, the analysis electronics provide the average reflectance of the whole susceptor, superimposed by the background heat radiation. The signal is recorded as an additional backup.

The A/D converter is a commercial module based on the chip LTC1290 (Linear Technology). It provides a resolution of 12 bit, which corresponds to a resolution of $\sim$1.2 mV at a maximum voltage of 5 V. The connection to the computer is implemented via the serial port.

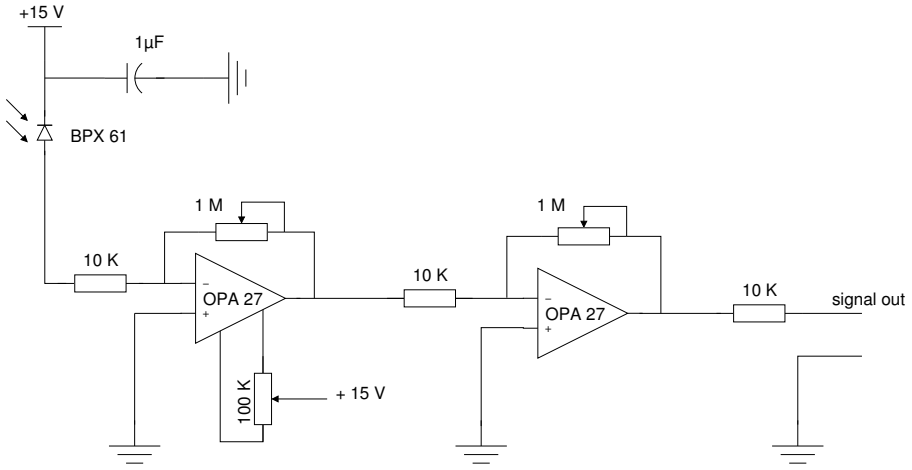

Figure B.2: Circuit of the optical sensor, which is mounted on the MOVPE showerhead.

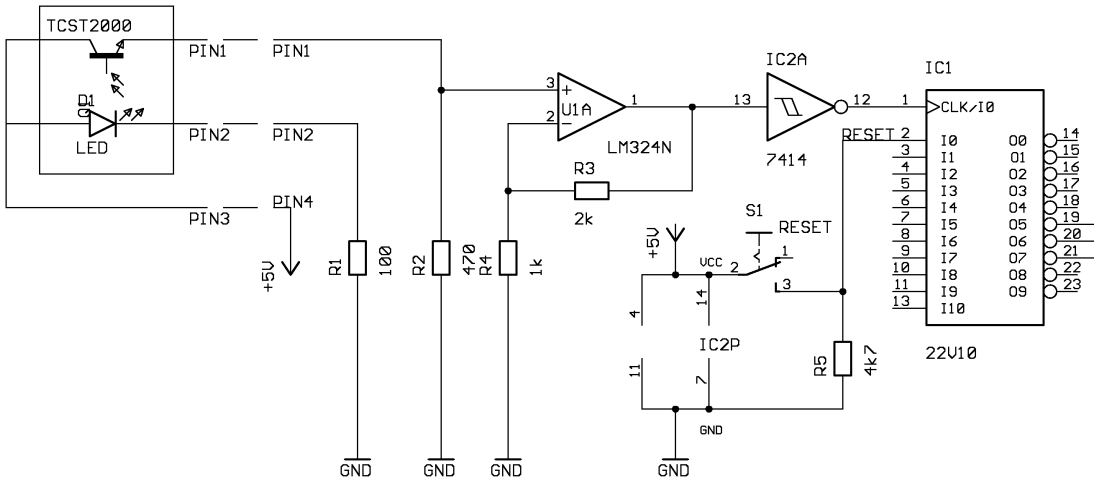

Figure B.3: Circuit of the shaft encoder, which is mounted on the susceptor axis.

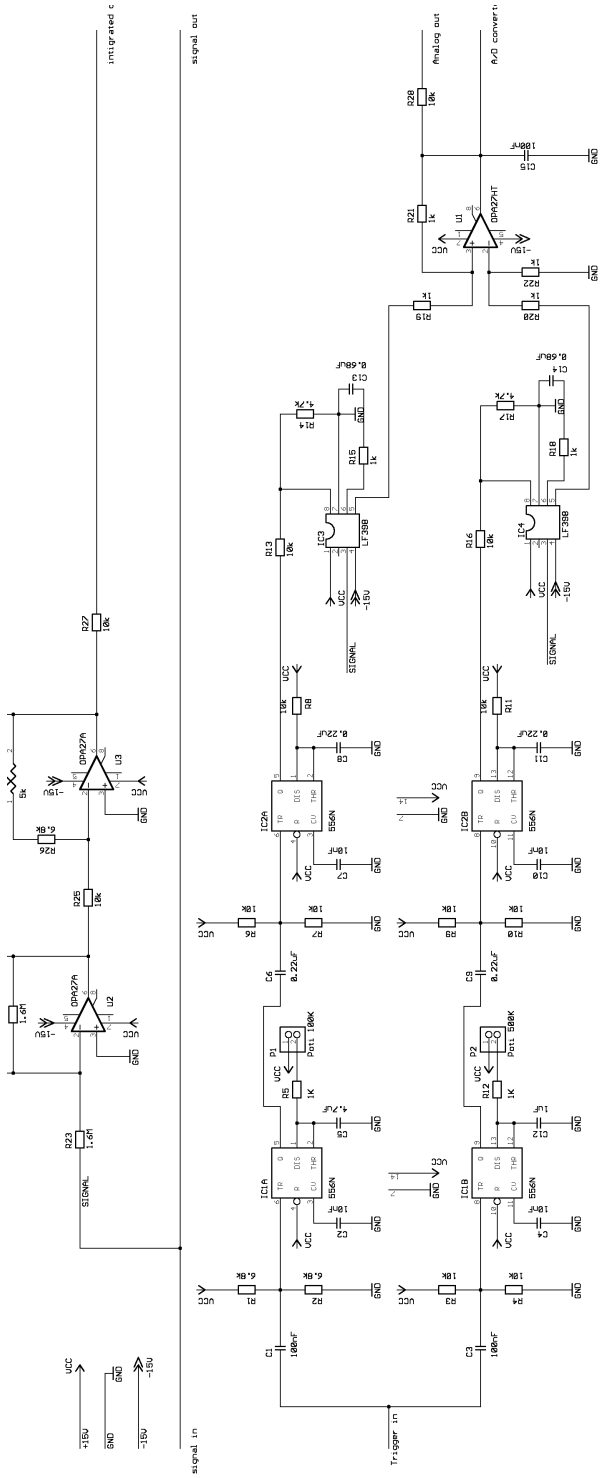

Figure B.4: Circuit of the signal analysis board, which generates a voltage proportional to the reflectance difference of two points on the susceptor.

Appendix C

Band structure simulations using 1DPoisson

The software was written by Prof. G. Snider, University of Notre Dame, USA. It numerically calculates the one-dimensional band structure of a semiconductor heterostructure based on the method of finite differences [217]. The structure is divided into several finite sections with a variable density of the mesh points. In order to obtain a meaningful result, it is important to choose the mesh spacing carefully, in particular at the interfaces of the individual layers and inside the quantum wells. Based on this mesh the program selfconsistently solves the Poisson equation to derive the distribution of the charge carriers and the structure of the conduction and the valence band. This band structure is the basis to solve Schrödinger´s equation and find the energy levels of the quantized states. The free charge carrier concentration is determined from the thermal activation of the doping atoms using Boltzmann statistics. The program is limited to calculations in thermodynamic equilibrium, i.e. current flow is not included.

Parameter	GaN	InGaN	References
Bandgap [eV]	3.42	3.42 - 3.93 x (x $<$ 0.15)	[26]
Conduction band offset [eV]	-	-2.751 x	[39]
Dielectric constant	8.9	8.9 + 6.4 x	[50, 11]
Donor binding energy [meV]	22	22 - 9 x	[43]
Acceptor binding energy [meV]	140	140	[218]
Rel. eff. electron mass [m_e]	0.2	0.2 - 0.09 x	[219, 220]
Rel. eff. heavy hole mass [m_e]	2.0	2.0 (for small x)	[221, 219]
Rel. eff. light hole mass [m_e]	0.74	0.74 (for small x)	[221, 219]
Electron mobility [cm^2/Vs]	250	250 + 550 x	(estimated)
Hole mobility [cm^2/Vs]	10	10	(estimated)
Electron recombination time [ns]	1	1	[222, 223]
Hole recombination time [ns]	1	1	[222, 223]

Table C.1: Parameter set used for the simulation of the quantum wells.

The specific material constants can be defined for binary as well as for ternary alloys, where the latter allows to define first and second order bowing parameters. Since the quantum-well structures of interest were limited to low indium mole fractions, only a linear variation of the material constants was assumed. Within the framework of literature values available, this seems to be justified for indium concentrations below 15%. The parameters contained in table C.1 were chosen after a wide literature review. They are either the most often reported ones, or for the case of inconsistent literature preferentially experimental values. The used references are listed in the table as well.

The program does not provide the possibility to include piezoelectric fields within the material definitions, therefore the fields were generated by 1Å thin highly doped layers at both interfaces of the quantum wells providing fixed δ-charges. As the volume of these layers is small, it does not disturb the doping profile of the whole structure. All calculations were done for single $In_xGa_{1-x}N$ quantum wells embedded in 300Å thick GaN. The program is limited to 500 mesh points, such that this came out to be a reasonable compromise of a density of mesh points and a sufficiently high layer thickness. The boundary conditions at the two surfaces were assumed to be ohmic, which ensures to have no potential drop across the whole structure.

Appendix D

Reactor-specific growth parameters

Besides the boundary conditions arising from the growth chemistry as described in section 3, the gas flow pattern in the reactor has significant influence on the growth. But without extensive numerical simulations of the flow geometry, it is impossible to gain any physical understanding of the experimental observations. Therefore, the objective of this appendix is to summarize the main growth parameters specific for the Thomas Swan 3×2″ close-spaced showerhead reactor. These data sets were collected in collaboration with Sven Einfeldt and Stephan Figge during the initial set-up of the reactor. The individual contributions can not be separated any more, such that this section should just be understood as a documentation. We studied the growth rate of GaN on sapphire in dependence on several different growth parameters, which will be plotted in the following. Basically, this section can be divided into two parts, each describing the growth at low and at atmospheric pressure.

The graphs characterizing the growth at **low pressure** are contained in Fig. D.1. The growth at low pressure is rather simple, since growth is possible in a wide parameter space. For example, the impacts of growth temperature, hydrogen flow, susceptor rotation and ammonia flow are small, and do not need to be detailed further. Important parameters are the temperature during nucleation layer growth, the TMG flow and the reactore pressure. The efficiency of the reactor is roughly constant, allowing to achieve very high growth rates without the waste of source material. Another advantage of the growth at low pressure is the high gas velocity, which reduces pre-reactions and the formation of particles contaminating the reactor.

Growth at **atmospheric pressure** (Figs. D.2 and D.3) is much more difficult, since the gas velocity is low and the flow pattern seems to be affected severely. The former enhances pre-reactions and particle formation, causing a lot of system maintenance. Basically, the growth was sensitive to almost all growth parameters investigated. The decomposition of the material is important, thus the growth rate quickly drops with temperature. The pre-reactions produce an offset of the TMG flow to achieve any growth. The flow pattern seems to change with the total flow and the susceptor rotation, since the growth rate collapses for high total gas flows or high rotation speeds. This could also be the case for the admixture of nitrogen to the gas phase, as the viscosity of nitrogen is different. The effect of the ammonia flow probably has to be ascribed to pre-reactions, as the growth rate drops with the ammonia flow.

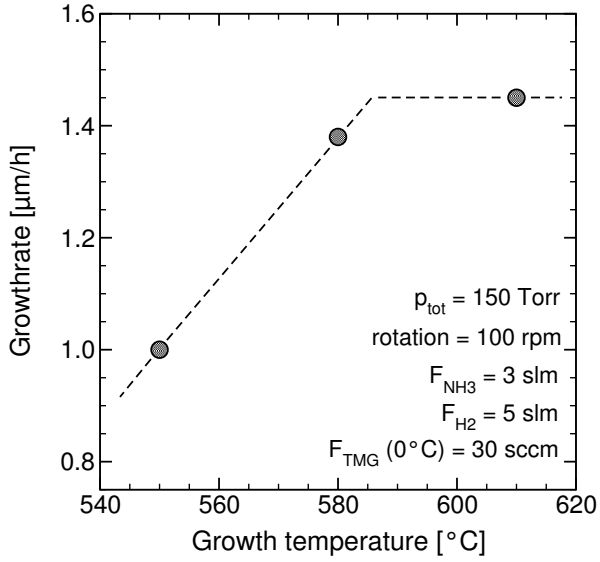

(a) Nucleation layer growth temperature

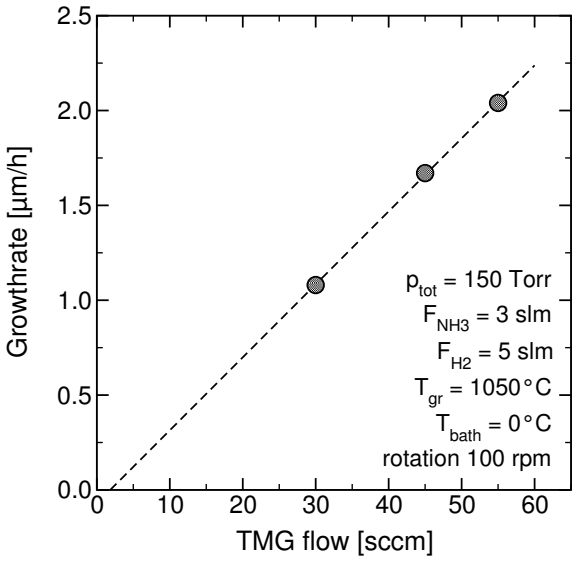

(b) TMG flow during epilayer growth

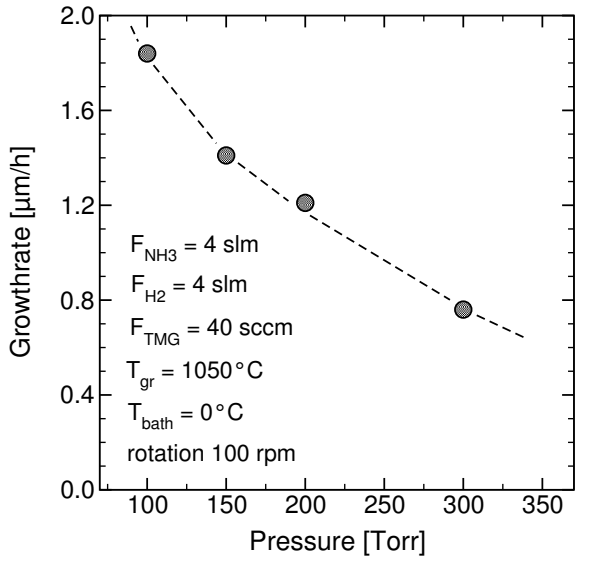

(c) Reactor pressure during epilayer growth

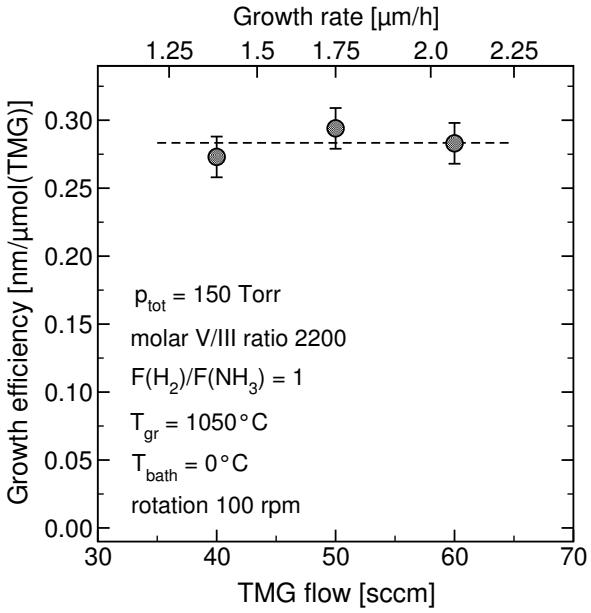

(d) Reactor efficiency during epilayer growth

Figure D.1: Characterization of the growth at **low pressure**. Shown are the growthrates (or the growth efficiency) in dependence on the denoted parameters.

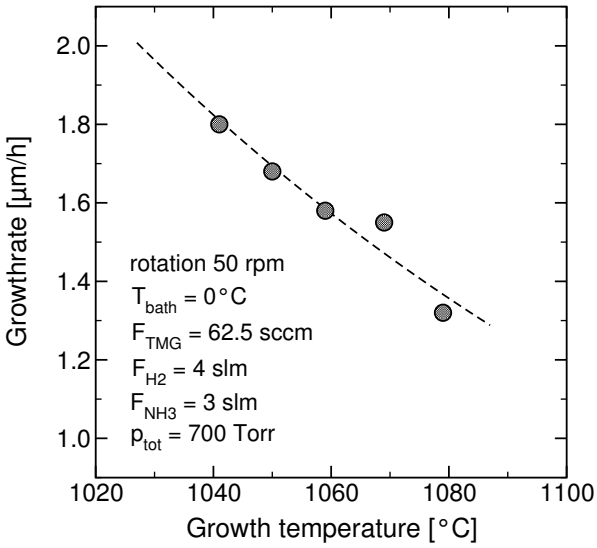

(a) Growth temperature

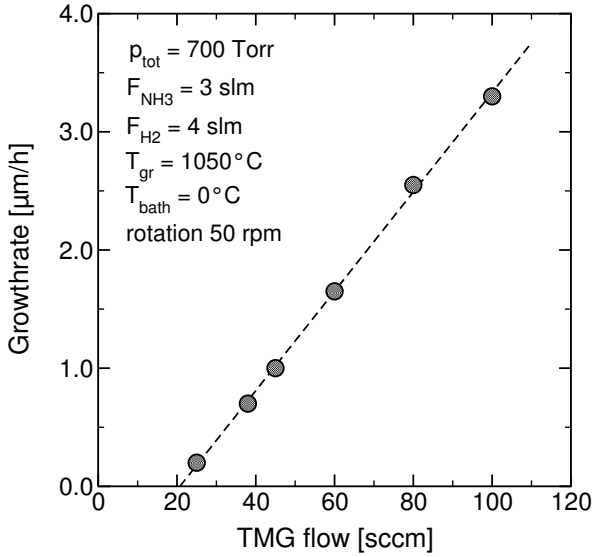

(b) TMG flow

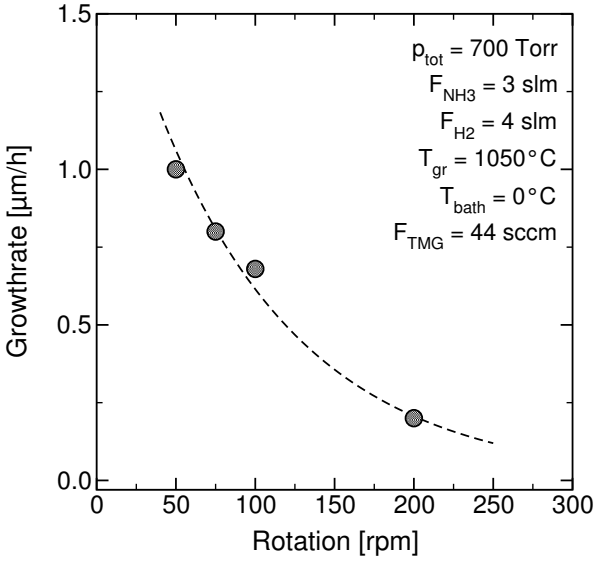

(c) Susceptor rotation speed

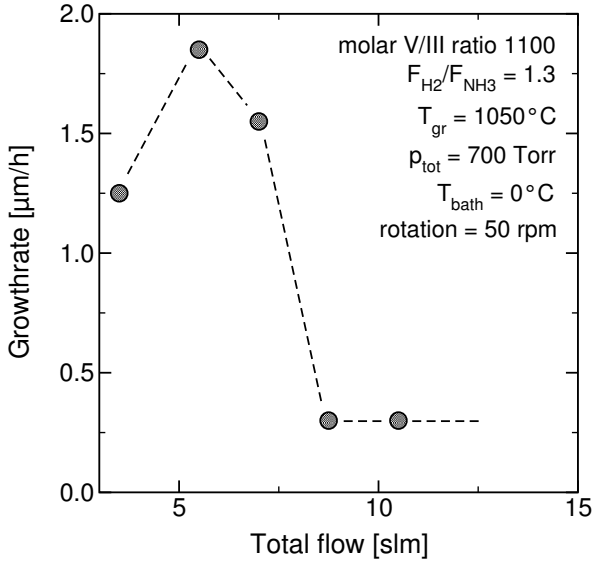

(d) Total gas flow

Figure D.2: Characterization of the epilayer growth at **atmospheric pressure**. Shown are the growthrates in dependence on the denoted parameters. The growth of nucleation layer material is not problematic and does not need to be discussed.

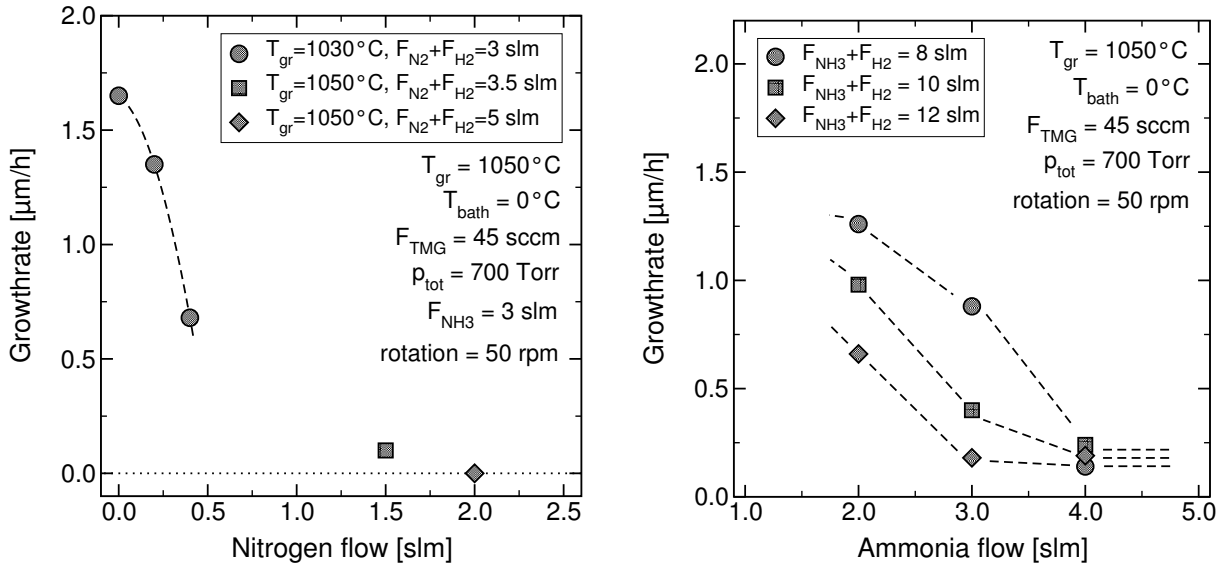

(a) Nitrogen flow under admixture

(b) Ammonia flow

Figure D.3: Characterization of the epilayer growth at **atmospheric pressure** in dependence on the denoted parameters.

Publications

First-author publications

1. T. Böttcher, S. Einfeldt, S. Figge, R. Chierchia, H. Heinke, D. Hommel and J.S. Speck
   The role of high-temperature island coalescence in the development of stresses in GaN films
   Appl. Phys. Lett. **78**, 1976 (2001).

2. T. Böttcher, S. Einfeldt, S. Figge, V. Kirchner, H. Heinke, D. Hommel, D. Rudloff, T. Riemann and J. Christen
   On the impact of microstructure on luminescence of InGaN/GaN multi quantum wells grown by molecular beam epitaxy
   phys. stat. sol. (a) **176**, 291 (1999).

3. T. Böttcher, S. Einfeldt, V. Kirchner, S. Figge, H. Heinke, D. Hommel, H. Selke und P.L. Ryder
   Incorporation of In during molecular beam epitaxy of InGaN
   Appl. Phys. Lett. **73**, 3232 (1998).

4. T. Böttcher, S. Einfeldt, S. Figge, V. Kirchner, H. Heinke, D. Hommel, F. Bertram and J. Christen
   Optical properties and the microstructure of InGaN grown by molecular beam epitaxy
   Acta Phys. Pol. A **94**, 260 (1998).

Co-authored publications

1. M. Godlewski, T. Böttcher, S. Figge, D. Hommel, T. Paskova and B. Monemar
   Influence of microstructure of GaN epilayers on light emission properties
   submitted to Appl. Phys. Lett.

2. S. Figge, R. Kröger, T. Böttcher, P.L. Ryder and D. Hommel
   Pyramidal defects in Mg-doped nitrides : A segregation model
   submitted to Appl. Phys. Lett.

3. S. Figge, T. Böttcher, C. Zellweger, M. Ilegems and D. Hommel
   Current spreading in AlGaN:Mg cladding layers of laser structures
   Proceedings of the Materials Research Society, accepted for publication

4. R. Kröger, S. Figge, T Böttcher, P.L. Ryder and D. Hommel
Mg-related defect formation during MOVPE growth of GaN based films studied by transmission electron microscopy
Proceedings of the Materials Research Society, accepted for publication

5. L. Plucinski, T. Strasser, B.J. Kowalski, K. Rossnagel, T. Böttcher, S. Einfeldt, D. Hommel, I. Grzegory, S. Porowski, B.A. Orlowski, W. Schattke, R.L. Johnson
Electronic band structure of gallium nitride – a comparative angle-resolved photoemission study of single crystals and thin films
Surface Science, in press (2002).

6. R. Chierchia, T. Böttcher, S. Figge, M. Diesselberg, H. Heinke and D. Hommel
Mosaicity of GaN Epitaxial Layers: Simulation and Experiment
phys. stat. sol. (b) **228**, 403 (2001).

7. C. Kruse, S. Einfeldt, T. Böttcher and D. Hommel
In as a surfactant for the growth of GaN (0001) by plasma-assisted molecular-beam epitaxy
Appl. Phys. Lett. **79**, 3425 (2001).

8. K. Lawniczak-Jablonska, R.J. Iwanowski, I.N. Demchenko, T. Böttcher, S. Einfeldt, D. Hommel, R. Cortes, R.C.C. Perera
Polarization dependent X-ray absorption studies of the chemical bonds anisotropy in wurtzite GaN grown at different conditions
J. Alloy. Compunds **328**, 77 (2001).

9. S. Einfeldt, T. Böttcher, S. Figge and D. Hommel
Thermally induced stress in GaN layers with regard to film coalescence
J. Cryst. Growth **230**, 357 (2001).

10. C. Kruse, S. Einfeldt, T. Böttcher, D. Hommel, D. Rudloff and J. Christen
Spatially modified layer properties related to the formation of gallium droplets on GaN (0001) surfaces during plasma-assisted molecular-beam epitaxy
Appl. Phys. Lett. **78** , 3827 (2001).

11. S. Figge, T. Böttcher, S. Einfeldt and D. Hommel
In-situ and ex-situ evaluation of the film coalescence for GaN growth on GaN nucleation layers
J. Cryst. Growth **221**, 262 (2000)

12. A. Kaschner, A. Hoffmann, C. Thomsen, T. Böttcher, S. Einfeldt and D. Hommel
Evidence for phase seperation in InGaN by resonant Raman scattering
phys. stat. sol. (a) **179**, R4 (2000).

13. H.Selke, M.Amirsawadkouhi, P.Ryder, T.Böttcher, S.Einfeldt, D.Hommel, F.Bertram and J.Christen
Compositional inhomogeneities in InGaN studied by transmission electron microscopy and spatially resolved cathodoluminescence
Mater. Sci. Eng. B **59**, 279 (1999).

14. S. Einfeldt, T. Böttcher, D. Hommel, H. Selke, P.L. Ryder, F. Bertram, T. Riemann, D. Rudloff and J. Christen
Statistical analysis of local composition and luminescence in InGaN grown by molecular beam epitaxy
MRS Internet J. Nitride Semicond. Res. **4S1**, G 3.33 (1999).

15. S. Figge, T. Böttcher, S. Einfeldt, D. Hommel, H. Selke, P.L. Ryder, S. Keller and S.P. DenBaars
On the photoluminescence of InGaN quantum well structures grown by different techniques
Proc. 8th Europ. Workshop on MOVPE and Related Growth Techniques, 65 (1999).

16. D. Rudloff, F. Bertram, T. Riemann, J. Christen, H. Selke, T. Böttcher, S. Einfeldt, D. Hommel and K. Hiramatsu
Direct imaging of the crystalline and chemical nanostrucure of Ga, In - Nitrides by highly spatially, spectrally and time-resolved cathodoluminescence
Solid State Phenom. **63**, 221 (1998).

17. M. Rajeswari, R. Shreekala, A. Goyal, S.E. Lofland, S.M. Bhagat, K. Gosh, R.P. Sharma, R.L. Greene, R. Ramesh, T. Venkatesan and T. Böttcher
Correlation between homogeneity, oxygen content, and electrical and magnetic properties of perovskite manganite thin films
Appl. Phys. Lett. **73**, 260 (1998).

18. A. Goyal, M. Rajeswari, R. Shreekala, S.E. Lofland, S.M. Bhagat, T. Böttcher, C. Kwon, R. Ramesh and T. Venkatesan
Material characteristics of perovskite manganese oxide thin films for bolometric applications
Appl. Phys. Lett. **71**, 2535 (1997).

19. R. Shreekala, M. Rajeswari, K. Gosh, A. Goyal, J.Y. Gu, C. Kwon, Z. Trajanovic, T. Böttcher, R.L. Greene, R. Ramesh and T. Venkatesan
Effect of crystallinity on the magnetoresistance in perovskite manganese oxide thin films
Appl. Phys. Lett. **71**, 282 (1997).

20. Z.W. Dong, Z. Trajanovic, T. Böttcher, I. Takeuchi, V. Talyanski, C-H. Chen, R.P. Sharma, R. Ramesh and T. Venkatesan
Studies of ferroelectric field effects in Pt/PZTO/YBCO heterostructures
IEEE Trans. Appl. Supercond. **7**, 3516 (1997).

21. Z.W. Dong, T. Böttcher, C.H. Chen, I. Takeuchi, M. Rajeswari, R.P. Sharma and T. Venkatesan
Enhancement of low field magnetoresistance in YBCO/NSMO Heterostructures
IEEE Trans. Appl. Supercond. **7**, 2173 (1997).

22. Z.W. Dong, Z. Trajanovic, T. Böttcher, I. Takeuchi, V. Talyanski, C.H. Chen, R. Ramesh and T. Venkatesan
Ferroelectric field effects in YBCO/PZTO/Au Heterostructures
Proceedings of the "3rd HTS-Workshop on digital applications, josephson junctions and 3-terminal devices", Enschede, Netherlands, 93 (1997).

23. Z.W. Dong, T. Böttcher, C.H. Chen, I. Takeuchi, M. Rajeswari, R.P. Sharma and T. Venkatesan
Enhanced magnetoresistance in YBCO/NSMO heterostructures using magnetic flux focusing
Appl. Phys. Lett. **69**, 3432 (1996).

First-author conference presentations :

1. T. Böttcher, R. Chierchia, L. Kahrs, H. Heinke, S. Einfeldt, D. Hommel, J. Speck
Mosaicity and strain in high temperature island coalescence of GaN
The Fourth International Conference on Nitride Semiconductors, Denver, USA (2001).

2. T. Böttcher, S. Einfeldt, S. Figge, M. Dießelberg, R. Chierchia, V. Kirchner, H. Heinke, D. Hommel and J.S. Speck
Einfluss der Inselkoaleszenz auf die Verspannung von GaN Schichten
Tagung der Deutschen Physikalischen Gesellschaft, Hamburg, Germany (2001).

3. T. Böttcher, S. Einfeldt, S. Figge, M. Dießelberg, R. Chierchia, V. Kirchner, H. Heinke and D. Hommel
The role of film coalescence for defect formation and thermally induced strain in GaN epilayers
Fall Meeting of the Materials Research Society, Boston (2000).

4. T. Böttcher, S. Figge, S. Einfeldt, H.Tran, P.L.Ryder and D. Hommel
Evolution of GaN films and defect generation during MOVPE growth at different pressures
Fourth European GaN Workshop, Nottingham, Great Britain (2000).

5. T. Böttcher, S. Einfeldt, S. Figge, V. Kirchner, H. Heinke, D. Hommel, H. Selke, H. Tran, P.L. Ryder, D. Rudloff, T. Riemann and J. Christen
Einfluß der Defektdichte und Grenzflächenrauhigkeit auf die Lumineszenz von InGaN/GaN Mehrfachquantentrögen
Photonik-Symposium der Volkswagen-Stiftung, HANIEL-Akademie, Duisburg, Germany (1999).

6. T. Böttcher, S. Einfeldt, S. Figge, V. Kirchner, H. Heinke, D. Hommel, D. Rudloff, T. Riemann and J. Christen
On the impact of microstructure on luminescence of InGaN/GaN multi quantum wells grown by molecular beam epitaxy
The Third International Conference on Nitride Semiconductors, Montpellier, France (1999).

7. T. Böttcher, S. Einfeldt, S. Figge, V. Kirchner, H. Heinke, D. Hommel, F. Bertram and J. Christen
Molecular Beam Epitaxy and Microstructure of InGaN
International School on Physics of Semiconducting Compounds, Jaszowiec, Poland (1998).

8. T. Böttcher, S. Einfeldt, C. Fechtmann, V. Kirchner, H. Selke, F. Bertram, J. Christen and D. Hommel
MBE Wachstum von InGaN
Tagung der Deutschen Physikalischen Gesellschaft, Regensburg, Germany (1998).

9. T. Böttcher, S. Einfeldt, C. Fechtmann, V. Kirchner, H. Heinke and D. Hommel
MBE Growth of InGaN
International Workshop on Surface Morphology, Interfaces and Growth of the III-Nitrides, Rottach-Egern, Germany (1998).

10. T. Böttcher, Z.W. Dong, C.H. Chen, V. Talyanski, C. Kwon, M. Rajeswari and T. Venkatesan
Possibility of enhanced low field MR effects in HTS/CMR heterostructures
March meeting of the American Physical Society, St. Louis, USA (1996).

Patent :

1. *Magnetic Flux Focusing of High-Tc Superconductors for Improvement of Magnetoresistive Effects*
University of Maryland Invention Disclosure PS-96-016

Bibliography

[1] F. Fichter, Z. Anorg. Chem. **54**, 322 (1907).

[2] W. Johnson, J. Parsons, M. Crew, J. Phys. Chem. **234**, 2651 (1932).

[3] H. Manasevit, F. Erdmann, W. Simpson, J. Electrochem. Soc. **118**, 1864 (1971).

[4] R. Dingle, D. Sell, S. Stokowski, M. Ilegems, Phys. Rev. B **4**, 1211 (1971).

[5] H. Maruska, J. Tietjen, Appl. Phys. Lett. **15**, 327 (1969).

[6] J. Pankove, *Nitride Semiconductors and Devices*, page XV, Springer, New York, 1999.

[7] H. Amano, M. Kito, K. Hiramatsu, I. Akasaki, Jpn. J. Appl. Phys. (Part 2) **28**, 2112 (1989).

[8] S. Nakamura, T. Mukai, M. Senoh, Jpn. J. Appl. Phys. (Part 2) **30**, 1998 (1991).

[9] S. Nakamura, M. Senoh, N. Iwasa, S. Nagahama, Jpn. J. Appl. Phys. (Part 1) **34**, 1797 (1995).

[10] S. Nakamura, G. Fasol, *The blue laser diode*, Springer Verlag, Berlin Heidelberg New York, 1997.

[11] H. Morkoc, *Nitride Semiconductors and Devices*, Springer Series in Materials Science, Springer, New York, 1999.

[12] O. Ambacher, B. Foutz, J. Smart, J. Shealy, N. Weimann, K. Chu, M. Murphy, A. Sierakowski, W. Schaff, L. Eastman, R. Dimitrov, A. Mitchell, M. Stutzmann, J. Appl. Phys. **87**, 334 (1999).

[13] J. Neugebauer, phys. stat. sol. (b) **227**, 93 (2001).

[14] A. Smith, R. Feenstra, D. Greve, J. Neugebauer, J. Northrup, Appl. Phys. A **66**, S947 (1998).

[15] A. Smith, R. Feenstra, D. Greve, M. Shin, M. Skowronski, J. Neugebauer, J. Northrup, Surf. Sci. **423**, 70 (1999).

[16] S. Pearton, J. Zolper, R. Shul, F. Ren, J. Appl. Phys. **86**, 1 (1999).

[17] F. Ponce, *Group III Nitride Semiconductor Componds*, Oxford University Press, New York, 1998.

[18] T. Ochalski, B. Gil, P. Lefebvre, F. Grandjean, M. Leroux, J. Massies, S. Nakamura, Morkoc H, Appl. Phys. Lett. **74**, 3353 (1999).

[19] W. Yim, E. Stofko, P. Zanzucchi, J. Pankove, M. Ettenberg, S. Gilbert, J. Appl. Phys. **44**, 292 (1973).

[20] H. Jiang, G. Zhao, H. Ishikawa, T. Egawa, T. Jimbo, M. Umeno, J. Appl. Phys. **89**, 1046 (2001).

[21] S. Lee, A. Wright, M. Crawford, G. Petersen, J. Han, R. Biefeld, Appl. Phys. Lett. **74**, 3344 (1999).

[22] G. Steude, B. Meyer, A. Göldner, A. Hoffmann, F. Bertram, J. Christen, H. Amano, I. Akasaki, Appl. Phys. Lett. **74**, 2456 (1999).

[23] T. Takeuchi, H. Takeuchi, S. Sota, H. Sakai, H. Amano, I. Akasaki, Jpn. J. Appl. Phys. (Part 2) **36**, 177 (1997).

[24] G. Popovici, H. Morkoc, S. Mohammad, *Group III Nitride Semiconductor Compounds*, 19 – 69, Clarendon University Press, Oxford, 1998.

[25] S. Pereira, M. Correia, T. Monteiro, E. Pereira, M. Soares, E. Alves, J. Cryst. Growth **230**, 448 (2001).

[26] M. McCluskey, C. Van der Walle, C. Master, L. Romano, N. Johnson, Appl. Phys. Lett. **72**, 2725 (1998).

[27] L. Bellaiche, T. Mattila, L. Wang, S. Wei, A. Zunger, Appl. Phys. Lett. **74**, 1842 (1999).

[28] H. Schenk, P. de Mierry, M. Laugt, F. Omnes, M. Leroux, B. Beaumont, P. Gibart, Appl. Phys. Lett. **75**, 2587 (1999).

[29] G. Martin, S. Strite, B. Botchkarev, A. Agarwal, A. Rockett, H. Morkoc, W. R. L. Lambrecht, B. Segall, Appl. Phys. Lett. **65**, 610 (1994).

[30] J. Baur, K. Mauer, M. Kunzer, U. Kaufmann, J. Schneider, Appl. Phys. Lett. **65**, 2211 (1994).

[31] J. Waldrop, R. Grant, Appl. Phys. Lett. **68**, 2879 (1996).

[32] S. King, C. Ronning, R. Davis, M. Benjamin, R. Nemanich, J. Appl. Phys. **84**, 2086 (1998).

[33] S. H. Ke, K. M. Zhang, X. Xie, J. Appl. Phys. **80**, 2918 (1996).

[34] M. Nardelli, K. Rapcewicz, J. Bernholc, Phys. Rev. B **55**, 7323 (1996).

[35] M. B. Nardelli, K. Rapcewicz, J. Bernholc, J. Vac. Sci. Tech. B **15**, 1144 (1997).

[36] F. Bernardini, V. Fiorenzini, Phys. Rev. B **57**, 9427 (1997).

[37] J. A. Majewski, M. Städele, Mat. Res. Soc. Symp. Proc. Vol. **482**, 917 (1998).

[38] C. VanderWalle, J. Neugebauer, Appl. Phys. Lett. **70**, 2577 (1997).

[39] S. Wei, A. Zunger, Appl. Phys. Lett. **69**, 2719 (1996).

[40] C. Chen, H. Chuang, G. Chi, C. Chuo, J. Chyi, Appl. Phys. Lett. **77**, 3758 (2000).

[41] C. Manz, M. Kunzer, H. Obloh, A. Ramakrishnan, K. U, Appl. Phys. Lett. **15**, 3993 (1999).

[42] D. Wood, *Optoelectronic Semiconductor Devices*, Prentice Hall, London, 1994.

[43] W. Goetz, N. Johnson, C. Chen, Appl. Phys. Lett. **68**, 3144 (1996).

[44] C. Yi, B. Wessels, Appl. Phys. Lett. **69**, 3026 (1996).

[45] S. Jain, M. Willander, J. Narayan, R. Van Overstraeten, J. Appl. Phys. **87**, 965 (2000).

[46] O. Ambacher, H. Angerer, R. Dimitrov, W. Rieger, M. Stutzmann, G. Dollinger, A. Bergmaier, phys. stat. sol. (a) **159**, 105 (1997).

[47] J. Neugebauer, W. Gotz, C. Van der Walle, in *Silicon Carbide and related materials*, vol. 142 from *Institute of Physics Conference Series*, page 1035 (1996).

[48] H. Amano, N. Sawaki, I. Akasaki, Y. Toyoda, Appl. Phys. Lett. **48**, 353 (1986).

[49] F. Bernardini, V. Fiorentini, D. Vanderbilt, Phys. Rev. B **56**, R10024 (1997).

[50] S. Mohmmad, H. Morkoc, Prog. Quant. Electron. **20**, 361 (1996).

[51] J. F. Nye, *Physical Properties of Crystals*, Oxford University Press, London, 1969.

[52] S. Chichibu, T. Sota, K. Wada, O. Brandt, K. Ploog, S. DenBaars, S. Nakamura, phys. stat. sol. (a) **183**, 91 (2001).

[53] C. Wetzel, S. Nitta, T. Takeuchi, S. Yamaguchi, H. Amano, I. Akasaki, MRS Internet J. Nitride Semicond. Res. **3**, 31 (1998).

[54] A. Hangleiter, J. Im, J. Off, F. Scholz, phys. stat. sol. (b) **216**, 427 (1999).

[55] C. Wetzel, T. Takeuchi, H. Amano, I. Akasaki, Jpn. J. Appl. Phys. (Part 2) **38**, 163 (1999).

[56] S. Chichibu, A. Abare, M. Minsky, T. Deguchi, S. Fleischer, S. Keller, J. Speck, J. Bowers, E. Hu, U. Mishra, L. Coldren, S. DenBaars, Appl. Phys. Lett. **73**, 2006 (1998).

[57] S. Chichibu, A. Shikanai, T. Deguchi, A. Setoguchi, R. Nakai, H. Nakanishi, K. Wada, S. DenBaars, T. Sota, S. Nakamura, Jpn. J. Appl. Phys. (Part 1) **39**, 2417 (2000).

[58] C. F. Klingshirn, *Semiconductor Optics*, Springer-Verlag, Berlin, 1997.

[59] E. Berkowicz, D. Geshoni, G. Bahir, E. Lakin, D. Shilo, E. Zolotoyabko, A. Abare, S. DenBaars, L. Coldren, Phys. Rev. B **61**, 10994 (2000).

[60] M. Leszczynski, H. Teisseyre, T. Suski, I. Grzegory, M. Bockowski, J. Jun, S. Porowski, K. Pakula, J. M. Baranowski, C. T. Foxon, T. S. Cheng, Appl. Phys. Lett. **1**, 73 (1996).

[61] K. Wang, R. R. Reeber, Mater. Res. Soc. Symp. Proc. **482**, 863 (1998).

[62] W. Paszkowicz, J. Adamczyc, S. Krukowski, M. Leszczynski, S. Porowski, J. A. Sokolowski, M. Michalec, W. Lasocha, Phil. Mag. A **79**, 1145 (1999).

[63] V. W. L. Chin, T. L. Tansley, T. Osotchan, J. Appl. Phys. **75**, 7365 (1996).

[64] H. Schulz, K. H. Thiemann, Solid State Commun. **23**, 815 (1977).

[65] E. Ruiz, S. Alvarez, P. Alemany, Phys. Rev. B **49**, 7115 (1994).

[66] T. Deguchi, D. Ichiryu, K. Toshikawa, K. Sekiguchi, T. Sota, R. Matsuo, T. Azuhata, M. Yamaguchi, T. Yagi, S. Chichibu, S. Nakamura, J. Appl. Phys. **86**, 1860 (1999).

[67] A. Polian, M. Grimsditch, I. Grzegory, J. Appl. Phys. **79**, 3343 (1996).

[68] K. Shimada, T. Sota, K. Suzuki, J. Appl. Phys. **84**, 4951 (1998).

[69] A. F. Wright, J. Appl. Phys. **82**, 2833 (1997).

[70] K. Kim, W. R. L. Lambrecht, B. Segall, Phys. Rev. B **56**, 16310 (1996).

[71] A. Deger, E. Born, H. Angerer, O. Ambacher, M. Stutzmann, J. Hornsteiner, E. Riha, G. Fischerauer, Appl. Phys. Lett. **72**, 2400 (1998).

[72] L. E. McNeil, M. Grimsditch, R. H. French, J. Am. Ceram. Soc. **76**, 1132 (1993).

[73] H. M. Manasevit, W. I. Simpson, J. Electrochem. Soc. **12**, 156 (1968).

[74] H. M. Manasevit, Appl. Phys. Lett. **116**, 1725 (1969).

[75] O. Ambacher, J. Phys. D **31**, 2653 (1997).

[76] G. Briot, *Group III Nitride Semiconductor Compounds*, Series on Semiconductor Science and Technology, Clarendon Press, Oxford, 1998.

[77] G. B. Stringfellow, *Organometalic vapor phase epitaxy*, Academic Press, San Diego, 1989.

[78] K. Günther, Z. Naturforsch. **13a**, 1081 (1958).

[79] J. Davey, T. Pankey, J. Appl. Phys. **39**, 1941 (1968).

[80] M. Herman, H. Sitter, *Molecular Beam Epitaxy, 2nd Edition*, Springer Verlag, Berlin, 1996.

[81] D. E. Aspnes, W. E. Quinn, S. Gregory, Appl. Phys. Lett. **56**, 2569 (1990).

[82] M. Ebert, K. A. Bell, S. D. Yoo, K. Flock, D. E. Aspnes, Thin Solid Films **364**, 22 (2000).

[83] S. Hearne, E. Chson, J. Han, J. A. Floro, J. Figiel, J. Hunter, H. Amano, I. S. T. Tsong, Appl. Phys. Lett. **74**, 356 (1999).

[84] K. Sugawara, T. Yoshimi, H. Okuyama, Y. Homma, J. Electrochem. Soc. **121**, 1233 (1974).

[85] S. J. C. Irvine, J. Bajaj, H. O. Sankur, J. Cryst. Growth **124**, 654 (1992).

[86] J. Hollemann, A. Hasper, J. Middelhoek, J. Electrochem. Soc. **138**, 783 (1991).

[87] O. Stenzel, *Das Dünnschichtspektrum*, Akademie Verlag, Berlin, 1996.

[88] H. A. Macleod, *Thin-film optical filters*, Adam Hilger Ltd., London, 1969.

[89] J. Petalas, S. Logothedis, S. Boultadakis, M. Aluani, J. M. Wills, J. Appl. Phys. **52**, 8082 (1995).

[90] U. Tisch, B. Meyler, O. Katz, E. Finkman, J. Salzman, J. Appl. Phys. **89**, 2676 (2001).

[91] A. Djusiric, E. H. Li, J. Appl. Phys. **85**, 2848 (1999).

[92] D. Brunner, H. Angerer, E. Bustarret, F. Freudenberg, R. Höpler, R. Dimitrov, O. Ambacher, M. Stutzmann, J. Appl. Phys. **82**, 5090 (1997).

[93] T. Kawashima, H. Yoshikawa, S. Adachi, S. Fuke, K. Ohtsuka, J. Appl. Phys. **82**, 3528 (1997).

[94] M. J. Bergmann, . Özgür, H. C. Casey, H. O. Everitt, J. F. Muth, Appl. Phys. Lett. **75**, 67 (1999).

[95] G. Yu, H. Ishikawa, M. Umeno, T. Egawa, J. Watanabe, T. Jimbo, T. Soga, Appl. Phys. Lett. **72**, 2202 (1998).

[96] Sapphire specification sheet, Roditi, 2001.

[97] W. D. Driscoll (Ed.), *Handbook of Optics*, McGraw-Hill, New York, 1978.

[98] T. Ng, J. Han, R. Biefeld, M. Weckwerth, J. Electr. Mat. **27**, 190 (1998).

[99] H. E. Bennett, J. O. Porteus, J. Opt. Soc. Am. **51**, 123 (1961).

[100] M. Schuster, P. O. Gervais, B. Jobst, W. Hösler, R. Averbeck, H. Riechert, A. Iberl, R. Stömmer, J. Phys. D **32**, A56 (1999).

[101] D. B. Williams, C. B. Carter, *Transmission Electron Microscopy*, Plenum Press, New York and London, 1996.

[102] K. Harafuji, Y. Hasegawa, A. Ishibashi, A. Tsujimura, I. Kidoguchi, Y. Ban, K. Ohnaka, Jpn. J. Appl. Phys. **39**, 6180 (2000).

[103] V. S. Ban, J. Electrochem. Soc. **119**, 761 (1972).

[104] A. Koukitu, T. Taki, N. Takahashi, H. Seki, J. Cryst. Growth **197**, 99 (1999).

[105] A. F. Hollemann, E. Wiberg, N. Wiberg, *Lehrbuch der Anorganischen Chemie*, Walter de Gruyter, Berlin, 1995.

[106] A. Koukitu, N. Takahashi, H. Seki, Jpn. J. Appl. Phys. **36**, L1136 (1997).

[107] D. D. Koleske, A. E. Wickenden, R. L. Henry, J. C. Culbertson, M. E. Twigg, J. Cryst. Growth **223**, 466 (2001).

[108] Z. A. Munir, A. W. Searcy, J. Chem. Phys. **42**, 4223 (1965).

[109] M. Furado, F. Jacob, J. Cryst. Growth **64**, 257 (1983).

[110] R. Logan, C. Thurmaond, J. Electrochem. Soc. **119**, 1727 (1972).

[111] D. D. Koleske, A. E. Wickenden, R. L. Henry, M. E. Twigg, J. C. Culbertson, Appl. Phys. Lett. **73**, 2018 (1998).

[112] M. Mayumi, F. Satoh, Y. Kumagai, K. Takemoto, A. Koukitu, Jpn. J. Appl. Phys. **39**, L707 (2000).

[113] M. Mayumi, F. Satoh, Y. Kumagai, A. Koukitu, Jpn. J. Appl. Phys. **40**, L654 (2001).

[114] S. Duan, D. Lu, Mat. Res. Soc. Symp. Proc. **468**, 81 (1997).

[115] J. Matthews, A. Blakeslee, J. Cryst. Growth **32**, 265 (1974).

[116] V. Kirchner, H. Heinke, D. Hommel, J. Z. Domagala, M. Leszczynski, Appl. Phys. Lett. **77**, 1434 (2000).

[117] T. Boettcher, S. Einfeldt, S. Figge, R. Chierchia, H. Heinke, D. Hommel, J. Speck, Appl. Phys. Lett. **78**, 1976 (2001).

[118] B. Kosicki, D. Kahng, J. Vac. Sci. Tech. **6**, 593 (1969).

[119] I. Akasaki, H Amano, Y Koide, K Hiramatsu, N Sawaki, J. Cryst. Growth **98**, 209 (1988).

[120] X. Wu, L. Brown, D. Kapolnek, S. Keller, B. Keller, S. DenBaars, J. Speck, J. Appl. Phys. **80**, 3228 (1996).

[121] J. Kim, S. Choi, J. Choi, K. Kim, G. Yang, C. Hong, K. Lim, H. Lee, Jpn. J. Appl. Phys. (Part 1) **38**, 2721 (1999).

[122] M. Diesselberg, *MOVPE Wachstum von AlGaN*, Diploma thesis, University of Bremen, 2001.

[123] X. Wu, P. Fini, E. Tarsa, B. Heying, S. Keller, U. Mishra, S. DenBaars, J. Speck, J. Cryst. Growth **189/190**, 231 (1998).

[124] S. Keller, B. Keller, Y. Wu, B. Heying, D. Kapolnek, J. Speck, U. Mishra, S. DenBaars, Appl. Phys. Lett. **68**, 1525 (1996).

[125] X. Wu, D. Kapolnek, E. Tarsa, B. Heying, S. Keller, B. Keller, U. Mishra, S. DenBaars, J. Speck, Appl. Phys. Lett. **68**, 1371 (1996).

[126] A. Munkholm, C. Thompson, C. Foster, J. Eastman, O. Auciello, G. Stephenson, P. Fini, S. DenBaars, J. Speck, Appl. Phys. Lett. **72**, 2972 (1998).

[127] R. M. A. Azzam, N. M. Bashara, *Ellipsomety and polarized light*, North Holland, New York, 1988.

[128] P. Fini, *Threading dislocation reduction in Gallium Nitride thin films on sapphire via lateral overgrowth*, Ph.D. thesis, University of Santa Barbara at California, USA, 2000.

[129] K. Kim, C. Oh, K. Lee, G. Yang, C.-H. Hong, K. Lim, H. Lee, A. Yoshikawa, J. Appl. Phys. **85**, 8441 (1999).

[130] A. Wickenden, D. Koleske, R. Henry, R. Gorman, J. Culbertson, M. Twigg, J. Electr. Mat. **28**, 301 (1999).

[131] K. Hiramatsu, S. Itoh, H. Amano, I. Akasaki, N. Kuwano, T. Shiraishi, K. Oh, J. Cryst. Growth **115**, 628 (1991).

[132] X. Wu, P. Fini, S. Keller, E. Tarsa, B. Heying, U. Mishra, S. DenBaars, J. Speck, Jpn. J. Appl. Phys. (Part 2) **35**, 1648 (1996).

[133] P. Fini, X. Wu, E. Tarsa, Y. Golan, V. Srikant, S. Keller, S. DenBaars, J. Speck, Jpn. J. Appl. Phys. **37 Part I**, 4460 (1998).

[134] H. Marchand, J. Ibbetson, P. Fini, X. Wu, S. Keller, S. DenBaars, J. Speck, U. Mishra, MRS Internet J. Nitride Semicond. Res. **4S1**, G4.5 (1999).

[135] F. Ponce, MRS Bulletin **22**, 51 (1997).

[136] T. Hino, S. Tomiya, T. Miyajima, K. Yanashima, S. Hasimoto, M. Ikeda, Appl. Phys. Lett. **76**, 3421 (2000).

[137] S. Figge, T. Böttcher, S. Einfeldt, D. Hommel, J. Cryst. Growth **221**, 262 (2000).

[138] S. Haffouz, H. Lahreche, P. Vennegues, P. DeMierry, B. Beaumont, F. Omnes, P. Gibart, Appl. Phys. Lett. **73**, 1278 (1998).

[139] H. Amano, M. Iwaya, T. Kashima, M. Katsuragawa, I. Akasaki, J. Han, S. Hearne, J. Floro, E. Chason, J. Figiel, Jpn. J. Appl. Phys. (Part 2) **37**, L1540 (1998).

[140] A. Sakai, H. Sunakawa, A. Usui, Appl. Phys. Lett. **71**, 2259 (1997).

[141] S. Keller, D. Kapolnek, Y. Wu, B. Heying, J. S. Speck, U. K. Mishra, S. P. DenBaars, Jpn. J. Appl. Phys (Part 2). **35**, L285 (1996).

[142] T. Yang, K. Uchida, T. Mishima, J. Kasai, J. Gotoh, phys. stat. sol. (a) **180**, 45 (2000).

[143] S. Tanaka, M. Takeuchi, Y. Aoyagi, Jpn. J. Appl. Phys. (Part 2) **39**, L831 (2000).

[144] Y. Ohuchi, K. Tadatomo, H. Nakayama, N. Kaneda, T. Detchprohm, K. Hiramatsu, N. Sawaki, J. Cryst. Growth **170**, 325 (1997).

[145] S. Tanaka, I. Suemune, P. Ramvall, Y. Aoyagi, phys. stat. sol. (b) **216**, 431 (1999).

[146] T. Zheleva, O. Nam, M. Bremser, R. Davis, Appl. Phys. Lett. **71**, 2472 (1997).

[147] P. Vennegues, B. Beaumont, V. Bousquet, M. Vaille, P. Gibart, J. Appl. Phys. **87**, 4175 (2000).

[148] V. Belyi, *Silicon Nitride in Electronics*, vol. 34 from *Materials Science Monographs*, Elsevier, Amsterdam, 1988.

[149] M. Benyoucef, M. Kuball, H. H. Wills, G. Hill, M. W. B. Beaumont, P. Gibart, Appl. Phys. Lett **79**, 4127 (2001).

[150] P. Fewster, *X-Ray Scattering from Semiconductors*, Imperial College Press, London, 2000.

[151] B. Heying, X. Wu, S. Keller, Y. Li, D. Kapolnek, B. Keller, S. DenBaars, J. Speck, Appl. Phys. Lett. **68**, 643 (1996).

[152] V. Srikant, J. Speck, D. Clarke, J. Appl. Phys. **82**, 4286 (1997).

[153] L. Schwartz, J. Cohen, *Diffraction from Materials*, Academic Press, New York, 1977.

[154] T. Metzger, R. Höpler, E. Born, O. Ambacher, M. Stutzmann, R. Stömmer, M. Schuster, H. Göbel, S. Christiansen, M. Albrecht, H. Strunk, Philos. Mag. A **77**, 1013 (1998).

[155] J. Ayers, J. Cryst. Growth **135**, 71 (1994).

[156] C. Dunn, E. Koch, Acta metall. **5**, 548 (1957).

[157] H. Heinke, V. Kirchner, S. Einfeldt, D. Hommel, phys. stat. sol. (a) **176**, 391 (1999).

[158] B. Heying, E. Tarsa, C. Elsass, P. Fini, S. DenBaars, J. Speck, J. Appl. Phys. **85**, 6470 (1999).

[159] H. Heinke, V. Kirchner, S. Einfeldt, D. Hommel, Appl. Phys. Lett. **77**, 2145 (2000).

[160] A. Shikanai, T. Azuhata, T. Sota, S. Chichibu, A. Kuramata, A. Horino, S. Nakamura, J. Appl. Phys. **81**, 417 (1997).

[161] K. Funato, S. Hashimoto, K. Yanashima, F. Nakamura, M. Ikeda, Appl. Phys. Lett. **75**, 1137 (1999).

[162] R. Koch, J. Phys.: Cond. Matter **6**, 9519 (1994).

[163] Y. Touloukian, R. Kirby, R. Taylor, *Thermal Expansion-Nonmetallic Solids*, IFI/Plenum, New York, 1970.

[164] M. Lesczcynski, T. Suski, H. Teisseyre, P. Perlin, I. Grzegory, J. Jun, S. Porowski, T. Moustakas, J. Appl. Phys. **76**, 4909 (1994).

[165] M. Yi, D. Noh, Appl. Phys. Lett. **78**, 2443 (2001).

[166] S. Kaiser, H. Preis, W. Gebhardt, O. Ambacher, H. Angerer, M. Stutzmann, A. Rosenauer, D. Gerthsen, Jpn. J. Appl. Phys. **38**, 84 (1998).

[167] C. Kim, J. Je, M. Yi, D. Noh, F. Degave, P. Ruterana, Mat. Sci Eng. B **82**, 108 (2001).

[168] J. Fingegan, R. Hoffman, J. Appl. Phys. **30**, 587 (1959).

[169] D. Hull, D. Bacon, *Introduction to dislocations*, Butterworth - Heinemann, Oxford, 1984.

[170] W. D. Nix, B. M. Clemens, J. Mater. Res. **14**, 3467 (1999).

[171] B. Sheldon, H. Lau, A. Rajamani, Appl. Phys. Lett. **90**, 5097 (2001).

[172] J. Floro, E. Chason, R. Cammarata, D. Srolovitz, MRS Bulletin **27**, 19 (2002).

[173] V. Potin, P. Ruterana, G. Nouet, R. Pond, H. Morkoc, Phys. Rev. B **61**, 5587 (2000).

[174] S. Einfeldt, T. Böttcher, S. Figge, D. Hommel, J. Cryst. Growth **230**, 357 (2001).

[175] W. Shan, B. Little, A. Fischer, J. Song, D. Goldenberg, W. Perry, M. Bremser, R. Davis, Phys. Rev. B **54**, 16369 (1996).

[176] J. Baranowski, S. Porowski, *23rd Int. Conf. on The Physics of Semiconductors*, chapter 1, page 497, World Scientific, Singapore, 1996.

[177] N. Itoh, J. Rhee, T. Kawabata, S. Koike, J. Appl. Phys. **58**, 1828 (1985).

[178] J. Northrup, J. Neugebauer, R. Feenstra, A. Smith, Phys. Rev. B **61**, 9932 (2000).

[179] J. Neugebauer, T. Zywietz, M. Scheffler, J. Northrup, Appl. Surf. Sci. **159**, 359 (2000).

[180] E. Tarsa, B. Heying, X. Wu, P. Fini, S. DenBaars, J. Speck, J. Appl. Phys. (1997).

[181] T. Boettcher, S. Einfeldt, V. Kirchner, S. Figge, H. Heinke, D. Hommel, H. Selke, P. Ryder, Appl. Phys. Lett. **73**, 3232 (1998).

[182] T. Boettcher, *Molecular beam epitaxy of InGaN and its application in quantum well structures*, Diploma thesis, University of Bremen, 1998.

[183] H. Riechert, Molecular Beam Epitaxy of Group-III Nitrides, Presentation on International Workshop on Surface Morphology, Interfaces and Growth of the III-Nitrides, Rottach-Egern, Germany (1998), 1998.

[184] R. Averbeck, H. Riechert, phys. stat. sol. (a) **176**, 301 (1999).

[185] T. Boettcher, S. Einfeldt, S. Figge, V. Kirchner, H. Heinke, D. Hommel, D. Rudloff, T. Riemann, J. Christen, phys. stat. sol (a) **176**, 291 (1999).

[186] C. Wetzel, S. Fischer, J. Krüger, E. E. Haller, R. J. Molnar, T. D. Moustakas, M. E. N, P. G. Baranov, Appl. Phys. Lett. **68**, 2556 (1996).

[187] K. Uchida, T. Tang, S. Goto, T. Mishima, A. Niwa, J. Gotoh, Appl. Phys. Lett. **74**, 1153 (1999).

[188] L. Romano, J. Northrup, A. Ptak, T. Myers, Appl. Phys. Lett. **77**, 2479 (2000).

[189] S. Keller, S. Chichibu, M. Minsky, Hu. E, U. Mishra, S. DenBaars, J. Cryst. Growth **195**, 258 (1998).

[190] E. Piner, M. Behbehani, N. El-Masry, F. McIntosh, J. Roberts, K. Boutros, S. Bedair, Appl. Phys. Lett. **70**, 461 (1997).

[191] A. Koukitu, N. Takahashi, T. Taki, H. Seki, Jpn. J. Appl. Phys. (Part 2) **35**, 673 (1996).

[192] S. Keller, B. Keller, D. Kapolnek, A. Abare, L. Coldren, U. Mishra, S. Den Baars, Appl. Phys. Lett. **68**, 3147 (1996).

[193] J. Harris, H. Brisset, T. Someya, Y. Arakawa, Jpn. J Appl. Phys (Part 1) **38**, 2613 (1999).

[194] T. Matsuoka, N. Yoshimoto, T. Sasaki, A. Katsui, J. Electr. Mat. **21**, 157 (1992).

[195] S. Nakamura, T. Mukai, M. Senoh, Jpn. J. Appl. Phys. (Part 2) **32**, 16 (1993).

[196] P. Grudowski, C. Eiting, J. Park, B. Shelton, D. Lambert, R. Dupuis, Appl. Phys. Lett. **71**, 1537 (1997).

[197] M. Minsky, S. Chichibu, S. Fleischer, A. Abare, J. Bowers, E. Hu, S. Keller, U. Mishra, S. DenBaars, Jpn. J. Appl. Phys. (Part 2) **37**, 1362 (1998).

[198] Y. Cho, J. Song, S. Keller, M. Minsky, E. Hu, U. Mishra, S. DenBaars, Appl. Phys. Lett. **73**, 1128 (1998).

[199] S. Nakamura, M. Senoh, S. Nagahama, N. Iwasa, T. Yamada, T. Matsushita, Y. Sugimoto, H. Kiyoku, Appl. Phys. Lett. **70**, 1417 (1997).

[200] A. Munkholm, G. Stephenson, J. Eastman, O. Auciello, M. Ramana Murty, C. Thompson, P. Fini, J. Speck, S. DenBaars, J. Cryst. Growth **221**, 98 (2000).

[201] S. Chichibu, A. Abare, M. Mack, M. Minsky, T. Deguchi, D. Cohen, P. Kozodoy, S. Fleischer, S. Keller, J. Speck, J. Bowers, E. Hu, U. Mishra, L. Coldren, S. DenBaars, K. Wada, T. Sota, S. Nakamura, Materials Science and Engineering B **59**, 298 (1999).

[202] G. Snider, I. Tan, E. Hu, J. Appl. Phys. **68**, 2849 (1990).

[203] I. Tan, G. Snider, E. Hu, J. Appl. Phys. **68**, 4071 (1990).

[204] S. Rosner, G. Girolami, H. Marchand, P. Fini, J. Ibbetson, L. Zhao, S. Keller, U. Mishra, S. DenBaars, J. Speck, Appl. Phys. Lett. **74**, 2035 (1999).

[205] K. Leung, A. Wright, E. Stechel, Appl. Phys. Lett. **74**, 2495 (1999).

[206] J. Speck, S. Rosner, Physica B **273-274**, 24 (1999).

[207] S. Rosner, E. Carr, M. Ludowise, G. Girolami, H. Erikson, Appl. Phys. Lett **70**, 420 (1996).

[208] D. Cherns, S. J. Henley, F. A. Ponce, Appl. Phys. Lett. **78**, 2691 (2001).

[209] J. Speck, H. Marchand, P. Kozodoy, P. Fini, X. Wu, J. Ibbetson, S. Keller, S. DenBaars, S. Rosner, in *Proc. 2nd Int. Symp. Blue Laser and Light Emitting Diodes*, page 37 (1998).

[210] F. Ponce, S. Galloway, W. Goetz, R. Kern, Mater. Res. Soc. Symp. Proc. **482**, 625 (1998).

[211] H. Selke, M. Amirsawadkouhi, P. Ryder, T. Böttcher, S. Einfeldt, D. Hommel, F. Bertram, J. Christen, Mater. Sci. Eng. B **59**, 279 (1999).

[212] I. Ho, G. Stringfellow, J. Cryst. Growth **178**, 1 (1997).

[213] T. Miyajima, Y. Kudo, K. Liu, T. Uruga, T. Asatsuma, T. Hino, T. Kobayashi, phys. stat. sol. (b) **228**, 45 (2001).

[214] S. Keller, U. Mishra, S. DenBaars, W. Seifert, Jpn. J. Appl. Phys. (Part 2) **37**, 431 (1998).

[215] T. Miyajima, T. Hino, S. Tomiya, K. Yanashima, H. Nakajima, T. Araki, Y. Nanishi, A. Satake, Y. Masumoto, Y. Akimoto, T. Kobayashi, M. Ikeda, phys. stat. sol. (b) **228**, 395 (2001).

[216] W. G. Breiland, K. P. Killeen, J. Appl. Phys. **78**, 6726 (1995).

[217] G. Snider, *1DPoisson/Srödinger User´s manual*, University of Notre Dame, 1997.

[218] J. Huang, T. Kuech, H. Lu, I. Bhat, Appl. Phys. Lett. (1996).

[219] K. Kim, W. R. L. Lambrecht, B. Segall, M. van Schilfgaarde, Phys. Rev. B **56**, 7363 (1997).

[220] I. Vurgaftman, J. Meyer, L. Ram-Mohan, J. Appl. Phys. **89**, 5815 (2001).

[221] J. A. Majewski, M. Städele, P. Vogl, Mat. Res. Symp. Proc. **449**, 887 (1997).

[222] A. Satake, Y. Masumoto, T. Miyajima, T. Asatsuma, F. Nakamura, M. Ikeda, Phys. Rev. B **57**, R2040 (1997).

[223] G. Bunea, W. Herzog, M. Unlu, B. Goldberg, R. Molnar, Appl. Phys. Lett. **75**, 838 (1999).

Acknowledgment

The probably most essential ingredient for a successful and enjoyable work as a Ph.D. student is the surrounding atmosphere experienced every day. I had the luck to enjoy this truly stimulating and interdisciplinary environment in all research groups I have joined so far. I have spent most of this time in the group of Prof. D. Hommel, whose free understanding of research allowed me to develop my own direction of research and explore the wide diversity of science. The same applies to Prof. J. Speck, whose critical review of ideas helped me a lot to develop a consistent model of coalescence.

From the early days on, Sven Einfeldt supported my research with patience and attention, and was always open to questions of any kind. He was not only my comrade-in-arms during the early days of MOVPE, but became a good friend beyond life in university. Together with him and Stephan Figge I felt the power of teamwork, since we formed the core of the GaN epitaxy team.

In spite of the sometimes very discouraging findings, I am indebted to Roland Kröger, Hartmut Selke, Jin-Ping Zhang and Lifan Chen, who characterized many of the structures I grew and introduced me to the world of transmission electron microscopy. In particular, I have enjoyed the deep dicussions with Roland and Hartmut, sometimes deviating from the subject of science. Much of the structural characterization was supported by the ladies from reciprocal space - Heidrun Heinke, Rosa Chierchia and Claudia Roder, who only rarely complained about extensive measurement sessions. Their enormous flexibility enabled the rapid progress we made in epitaxy.

The progress in devices was only possible due to the support of Sonja Hesselmann and Kalle Vennen-Damm, who kept all the equipment running. And there would probably be no operating laser diode in Bremen without Christoph Zellweger and Christian Petter, who processed all the grown structures. In this context all the people performing additional measurements should be mentioned. Carsten Kruse, Lüder Kahrs and Lutz Menzel helped with the measurement of many samples in photoluminescence, Frank Bertram and Dirk Rudloff provided insight into the structure of luminescence from their cathodoluminescence images, Alex Kasic sent experimental data describing the dispersion relation of the nitrides, Martin Vehse, Manfred Röwe and Stefan Strauf were excellent housemates during the last ICNS in Denver and were spending weeks on the detailed optical characterization of my samples. Arne Gust and Jens Dennemarck performed a lot of pioneering work in the setup of new equipment within the workgroup, which will hopefully be fruitful in future.

I would not have enjoyed the life at university as I did without my officemates Stephan, Matthias, Rosa, Claudia, Dan, Christy and Peter. We shared much of the joy and frustration of research, in particular epitaxy by-which-method-ever (MBE = **m**ostly

broken **e**quipment...). Dropping everything and enjoying a life out of university was encouraged by the friends I found at school, as there were in no particular order Sven, Stephan, Matthias, Christoph, Ed and Arne, Jose, Tadao, Anil, Fred and Cindy.

Last, but certainly not least, I would like to thank my large (and in future even extended) family. Without their encouragement I would probably never have studied physics. My girlfriend and future wife Anja has always helped me to keep in touch with the "real" life and supported me when I most needed it. Specially, the last half year would not have been as easy as it was with hindsight.

Curriculum Vitae

Name	Tim Böttcher
Born	21. August 1970 in Bremen
Address	Schlehenkamp 19 28844 Weyhe
Education	1998 until today - Ph.D. student in physics, University of Bremen September until December 2000 - exchange student at the University of California at Santa Barbara, USA March 1998 - Diplom ´Molecular beam epitaxy of InGaN and its application in quantum well structures´ (1.0) 1995 until 1996 - exchange student at the University of Maryland at College Park, USA (one academic year) 1992 until 1998 - Diplomstudium in physics, University of Bremen
Professional Activities	1992 - occupation as Emergency Medical Technician
Civilian Service	1990 until 1991 - Rettungswache Wildeshausen education as Emergency Medical Technician